Micromechanical Modelling of Rubbery Networks: Discrete and Continuum Approaches

Lucas Mangas Araujo

Department of Engineering Science
University of Oxford
Jesus College

A thesis submitted for the degree of

Doctor of Philosophy

Trinity Term, 2025

Abstract

Many soft materials consist of rubbery networks of polymer chains held together by crosslinks. These materials can undergo large elastic deformations, making them attractive to engineering, biomedical and consumer applications. Their mechanical response is intimately linked to the architecture of the underlying network. Consequently, understanding and predicting their behaviour requires models that account for their microstructure. This thesis contributes to this goal through the development of a comprehensive micromechanical modelling framework that combines discrete network (DN) simulations with continuum theories, enabling systematic investigations of elasticity, failure, and chemical degradation in rubber-like materials. In elasticity, we use DN simulations to link network structure to macroscopic mechanical properties, identifying the distribution of initial chain end-to-end distances as a key factor. Using DN results as a reference, we further show that many of the underlying assumptions of continuum micromechanics models do not hold. In modelling failure, the DN model augmented with deterministic chain scission reveals that damage is a localised process significantly impacted by local microstructural heterogeneities. Our results also show that classical semi-analytical estimates cannot predict failure in DNs. In chemical degradation, our DN model combined with stochastic chain scission shows that force-biased chain cleavage accelerates degradation, a feature captured by the continuum model we proposed. However, DN simulations reveal additional effects that cannot be reproduced by the continuum model, such as anisotropic damage and more severe deterioration of elastic properties as scissions become increasingly force-biased. Altogether, this thesis gives fresh insights into the mechanics of rubbery networks, important for the development of constitutive theories with improved predictive capabilities.

Acknowledgments

Foremost, I would like to express my sincere gratitude to my supervisor, Professor Laurence Brassart, for her continuous guidance, support, and genuine interest in my work. Your expertise, thoughtful feedback, and encouragement have been fundamental to my growth as both a mechanician and a researcher. It has been a privilege to work with you, and I have truly valued the years we worked together.

I want to thank Ivan Kryven, who kindly hosted me at Utrecht University. Your guidance was instrumental in developing the computational framework that underpins much of this thesis. Your contribution was important at several key stages.

I am grateful to the Clarendon Fund and Jesus College for their generous financial support, which made my doctoral studies at Oxford possible.

To my office friends Dr. Gordon, Dr. Huanming, Jie, Thales, Yifei, and Professor Zhouzhou, thank you for making our shared space both enjoyable and enriching. Your support made a real difference in my daily life.

To my Brazilian friends at Oxford, Ana Andrade, Ana Dallagnol, Arthur, Caio, Fernanda Galera, Fernanda Gonçalves, Igor, and Juliana, thank you for the laughter, companionship, and unforgettable moments. Your friendship brought joy and a sense of home throughout this journey.

To my friends Christoforos, Dany, Francis, Frank, Kyu Min, Munib, and Sigbjorn, thank you for the memorable moments we shared during our time at Jesus College. Your friendship made this experience meaningful.

To Dr. Katarzyna Chwalenia, thank you for your support, encouragement, and the many meaningful moments we shared. Your companionship during an important part of this journey was deeply appreciated and contributed to my personal growth.

I would like to thank my former undergraduate and master's supervisor, Professor Lucival

Malcher, for his unwavering support and guidance. I am sincerely grateful for the many opportunities he provided, which played a fundamental role in shaping my academic and professional path.

To my dear friends in Brasília, Alexandre, André, Estevan, Flávia, Gabriel, Igor, Karen, Leônidas, Lívia, Luisa, Luiz Gustavo, Marcos, Pedro, Rafael, Dr. Raíssa, and Victor, thank you for your constant encouragement and for always welcoming me home with warmth and joy. Your friendship remains a lasting source of strength.

I would like to thank my grandparents, Edith, Francisco, Gloria, and Oyma, for their love, support, and prayers. The values you passed on and the care you have always shown gave me strength and direction throughout this journey. I am also grateful to my uncle Guga, my aunt Lilian, and my cousins Giulia and Luisa for their support and the many joyful family moments we shared. Your presence and affection have always meant a great deal to me. To my brother Rafael, thank you for your love, support, and constant companionship. Growing up with you has been one of the greatest joys of my life.

I would also like to thank Marlucy for her dedication and care over the years. Your support allowed me to focus on my studies, and your kindness to my family has always meant more than words can say.

Finally, and most importantly, I would like to thank my parents, Alex and Bia. Your unconditional love, support, and wisdom have shaped the person I am today. I am deeply grateful for everything you have done for me and Rafael, for the education, peace, tenderness, and stability you always provided. Your presence has been a foundation in our lives, and I carry your values with me every day.

Contents

Chapter 1

Introduction

Many soft materials, such as elastomers and hydrogels, are rubbery networks consisting of polymer chains held together by crosslinks (Fig. 1.1). These materials are appealing in a range of applications due to their remarkable properties, such as high stretchability, low stiffness, low weight, and biocompatibility. For instance, elastomers are the primary choice in many engineering applications, such as tyres (Pal et al., 2011; Hashemi et al., 2020), hoses (Mars and Fatemi, 2002), seals (Patel et al., 2019), and belts (Mars and Fatemi, 2002). Hydrogels have been extensively used in biomedical applications, ranging from everyday items like diapers (Masuda, 1994) and contact lenses (Caló and Khutoryanskiy, 2015), to advanced ones such as drug delivery (Huebsch et al., 2014; Merino et al., 2015) and tissue engineering (Censi et al., 2012; Wang et al., 2017; Xue et al., 2021). Moreover, rubbery networks are increasingly being explored in emerging fields like stretchable electronics (Lee et al., 2018; Bian et al., 2020), soft robotics (Breger et al., 2015; Coyle et al., 2018) and energy harvesting (Manikkavel et al., 2020).

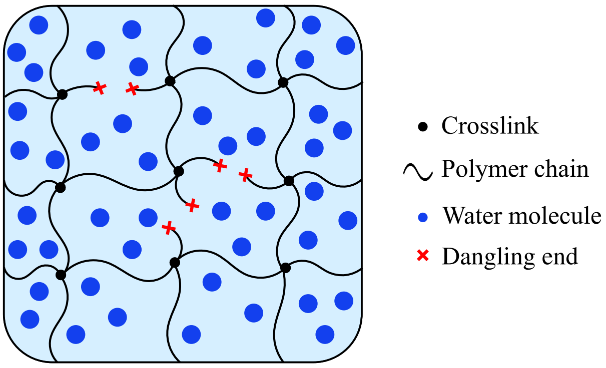

Fig. 1.1: Illustration of a rubbery polymer network. In hydrogels, the network is swollen by water.

The mechanical behaviour of rubbery networks is intimately linked with the underlying architecture of the network. For example, the remarkable elasticity and strength exhibited by tetra-PEG gels have been attributed to their near-ideal structure containing very few structural defects (e.g. loops and dangling chains) (Sakai et al., 2008; Matsunaga et al., 2009). Therefore, understanding and predicting the behaviour of rubbery networks requires modelling approaches that account for their microstructure. Micromechanical models achieve this by adopting a bottom-up approach, in which the overall macroscopic response is obtained from a description of the network architecture and the behaviour of individual chains, as illustrated in Fig. 1.2. Consequently, the predicted macroscopic behaviour reflects both the response of single chains and their collective deformation when the network is subjected to external loads.

The network architecture plays a central role in micromechanical models, as it controls the partitioning of forces among the chains. In realistic networks, chains are randomly distributed in space with varying lengths, and the structure often includes defects. This architectural complexity presents significant challenges for micromechanical modelling. To circumvent these difficulties, current continuum micromechanics models for rubber elasticity adopt simplifying assumptions that reduce the network to a set of representative chains, whose response is averaged over all or specific orientations in space (Wu and Van Der Giessen, 1993; Arruda and Boyce, 1993; Miehe et al., 2004). As a result, the overall macroscopic response can be obtained without resolving microstructural features, thus providing a convenient mechanistic modelling tool. However, this also makes these models intrinsically limited, as the structure of the polymer network is overlooked.

Discrete Network (DN) models have recently emerged as promising tools to address these limitations. This mesoscopic approach represents the molecular network as a collection of springs that mimic the behaviour of single chains. These springs are connected at junction points, and their positions are dictated by mechanical equilibrium. This approach maintains the single chain treatment of rubber elasticity while explicitly accounting for the network architecture. As such, DN models offer a convenient framework for systematically investigating the structure-property relationships in soft materials, such as the role of network defects in mechanical behaviour (Sugimura et al., 2013; Alamé and Brassart, 2020; Wagner et al., 2022; Araujo et al., 2024a), and the connections between microscopic chain scissions and macroscopic

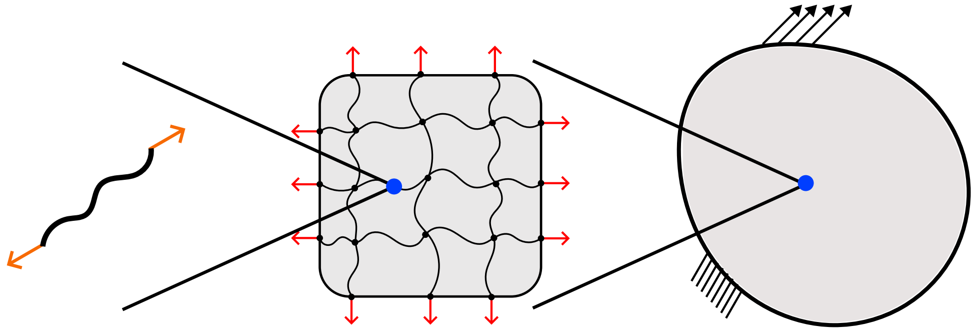

Fig. 1.2: Illustration of the bottom-up modelling strategy employed in micromechanical models for rubbery networks.

failure (Ghareeb and Elbanna, 2020; Lei and Liu, 2022; Deng et al., 2023).

By explicitly resolving essential microstructural features of the network, DN models serve as computationally efficient alternatives to high-fidelity molecular dynamics simulations. At the same time, they can reveal mechanisms inaccessible to conventional continuum approaches. Moreover, due to their shared theoretical foundations, DNs can serve as a benchmark to assess and validate assumptions underlying continuum theories. In fact, continuum micromechanics models can be interpreted as mean-field approximations of DNs. Insights gained from DN simulations can further guide refinements to existing continuum approaches or support the development of new constitutive models that better capture the interplay between network structure and mechanical response (Alamé and Brassart, 2020; Britt and Ehret, 2022; Araujo et al., 2024a).

The central objective of this thesis is to develop a comprehensive micromechanical modelling framework capable of addressing multiple scenarios relevant to rubbery networks. Specific objectives include:

- Developing a general DN-based simulation platform to model the deformation and failure response of rubber-like materials.
- Investigating how microstructural features govern the macroscopic behaviour of rubbery networks using the new DN model.
- Assessing the predictive performance and underlying assumptions of continuum micromechanics models by benchmarking them against DN results.
- Refining existing continuum approaches or formulating new ones based on insights gained through DN simulations.

Taken together, the work presented in this thesis contributes to a deeper understanding of the mechanics of rubbery networks. By combining discrete and continuum approaches, it highlights the critical role of network architecture in determining the macroscopic behaviour and failure mechanisms. The DN-based framework developed here serves both as a predictive tool and a reference platform for evaluating theoretical assumptions, while the refinements proposed for the continuum approaches offer a more general foundation for future investigations. These contributions provide fresh insights that may inform the design and predictive modelling of advanced soft materials.

The remainder of this thesis is organised as follows. Chapter 2 presents an overview of modelling strategies for rubbery materials, with emphasis on micromechanical approaches and their theoretical foundations. A brief discussion of phenomenological models is also included for completeness. Chapter 3 introduces the new DN-based modelling tool, including the random network generation algorithm underpinning it. The framework is then used to investigate the elastic response of rubbery networks and to assess the performance of conventional micromechanical models. Chapter 4 incorporates deterministic chain scission into the DN model to analyse the role of force redistribution in fracture. The failure response obtained from DN simulations is then compared with predictions from semi-analytical models. Chapter 5 presents an extension of the DN platform to model chemical degradation in rubbery networks. Predictions from a state-of-the-art micromechanics-based continuum model are also compared with the discrete results. Finally, Chapter 6 summarises the key findings and discusses future research directions.

Supporting publications

- Araujo, L. M., Kryven, I., and Brassart, L. (2024a). Micromechanical modelling of rubbery networks: The role of chain pre-stretch. *International Journal of Non-Linear Mechanics*, 166:104834

- Araujo, L. M. and Brassart, L. (2025a). Force-biased chemical degradation in rubbery networks: Insights from discrete network simulations. *Extreme Mechanics Letters*, 77:102344

- Araujo, L. M. and Brassart, L. (2025b). Micromechanical modelling of failure in rubbery networks: the role of local heterogeneities. Manuscript in preparation

Chapter 2

Background

This chapter presents the theoretical foundations underpinning rubbery materials modelling and a detailed overview of the current approaches in this field. While a brief discussion of phenomenological models is included for completeness, we focus on micromechanics-based models. Both continuum and discrete approaches are discussed, covering elasticity, damage via chain scission and coupled problems.

2.1 Fundamentals of continuum mechanics

This section introduces the essential concepts and definitions of continuum mechanics that underpin the theoretical developments presented in this thesis. We outline notations and conventions, kinematic descriptions, balance equations and thermodynamic principles that serve as the groundwork for the models discussed in subsequent chapters. These fundamentals provide the theoretical foundation for the models and analyses developed throughout the thesis.

With a few exceptions, bold lowercase and uppercase letters denote vectors and second-order tensors, respectively, while scalars are represented by regular (non-bold) letters. The inner product between vectors $\boldsymbol{a}$ and $\boldsymbol{b}$ is written as $\boldsymbol{a} \cdot \boldsymbol{b}$, and the double contraction between second-order tensors $\boldsymbol{A}$ and $\boldsymbol{B}$ is denoted by $\boldsymbol{A} : \boldsymbol{B}$. The Euclidean norm of a vector $\boldsymbol{a}$ is denoted by $\|\boldsymbol{a}\|$. The dyadic (outer) product is expressed by the symbol $\otimes$. The trace and determinant of a second-order tensor $\boldsymbol{A}$ are written as $\mathrm{tr}(\boldsymbol{A})$ and $\det(\boldsymbol{A})$, respectively. The transpose of a tensor $\boldsymbol{A}$ is indicated by a superscript T, as in $\boldsymbol{A}^T$. The second-order identity tensor is denoted by $\mathbf{1}$. Additional symbols and operations will be defined in context as they

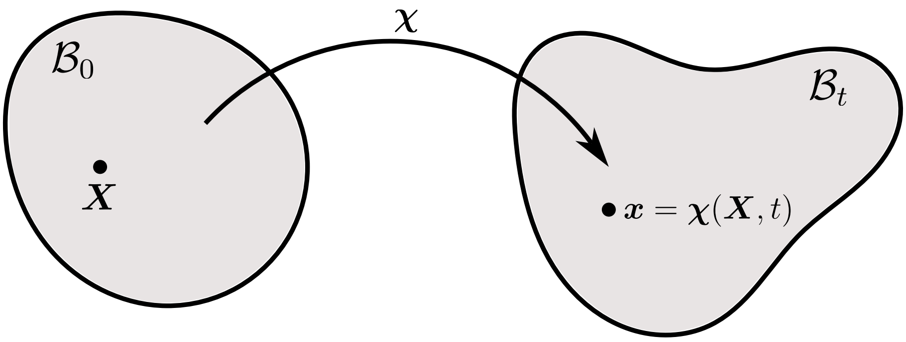

Fig. 2.1: Reference configuration $\mathcal{B}_0$ and current configuration $\mathcal{B}_t$ of a continuum body. The deformation map $\boldsymbol{\chi}$ indicates the position $\boldsymbol{x}$ in the current configuration occupied by a material point initially located at $\boldsymbol{X}$ in the reference configuration.

arise in subsequent chapters.

2.1.1 Kinematics

We consider a macroscopically homogeneous body described by a continuous distribution of matter in space and time. The regions of space that the body occupies at different times during deformation are referred to as configurations. In solid mechanics, it is customary to select one of these configurations as a reference. We denote this reference configuration by $\mathcal{B}_0$, which is assumed to correspond to time $t = 0$. The points in $\mathcal{B}_0$ are called material points and are represented by the vector $\boldsymbol{X}$. The current configuration of the body at a later time t is denoted by $\mathcal{B}_t$. The deformation of the body at any time t is described by a mapping $\boldsymbol{x} = \boldsymbol{\chi}(\boldsymbol{X}, t)$, which gives the position $\boldsymbol{x}$ currently occupied by the material point initially located at $\boldsymbol{X}$, as illustrated in Fig. 2.1.

The local deformation at $\boldsymbol{X}$ is described by the deformation gradient tensor $\boldsymbol{F}(\boldsymbol{X}, t)$:

$$\boldsymbol{F}(\boldsymbol{X}, t) \coloneqq \frac{\partial \boldsymbol{x}}{\partial \boldsymbol{X}} = \frac{\partial \boldsymbol{\chi}}{\partial \boldsymbol{X}}, \tag{2.1}$$

which maps infinitesimal material vectors $d\boldsymbol{X}$ to infinitesimal current vectors $d\boldsymbol{x}$. Moreover, the determinant $J = \det(\boldsymbol{F}(\boldsymbol{X}, t)) > 0$ represents the local volume change at $\boldsymbol{X}$. For brevity, the explicit dependence on spatial position and time will be omitted in the remainder of this chapter, unless required for clarity.

The polar decomposition theorem allows the deformation gradient $\boldsymbol{F}$ to be expressed as a combination of a stretch and a rotation:

$$\boldsymbol{F} = \boldsymbol{R}\boldsymbol{U} = \boldsymbol{V}\boldsymbol{R}, \tag{2.2}$$

where $\boldsymbol{U}$ and $\boldsymbol{V}$ are the right and left stretch tensors, respectively, and $\boldsymbol{R}$ is a rotation tensor. The tensors $\boldsymbol{U}$ and $\boldsymbol{V}$ are symmetric and positive-definite, whereas the rotation $\boldsymbol{R}$ satisfies $\boldsymbol{R}^T\boldsymbol{R} = \boldsymbol{R}\boldsymbol{R}^T = \mathbf{1}$ and $\det(\boldsymbol{R}) = 1$. It is often more convenient to work with the right $\boldsymbol{C}$ and left $\boldsymbol{B}$ Cauchy-Green tensors, defined as:

$$\boldsymbol{C} \coloneqq \boldsymbol{F}^T\boldsymbol{F}, \qquad \boldsymbol{B} \coloneqq \boldsymbol{F}\boldsymbol{F}^T, \tag{2.3}$$

from which, using Eq. (2.2), it follows that $\boldsymbol{C} = \boldsymbol{U}^2$ and $\boldsymbol{B} = \boldsymbol{V}^2$.

Since the stretch tensors $\boldsymbol{U}$ and $\boldsymbol{V}$ are symmetric and positive-definite, they admit the following spectral decompositions:

$$\boldsymbol{U} = \sum_{i=1}^{3} \lambda_i\, \boldsymbol{r}_i \otimes \boldsymbol{r}_{\boldsymbol{i}}, \qquad \boldsymbol{V} = \sum_{i=1}^{3} \lambda_i\, \boldsymbol{l}_i \otimes \boldsymbol{l}_{\boldsymbol{i}}, \tag{2.4}$$

where the principal stretches λ_i are the eigenvalues of both $\boldsymbol{U}$ and $\boldsymbol{V}$, and the principal directions $\boldsymbol{r}_i$ and $\boldsymbol{l}_i$ are the corresponding eigenvectors of $\boldsymbol{U}$ and $\boldsymbol{V}$, respectively. The principal directions $\boldsymbol{r}_i$ and $\boldsymbol{l}_i$ form orthonormal bases, i.e., $\boldsymbol{r}_i \cdot \boldsymbol{r}_j = 1$ if $i = j$ and 0 otherwise, and likewise for $\boldsymbol{l}_i$. From the spectral representation (2.4) and Eq. (2.2), it follows that $\boldsymbol{r}_i$ and $\boldsymbol{l}_i$ are related by $\boldsymbol{l}_i = \boldsymbol{R}\boldsymbol{r}_i$. Next, since $\boldsymbol{C} = \boldsymbol{U}^2$ and $\boldsymbol{B} = \boldsymbol{V}^2$, the Cauchy-Green tensors can also be represented in principal form as:

$$\boldsymbol{C} = \sum_{i=1}^{3} \lambda_i^2\, \boldsymbol{r}_i \otimes \boldsymbol{r}_{\boldsymbol{i}}, \qquad \boldsymbol{B} = \sum_{i=1}^{3} \lambda_i^2\, \boldsymbol{l}_i \otimes \boldsymbol{l}_{\boldsymbol{i}}. \tag{2.5}$$

2.1.2 Balance equations

Let $\mathcal{P}_0$ denote a subregion of the reference configuration $\mathcal{B}_0$, with $\boldsymbol{N}$ the outward unit normal to the surface $\partial\mathcal{P}_0$ of $\mathcal{P}_0$. Consider that $\mathcal{P}_0$ is subjected to surface tractions $\boldsymbol{t}_0(\boldsymbol{X}, t)$ (force per unit area in the reference configuration), and a field of body forces $\boldsymbol{b}_0(\boldsymbol{X}, t)$ (force per unit volume in the reference configuration). Neglecting inertial effects, force balance over an infinitesimally small subregion implies the local form:

$$\boldsymbol{\nabla} \cdot \boldsymbol{P} + \boldsymbol{b}_0 = \boldsymbol{0}, \tag{2.6}$$

where $\boldsymbol{P}$ denotes the first Piola-Kirchhoff stress tensor and $\boldsymbol{\nabla}\cdot$ represents the divergence operator taken with respect to the material coordinate $\boldsymbol{X}$. $\boldsymbol{P}$ and $\boldsymbol{t}_0$ are related by Cauchy's relation:

$$\boldsymbol{t}_0 = \boldsymbol{P}\boldsymbol{N}. \tag{2.7}$$

The balance of angular momentum requires that:

$$\boldsymbol{P}\boldsymbol{F}^T = \boldsymbol{F}\boldsymbol{P}^T. \tag{2.8}$$

We also recall the usual relations between the Cauchy stress tensor $\boldsymbol{\sigma}$ and the first Piola-Kirchhoff tensor:

$$\boldsymbol{P} = J\boldsymbol{\sigma}\boldsymbol{F}^{-T}, \qquad \boldsymbol{\sigma} = \frac{1}{J}\boldsymbol{P}\boldsymbol{F}^T. \tag{2.9}$$

Substituting Eq. (2.9) into Eq. (2.8) implies that $\boldsymbol{\sigma} = \boldsymbol{\sigma}^T$, and hence that the Cauchy stress tensor is symmetric, as expected.

Problems involving the transport of mobile species require the balance of species mass. Such problems are particularly relevant for hydrogels, where water migration plays a central role in the behaviour of the material. In this context, consider that the body in the reference configuration is in contact with a reservoir of water, and assume that water molecules are the only relevant mobile species. Let $C(\boldsymbol{X}, t)$ represent the concentration of water molecules (number of molecules per volume in the reference configuration). The local form of species mass conservation is given by:

$$\dot{C} = \boldsymbol{\nabla} \cdot \boldsymbol{J}, \tag{2.10}$$

where $\dot{C}$ denotes the material time derivative of the concentration C, and $\boldsymbol{J}(\boldsymbol{X}, t)$ represents the nominal water flux (number of molecules per unit area in the reference configuration). Note that in writing Eq. (2.10) we have neglected any source terms.

2.1.3 Thermodynamics

Balance equations for the conservation of linear momentum and mass are complemented by the first and second laws of thermodynamics. For isothermal processes, the first and second laws are often combined into a single expression to form the free energy imbalance. In this context, we first introduce the (Helmholtz) free energy $\psi(\boldsymbol{X}, t)$ field (energy per unit volume in the reference configuration), which physically represents the amount of internal energy available for mechanical processes at constant temperature. Assuming isothermal conditions and local thermodynamic equilibrium, the free energy imbalance takes the form:

$$\mathcal{D} = \dot{W}_{\text{ext}} - \dot{\psi} \geq 0, \tag{2.11}$$

where $\dot{\psi}$ is the material time derivative of ψ, $\dot{W}_{\text{ext}}$ is the external power input, and $\mathcal{D}$ is the net dissipation. Inequality (2.11) states that any power input at a material point not converted into free energy changes must be dissipated, for instance, as heat or other internal dissipative mechanisms (Holzapfel, 2002; Gurtin et al., 2010; Anand and Govindjee, 2020). Equality holds only in the absence of dissipative processes. In this thesis, the most general form of the external power input $\dot{W}_{\text{ext}}$ considered is:

$$\dot{W}_{\text{ext}} = \boldsymbol{P} : \dot{\boldsymbol{F}} + \mu \dot{C}, \tag{2.12}$$

where μ is the chemical potential of water, representing the energy flow due to water transport. The free energy imbalance (2.11) then becomes:

$$\mathcal{D} = \boldsymbol{P} : \dot{\boldsymbol{F}} + \mu \dot{C} - \dot{\psi} \geq 0. \tag{2.13}$$

Materials that undergo negligible volume changes during deformation, like rubbery networks (Treloar, 1973; Rubinstein and Colby, 2003; Sakai, 2020), are frequently modelled as incompressible. Within the thermodynamic framework, incompressibility is introduced as a constraint on the free energy function ψ. In purely mechanical settings, incompressibility is expressed by the constraint $J = 1$. When solvent transport is involved, the incompressibility condition must account for volume changes arising from water uptake. A commonly adopted form is the molecular incompressibility constraint (Hong et al., 2008; Chester and Anand, 2010):

$$J = 1 + \Omega(C - C_0), \tag{2.14}$$

where C and C_0 denote the current and initial concentrations of water molecules per volume in the reference configuration, and Ω is the volume per water molecule. To enforce this constraint, the free energy is augmented by a Lagrange multiplier P:

$$\psi \to \psi - P(J - 1 - \Omega(C - C_0)). \tag{2.15}$$

Substituting the augmented free energy (2.15) into Eq. (2.13) yields the modified inequality:

$$\mathcal{D} = \boldsymbol{P} : \dot{\boldsymbol{F}} + \mu\dot{C} - \dot{\psi} + P(\dot{J} - \Omega\dot{C}) \geq 0. \tag{2.16}$$

2.1.4 Constitutive relations

The balance equations and the free energy imbalance are universally valid and independent of the specific constitution of the material. Constitutive assumptions must be introduced to describe the mechanical behaviour of a given material or class of materials. These assumptions specify the particular form of the material time derivative of the free energy $\dot{\psi}$ in terms of the relevant state variables. In the most general case considered in the thesis, the thermodynamic state at a material point $\boldsymbol{X}$ is fully characterised by the deformation gradient $\boldsymbol{F}$ and the concentration of water molecules C.

The free energy is assumed to depend solely on the state variables, i.e., $\psi = \psi(\boldsymbol{F}, C)$. The material time derivative $\dot{\psi}$ is then computed via the chain rule:

$$\dot{\psi} = \frac{\partial \psi}{\partial \boldsymbol{F}} : \dot{\boldsymbol{F}} + \frac{\partial \psi}{\partial C} : \dot{C}. \tag{2.17}$$

The specific functional form of $\psi(\boldsymbol{F}, C)$ depends on the material behaviour under consideration, but it must satisfy the principle of material objectivity, i.e., it must be invariant under changes of observer (Noll et al., 1974; Gurtin et al., 2010). Substituting Eq. (2.17) into the free energy imbalance (2.16) yields the following state laws for the first Piola–Kirchhoff stress tensor $\boldsymbol{P}$

and the chemical potential μ:

$$\boldsymbol{P} = \frac{\partial \psi}{\partial \boldsymbol{F}} - JP\boldsymbol{F}^{-T}, \tag{2.18}$$

$$\mu = \frac{\partial \psi}{\partial C} + \Omega P, \tag{2.19}$$

where we have used the identity $\dot{J} = J\boldsymbol{F}^{-T} : \dot{\boldsymbol{F}}$. Using Eq. (2.18) in Eq. (2.9) gives the Cauchy stress tensor as:

$$\boldsymbol{\sigma} = \frac{1}{J}\frac{\partial \psi}{\partial \boldsymbol{F}}\boldsymbol{F}^{T} - P\boldsymbol{1}, \tag{2.20}$$

which shows that the Lagrange multiplier plays the role of a hydrostatic stress. Importantly, P is not determined by the constitutive response of the material, but rather by the imposed boundary conditions.

Considerations of material symmetry can further restrict the specific functional form that the free energy $\psi(\boldsymbol{F}, C)$ may adopt. If the material is isotropic in the undeformed state, its mechanical response is independent of the loading direction. The isotropy assumption, combined with the principle of material objectivity, implies that the free energy ψ must depend on the deformation gradient $\boldsymbol{F}$ through the principal invariants of the right Cauchy-Green tensor $\boldsymbol{C}$:

$$I_1 = \mathrm{tr}(\boldsymbol{C}), \qquad I_2 = \frac{1}{2}\left[I_1^2 - \mathrm{tr}(\boldsymbol{C}^2)\right], \qquad I_3 = \det(\boldsymbol{C}). \tag{2.21}$$

Under the incompressibility constraint, $I_3 = 1$, which reduces the free energy to a function of I_1 and I_2 only. Alternatively, due to the spectral decomposition (2.5), the free energy can be formulated in terms of the principal stretches λ_i, which is often more convenient in micromechanical modelling.

2.2 Phenomenological modelling of rubber elasticity

Before presenting micromechanical models for rubbery networks, we briefly present phenomenological approaches. Although these models can also describe inelastic effects (Shariff, 2014; Anssari-Benam and Hossain, 2024), our focus is restricted to hyperelasticity, where all deformations are reversible and dissipative mechanisms are absent. Unlike micromechanical models, phenomenological approaches do not seek to reproduce material behaviour from molecular-level mechanisms. Instead, they aim to capture the observed elastic response through mathematical formulations, typically designed to incur minimal computational cost and require minimal experimental data for calibration. While this makes them appealing for structural-scale simulations, their associated parameters typically lack clear physical meaning and are best regarded as curve-fitting tools. Phenomenological hyperelastic models generally assume isotropy and incompressibility. As described in Section 2.1.4, these assumptions imply that the free energy density ψ depends on the principal invariants I_1 and I_2 of the right Cauchy–Green tensor $\boldsymbol{C}$, or equivalently, on the principal stretches λ_1, λ_2, and λ_3. Based on this distinction, phenomenological models are commonly classified as either invariant-based or principal stretch-based.

2.2.1 Invariant-based models

In an invariant-based model, the free energy is expressed as a function of the invariants I_1 and I_2, i.e., $\psi = \psi(I_1, I_2)$. Due to their simple implementation, these approaches are often preferred over their principal stretch counterparts in finite element codes. However, identifying an appropriate functional form of $\psi(I_1, I_2)$ directly from experimental data is not straightforward (Valanis and Landel, 1967; Treloar, 1973). Although many models neglect the dependence on I_2, it is well established that both invariants are required to accurately capture the behaviour of soft materials under general loading conditions (Anssari-Benam et al., 2021; Dal et al., 2021).

neo-Hookean model. The neo-Hookean model is the simplest invariant-based model, in which the free energy depends linearly on the first invariant I_1:

$$\psi = \frac{G}{2}\left(I_1 - 3\right), \tag{2.22}$$

where G represents the shear modulus of the material. This model performs well for small to moderate deformations when appropriately calibrated. However, it becomes increasingly inaccurate at large deformations, as it fails to reproduce the characteristic upturn observed in the stress–strain response of rubber-like materials. Phenomenological models depending solely on I_1 are sometimes referred to as generalised neo-Hookean models (Wineman, 2005; Anssari-Benam and Bucchi, 2021; Anssari-Benam et al., 2021; Horgan, 2021; Kuhl and Goriely, 2024).

Gent model. The Gent model is a popular generalised neo-Hookean model capable of predicting the characteristic upturn in the stress-strain curve of rubber-like materials. The free energy function is given by (Gent, 1996):

$$\psi = -\frac{G}{2} J_m \log \left(1 - \frac{I_1 - 3}{J_m} \right), \tag{2.23}$$

where J_m is a parameter that sets the maximum admissible value of $I_1 - 3$. This functional form emulates the effect of finite chain extensibility typically present in micromechanical models. As $J_m \to \infty$, Eq. (2.23) converges to the classic neo-Hookean model.

Mooney-Rivlin model. The Mooney–Rivlin model is the simplest formulation that includes dependence on both I_1 and I_2. The free energy function is a linear combination of the two invariants (Mooney, 1940; Rivlin, 1948):

$$\psi = C_{10}(I_1 - 3) + C_{01}(I_2 - 3), \tag{2.24}$$

where C_{10} and C_{01} are fitting constants. As I_2 is geometrically associated with shape changes of infinitesimal area elements averaged over orientations (Kearsley, 1989; Kuhl and Goriely, 2024), the Mooney-Rivlin formulation offers better predictions in shear-dominated deformation modes compared to the neo-Hookean model. However, its validity remains largely restricted to small and moderate elongations, and its predictions in biaxial loading are too stiff (Boyce and Arruda, 2000). Eq. (2.24) reduces to the neo-Hookean model when $C_{01} = 0$, with C_{10} identified as $\frac{G}{2}$.

Generalised Rivlin model The generalised Rivlin model expresses the free energy function as a power series in I_1 and I_2 (Rivlin and Saunders, 1951):

$$\psi = \sum_{i,j=0}^{\infty} C_{ij} (I_1 - 3)^i \, (I_2 - 3)^j \,, \tag{2.25}$$

where C_{ij} represent the coefficients of this series. The generalised Rivlin formulation embodies many of the existing invariant-based models, including Eqs (2.22)-(2.24). However, care must be taken with the number of terms retained in Eq. (2.25), as increasing the number of terms does not necessarily improve accuracy (Ogden, 1972) and may lead to unrealistic behaviour under loading conditions far from the calibration point (Yeoh, 1997).

2.2.2 Principal stretch-based models

Principal stretch-based models express the free energy as a symmetric function of the principal stretches λ_1, λ_2, and λ_3, i.e., $\psi = \psi(\lambda_1, \lambda_2, \lambda_3)$. Compared to their invariant-based counterparts, principal stretch-based models are more computationally expensive due to the eigenvalue problem involved in obtaining the principal stretches. However, these models offer simpler analytical structures (Ogden, 1972), and identifying suitable expressions for $\psi(\lambda_1, \lambda_2, \lambda_3)$ from experimental data is typically more straightforward (Valanis and Landel, 1967). While any invariant-based model can be recast in principal stretch form, the reverse is not always possible, as some principal stretch-based formulations do not admit an equivalent expression in terms of invariants alone.

Valanis-Landel hypothesis. Valanis and Landel (1967) proposed that the free energy function $\psi(\lambda_1 , \lambda_2, \lambda_3)$ can be additively decomposed into the sum of a function w evaluated at each principal stretch:

$$\psi(\lambda_1 , \lambda_2, \lambda_3) = w(\lambda_1) + w(\lambda_2) + w(\lambda_3). \tag{2.26}$$

This separable form simplifies experimental identification of ψ, as it reduces the problem to determining a single-variable function. Hypothesis (2.26) has been shown to describe many rubber-like materials well up to moderate deformations (Valanis and Landel, 1967). The authors also proposed the following single-parameter form for the free energy valid in this deformation regime:

$$\psi = 2G \sum_{i=1}^{3} \lambda_i (\log(\lambda_i) - 1). \tag{2.27}$$

Ogden model. The Ogden model is one of the most widely used principal stretch-based formulations. The free energy is expressed as:

$$\psi = \sum_{i=1}^{N} \frac{\mu_i}{\alpha_i} \left(\lambda_1^{\alpha_i} + \lambda_2^{\alpha_i} + \lambda_3^{\alpha_i} - 3\right), \tag{2.28}$$

where μ_i and α_i are fitting parameters, and N is the number of terms in the series. Good agreement with the experimental data is usually obtained with $N = 2$ or $N = 3$. However, increasing the number of terms can introduce numerical sensitivity and lead to non-unique sets of optimal parameters, as multiple combinations may fit the data equally well (Ogden et al., 2004).

Anssari-Benam model. Anssari-Benam (2023) recently proposed a principal stretch-based model capable of embodying many phenomenological models:

$$\psi = \sum_{i=1}^{Q} \frac{3(n_i - 1)}{2n_i} \mu_i N \left[\frac{\lambda_1^{\alpha_i} + \lambda_2^{\alpha_i} + \lambda_3^{\alpha_i} - 3}{3N(n_i - 1)} - \log\left(\frac{\lambda_1^{\alpha_i} + \lambda_2^{\alpha_i} + \lambda_3^{\alpha_i} - 3N}{3 - 3N} \right) \right], \tag{2.29}$$

where n_i, μ_i, α_i are fitting parameters, Q is the number of terms in the series, and N (not subscripted) represents the extensibility limit. For $Q = 1$, Eq. (2.29) converges to the Ogden model (2.28) as $N \to \infty$, whereas the Gent model is recovered by setting $\alpha = 2$. Like the Ogden model, Eq. (2.29) may exhibit parameter non-uniqueness and numerical sensitivity when too many terms are retained.

2.2.3 Limitations of phenomenological models

Despite their practical appeal, phenomenological models offer limited insights into how microstructural features govern the mechanical behaviour of rubbery networks. Their parameters are typically obtained by fitting macroscopic data and lack direct connection to the underlying molecular architecture. As a result, these models fail to capture effects arising from the interplay between the response of individual chains and the heterogeneous structure of the network. In contrast, micromechanical approaches adopt a bottom-up strategy, where the macroscopic response emerges from the collective behaviour of individual chains. The next sections establish the foundations of this modelling framework, starting with the description of the single chain behaviour.

2.3 Single chain

2.3.1 Force-extension relationship

The force-extension relationship of an isolated polymer chain forms the fundamental building block of micromechanical models. Polymer chains consist of long sequences of repeated units, called monomers, connected by covalent bonds. Due to thermal fluctuations, the torsion angles between adjacent bonds can vary, giving the chain a high degree of flexibility. This internal mobility allows the chain to adopt multiple conformations. Consequently, an isolated polymer chain is intrinsically a stochastic object, governed by the probabilities of its many possible configurations (Rubinstein and Colby, 2003; Weiner, 2012). These conformations and their associated probabilities play a central role in the force-extension response of a chain. We consider ideal chains, in which interactions between monomers far apart along the chain are neglected, even if they eventually approach each other. Our discussion will be limited to the Freely Jointed Chain model (FJC), although other ideal chain models exist (see Rubinstein and Colby (2003) for a detailed overview of such models and their assumptions).

The FJC model is one of the simplest models for ideal chains that captures the finite extensibility of polymer chains while providing a closed-form expression for the force–extension relation. Moreover, the concept of equivalent freely jointed chain further offers a unified description of all ideal polymers (Rubinstein and Colby, 2003). In the FJC model, the chain is described as a collection of N rigid Kuhn segments of length b that are free to rotate relative to each other, as illustrated in Fig. 2.2(a). The separation between the ends of the chain is described by the end-to-end vector $\boldsymbol{r}$. The maximum possible end-to-end distance is the contour length Nb, which occurs when the chain is fully extended, with all segments aligned in a straight configuration (Fig. 2.2(b)). The Helmholtz free energy w of a freely jointed chain at a given end-to-end vector is given by:

$$w = u - Ts, \tag{2.30}$$

where u, T and s are the internal energy, absolute temperature, and entropy, respectively. In ideal chains, the internal energy does not depend on the end-to-end vector, so that without loss

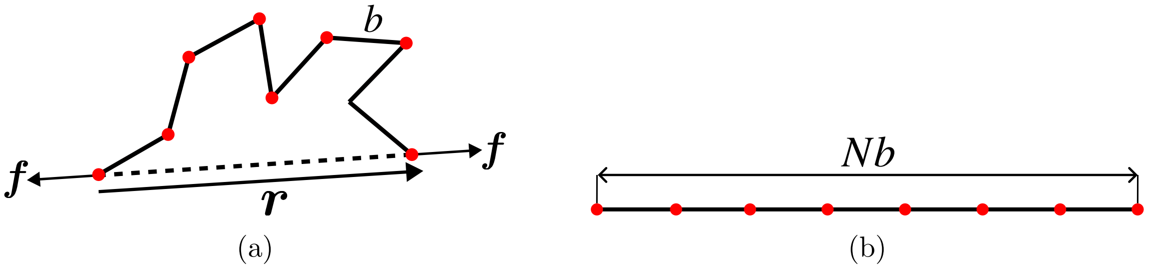

Fig. 2.2: (a) A conformation of a chain formed by N freely jointed segments of length b at given chain end-to-end vector $\boldsymbol{r}$. To keep the chain ends separated by a distance $r = \|\boldsymbol{r}\|$, a force $\boldsymbol{f}$ needs to be applied to the chain ends. (b) The contour length Nb of the chain represents the maximum separation distance between the chain ends, which occurs when the segments are all aligned and in a straight configuration.

of generality, we may write:

$$w = -Ts. \tag{2.31}$$

Eq. (2.31) shows that changes in the free energy arise only from entropy variations, which in turn reflect the configurational changes of the chain.

The entropy of a chain with a given end-to-end vector $\boldsymbol{r}$ depends on the number of accessible conformations $\Omega_B(\boldsymbol{r})$ the chain can adopt via Boltzmann's entropy equation:

$$s(\boldsymbol{r}) = k_B \log \Omega_B(\boldsymbol{r}), \tag{2.32}$$

where k_B is the Boltzmann constant. The number of conformations and the distribution of end-to-end vectors $P(\boldsymbol{r})$ are related through:

$$P(\boldsymbol{r}) = \frac{\Omega_B(\boldsymbol{r})}{\Omega_T}, \tag{2.33}$$

where Ω_T denotes the total number of conformations, i.e., the integral of $\Omega_B(\boldsymbol{r})$ over the configurational space $\mathcal{S}_c$. Since Ω_T is constant, we can equivalently write Eq. (2.32) in terms of the distribution $P(\boldsymbol{r})$:

$$s(\boldsymbol{r}) = k_B \log P(\boldsymbol{r}), \tag{2.34}$$

up to a constant.

There are multiple spatial arrangements of the N segments corresponding to a given end-to-end vector $\boldsymbol{r}$. Each arrangement may be viewed as a random walk of N steps of length b. In the limit of large N, the corresponding distribution of end-to-end vectors $P(\boldsymbol{r})$ is approximated by a Gaussian distribution (Treloar, 1973; Rubinstein and Colby, 2003; Weiner, 2012):

$$P(\boldsymbol{r}) = \left(\frac{3}{2\pi N b^2}\right)^{3/2} \exp\left(-\frac{3}{2}\frac{r^2}{N b^2}\right), \tag{2.35}$$

where $r = \|\boldsymbol{r}\|$ is the end-to-end distance. This approximation holds for ideal chains that are sufficiently long to justify the use of the Central Limit Theorem. Gaussian distributions like Eq. (2.35) are spherically symmetric, reflecting the lack of orientation bias of the random walk. This distribution has a maximum when the chain adopts a fully coiled configuration, i.e., $\boldsymbol{r} = \boldsymbol{0}$. On the other hand, the mean square end-to-end distance $\langle \boldsymbol{r}^2 \rangle \equiv \langle \boldsymbol{r} \cdot \boldsymbol{r} \rangle$ is obtained as Nb^2. This implies that the root mean square (rms) end-to-end distance is $\sqrt{N}b$. Chains whose distribution of end-to-end vectors may be approximated by Eq. (2.35) are referred to as Gaussian chains.

Substituting Eqs (2.34) and (2.35) back into Eq. (2.31), we obtain the free energy w of a Gaussian chain as:

$$w(\boldsymbol{r}) = \frac{3k_B T}{2Nb^2} r^2. \tag{2.36}$$

The average force $\langle \boldsymbol{f} \rangle$ needed to maintain the chain ends at a distance $r = \|\boldsymbol{r}\|$ is obtained by differentiating w with respect to $\boldsymbol{r}$ (James and Guth, 1943):

$$\langle \boldsymbol{f} \rangle = \frac{3k_B T}{Nb^2} \boldsymbol{r}. \tag{2.37}$$

Eq. (2.37) shows that, on average, Gaussian chains behave as Hookean springs with zero rest length. However, the Gaussian distribution (2.35) allows for infinitely large end-to-end distances, assigning a non-zero probability for $r \geq Nb$, which is unrealistic. Therefore, Eq. (2.37) is only valid for long chains that are far from fully extended.

At larger chain extensions, the increasing alignment of the segments needs to be accounted for in the statistical analysis, leading to non-Gaussian behaviour. In this regime, it is more convenient to prescribe the force applied to the chain ends rather than the end-to-end vector (Kuhn and Grün, 1946; Weiner, 2012). Accordingly, the Helmholtz free energy is replaced by the Gibbs free energy g, given by:

$$g(\boldsymbol{f}) = -k_B T \log Z(\boldsymbol{f}), \tag{2.38}$$

where $Z(\boldsymbol{f})$ is the partition function. $Z(\boldsymbol{f})$ is defined as the integral of Boltzmann factors over the configurational space. For N freely jointed segments, the partition function is obtained as (Rubinstein and Colby, 2003; Weiner, 2012):

$$Z(\boldsymbol{f}) = \left(4\pi \frac{\sinh \beta}{\beta}\right)^N , \tag{2.39}$$

where $\beta = \frac{fb}{k_B T}$ represents the normalised chain force, and $f = \|\boldsymbol{f}\|$ is the chain force magnitude. Inserting Eq. (2.39) back into Eq. (2.38) gives the Gibbs free energy as:

$$g(\boldsymbol{f}) = k_B T N \left[\beta - \log\left(4\pi \sinh \beta\right)\right] , \tag{2.40}$$

from which the average end-to-end distance $\langle r \rangle$ can be obtained by differentiation with respect to f as:

$$\langle r \rangle = Nb\mathcal{L}(f), \tag{2.41}$$

where $\mathcal{L}(x) = \coth x - 1/x$ is the Langevin function. The inversion of Eq. (2.41) yields the force-extension relation as:

$$f = \frac{k_B T}{b} \mathcal{L}^{-1}\left(\frac{\langle r \rangle}{Nb}\right) . \tag{2.42}$$

Eq. (2.42) shows that the force in non-Gaussian chains tends to infinity as the average end-to-end distance approaches the contour length Nb. For small elongations ($\langle r \rangle \lessapprox 0.3Nb$), Eq. (2.42) recovers the Gaussian force-extension response. The Helmholtz free energy is derived when the end-to-end distance is prescribed, which is equivalent to the fixed force case used to obtain Eq. (2.42) in the long chain limit (Weiner, 2012). Under this assumption, it is possible to show that the Helmholtz free energy of a non-Gaussian chain is given by (Treloar, 1973; Boyce and Arruda, 2000):

$$w(\boldsymbol{r}) = k_B T N \left[\frac{r}{Nb}\beta + \log\left(\frac{\beta}{\sinh \beta}\right)\right] , \tag{2.43}$$

yielding the same functional form for the force-extension relationship as that of Eq. (2.42).

The statistical framework provides force-extension relationships in which the end-to-end distance is prescribed to obtain the thermal average chain force, or vice versa. For the remainder of the thesis, we drop this formal distinction and treat Eqs (2.37) and (2.42) as deterministic springs. Accordingly, we adopt the following expressions for the Gaussian regime:

$$w = \frac{3k_BT}{2Nb^2}r^2, \tag{2.44}$$

$$f = \frac{3k_BT}{Nb^2}r, \tag{2.45}$$

and for the non-Gaussian regime:

$$w = k_BTN\left[\frac{r}{Nb}\beta + \log\left(\frac{\beta}{\sinh\beta}\right)\right], \tag{2.46}$$

$$f = \frac{k_BT}{b}\mathcal{L}^{-1}\left(\frac{r}{Nb}\right). \tag{2.47}$$

2.3.2 Chain scission

The FJC model presented in Section 2.3.1 assumes that the free energy of a single chain w is purely entropic, with variations arising solely from configuration changes of the chain. However, it is well accepted that chain scission is an energy-dominated process associated with the elongation of covalent bonds along the chain backbone (Lake and Thomas, 1967; Wang et al., 2019, 2021; Mao et al., 2017; Mulderrig et al., 2023). As such, the FJC model is fundamentally incompatible with this energetic description of scission, motivating the development of modified models that incorporate bond extensibility.

Phenomenological extensions to the FJC model account for energetic contributions by replacing the rigid Kuhn segments with deformable ones. Smith et al. (1996) first conceptualised this idea by directly incorporating two stiffness parameters to capture the transition between entropic and energetic regimes in the force-extension behaviour of the chain. Inspired by this work, Mao et al. (2017) augmented the free energy (2.46) with an energetic term that depends on the bond stretch, thus allowing the length of the segments to vary. In this case, the bond stretch is obtained by minimising the free energy w under a constant chain stretch. In parallel, models grounded on statistical mechanics have been developed to obtain extensions to the FJC model from more fundamental principles. These approaches offer greater flexibility than their phenomenological counterparts, allowing the inclusion of additional effects such as bond length fluctuations and more complex bond potentials (Buche and Silberstein, 2021; Buche et al., 2022; Mulderrig et al., 2023).

Although both phenomenological and mechanistic extensible FJC models capture the energetic contributions consistent with chain scission, there are a few limitations worth mentioning. A primary drawback is that the bond stretch is typically obtained by solving an implicit equation, which introduces additional computational effort. This has motivated the development of semi-analytical approximations for the bond-stretch to reduce computational cost while maintaining reasonable accuracy (Li and Bouklas, 2020; Mulderrig et al., 2023). Moreover, atomic force microscopy (AFM) data and quantum-chemical calculations suggest that the energetic dominance near chain rupture stems not only from bond stretching but also from bond angle opening (Hugel et al., 2005; Cai et al., 2019). Therefore, single chain models aiming to accurately describe the energetic regime, and consequently chain scission, should incorporate bond angle opening effects, as in Lavoie et al. (2020), Guo and Zaïri (2021) and Zhu and Brassart (2025).

In micromechanical models, chain scission can be described using either rate-independent or rate-dependent approaches. A commonly adopted rate-independent strategy in both discrete and continuum formulations involves introducing a breaking criterion based on a scission threshold. For example, in chain models accounting for bond extensibility, scission occurs when the bond stretch or bond force exceeds a critical value (Lake and Thomas, 1967; Mao et al., 2017; Li and Bouklas, 2020; Deng et al., 2023). Alternatively, a critical chain elongation can be used as the cleavage threshold in chain models that neglect energetic effects (Vernerey et al., 2018; Li and Liu, 2020; Lei et al., 2021, 2025). A key limitation of these rate-independent criteria is that the scission threshold adopted is usually arbitrary, raising doubts about its physical meaning. Moreover, these approaches cannot be directly applied to rate-dependent problems without introducing additional, often heuristic, rate-dependent terms (Talamini et al., 2018; Mao and Anand, 2018; Arunachala et al., 2023; Mousavi et al., 2025).

The rate-dependent approach is based on the interpretation that chain scission is a thermally activated process governed by reaction kinetics. To illustrate this concept, we consider that scission is characterised by an activation energy U_b separating the two minima in the double-well potential illustrated in Fig. 2.3(a). The local maximum corresponds to the unstable transition state, from which the system can proceed to either energy minima. The distance between the energy minima and the transition state along the reaction coordinate is referred to as the activation length a, which is assumed to be the same for the forward and backward reaction. When the chain experiences a force f, the force-free energetic landscape tilts, and the energy barrier for scission becomes $U_b - fa$ (Fig. 2.3(b)). Assuming a single reactive bond per chain for simplicity, the rate of chain scission under the applied force f is directly obtained from an Eyring-type model as (Kauzmann and Eyring, 1940; Bell, 1978):

$$k = \gamma \exp\left(-\frac{U_b - fa}{k_B T}\right) = k_0 \exp\left(\frac{fa}{k_B T}\right), \tag{2.48}$$

where γ is the attempt frequency, and $k_0 \equiv \gamma \exp\left(-\frac{U_b}{k_B T}\right)$ represents the force-free scission rate. An important nuance often overlooked is that the chain force f is identified with the bond force in writing Eq. (2.48). This equivalence is reasonable when the segments are fully aligned in single chain models with bond stretching. However, the bond force becomes significant only at high chain stretches, where energetic effects dominate over entropic ones. Moreover, this approximation becomes less accurate when bond angle opening effects are present.

In micromechanical models based on a population of chains, chain scission rates are often converted into chain scission probabilities. For a sufficiently large population of identical chains subjected to the same force f, the survival probability $p_s(t)$, which represents the fraction of intact chains at time t, is given by $p_s(t) = \exp(-kt)$. This expression provides a probabilistic interpretation of the scission rate k, which allows chain breakage to be implemented using random sampling techniques (Arora et al., 2022; Beech et al., 2023; Araujo and Brassart, 2025a). Alternatively, many models define a chain damage variable governed by an evolution law that depends on k (Lavoie et al., 2016; Kothari et al., 2018; Ghareeb and Elbanna, 2021), or directly linked to the survival probability (Guo and Zaïri, 2021; Ogouari et al., 2024a,b).

Experimental evidence supports the interpretation of scission as a thermally activated process. For instance, some rubber-like materials exhibit rate-dependent failure in the absence of noticeable viscoelastic effects (Wang and Fan, 2023; Wang et al., 2024). Force-accelerated chain scission has been linked with environmental cracking in elastomers (Yang et al., 2019b; Qari and Cai, 2024), and with the strength of polymers degrading under loads (Zhurkov and Korsukov, 1974; Bershtein et al., 1977). Recently, the increasing interest in force-reactive bonds (mechanophores) has further reinforced the kinetic treatment for chain scission (Ducrot et al., 2014; Wang et al., 2021; Beech et al., 2023; Li and Gong, 2024).

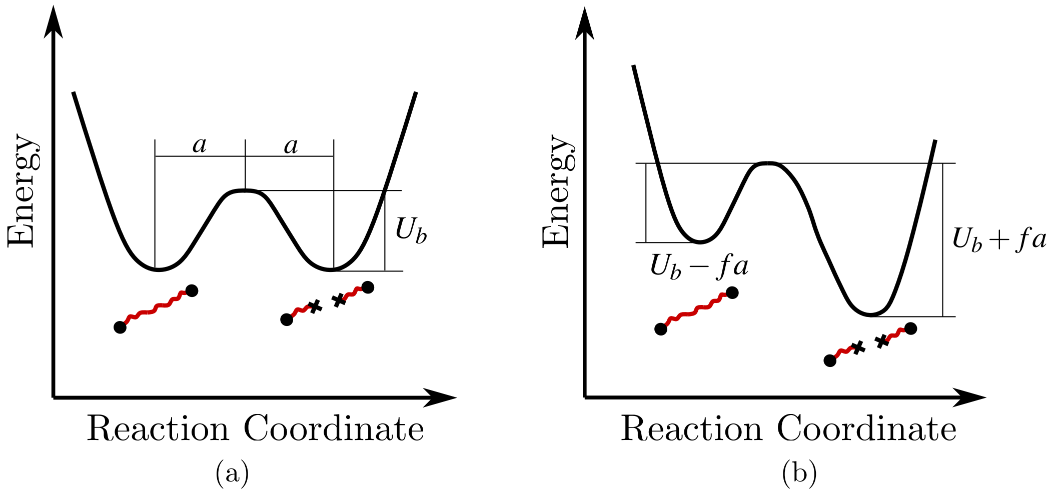

Fig. 2.3: (a) Double well potential characterising chain scission as a thermally activated process. The two minima in the potential define the intact and broken states of the chain, separated by an energy barrier U_b. The local maximum represents an unstable transition state, from which the system can proceed to either energy minima. The distance between the minima and the transition state along the reaction coordinate is the activation length a. (b) When a force f is applied to the chain ends, the energetic landscape is tilted and the energy barrier for scission becomes $U_b - fa$.

2.4 Discrete Networks

Discrete Networks (DNs) are micromechanical modelling approaches that represent a polymer network as a collection of springs, each governed by the force-extension behaviour of an isolated single chain. The springs are connected at nodes corresponding to crosslinks, whose positions are determined by mechanical equilibrium. As such, DNs eliminate the need for a priori assumptions relating deformations at macroscopic and chain levels, as required in the continuum models discussed later. Moreover, DN models offer a good compromise between physical fidelity and computational cost, being considerably more efficient than coarse-grained molecular dynamics simulations, while retaining essential microstructural features.

2.4.1 General framework

The conceptual foundations of the DN framework originate from the statistical mechanics treatment of polymer networks. Consider a network of n fluctuating phantom[1] Gaussian chains held together by internal junctions and occupying a volume V_0 in the reference configuration, as illustrated in Fig. 2.4. Fixed junctions are used to prevent the network from collapsing

---

[1] The term “phantom” indicates that chains interact only through crosslinks, without chain-to-chain interactions.

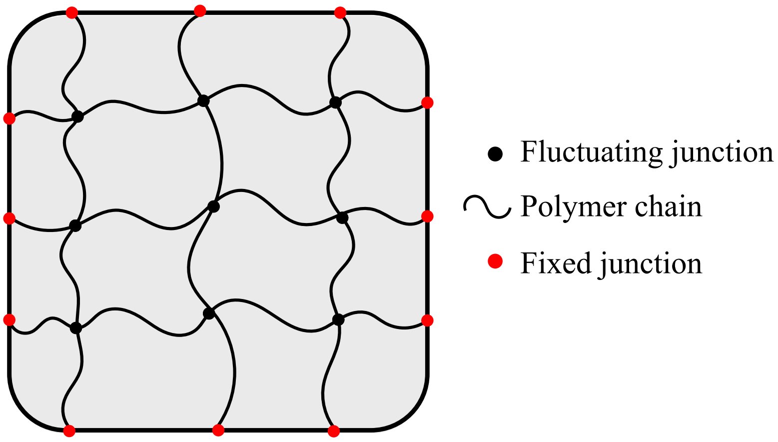

Fig. 2.4: Rubbery network composed of fluctuating Gaussian chains held together by internal junctions. Additional fixed junctions are added to prevent the network from collapsing to a point due to the zero rest length of the spring behaviour (2.45).

to a point due to the force-extension relation (2.45). These fixed junctions are subjected to affine displacements corresponding to the macroscopic deformation gradient $\boldsymbol{F}$. In real rubbery networks, the network collapse does not occur due to excluded volume effects arising from intrachain and interchain interactions (Flory, 1979; Bergström and Boyce, 2001; Weiner, 2012). In swollen networks, local osmotic pressure also contributes to preventing this collapse (Horkay and Lin, 2009; Wagner et al., 2022).

James and Guth (1943) rigorously demonstrated that the most probable positions of the free junctions follow affine motion and are governed by the same equations (see Section 3.2.3) that dictate the equilibrium positions of nodes in a spring network with force-extension behaviour given by Eq. (2.45). Furthermore, they showed that the fluctuations of the inner junctions around their most probable position are independent of $\boldsymbol{F}$. These key results establish an exact equivalence between a molecular fluctuating network and a mechanical spring network in the case of Gaussian chains. In the non-Gaussian case, this equivalence holds under the following assumptions: (i) the most probable positions of the junctions coincide with their thermal averages, and (ii) fluctuations around the thermal average are independent of $\boldsymbol{F}$ (Wang and Guth, 1952). While these assumptions are exact for a Gaussian network, they have not been formally proven for non-Gaussian networks.

The statistical mechanics foundations underlying DN models provide a mechanistic justification for representing a molecular network by an ensemble of springs. Based on this correspondence, the free energy density (energy per unit volume in the reference configuration) of the network is written as:

$$\psi(\boldsymbol{F}) = \frac{1}{V_0}\sum_{i=1}^{n} w_i, \tag{2.49}$$

where w_i represents the free energy of the ith spring[2], given by either Eq. (2.45) or Eq. (2.47). Note that the free energy (2.49) is evaluated at the mechanical equilibrium state of the network, which is found by minimising the energy of the network under a prescribed macroscopic deformation gradient $\boldsymbol{F}$.

Eq. (2.49) exactly represents the free energy of a Gaussian fluctuating network, and that of a non-Gaussian network under the assumptions outlined previously. In the Gaussian case, we can show that if the network is isotropic, the free energy ψ is expressed as:

$$\psi(\boldsymbol{F}) = \frac{1}{2}\nu kT\left\langle \frac{r_0^2}{Nb^2}\right\rangle I_1, \tag{2.50}$$

where ν is the number density of chains (per volume in the reference configuration), r_0 represents the end-to-end distance of a chain in the reference configuration, and I_1 is the first invariant of the right Cauchy-Green tensor $\boldsymbol{C}$. The notation $\langle\cdot\rangle$ represents the ensemble average:

$$\langle\cdot\rangle = \frac{1}{n}\sum_{i=1}^{n}(\cdot). \tag{2.51}$$

Eq. (2.50) has the same functional form as the neo-Hookean model (2.22), up to a constant. Therefore, we conclude that the shear modulus G of an isotropic network of Gaussian chains is exactly given by:

$$G = \nu k_B T\left\langle \frac{r_0^2}{Nb^2}\right\rangle = \nu k_B T\langle\lambda_0^2\rangle, \tag{2.52}$$

where we have introduced the chain pre-stretch λ_0 defined as the ratio between the initial end-to-end distance and the random-walk distance $\sqrt{N}b$, i.e., $\lambda_0 \equiv \frac{r_0}{\sqrt{N}b}$. Note that no assumptions are made about the initial end-to-end distance or the number of segments of the chains, highlighting the generality of Eq. (2.52). In particular, the classical estimate $G = \nu k_B T$ is recovered when all chains adopt their random-walk distance in the reference configuration.

To obtain the macroscopic stress $\boldsymbol{P}^e$ in a DN model, we associate each material point of an elastic body $\mathcal{B}_0$ at equilibrium with a Representative Volume Element (RVE), as illustrated

---

[2] We use the words "chain" and "springs" interchangeably from this point forward.

in Fig. 2.5. The RVE serves as a mesoscale that bridges microscale features with macroscale response. The RVE is represented by a sufficiently large discrete network, and its n_b boundary nodes are subjected to affine boundary conditions:

$$\boldsymbol{x}_\alpha = \boldsymbol{F}\boldsymbol{X}_\alpha, \tag{2.53}$$

where $\boldsymbol{x}_\alpha$ and $\boldsymbol{X}_\alpha$ represent the position of the αth boundary node in the current and reference configurations, respectively. The reference configuration is identified with the initial configuration, and $\boldsymbol{F} = \mathbf{1}$ at this stage. In any deformation stage, the network is assumed to be in equilibrium with external loads. As a fundamental requirement for homogenisation problems involving RVEs, we impose the energetic consistency between microscale and macroscale (Hill, 1967; Blanco et al., 2016). This implies that the work done by the first Piola-Kirchoff stress $\boldsymbol{P}^e$ over virtual deformations $\boldsymbol{F}$ is equal to the work done by the external forces over compatible displacements $\delta\boldsymbol{x}_\alpha$ with $\delta\boldsymbol{F}$:

$$\boldsymbol{P}^e : \delta\boldsymbol{F} = \frac{1}{V_0}\sum_{\alpha=1}^{n_b} \boldsymbol{f}_\alpha \cdot \delta\boldsymbol{x}_\alpha, \tag{2.54}$$

where $\boldsymbol{f}_\alpha$ is the reaction force at the αth boundary node. Substituting the affine boundary condition (2.53) into Eq. (2.54), we arrive at (Kouznetsova, 2002; Andia et al., 2005; Weiner, 2012; Argento et al., 2012; Zündel et al., 2017; Alamé and Brassart, 2020):

$$\boldsymbol{P}^e = \frac{1}{V_0}\sum_{\alpha=1}^{n_b} \boldsymbol{f}_\alpha \otimes \boldsymbol{X}_\alpha. \tag{2.55}$$

Considering the state law (2.18), particularised for hyperelasticity, we conclude that the first Piola–Kirchhoff stress tensor $\boldsymbol{P}$, accounting for incompressibility ($J = 1$), is given by:

$$\boldsymbol{P} = \boldsymbol{P}^e - JP\boldsymbol{F}^{-T}, \qquad \boldsymbol{P}^e \equiv \frac{\partial\psi}{\partial\boldsymbol{F}} = \frac{1}{V_0}\sum_{\alpha=1}^{n_b} \boldsymbol{f}_\alpha \otimes \boldsymbol{X}_\alpha. \tag{2.56}$$

The corresponding Cauchy stress is obtained as:

$$\boldsymbol{\sigma} = \boldsymbol{\sigma}^e - P\mathbf{1}, \tag{2.57}$$

where $\boldsymbol{\sigma}^e = (1/J)\boldsymbol{P}^e\boldsymbol{F}^{-T}$. Note that forces must be applied to the boundary nodes in the reference configuration to prevent network collapse due to the force-extension relations (2.45) and (2.47). Consequently, $\boldsymbol{P}^e$ and $\boldsymbol{\sigma}^e$ do not vanish in the reference configuration.

Remark 1 *Note that homogenised stress tensors* $\boldsymbol{P}^e$ *(Eq. (2.56)) and* $\boldsymbol{\sigma}^e$ *(Eq. (2.57)) are objective, provided that the network is in equilibrium. Under a superposed rigid body motion of the current configuration, the boundary positions transform as*

$$\boldsymbol{x}_\alpha^* = \boldsymbol{c} + \boldsymbol{Q}\boldsymbol{x}_\alpha, \tag{2.58}$$

where $\boldsymbol{c}$ *and* $\boldsymbol{Q}$ *are a translation and a rotation, respectively. In general,* $\boldsymbol{c}$ *and* $\boldsymbol{Q}$ *can be time-dependent. The reaction forces transform as* $\boldsymbol{f}_\alpha^* = \boldsymbol{Q}\boldsymbol{f}_\alpha$*, while the reference positions* $\boldsymbol{X}_\alpha$ *are invariant (Holzapfel, 2002; Gurtin et al., 2010). Substituting into Eq. (2.56) gives*

$$\boldsymbol{P}^{e*} = \boldsymbol{Q}\boldsymbol{P}^e, \tag{2.59}$$

as required. Moreover, the equilibrium condition $\sum_\alpha \boldsymbol{f}_\alpha = 0$ *ensures that* $\boldsymbol{P}^e$ *is independent of arbitrary origin shifts in the reference configuration, and it implies that the Cauchy stress* $\boldsymbol{\sigma}^e$ *transforms as*

$$\boldsymbol{\sigma}^{e*} = \boldsymbol{Q}\boldsymbol{\sigma}^e\boldsymbol{Q}^T. \tag{2.60}$$

Hence, the homogenised stresses satisfy objectivity and are free of spurious coordinate dependence. For more general discussions of homogenised stresses in molecular and discrete simulations, see Andia et al. (2005) and Zimmerman et al. (2010).

The technique employed to generate the network topology is a key component in a DN framework, as it dictates the range of architectures accessible for analysis. Regular lattice-based networks, both in 2D (Deng et al., 2023; Hartquist et al., 2025b) and in 3D (Sugimura et al., 2013; Deng et al., 2023; Hartquist et al., 2025a), are commonly used due to their simplicity. However, rubbery networks are intrinsically irregular and inevitably contain topological defects, raising doubts about the applicability of the conclusions drawn from DN models based on regular lattices. Another common strategy involves obtaining random network topologies by connecting the centres of elements in unstructured finite element meshes when they share a face (3D) or an edge (2D) (Alamé and Brassart, 2019, 2020; Lei et al., 2021; Lei and Liu, 2022).

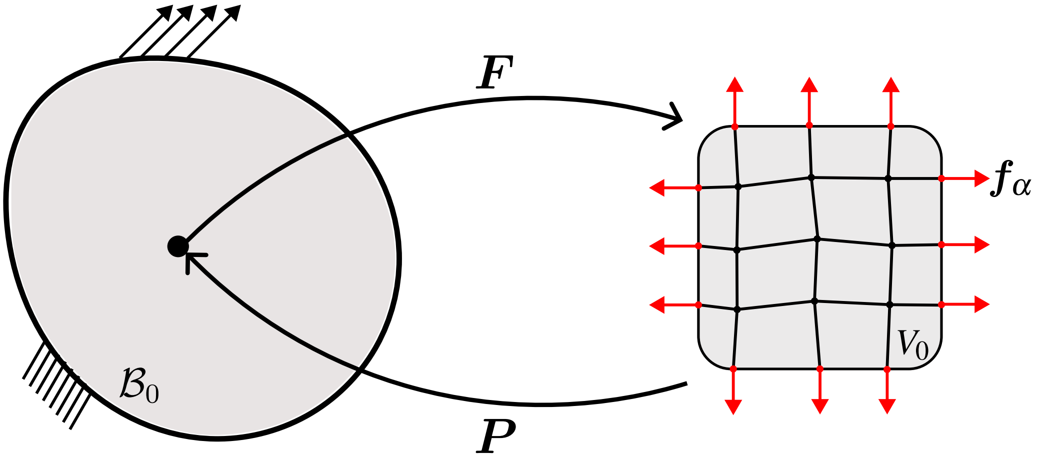

Fig. 2.5: Within every material point of the elastic body $\mathcal{B}_0$ experiencing external loads, there exists a Representative Volume Element (RVE) represented by a DN. The input from the macroscopic scale is the deformation gradient $\boldsymbol{F}$, from which the macroscopic stress $\boldsymbol{P}^e$ is obtained based on the reaction forces $\boldsymbol{f}_\alpha$, with $\alpha = 1, \ldots, n_b$, developed at the boundary nodes of the DN.

Networks can also be generated from a Voronoi tessellation of points randomly sampled within the computational domain (Islam and Picu, 2018; Britt and Ehret, 2022). Other methods have been developed to emulate the gelation process of rubber-like materials (Gusev, 2019; Wagner et al., 2021, 2022; Assadi et al., 2025). The overall idea of these techniques is to stochastically place connections between a set of randomly distributed points. A key limitation shared by many of these network generation strategies is that the end-to-end distance distribution and the chain density cannot be tuned independently, limiting the range of network architectures that can be analysed.

The zero rest length of the spring behaviours (2.45) and (2.47) poses a fundamental challenge in DN models, as it leads to network collapse in the absence of additional forces on the boundary nodes. As a result, networks cannot have traction-free boundaries in the reference configuration. One possible solution to this problem is through the inclusion of extra terms to the free energy that penalise local volume changes within the network. In models where the network architectures are obtained from finite element meshes, the collapse problem was avoided by introducing an extra pressure-like field that penalises volume changes of the elements, solved concurrently with the position of the nodes during the energy minimisation step (Lei et al., 2021; Lei and Liu, 2022; Li et al., 2024). The major drawback of this approach is that it relies on the underlying mesh. Recent elegant solutions that bypass this necessity and retain the penalisation idea involve the definition of regions surrounding each node through Voronoi tessellations (Lamont et al., 2025), while others use an underlying grid to describe a spatially distributed osmotic pressure (Wagner et al., 2022). However, these solutions add more complexity to the model and require more computational effort. Another class of collapse-prevention approaches consists of the introduction of pair-wise potentials between the nodes to represent excluded volume effects (Assadi et al., 2025; Wagner and Silberstein, 2025). Nevertheless, selecting a physically appropriate potential remains a non-trivial task.

2.4.2 Elasticity

DNs have been used as tools to gain a fundamental understanding of the elastic response of rubber-like materials. Since the network topology is incorporated into the DN framework, links between network structural parameters and their influence on emerging macroscopic properties can be established to obtain structure-property relationships (Alamé and Brassart, 2019, 2020; Araujo et al., 2024a). In this context, the analytical expression for the shear modulus of Gaussian networks (Eq. (2.52)) is a central result which has recently been validated through DN simulations. Notably, this analytical result holds even in networks containing topological defects, such as dangling ends and loops, as well as a distribution of chain lengths (i.e., polydispersity). Moreover, Eq. (2.52) assisted in elucidating the scaling relations that deviate from classic rubber elasticity theory, especially in systems where the chain end-to-end distances are coupled with chain density, such as near-ideal tetra-PEG gels (Sakai et al., 2008; Matsunaga et al., 2009; Akagi et al., 2013).

In practice, estimating the shear modulus from Eq. (2.52) is not straightforward, as it requires the ensemble average of the squared chain pre-stretch, which in turn depends on the knowledge of the network topology. This challenge has motivated the development of mean-field approaches, where the full network structure is replaced by an effective medium. Examples include the tree-like structure (Rubinstein and Colby, 2003; Mark and Erman, 2007), as well as lattice-based models incorporating topological defects (Nishi et al., 2012; Lin et al., 2019) and polydispersity (Lin et al., 2019).

Beyond structure-property relationships, DNs can also provide insights into how the deformation at the chain level is related to the macroscopic deformation, since chain deformation is dictated by force balance at the nodes, instead of ad hoc kinematic assumptions. For example, deviations from affinity were systematically investigated using DN models (Alamé and Brassart, 2020; Britt and Ehret, 2022; Araujo et al., 2024a). This information is fundamental for semi-analytical models relying on the affine assumption, as it provides a direct way to evaluate its validity.

2.4.3 Failure and Fracture

Extending DN models for failure and fracture requires including chain scission in the general framework outlined in Section 2.4.1. Typically, this is done by deleting chains from the network that satisfy a deterministic breaking criterion, as discussed in Section 2.3.2. Although straightforward to implement, this deterministic formulation limits the corresponding DN model to rate-independent problems.

In the context of fracture, DNs have been primarily used to investigate the mechanisms underlying crack propagation in rubber-like materials. Recent works using DN models have provided new insights into the origins of the discrepancies between the intrinsic fracture energy predicted by the Lake-Thomas model and the values obtained experimentally for many rubber-like materials (Lin and Zhao, 2020; Wang et al., 2021; Barney et al., 2022). The presence of defects intrinsic to polymer networks is one of the proposed explanations for these discrepancies, which can be accounted for through mean-field models based on the tree-like approximation (Lin and Zhao, 2020; Barney et al., 2022; Lu et al., 2025). However, crack propagation simulations using DNs have demonstrated that even defect-free networks exhibit intrinsic fracture energies that exceed those predicted by the Lake-Thomas model due to the unloading of chains far from the crack tip (Lei and Liu, 2022; Deng et al., 2023; Hartquist et al., 2025a). These simulations have also shown that the tortuous crack paths observed in soft materials can be attributed to network randomness (Lei et al., 2021; Lei and Liu, 2022; Ghareeb and Elbanna, 2020), polydispersity (Ghareeb and Elbanna, 2020), and the preferential scission of weaker chains (Hartquist et al., 2025b).

Despite the interesting mechanistic insights, the applicability of the conclusions obtained from DN models for crack propagation remains unclear due to some limitations of the framework. First, the creation of traction-free crack surfaces is not possible in conventional DN models due to the network collapse problem discussed in Section 2.4.1. This limitation seems to have been overlooked by many recent works (Ghareeb and Elbanna, 2020, 2021; Deng et al., 2023; Hartquist et al., 2025a,b). A notable exception is the work of Lei et al. (2021), who circumvented this problem by introducing a pressure-like field penalising local volume changes of the elements of the underlying finite element mesh. While alternative collapse-preventing solutions relying solely on the position of the nodes exist (see Section 2.4.1), they have been primarily applied to 2D periodic networks with a relatively small number of chains, leaving their applicability to fracture problems uncertain. Second, the network architectures considered in these crack propagation simulations are defect-free, whereas real rubbery networks inevitably contain defects. Finally, the macroscopic stress quantities obtained in these models are generally not derived from rigorous homogenisation principles, raising concerns about scale separation. Ghareeb and Elbanna (2020) partially addressed this issue using a quasi-continuum approach, relying on the affine deformation of chains. However, a generalisation to the non-affine case has yet to be developed.

On the other hand, the insights gained from DN models used to simulate failure can be more reliably extrapolated to real polymer network systems. For example, DNs were used to systematically evaluate the role of dangling ends (Sugimura et al., 2013), loops (Arora et al., 2022), and pre-polymer parameters (e.g. molecular weight, functionality) (Wagner et al., 2022) on key mechanical properties of tetra-PEG gels, such as toughness, peak stress, and peak stretch. Finally, DNs represent promising tools to identify which fabrication parameters ultimately control the failure of rubber-like materials (Wagner et al., 2022; Lei et al., 2025).

2.4.4 Rate-dependent problems

To model rate-dependent failure, chain scissions have to be included in DN models following the thermally activated interpretation described in Section 2.3.2. Given the probabilistic nature of scissions in this description, some DN models adopt random sampling methods, such as Kinetic Monte Carlo, to break chains. The core idea is to transform the scission rates computed from Eq. (2.48) into probabilities, as explained in Section 2.3.2. As such, chain-breaking is inherently force-biased, as chains carrying large loads are more likely to be selected for scission. Besides rate-dependent damage (Arora et al., 2022), this approach was recently used to elucidate the mechanisms underlying the failure of tetra-PEG gels with different fractions of strong linkers (Wang et al., 2021; Beech et al., 2023). Other DN models adopted a deterministic approach to account for thermally activated scissions through a damage variable at the chain level whose evolution depends on the underlying kinetics. These models have been applied to capture different crack propagation regimes in rate-dependent fracture (Ghareeb and Elbanna, 2021), and to investigate the role of sacrificial bonds and self-healing mechanisms in failure (Kothari et al., 2018).

The random sampling approach has also been used to model the rate-dependent response of networks with reversible bonds (Wagner et al., 2021; Wagner and Vernerey, 2023; Wagner et al., 2024; Wagner and Silberstein, 2025). The combination of reversible and permanent bonds has emerged as an effective design strategy to enhance the toughness of rubber-like materials (Gong et al., 2016; Creton and Ciccotti, 2016; Bai et al., 2018). Beyond synthetic systems, networks with transient bonds can also describe the dynamic response of biological systems, such as insect swarms (Peleg et al., 2018; Wagner et al., 2024), as well as certain viscoelastic fluids (Tabuteau et al., 2009).

While DNs have been extensively used in transient networks and rate-dependent failure, they have rarely been applied to chemical degradation, which is an important topic in biomedical and sustainability applications (Bryant and Vernerey, 2018; Turner et al., 2022; Bensalem et al., 2023). In addition to the advantages discussed in the previous sections, modelling chemical degradation with DN models is appealing for a few reasons. The deterioration of the elastic properties of the network, quantified by the degraded modulus, was found to play a central role in the degradation-induced swelling response of hydrogels (Li et al., 2011; Pan and Brassart, 2022). The degraded modulus is typically modelled using mean-field models, which are also used to predict reverse gelation. However, these mean-field approaches have unclear micromechanics foundations, and cannot capture force-bias effects beyond the acceleration of the reaction kinetics. In contrast, DNs explicitly account for the time-evolving network architecture, allowing the degraded modulus to be computed without relying on ad hoc assumptions. Moreover, the combination of graph theory with DNs enables the direct analysis of network connectivity during degradation, facilitating the estimation of the reverse gelation threshold.

2.5 Continuum models

Discrete Networks offer a robust framework for understanding the mechanics of rubber-like materials, providing mechanistic insights by explicitly accounting for network topology and chain-level behaviour. However, their computational cost hinders their applicability in structural-scale simulations. More computationally tractable continuum models can be obtained by adopting approximations that describe the full-field problem in an average sense. This approach enables the derivation of mechanistic free energy expressions without explicitly resolving the network structure. In what follows, we focus our discussion on the so-called microsphere or full-network models (Treloar, 1954; Wu and Van Der Giessen, 1993).

2.5.1 Microsphere models

2.5.1.1 Network elastic free energy

Microsphere models consider a continuous distribution of chains in space in the reference configuration. The free energy ψ of the network still takes the general form as in Eq. (2.49). Each chain is identified by its initial orientation in the reference configuration characterised by a unit vector $\boldsymbol{n}_0 = \frac{\boldsymbol{r}_0}{\|\boldsymbol{r}_0\|}$, with $\boldsymbol{r}_0$ denoting the initial end-to-end vector of the chain. Upon deformation, the network is subjected to the macroscopic deformation gradient $\boldsymbol{F}$, and the end-to-end vector becomes $\boldsymbol{r}$. To bypass the necessity of having access to the network topology to evaluate ψ, microsphere models invoke the following assumptions: (i) chains are randomly oriented in the reference configuration, (ii) chains having the same length N and initial orientation $\boldsymbol{n}_0$ experience the same stretch λ_c, and (iii) chains of the same length N have the same initial end-to-end distance r_0, i.e., $r_0 = r_0(N)$. These assumptions allow us to rewrite Eq. (2.49) as:

$$\psi(\boldsymbol{F}) = \nu \int_N p_N(N) \iint_{\mathcal{S}_u} w(\lambda_c; N)\, d\mathcal{S}_u\, dN, \tag{2.61}$$

where ν is the chain density and p_N is the polydispersity distribution. The notation $\iint_{\mathcal{S}_u} (\cdot) d\mathcal{S}_u$ denotes the integration over the unit sphere:

$$\iint_{\mathcal{S}_u} (\cdot)\, d\mathcal{S}_u = \frac{1}{4\pi} \iint (\cdot)\, \sin(\phi)\, d\phi d\theta, \tag{2.62}$$

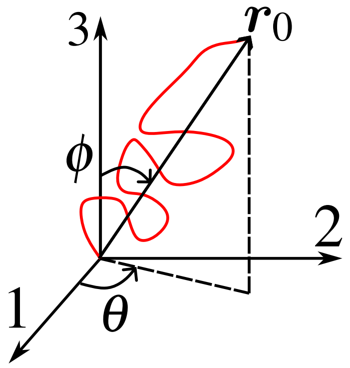

Fig. 2.6: The azimuthal θ and polar ϕ angles parametrise the orientation of the initial end-to-end vector $\boldsymbol{r}_0$ of a chain in spherical coordinates.

where θ and ϕ represent the azimuthal and polar angles in spherical coordinates, respectively, as illustrated in Fig. 2.6 for the initial end-to-end vector of a chain. When all the chains have the same length, the network is monodispersed, and Eq. (2.61) simplifies to:

$$\psi(\boldsymbol{F}) = \nu \iint_{\mathcal{S}_u} w(\lambda_c)\, d\mathcal{S}_u. \tag{2.63}$$

Overall, Eqs (2.61) and (2.63) show that the microsphere approach reduces the complex network architecture to a representative chain whose response is averaged over all orientations.

The integral over orientations present in microsphere models cannot be solved analytically in general. In practice, such integrals are approximated using quadrature schemes that replace the continuous orientation space by a set of Q discrete points on the unit sphere. Accordingly, the integral of a quantity x is approximated as:

$$\iint_{\mathcal{S}_u} x\, d\mathcal{S}_u \approx \sum_{i=1}^{Q} x_i \omega_i, \tag{2.64}$$

where x_i is the evaluation of x at the ith quadrature point and ω_i is its corresponding weight. Many schemes can be found in the literature, and the particular choice depends on the application.

2.5.1.2 Micro-macro transition

The assumptions used to reduce the free energy of the network to the more tractable forms (2.61) and (2.63) do not, on their own, establish the relation between macroscopic deformation and the deformation experienced by the chains. In microsphere models, this link is typically postulated without a clear physical justification. In what follows, we outline the main approaches used to establish this micro-macro transition.

Affine model In the affine microsphere model, the chain stretch λ_c is identified with the line stretch of the continuum for the initial orientation $\boldsymbol{n}_0$:

$$\lambda_c = \lambda_{\text{aff}}, \qquad \lambda_{\text{aff}} = \|\boldsymbol{F}\boldsymbol{n}_0\|. \tag{2.65}$$

Provided that the chains remain Gaussian during deformation, the affine stretch (2.65) is mechanistically justified, as discussed previously in Section 2.4.2. However, DN simulations have shown (Alamé and Brassart, 2020; Britt and Ehret, 2022; Araujo et al., 2024a) that this assumption breaks down at larger deformations, where the chains enter the non-Gaussian regime and non-affine deformation takes place. In these situations, the deformation of the chains is better described from an energy minimisation perspective.

The three-chain (James and Guth, 1943) and eight-chain (Arruda and Boyce, 1993) models can be viewed as reductions of the affine microsphere model in which only some orientations are sampled. The three-chain model only considers the chains that are initially aligned with the principal stretch directions (Fig. 2.7(a)). For monodispersed networks, the free energy is expressed as:

$$\psi(\boldsymbol{F}) = \frac{\nu}{3}\sum_{i=1}^{3} w(\lambda_i), \tag{2.66}$$

where λ_i are principal stretches. In the eight-chain model, only chains initially aligned with the diagonals of a cube aligned with the principal stretch directions are considered (Fig. 2.7(b)), yielding for a monodispersed network:

$$\psi(\boldsymbol{F}) = \nu w(\Lambda), \tag{2.67}$$

where:

$$\Lambda = \sqrt{\frac{I_1}{3}}. \tag{2.68}$$

It can be shown that the eight-chain stretch Λ corresponds to the root-mean-square affine stretch. This correspondence has been used to develop semi-analytical solutions for orientation integrals, thus circumventing the need for quadrature schemes in microsphere models (Beatty,

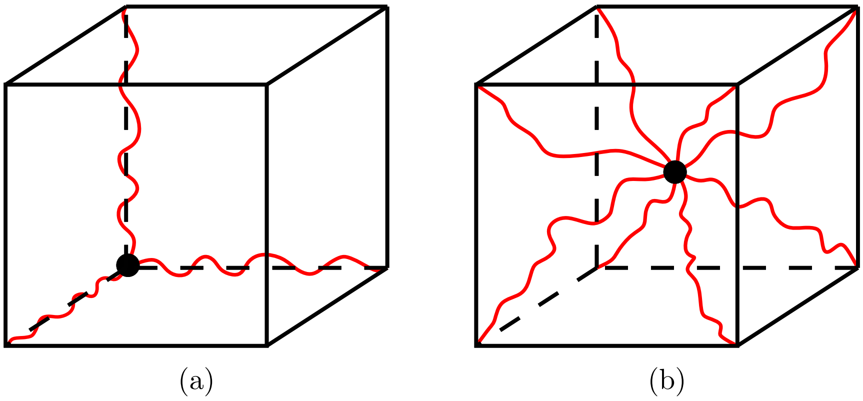

Fig. 2.7: Unit cells corresponding to the (a) three-chain and (b) eight-chain reductions.

2003; Khiêm and Itskov, 2016; Kumar and Brassart, 2023).

Fully-relaxed model In the fully-relaxed microsphere model (Tkachuk and Linder, 2012; Diani and Le Tallec, 2019; Govindjee et al., 2019; Mulderrig et al., 2021; Araujo et al., 2024a), the chain deformation is determined by minimising the elastic energy of the network subjected to a kinematic constraint. Physically, this constraint enforces the consistency between the macroscopic deformation gradient $\boldsymbol{F}$ and the microscopic deformation averaged over all orientations. Let $\boldsymbol{F}_m$ denote the microscopic deformation such that $\boldsymbol{r} = \boldsymbol{F}_m \boldsymbol{r}_0$, and let $\boldsymbol{n}$ represent the deformed orientation, expressed as $\boldsymbol{n} = r_0 \boldsymbol{r}$. It follows that:

$$\boldsymbol{F}_m = \boldsymbol{n} \otimes \boldsymbol{n}_0. \tag{2.69}$$

For monodispersed networks, the kinematic constraint takes the form (Tkachuk and Linder, 2012; Govindjee et al., 2019):

$$\frac{\boldsymbol{F}}{3} = \iint_{\mathcal{S}_u} \boldsymbol{n} \otimes \boldsymbol{n}_0 \, d\mathcal{S}_u, \tag{2.70}$$

while for the polydisperse case, a more intuitive expression is given by (Araujo et al., 2024a):

$$\frac{\boldsymbol{F}}{3} = \int_N p_N(N) \iint_{\mathcal{S}_u} \boldsymbol{n} \otimes \boldsymbol{n}_0 \, d\mathcal{S}_u \, dN, \tag{2.71}$$

although other forms have been proposed (Diani and Le Tallec, 2019; Mulderrig et al., 2021). It can be verified that the affine stretch (2.65) minimises the elastic energy of the network only in the Gaussian limit. Consequently, the affine and fully-relaxed models predict the same behaviour in the Gaussian regime.

Non-affine microsphere model Another non-affine model based on energy minimisation under a kinematic constraint is the non-affine microsphere model proposed by Miehe et al. (2004). In this formulation, the chain stretch λ_c is treated as a fluctuation around the affine stretch λ_{aff}, as:

$$\lambda_c = f\lambda_{\text{aff}}, \tag{2.72}$$

where f is a fluctuation field defined over the unit sphere. This field is obtained by minimising the elastic energy under the following kinematic constraint in the monodisperse case:

$$\left(\iint_{\mathcal{S}_u} \lambda_c^p \, d\mathcal{S}_u\right)^{1/p} = \left(\iint_{\mathcal{S}_u} \lambda_{\text{aff}}^p \, d\mathcal{S}_u\right)^{1/p}, \tag{2.73}$$

where p is a fitting parameter that controls the degree of non-affinity in the model. Eq. (2.73) enforces that the $p-$norm average of the non-affine chain stretches equals that of the affine stretches. For non-zero fluctuations, it follows from the optimality condition that all chains experience the same stretch given by the $p-$norm average of λ_{aff}. For the particular case $p = 2$, the model reduces to the well-known eight-chain model (Arruda and Boyce, 1993). Moreover, it can be shown that p impacts the small deformation response of the model, in contrast to fully-relaxed formulations. Recent works have applied the previous monodisperse results directly to the polydisperse case (Guo and Zaïri, 2021; Ogouari et al., 2024b,a), based on the assumption that λ_c is independent of chain length. A possible generalisation of the constraint (2.73) to account for the polydispersity distribution $p_N(N)$ is:

$$\int_N p_N(N) \left(\iint_{\mathcal{S}_u} \lambda_c^p \, d\mathcal{S}_u\right)^{1/p} dN = \left(\iint_{\mathcal{S}_u} \lambda_{\text{aff}}^p \, d\mathcal{S}_u\right)^{1/p}, \tag{2.74}$$

where the right-hand side is unchanged since the affine stretch is independent of chain length.

Equal-force model The previous non-affine models impose constraints on the microscopic deformation. Verron and Gros (2017) proposed an alternative approach in the context of polydispersity where the constraint is enforced on the force experienced by the chains. Specifically, chains of different lengths N but with the same initial orientation $\boldsymbol{n}_0$ are subjected to the same force. This equal-force constraint leads to the formation of a hybrid chain, in which polydisperse chains are assembled under the same force. The free energy ψ is then written as an average over orientations of the energy of the hybrid chain, as in Eq. (2.63). The deformation of the hybrid chain can be affine with the continuum (Verron and Gros, 2017; Li and Bouklas, 2020) or non-affine (Diani and Le Tallec, 2019; Mulderrig et al., 2021). In both cases, the macroscopic response is governed by the stiffness parameters of the hybrid chain, which in turn depend on the chain length distribution $p_N(N)$. However, it is possible to find a set of different distributions $p_N(N)$ yielding the same effective length of the hybrid chain, but different small deformation responses (Verron and Gros, 2017; Li and Bouklas, 2020).

Non-affine model without constrained minimisation A new class of non-affine models has recently emerged where the chain stretch is not obtained from energy minimisation under kinematic constraints. Instead, the chain stretch is directly defined as (Amores et al., 2021; Zhan et al., 2023):

$$\lambda_c = \boldsymbol{U} : \boldsymbol{n}_0 \otimes \boldsymbol{n}_0 = \boldsymbol{n}_0 \cdot \boldsymbol{U}\boldsymbol{n}_0, \tag{2.75}$$

where $\boldsymbol{U}$ is the right stretch tensor as defined in Eq. (2.2). The chain stretch (2.75) represents the directional change in length along the initial chain orientation $\boldsymbol{n}_0$, and is generally smaller than the affine stretch (2.65) due to the stretching in the direction perpendicular to $\boldsymbol{n}_0$. The affine and non-affine chain stretches coincide when $\boldsymbol{n}_0$ is aligned with one of the principal directions of $\boldsymbol{U}$. This new micro-macro transition was found to yield better predictions for biaxial and shear loads, while only requiring calibration against uniaxial data. Moreover, for Gaussian chains, it successfully predicts the slope of Mooney plots. However, the physical interpretation of Eq. (2.75) remains unclear.

2.5.2 Microsphere damage models

In the microsphere framework, chain scission is typically described through a damage variable $d \in [0, 1]$ at the chain level, with $d = 0$ and $d = 1$ representing the intact and fully-damaged states, respectively. Damage reduces the elastic energy stored in the network, and this is captured by a monotonically decreasing degradation function $g(d) \in [0, 1]$, with $g(0) = 1$ and $g(1) = 0$. For the polydisperse case, Eq. (2.61) is modified to:

$$\psi(\boldsymbol{F}) = \nu \int_N p_N(N) \iint_{\mathcal{S}_u} g(d) w(\lambda_c; N) d\mathcal{S}_u \, dN, \tag{2.76}$$

whereas for monodispersed networks, Eq. (2.63) becomes:

$$\psi(\boldsymbol{F}) = \nu \iint_{\mathcal{S}_u} g(d) w(\lambda_c) d\mathcal{S}_u. \tag{2.77}$$

For simplicity, we have considered the chain stretch λ_c as the only kinematic variable controlling the effective free energy w of the representative chain in Eqs (2.76) and (2.77). Existing microsphere damage models differ in the evolution of the damage variable d, the physical interpretation of d, the form of the degradation function $g(d)$, and the micro-macro transition used.

The phenomenological extension of the FJC model to include energetic effects motivated the formulation of damage models in which the evolution of the damage variable d is controlled by the bond stretch (Mao and Anand, 2018; Talamini et al., 2018; Li and Bouklas, 2020; Mulderrig et al., 2021; Arunachala et al., 2023, 2024). Many of these models were proposed within a phase-field framework, in which the degradation function typically adopts the quadratic form $g(d) = (1 - d)^2$. However, these approaches typically rely on prescribed scission thresholds to control damage initiation, aligned with the rate-independent cleavage criterion discussed in Section 2.3.2. Consequently, the physical meaning of d is unclear and mainly represents a heuristic way to describe the progressive loss of load-bearing capacity in a given orientation.

Microsphere damage models have also been proposed in which the damage variable d is given a physical interpretation grounded in kinetics, by associating it with the survival probability p_s of a population of identical chains stretched to the same value λ_c, as in $d = 1 - p_s$ (Guo and Zaïri, 2021; Ogouari et al., 2024b,a). Since this probability is controlled by the scission kinetics, this damage variable is also intrinsically rate-dependent. Under this probabilistic interpretation, the degradation function naturally takes the form $g(d) = 1 - d = p_s$, which simply represents the fraction of surviving chains at a given orientation.

Building on a similar rationale, Lavoie et al. (2016) proposed a damage model based on the eighth-chain model (Eq. (2.67)), in which rate-dependent scissions are incorporated into the evolution of the density of elastically effective chains ν. Specifically, they adopted an evolution law that mimics the differential equation of first-order kinetic processes[3]:

$$\dot{\nu} = -k\nu, \tag{2.78}$$

where k is the scission rate computed from Eq. (2.48) based on the force acting on the representative chain of the eight-chain model [4]. In the context of dynamic networks and multi-network systems, the decrease in ν has also been used as a macroscopic measure of damage in microsphere models in which damage represents the progressive erosion of the initial distribution of end-to-end vectors (Vernerey et al., 2018; Lamont et al., 2021).

2.5.3 Limitations

The microsphere framework enables the bottom-up formulation of constitutive models that are suitable for incorporation into finite element codes for structural-scale simulations. However, this framework effectively reduces the complex network architecture to an idealised medium represented by a single chain averaged over all orientations. As such, microsphere models overlook microstructural features that directly affect the macroscopic behaviour of rubber-like materials. Moreover, the validity of these assumptions and their physical interpretation remain unclear. This also raises doubts about the predictions for failure obtained from microsphere damage models, as they inherit the same foundational simplifications as their purely elastic counterparts.

Microsphere damage models with orientation-dependent chain deformation are convenient for modelling anisotropic damage, as damage evolution also depends on orientation. This feature has been extensively explored to model the Mullins effect (Govindjee and Simo, 1991; Dargazany and Itskov, 2009; Vernerey et al., 2018; Mulderrig et al., 2021; Diani and Le Tallec, 2019; Khiêm et al., 2019; Bresolin and Vassoler, 2022; Ogouari et al., 2024b), a phenomenon known for its pronounced anisotropy (Mullins, 1948, 1969; Diani et al., 2009). However, the same orientation-specific nature of damage also introduces a major limitation when applying these models to failure problems. Specifically, they cannot predict a fully damaged macroscopic state in general, leading to a persistent residual elastic energy in some deformation modes (Mul-

---

[3] See Chapter 5 for more details.

[4] Arguing that scission can happen in any of the backbone bonds, the authors multiply the right-hand side of Eq. (2.78) by the number of Kuhn segments of the chain in the original presentation.

derrig et al., 2021). This limitation can be readily verified when considering the three-chain model (Eq. (2.77)) with damage in a volume-preserving uniaxial tension test. Since damage can only evolve in tension, chains perpendicular to the loading direction remain intact. This effect becomes more pronounced as more orientations on the unit sphere are sampled. In contrast, this issue does not occur in microsphere damage models where all chains experience the same stretch, such as the eight-chain or the non-affine localisation rules (2.73) and (2.74). However, this advantage comes at the cost of losing the ability to capture anisotropic damage intrinsically.

2.6 Knowledge gaps

Despite increasing interest and recent advances, DNs are still in their infancy, leaving several unexplored research paths. As described in Section 2.4.1, the network generation technique is a key component in a DN model, as it limits the type of networks accessible for analysis. Many network generation methods lack independent control over key network parameters, such as chain density and initial end-to-end distance distribution. This hinders the development of generalised structure-property relationships and a deeper understanding of the mechanics of rubbery networks. Progress in these areas will require the development of more versatile and flexible network generation techniques capable of exploring a broader region of the design space.

In the context of damage and fracture, many works overlook the role of local heterogeneities and the evolving network architecture in shaping the failure response of polymer networks. While some attention was dedicated to the effects induced by structural defects, the impact of other heterogeneities, whether intrinsic to the network or emerging during loading due to chain scission, has not been systematically investigated. A deeper understanding of how these features influence failure progression would help clarify the link between local bond breaking and macroscopic failure (Ju et al., 2024), and could inform strategies to enhance material strength (Wang et al., 2021, 2023a). Although thermally activated scissions have been included in DN models to describe the response of dynamic networks and rate-dependent failure, their application to chemically induced degradation remains largely unexplored. Extending DN models to describe the gradual deterioration of rubbery networks could open new avenues for designing soft materials with tunable mechanical and degradation properties (Li et al., 2011; Huebsch et al., 2014; Diederich et al., 2017).

The computational tractability of microsphere-based models makes them appealing, mechanistically motivated approaches for structural-scale simulations. However, a systematic and comprehensive validation of the simplifying assumptions underlying these models is still missing. Due to their shared theoretical foundations, DNs can serve as a reference platform to assess and validate these assumptions. Insights gained from this analysis can be further used to guide the refinement of existing microsphere models or encourage the development of new tractable micromechanical frameworks.

Chapter 3

Micromechanical modelling of rubbery networks: The role of chain pre-stretch

This chapter presents work that has been published as "Araujo, L. M., Kryven, I., and Brassart, L. (2024a). Micromechanical modelling of rubbery networks: The role of chain pre-stretch. *International Journal of Non-Linear Mechanics*, 166:104834". The study investigates how the distribution of chain pre-stretches influences the elastic response of rubbery networks through discrete network simulations. To this end, we developed a novel network generation algorithm that enables independent control over chain pre-stretch, chain density, and chain length. Using networks generated with varying input parameters, we established generalised scaling relations and used discrete network predictions as a reference to critically assess the accuracy of conventional microsphere-based continuum models. The results highlight that the pre-stretch distribution plays a central role in determining both the elastic modulus and the extensibility limit of the material. Furthermore, by systematically evaluating the assumptions underpinning conventional continuum theories, this work offers new insights to inform the development of improved micromechanical continuum models. An overview of the open-source code published alongside the paper is presented in Chapter A.

3.1 Introduction

The mechanical properties of many soft materials such as elastomers and hydrogels primarily depend on the topology of the underlying network. Accordingly, recent design strategies have largely focused on designing network architectures to obtain soft materials with unprecedented mechanical properties in terms of elasticity, strength, and toughness. Representative examples are near-ideal tetra-arm PEG hydrogels obtained by crosslinking well-defined four-arm macromolecular precursors in solution. These hydrogels show high elasticity and strength, which has been attributed to their spatially homogeneous network structure with few topological defects such as dangling ends and entanglements (Sakai et al., 2008; Matsunaga et al., 2009). Alternatively, tough hydrogels have been obtained by incorporating dissipation mechanisms into the network, such as progressive failure of a secondary network (Gong et al., 2003; Zhou et al., 2020; Zhao et al., 2021) or the breaking and reforming of physical bonds (Sun et al., 2012; Ihsan et al., 2013; Zhang et al., 2016). Recently, highly entangled gels have been proposed as an effective way to increase elasticity and toughness simultaneously (Kim et al., 2021, 2022).

The rational design of advanced soft materials requires modelling tools that can link mechanical properties to the underlying network structure. In this respect, classical semi-analytical models of rubber elasticity (Treloar, 1973; Boyce and Arruda, 2000) are intrinsically limited, because they do not explicitly account for the network topology. In recent years, random Discrete Network (DN) models have been proposed to address this limitation. Like in rubber elasticity theory, chains in DN models are represented by entropic springs, but the partitioning of the chain stretches is dictated by the condition of mechanical equilibrium at each crosslink point in a representative network structure comprising many chains. By explicitly representing the network, DN models allow the systematic investigation of structure-property relationships, including the role of chain length and crosslink functionality, topological defects (dangling ends, loops), and damage by bond breakage (Sugimura et al., 2013; Kothari et al., 2018; Gusev, 2019; Alamé and Brassart, 2019, 2020; Wagner et al., 2022). Recently, DN models have also been used to investigate crack propagation in hydrogels and elastomers (Ghareeb and Elbanna, 2020; Lei et al., 2021) and to assess the validity of the Lake-Thomas model (Lei and Liu, 2022; Deng et al., 2023).

Often overlooked in both analytical and DN modelling studies is the role of initial chain stretch distribution on the emerging mechanical properties. Since entropic springs have a zero natural length, they are necessarily subjected to tensile forces in the reference state. This feature is present in both continuum and DN models based on entropic springs. In continuum models, the initial chain end-to-end distance is a model parameter that can be prescribed arbitrarily (it is usually set to the root-mean-square end-to-end distance of a freely-jointed chain). However, in DN models the distribution of these forces, and the corresponding stretches, is dictated by mechanical equilibrium at the junctions, and intrinsically depends on the network topology and chain density. Consider for example a network of Gaussian chains with N Kuhn segments of length b. The force-extension relation of a Gaussian chain is given by: $f = 3kTr/Nb^2$, where k is Boltzmann's constant, T is the absolute temperature, f is the force and r is the chain end-to-end distance. The elastic shear modulus G of an isotropic DN is exactly given by (Alamé and Brassart, 2020):

$$G = \nu kT \left\langle \frac{r_0^2}{Nb^2} \right\rangle, \tag{3.1}$$

where ν is the chain density, r_0 is the initial end-to-end distance of a chain, and the symbol $\langle \cdot \rangle$ represents an average over all the chains in the network. Eq. (3.1) shows that increasing the chain end-to-end distances at fixed ν, N and b results in a stiffer network. The classical affine model of rubber elasticity $G_{\text{aff}} = \nu kT$ is recovered only in the special case where all chains adopt the random walk end-to-end distance $\sqrt{N}b$ in the reference configuration. However, the effect of the chain pre-stretch distribution on the macroscopic response has not been systematically explored in DN-based studies.

In light of the above considerations, DN models where the chain end-to-end distance, chain density and chain length can be controlled independently are desirable. Commonly-used network generation methods are unable to achieve this, because they produce networks where crosslink points are essentially connected to their nearest neighbours, so that density ν and initial distance r_0 are coupled. Examples include regular lattices in 2D (Lei et al., 2021; Deng et al., 2023) or 3D (Sugimura et al., 2013), as well as random networks obtained from unstructured meshes where nodes are identified with crosslink points and edges with polymer chains (Kothari et al., 2018; Alamé and Brassart, 2019; Lei et al., 2021). 3D random networks with fourfold coordination can also be obtained by locating crosslink points at the centre of tetrahedral elements and connecting them through the element faces (Alamé and Brassart, 2020; Lei and Liu, 2022). In any of these methods, increasing the chain density is necessarily accompanied by a decrease in the initial chain end-to-end distance. This point was raised in our previous works (Alamé and Brassart, 2019, 2020), where we also showed that this coupling leads to scaling relations that differ from those of classical rubber elasticity theory.

The first objective of this work is to systematically investigate structure-property relationships of rubbery networks using DNs, explicitly accounting for the effect of the chain pre-stretch. To this end, we developed a random network generation algorithm that decouples the average chain end-to-end distance from the chain density by allowing interpenetration of the chains. Generalised scaling relations that account for the pre-stretch are proposed. We further use the DN model to investigate the properties of polydispersed network and show the impact of short chains on the extensibility limit. We made the codes for the generation of random networks and subsequent mechanical simulations using the open-source software LAMMPS (Thompson et al., 2022) freely available on Github repositories (Kryven, 2022; Araujo et al., 2024b).

While DN models are useful to elucidate the role of topology on properties, they remain too expensive for FE simulations at structural scale, and hence, continuum semi-analytical theories remain desirable. Therefore, the second objective of this work is to systematically compare DN predictions to affine and non-affine microsphere models. We show that (surprisingly) affine models overall perform better than non-affine models, but that this is likely due to the competition between affine assumption and the approximation of uniform initial chain stretch distribution, which have opposite effects. We also propose extended affine and non-affine models that account for a pre-stretch distribution, with the non-affine formulation showing significantly better agreement with DN results.

3.2 Discrete Network model

3.2.1 Chain behaviour

We use the freely-jointed chain model to describe the behaviour of network chains. The freely-jointed chain model is one of the simplest models for ideal chains capturing the finite extensibility of polymer chains while providing the force-extension relation in closed form. The concept of equivalent freely-jointed chain further provides a unified description of all flexible polymers in the ideal state (Rubinstein and Colby, 2003). For a freely-jointed chain with N rigid Kuhn segments of length b and a fixed end-to-end distance r, the Helhmoltz free energy is given by (Treloar, 1973; Weiner, 2012):

$$w = NkT \left[\frac{r\beta}{Nb} + \log \left(\frac{\beta}{\sinh \beta} \right) \right] \quad \text{with} \quad \beta = \mathcal{L}^{-1} \left(\frac{r}{Nb} \right), \tag{3.2}$$

where $\mathcal{L}(x) = \coth x - 1/x$ is the Langevin function. The force needed to maintain the end-to-end distance r is derived from the free energy as $f = dw/dr$:

$$f = \frac{kT}{b} \mathcal{L}^{-1} \left(\frac{r}{Nb} \right). \tag{3.3}$$

The force vanishes when $r = 0$, i.e. when the chain adopts a coiled configuration. In the small extension limit $r \ll Nb$, $\mathcal{L}^{-1}(x) \approx 3x$ and the force-extension relation reduces to the linear expression:

$$f = 3kT \frac{r}{Nb^2}, \tag{3.4}$$

which coincides with the Gaussian chain model. When r approaches the chain contour length Nb corresponding to the fully-straightened configuration, the force (3.3) tends to infinity. Let r_0 be the chain end-to-end distance in the initial configuration of the network. We define the chain pre-stretch as the ratio of the chain initial end-to-end distance to the ideal random walk distance $\sqrt{N}b$: $\lambda_0 = r_0/\sqrt{N}b$.

3.2.2 Network behaviour

We next consider a network of n freely-jointed chains connected at junction points. In the DN model, the chains are represented by springs with force-extension relation given by Eq. (3.3). We make the assumption of a phantom network, i.e. chains in the network only interact via their junction points. We write $\boldsymbol{X}_i$ and $\boldsymbol{x}_i$ the reference and current coordinates of the i^{th} junction in the network. We further distinguish inner junctions with index $i \in \mathcal{I} = (1, n_I)$ from boundary junctions with index $i \in \mathcal{B} = (n_I + 1, n_I + n_B)$, where n_I and n_B are the number of inner and boundary junctions, respectively. The displacements of the boundary junctions are subjected to affine boundary conditions corresponding to the macroscopic deformation gradient $\boldsymbol{F}$:

$$\boldsymbol{x}_k = \boldsymbol{F} \cdot \boldsymbol{X}_k, \quad k \in \mathcal{B}. \tag{3.5}$$

In the reference configuration, $\boldsymbol{F} = \boldsymbol{1}$. In the rest of this study, the reference configuration is identified with the initial configuration.

The positions of the inner junctions are determined from the conditions of force balance at each inner junction. Let W be the macroscopic free energy density of the network occupying a volume V_0 in the reference configuration. The macroscopic free energy of the network admits the following variational characterisation:

$$W(\boldsymbol{F}) = \inf_{\boldsymbol{x}_k, k \in \mathcal{I}} \frac{1}{V_0} \sum_i \sum_{j>i} w(r_{ij}; N_{ij}), \tag{3.6}$$

where r_{ij} is the end-to-end distance of a chain linking junction points i and j: $r_{ij} = \|\boldsymbol{r}_{ij}\|$ with $\boldsymbol{r}_{ij} = \boldsymbol{x}_i - \boldsymbol{x}_j$. N_{ij} represents the number of Kuhn segments of that chain, and we formally set $N_{ij} = \infty$ when the two junctions are not connected, so that the force along the chain is zero according to the freely-jointed chain model (3.3). The minimisation in Eq. (3.6) is carried out over the positions of the inner junctions, while the positions of the boundary junctions are fixed by the boundary conditions (3.5). Note that the summation on j in Eq. (3.6) extends over both inner and boundary junctions. The stationarity conditions lead to the requirement that the sum of the forces at each junction point should be zero. Condition (3.6) must also hold in the reference configuration of the network with $\boldsymbol{F} = \boldsymbol{1}$, so that chain forces are balanced in the reference configuration.

Let $\boldsymbol{f}_k^e$ be the reaction force on a boundary junction with $k \in \mathcal{B}$. In the following, we use the superscript e to refer to quantities related to the external reaction forces. We derive an expression for the macroscopic stress $\boldsymbol{P}^e$ conjugated to the macroscopic deformation gradient $\boldsymbol{F}$ from the condition of equivalence between the (virtual) macroscopic and microscopic works (Alamé and Brassart, 2020):

$$V_0 \boldsymbol{P}^e : \delta \boldsymbol{F} = \sum_k \boldsymbol{f}_k^e \cdot \delta \boldsymbol{x}_k, \tag{3.7}$$

where the summation extends over all the boundary junctions. Inserting the affine boundary conditions (3.5), the right-hand side of the above expression rewrites as:

$$\sum_k \boldsymbol{f}_k^e \cdot \delta \boldsymbol{x}_k = \sum_k (\boldsymbol{f}_k^e \otimes \boldsymbol{X}_k) : \delta \boldsymbol{F}. \tag{3.8}$$

The macroscopic stress is thus identified as:

$$\boldsymbol{P}^e = \frac{1}{V_0}\sum_k \boldsymbol{f}_k^e \otimes \boldsymbol{X}_k, \tag{3.9}$$

and can be interpreted as a first Piola-Kirchhoff stress. $\boldsymbol{P}^e$ can alternatively be derived from the free energy according to:

$$\boldsymbol{P}^e = \frac{\partial W}{\partial \boldsymbol{F}}, \tag{3.10}$$

which can be verified from Eq. (3.6) taking the stationarity condition on the internal node positions into account. Note that the stress $\boldsymbol{P}^e$ is not zero in the reference configuration, since external forces must be applied on the boundary nodes to balance the restoring forces of network chains with non-zero initial end-to-end distance, according to the force-extension relation (3.3).

In this work, we focus on deformations at constant volume, so that $J = \det(\boldsymbol{F}) = 1$. As is standard in the treatment of incompressible hyperelasticity, the incompressibility constraint is taken into account via a Lagrange multiplier P:

$$\boldsymbol{P} = \boldsymbol{P}^e - JP\boldsymbol{F}^{-T}. \tag{3.11}$$

The Lagrange multiplier is identified from the boundary conditions. The corresponding Cauchy stress tensor $\boldsymbol{\sigma}$ is obtained from the usual formula: $\boldsymbol{\sigma} = (1/J)\boldsymbol{P}\boldsymbol{F}^T$, giving:

$$\boldsymbol{\sigma} = \boldsymbol{\sigma}^e - P\mathbf{1}, \tag{3.12}$$

where $\boldsymbol{\sigma}^e = (1/J)\boldsymbol{P}^e\boldsymbol{F}^T$. Note that $\boldsymbol{\sigma}^e$ includes a hydrostatic component and is not deviatoric. Here we assume that the reference configuration is stress free, so that the Lagrange multiplier in the reference configuration is identified as $P = \frac{1}{3}tr(\boldsymbol{\sigma}^e)$. The deviatoric part of the Cauchy stress, $dev(\boldsymbol{\sigma}) = dev(\boldsymbol{\sigma}^e)$ is zero in the reference configuration provided that the network free energy is isotropic, see e.g. (Holzapfel, 2002).

3.2.3 Gaussian networks

When all the chains are in their Gaussian regime in the reference configuration of the network, i.e. Eq. (3.4) applies, the free energy of a chain linking junctions i and j can be expressed as: $w(r_{ij}; N_{ij}) = \frac{1}{2}\kappa_{ij} r_{ij}^2$, where $\kappa_{ij} = 3kT/N_{ij}b^2$ is the stiffness of the Gaussian chain. The corresponding force-extension relation is linear and given by Eq. (3.4). The minimisation problem (3.6) becomes:

$$W(\boldsymbol{F}) = \inf_{\boldsymbol{x}_k, k \in \mathcal{I}} \frac{1}{2V_0} \sum_i \sum_{j>i} \kappa_{ij} r_{ij}^2, \tag{3.13}$$

and the stationarity condition directly provides the condition of force balance at each inner junction:

$$\sum_{j \neq i} \kappa_{ij} \boldsymbol{r}_{ij} = \boldsymbol{0}, \quad \forall i \in \mathcal{I}, \tag{3.14}$$

where the summation on j extends over both inner and boundary junctions. Then, it can be easily verified that the displacements of the inner junctions are also affine. Indeed, assuming affine displacements of both inner and boundary junctions in the above equation gives:

$$\sum_{j \neq i} \kappa_{ij} (\boldsymbol{x}_i - \boldsymbol{x}_j) = \sum_{j \neq i} \kappa_{ij} \boldsymbol{F} \cdot (\boldsymbol{X}_i - \boldsymbol{X}_j) = \boldsymbol{F} \cdot \sum_{j \neq i} \kappa_{ij} (\boldsymbol{X}_i - \boldsymbol{X}_j) = \boldsymbol{0}, \tag{3.15}$$

where the last equality holds provided that the network is equilibrated in the reference configuration. The above equation shows that the affine displacement solution satisfies the stationarity condition of the minimisation problem and is the (unique) solution of the minimum problem[1].

Accounting for the affine displacement of the inner junctions, the free energy of the network can be rewritten in an explicit form. Here we switch notation and use the subscript $\alpha \in (1, n)$ to denote the α^{th} chain in the network. Writing $\boldsymbol{r}_{0,\alpha}$ the end-to-end vector of chain α in the reference configuration, and noting that $\boldsymbol{r}_\alpha = \boldsymbol{F} \cdot \boldsymbol{r}_{0,\alpha}$ due to the affine motion of the junctions,

---

[1] The uniqueness of the solution is based on the following considerations. First, note that the total potential energy of the spring network can be rewritten as (Weiner, 2012):

$$W = \{x\}^T [A] \{x\} + \{B\}^T \{x\} + C,$$

where $\{x\}$ is an array containing the coordinates of all the internal nodes, and the matrix $[A]$, array $\{B\}$ and constant C depend on the network topology, spring constants and the positions of the boundary nodes. The quadratic form has a unique minimum if (and only if) it is positive definite, which is indeed the case here, see (James, 1947; Flory, 1976).

the energy (3.13) rewrites as:

$$W(\boldsymbol{F}) = \frac{1}{2V_0}\sum_\alpha \kappa_\alpha r_\alpha^2 = \frac{1}{2V_0}\sum_\alpha \kappa_\alpha \boldsymbol{r}_{0,\alpha}\cdot(\boldsymbol{F}^T\cdot\boldsymbol{F})\cdot\boldsymbol{r}_{0,\alpha} = \frac{1}{2V_0}\sum_\alpha \kappa_\alpha(\boldsymbol{r}_{0,\alpha}\otimes\boldsymbol{r}_{0,\alpha}):\boldsymbol{C}, \quad (3.16)$$

where $\boldsymbol{C} = \boldsymbol{F}^T\cdot\boldsymbol{F}$ is the right Cauchy-Green strain tensor. If the network is isotropic in the reference configuration, we must also have that (Weiner, 2012):

$$\sum_\alpha \kappa_\alpha \boldsymbol{r}_{0,\alpha}\otimes\boldsymbol{r}_{0,\alpha} = \frac{1}{3}\sum_\alpha \kappa_\alpha r_0^2\mathbf{1}. \quad (3.17)$$

Inserting the above result into Eq. (3.16), we obtain (Weiner, 2012; Alamé and Brassart, 2020):

$$W(\boldsymbol{F}) = \frac{1}{2}\nu kT\left\langle\frac{r_{0,\alpha}^2}{Nb^2}\right\rangle I_1 \equiv \frac{1}{2}GI_1, \quad (3.18)$$

where $I_1 = tr(\boldsymbol{C})$ is the first invariant of the right Cauchy-Green tensor, $\nu = n/V_0$ is the chain density, and we have introduced the following notation for the ensemble average over all the chains in the network:

$$\langle\cdot\rangle = \frac{1}{n}\sum_{\alpha=1}^{n}(\cdot)_\alpha. \quad (3.19)$$

Eq. (3.18) shows that the energy density of a discrete network of Gaussian springs is of the neo-Hookean form with shear modulus given by:

$$G = \nu kT\left\langle\frac{r_0^2}{Nb^2}\right\rangle = \nu kT\langle\lambda_0^2\rangle. \quad (3.20)$$

When all the chains adopt their random-walk end-to-end distance in the reference configuration of the network, i.e $\lambda_0 = 1$ for all chains, the modulus recovers the estimate of the classical affine model of rubber elasticity theory: $G_{\text{aff}} = \nu kT$ (Treloar, 1973; Rubinstein and Colby, 2003).

Remark 2 *In the classical affine model of rubber elasticity theory, as presented for example in (Treloar, 1973; Rubinstein and Colby, 2003), the assumption of affine deformation of the chains is made a priori. In contrast, in the DN model of Gaussian chains, the affine deformation of the chains is an exact result. The classical affine model also relies on the a-priori assumption that all chains adopt their random-walk end-to-end distance in the initial configuration of the network. If this assumption is relaxed and the chain initial end-to-end distances are left unspecified, then* *the affine model of rubber elasticity gives (3.20), see Section 5.6 in (Weiner, 2012). However, for some reason, the effect of a chain pre-stretch distribution on the modulus has been largely ignored in the literature, and the expression $G_{\text{aff}} = \nu kT$ is usually retained as that of the "affine modulus", at the expense of the more general form (3.20).*

3.2.4 Numerical implementation

The DN model was implemented in LAMMPS (Thompson et al., 2022), treating junction points as atoms with bond behaviour described by the FJC model implemented in LAMMPS via C++ user subroutines. For given positions of the boundary junctions set by the affine boundary conditions (3.5) corresponding to a given deformation gradient $\boldsymbol{F}$, the equilibrium positions of the inner junctions are calculated by energy minimisation using the FIRE algorithm (Bitzek et al., 2006) implemented in LAMMPS. Note that networks are also equilibrated in their refence configuration with $\boldsymbol{F} = \mathbf{1}$, as the network generation algorithm (presented in the next section) does not produce an equilibrated network. The macroscopic stress $\boldsymbol{P}^e$ is calculated from the reaction forces on the boundary nodes according to Eq. (3.9), and the Lagrange multiplier P in Eq. (3.11) is identified from the boundary conditions.

3.3 Network generation algorithm

We now present a network generation algorithm allowing independent control of the average chain end-to-end distance, chain length and chain density. The algorithm was inspired by the work of Kryven and Versendaal (2022), and was implemented in Matlab. Network topologies in a unit cube are defined by a (theoretical) distribution of chain end-to-end distances in the reference configuration, taken of the Gaussian form:

$$p_d(d) = \frac{1}{\sqrt{2\pi s_d^2}} \exp\left(-\frac{1}{2}\left(\frac{(d-\mu_d)}{s_d}\right)^2\right), \tag{3.21}$$

where μ_d and s_d are the average and standard deviations of the distribution. DNs satisfying the above distribution are produced by sequentially adding links (chains) between nodes (junction points) randomly dispersed in the unit cube. For simplicity, we assume that all inner nodes have a functionality of four, however the algorithm below can be generalised to other, possibly non-uniform functionalities. Thus, if f_i denotes the available functionality of node i, then $f_i = 4$ for all $i \in \mathcal{I}$ at the start of the algorithm.

The network generation algorithm, illustrated in Fig. 3.1, involves the following steps:

1. The unit cube is seeded with $n/2$ randomly distributed nodes using a Poisson disk sampling algorithm to maintain a minimum separation distance δ_D between nodes (Cook, 1986) (Fig. 3.1(a)). In practice, the distance δ_D is set as $0.5\left(\frac{2}{n}\right)^{1/3}$.

2. A list containing all admissible connection distances $d_{ij} \geq 0, d_{ij} = d_{ji}$ is created. Here we assume periodicity and calculate distances between nodes across boundaries. Let $g_d(r)$ be the numerical probability density of the elements of this list. That is, $g_d(r)\mathrm{d}r$ is the probability that $d_{ij} \in [r, r + \mathrm{d}r)$.

3. The connection probability p_{ij} for each pair of nodes (i, j) with $i, j \in \mathcal{I}$ is calculated taking into the account the actual distance d_{ij} between the two nodes and the desired end-to-end distribution, Eq. (3.21),

$$p_{ij} := \frac{p_d(d_{ij})}{g_d(d_{ij})} f_i f_j. \tag{3.22}$$

4. From all admissible links, one is chosen using weighted sampling, using p_{ij} as the weights (Fig. 3.1(b)). Suppose the chosen link is (i, j), then the available functionalities of the nodes involved in this link are updated: $f_i = f_i - 1$ and $f_j = f_j - 1$.

5. The list of the connection probabilities p_{ij} is recalculated using equation (3.22), and, if the number of placed links is less than n, one goes to Step 4.

6. Once n links have been created by joining the inner nodes, additional nodes are added on the cube surface at the points where periodic links cross the boundaries (Fig. 3.1(c)). This process effectively replaces each periodic link by two shorter links. This procedure slightly changes the final number of chains in the network. However, they do not significantly impact the final chain density, provided that n is large enough.

All the networks considered in this work contain at least 60000 chains. This number is sufficiently large to ensure a good agreement between the distribution of end-to-end distances in

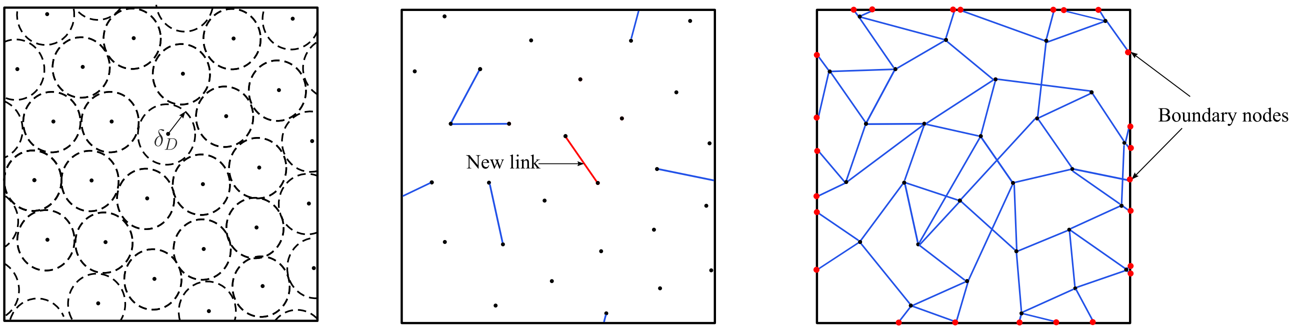

(a) Poisson disc sampling (b) Placement of connections (c) Creation of boundary nodes

Fig. 3.1: Steps involved in the generation of the discrete networks. (a) Seeding of the simulation volume with nodes using Poisson disc sampling with minimal separation distance δ_D. (b) Sequential linking of nodes based on a predefined probability of end-to-end distance. (c) Creation of additional boundary nodes.

the as-generated network and the theoretical distribution Eq. (3.21). Noticeable deviations were only observed for small prescribed average distances μ_d with deviations s_d large enough to produce the condition $\mu_d - s_d < 0$. Moreover, the average functionality $\langle f_i \rangle$ of the generated networks is typically not equal to four due to the presence of boundary nodes. However, 99% of the inner junctions have $f_i = 4$, demonstrating the robustness of the algorithm to produce networks with prescribed functionality, since the boundary nodes are created in a post-processing phase.

The algorithm produces networks with different degrees of interpenetration, depending on the chosen values for chain density and average distance μ_d. By interpenetrated networks, we mean networks in which the average distance between junctions is larger than the average nearest-neighbour distance. Specifically, we use the distance between two connected junctions in a diamond network as a reference for measuring interpenetration. In a unit cube, the distance between two neighbour junctions in a diamond lattice is given by $\frac{\sqrt{3}}{4^{1/3}} n^{-1/3}$. Thus, we define the degree of interpenetration ξ as:

$$\xi = \frac{4^{1/3}}{\sqrt{3}} n^{1/3} \mu_d, \tag{3.23}$$

which shows that ξ increases linearly with the average distance μ_d when the number of chains is kept constant. For illustration, Fig. 3.2 shows two 2D networks generated with the same number of chains $n = 1000$, but different degrees of interpenetration $\xi = 1$ (a) and $\xi = 4$ (b). The deviation s_d is the same for both networks: $s_d = 0.005$. Note that in 2D, interpenetration

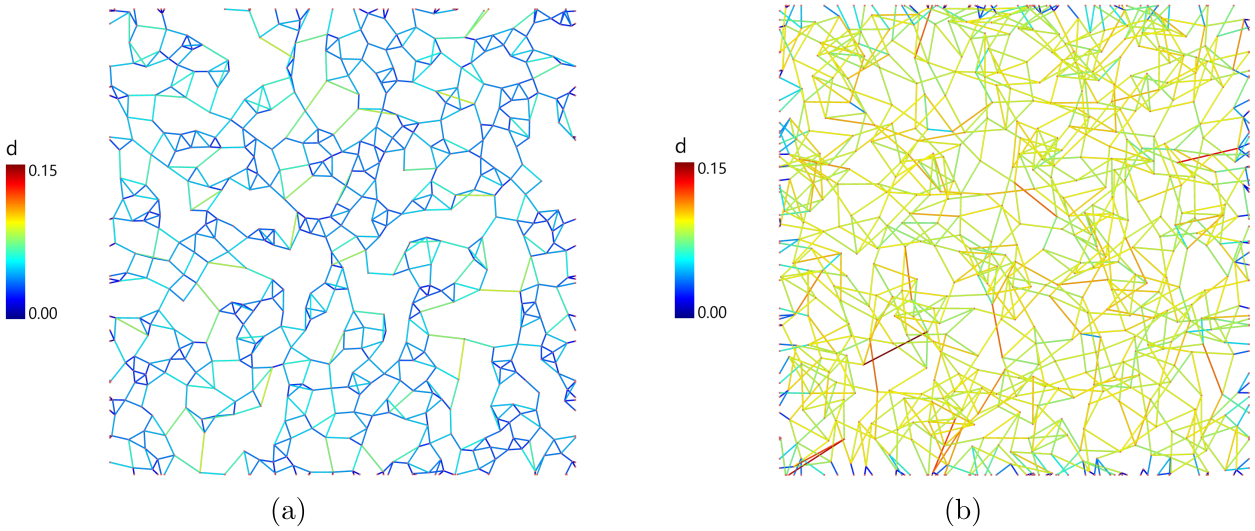

(a) (b)

Fig. 3.2: Illustration of 2D networks with different degrees of interpenetration: a) $\xi = 1$ and b) $\xi = 4$. For both networks $n = 1000$ and $s_d = 0.005$. d represents the end-to-end distance of a chain in the unit square. The maximum value of 0.15 was observed in Fig. (b), and the same colour scale was adopted in Fig. (a) to highlight the differences in end-to-end distance distributions in networks with different degrees of interpenetration.

is measured with respect to a square lattice taken as reference, and the definition of interpenetration becomes $\xi = \sqrt{2} n^{1/2} \mu_d$. Networks with higher degrees of interpenetration have more intricate structures.

After generating the network topologies, the number N of Kuhn segments is assigned to each chain. For polydispersed networks, N is drawn from a predefined distribution $p_N(N)$, treating N as a continuous random variable. Several probability distribution functions have been considered in the literature, including normal, log-normal, and exponential distributions (Wang et al., 2015; Itskov and Knyazeva, 2016; Verron and Gros, 2017; Guo and Zaïri, 2021; Mulderrig et al., 2021). For illustration, we limit ourselves to the log-normal distribution:

$$p_N(N) = \frac{1}{N\sqrt{2\pi s^2}} \exp\left(-\frac{(\ln N - \mu)^2}{2s^2}\right), \tag{3.24}$$

where the parameters μ and s are related to the mean μ_N and standard deviation s_N of the distribution by:

$$\mu = \ln\left(\frac{\mu_N^2}{\sqrt{\mu_N^2 + s_N^2}}\right), \quad s^2 = \ln\left(1 + \frac{s_N^2}{\mu_N^2}\right). \tag{3.25}$$

We have verified that the actual chain length distribution of the polydispersed DNs is in good agreement with the analytical expression (3.24).

Finally, the physical length $L_0 = (V_0)^{(1/3)}$ of the simulation volume was determined based on the actual chain density ν as:

$$\nu = \frac{n}{L_0^3}, \tag{3.26}$$

giving the physical end-to-end distance between nodes as dL_0. Effectively, this approach decouples the network topology from chain density. Networks with identical topologies (in the unit cube) but different chain densities can be simulated by simple rescaling of the lengths. At this stage, chains with (physical) end-to-end distance larger than their contour length Nb are removed from the simulation volume. Indeed, chains with end-to-end distances exceeding their contour length may be produced by the network generation algorithm for polydispersed networks with a broad distribution of chain lengths. In the simulations considered below, the fraction of chains removed from the simulation never exceeded 5%.

After rescaling, the equilibrated configuration of the as-generated network for a given macroscopic deformation was determined, as described in Section 3.2.4. For illustration, Fig. 3.3 shows the (a) as-generated and (b) relaxed ($\boldsymbol{F} = \mathbf{1}$) configurations of a 3D network generated with $\mu_d = 0.073$, $s_d = 0.015$ and $n = 10000$. The initial relaxation of the network alters the distribution of the chain end-to-distances, compared to the as-generated structure. Overall, relaxation tends to decrease the average end-to-end distance and to widen the distribution of end-to-end distances. To obtain DNs with a desired average end-to-end distance in the reference, relaxed configuration, a slightly higher average end-to-end distance target has to be prescribed. Trial-and-error tests suggest that setting the target value as 1.4 times larger than the desired one suffices to compensate for the relaxation effects.

3.4 Elastic properties of Discrete Networks

We illustrate the mechanical behaviour of discrete networks subjected to uniaxial tension. Under the assumption of incompressibility, the macroscopic deformation gradient is taken of the form: $\boldsymbol{F} = diag\{\lambda_1, \lambda_2, \lambda_3\}$ with $\lambda_2 = \lambda_3 = 1/\sqrt{\lambda_1}$. The Lagrange multiplier P is identified from the condition $\sigma_2 = \sigma_3 = 0$. The shear modulus G of the DN is calculated from the

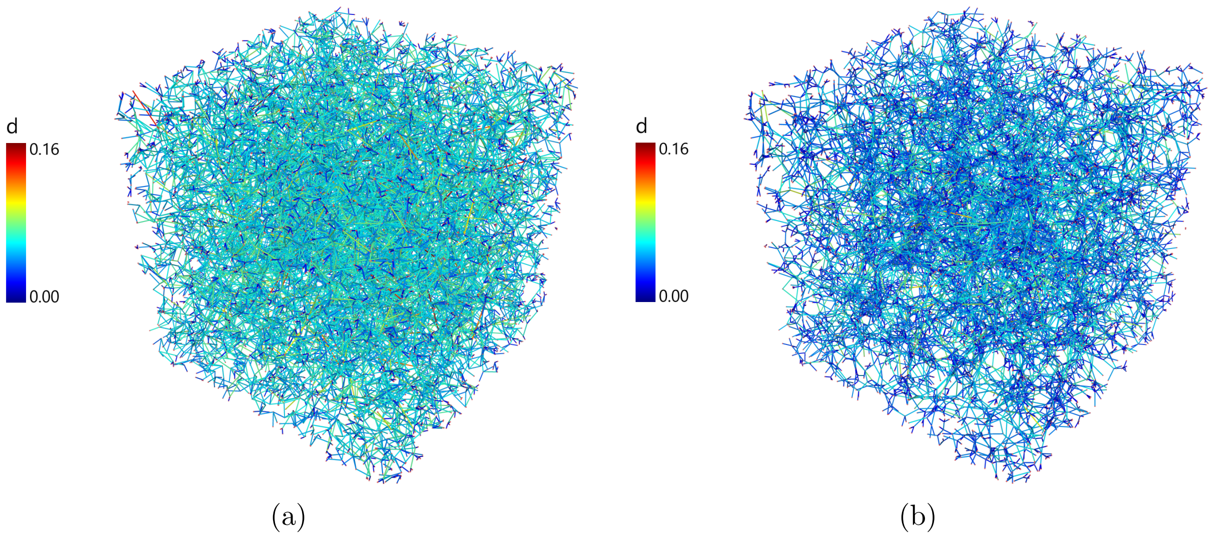

(a) (b)

Fig. 3.3: Comparison between the as-generated (a) and relaxed (b) configurations of a 3D DN generated with $\mu_d = 0.073$, $s_d = 0.015$ and $n = 10000$ for illustration. Networks used to calculate the effective properties contain at least 60000 chains. d represents the end-to-end distance of a chain in the unit cube. The maximum value of 0.16 was observed in Fig. (b), and the same colour scale was adopted in Fig. (a) to highlight the differences in end-to-end distance distributions in networks with different degrees of interpenetration.

stress-strain curves as[2]:

$$3G = \lim_{\lambda_1 \to 1} \frac{d\sigma_1}{d\lambda_1}. \tag{3.27}$$

The limit extensibility $\lambda_{\max}$ of the DN is defined as the macroscopic stretch at which the stress tends to infinity. In practice, DN simulations lose convergence before reaching the true extensibility limit, due to the divergence in the force-extension relation of highly-stretched chains. As a workaround, $\lambda_{\max}$ is estimated by fitting the DN stress-strain response using a mathematical expression borrowed from the 3-chain model, and extrapolating this expression to infinite stress, see (Alamé and Brassart, 2020). For each set of parameters, simulations were conducted for five DN realisations. Differences in the stress-stretch behaviour of DNs created with the same input parameters only became noticeable in the later stages of deformation, where locking effects occur. Therefore, in the following we only show the stress-stretch curve of one DN realisation.

---

[2] In practice, the shear modulus was obtained by fitting the stress-strain curve in the small-deformation region with the following expression (Sorichetti et al., 2021):

$$\sigma_1 = G\left[(\lambda - \lambda_{\text{ref}})^2 - \frac{1}{\lambda - \lambda_{\text{ref}}}\right],$$

where λ_{ref} is a numerical fitting parameter introduced to compensate for the fact that σ_1 is not exactly zero at $\lambda = 1$ in the DN simulations.

3.4.1 Monodispersed networks

We first consider monodispersed networks with $\nu b^3 = 0.001$ and $N = 100$. The networks were generated by varying μ_d (or ξ) while keeping the deviation $s_d = 0.2\mu_d$ constant. Distributions $p_{\lambda_0}(\lambda_0)$ of chain pre-stretches $\lambda_0 = \frac{r_0}{\sqrt{N}b}$ in the relaxed reference configuration are shown in Fig. 3.4(a). DN results show that networks generated with higher degrees of interpenetration exhibit broader pre-stretch distributions. The uniaxial tension response of these networks is shown in Fig. 3.4(b). Overall, higher degrees of pre-stretch lead to a stiffer response of the network and to a reduction in the limit extensibility.

Scaling relations for the elastic modulus of networks with three different chain densities and various average pre-stretches $\bar{\lambda}_0 \equiv \sqrt{\langle \lambda_0^2 \rangle} = \sqrt{\langle \frac{r_0^2}{Nb^2} \rangle}$ are shown in Fig. 3.4(c). The dashed line represents the modulus of the corresponding Gaussian network calculated using Eq. (3.20). As a rule of thumb, chains can be considered to be in their Gaussian regime in the reference configuration when $r_0 < 0.3Nb$, which for $N = 100$ approximately corresponds to $\lambda_0 < 3$. The agreement between DN predictions and the Gaussian estimate is very good overall. The discrepancy observed as the average pre-stretch increases is due to the fact that a larger portion of chains are pre-stretched beyond their Gaussian regime as the average pre-stretch increases, as seen in Fig. 3.4(a).

The limit extensibility of the networks is shown in Fig. 3.4(d). Considering that the limit extensibility of the network is reached when chains aligned with the maximum principal stretch direction reach their contour length, the following scaling relation is suggested: $\lambda_{\max} \sim \frac{\sqrt{N}}{\lambda_0}$ (shown as a dashed line). This scaling generalises the classical relation $\lambda_{\max} \sim \sqrt{N}$, which holds only in the particular case where $r_0 = \sqrt{N}b$ and $\lambda_0 = 1$. This scaling relation is independent of the chain density, which is verified in the DN simulations.

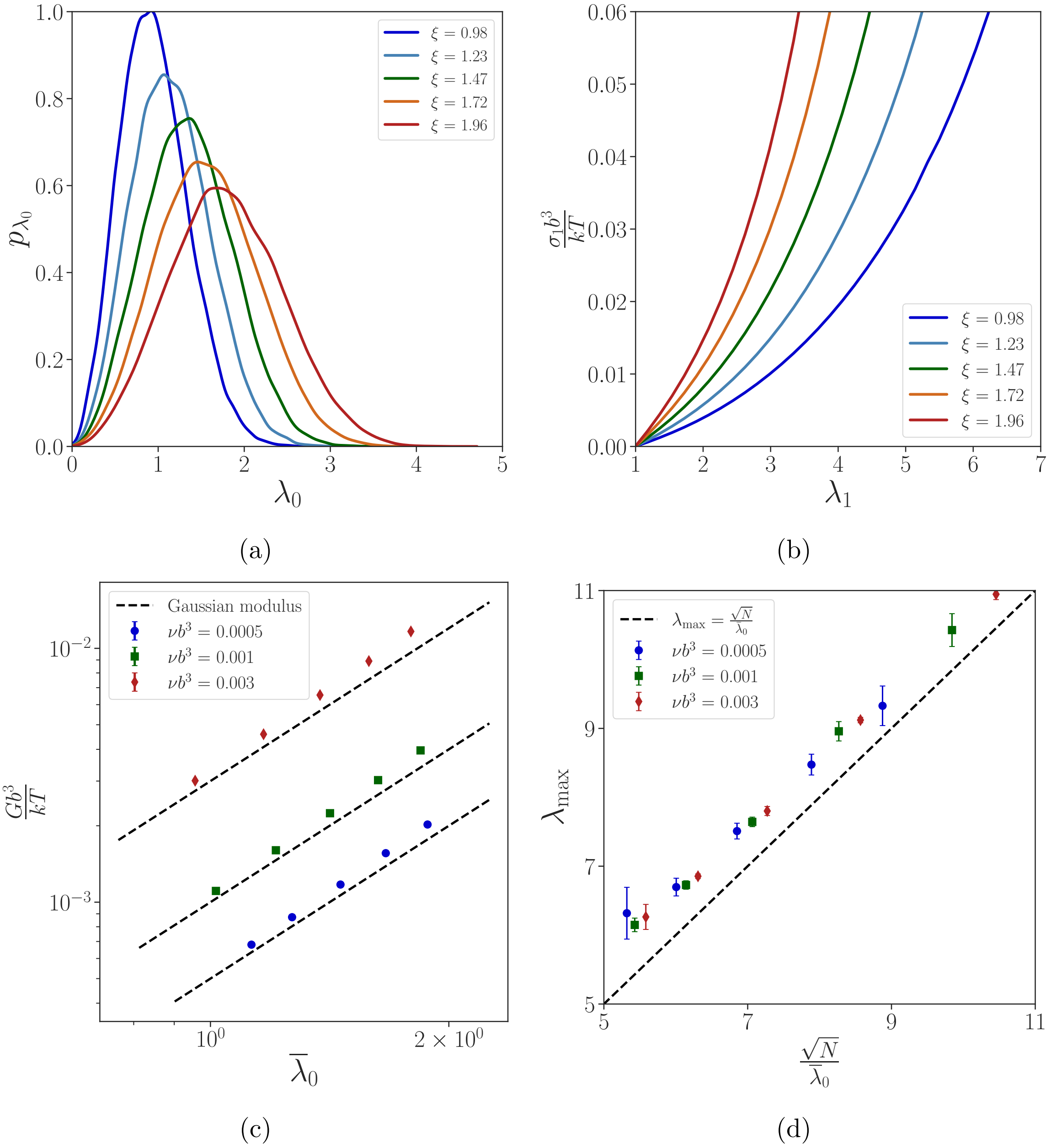

Fig. 3.4: a) Probability distributions of chain pre-stretch of Discrete Networks with $\nu b^3 = 0.001$, $N = 100$, and various degrees of interpenetration. b) Uniaxial tension response of the networks. c) Scaling of the elastic modulus with average pre-stretch in networks with different chain densities. d) Scaling of the extensibility limit with the average locking stretch.

3.4.2 Polydispersed networks

We next consider polydispersed networks with log-normal chain length distribution. The topologies of the polydispersed DNs are the same as the topologies of the corresponding monodispersed DNs with same density considered in Section 3.4.1. These networks all have the same average number of Kuhn segments per chain, $\mu_N = 100$ but differ in the spreading of the chain length distribution. Figs 3.5(a) and (b) show the pre-stretch distribution and uniaxial stress-stretch response of polydispersed networks Corresponding results for monodispersed networks with $N = 100$ are also shown for comparison. The initial slope of the stress-stretch response is similar in all networks, which is due to the fact that all networks have similar average pre-stretch $\bar{\lambda}_0$ and the same chain density. However, the response of polydispersed networks is stiffer than that of monodispersed networks at large deformation, and the stiffening effects is more pronounced as the standard deviation in the chain length distribution increases. The extensibility limit also decreases with an increase in s_N. These effects can directly be attributed to the presence of shorter chains which stiffen the network and reach their own limit extensibility earlier. Similar trends were observed for other values of the average pre-stretch.

Figs 3.5(c)-(d) shows the elastic modulus and extensibility limit of polydispersed networks with various degrees of interpenetration (the same ones as in Fig. 3.4a), and thus various degrees of average pre-stretch. Fig. 3.5(c) shows that the scaling $G \sim \bar{\lambda}_0^2$ still holds, and that the modulus is still satisfactorily predicted by the Gaussian estimate (3.20), as expected. However, the accuracy of the Gaussian estimate decreases as the average pre-stretch increases, due to the presence of chains stretched beyond their Gaussian regime in the initial configuration. Regarding the extensibility limit (Fig. 3.5(d)), to account for the presence of short chains, we propose a scaling relation of the form:

$$\lambda_{\max} \sim (\mu_N - \alpha s_N)^{1/2}\, \bar{\lambda}_0^{-1}, \tag{3.28}$$

where α is a constant. This expression effectively extends the corresponding monodispersed scaling relation by using an effective number of Kuhn segment $N_{\text{eff}} = \mu_N - \alpha s_N$ and recovers the monodispersed scaling relation when $s_N = 0$. The extensibility limits of all considered networks collapse onto a single master curve when $\alpha = 0.2$, as shown in Fig. 3.5(d), corresponding to $N_{\text{eff}} = 98$, 94 and 90 in the cases $s_N = 10$, 30 and 50, respectively.

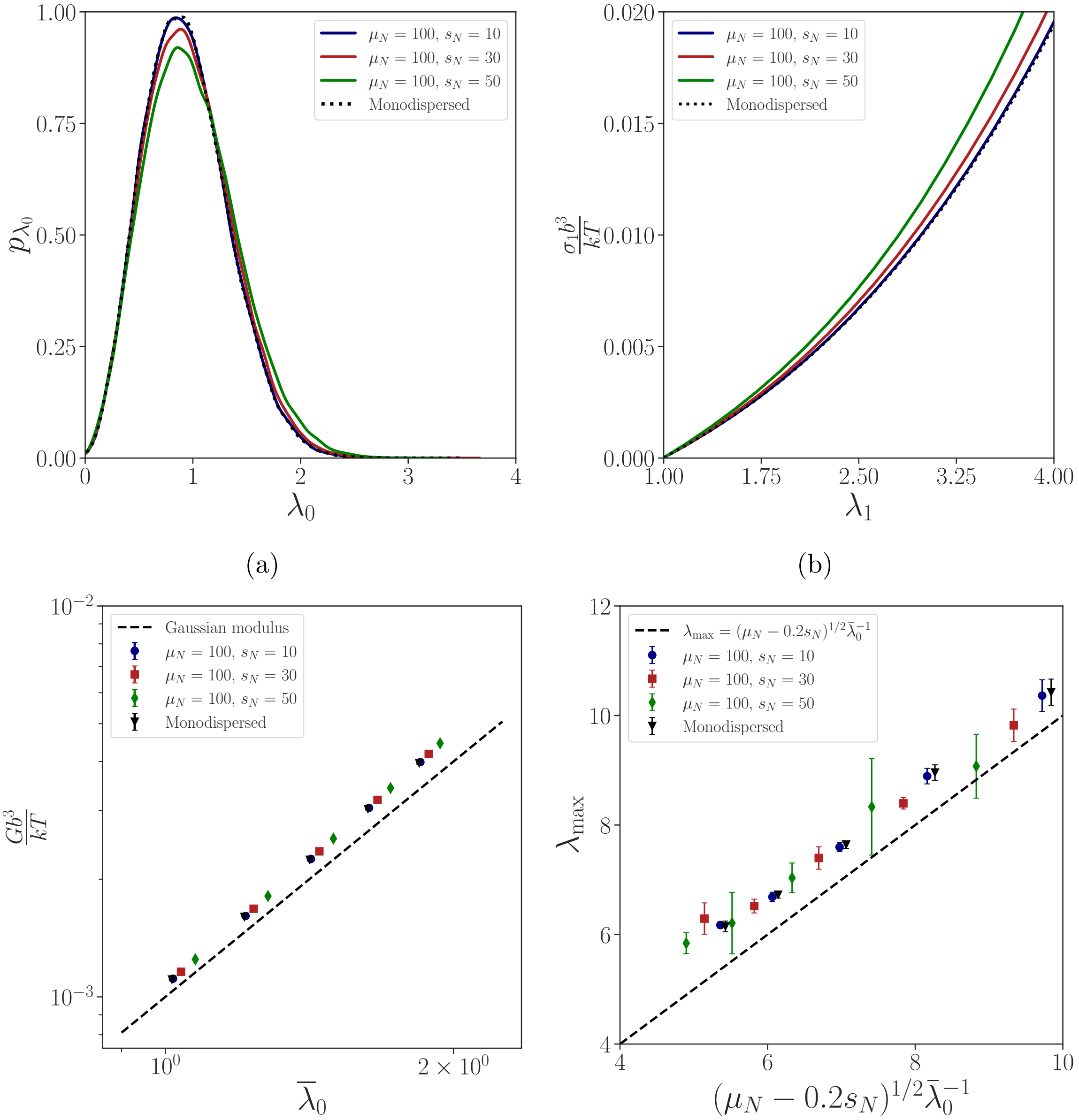

(a) (b)

(c) (d)

Fig. 3.5: a) Probability distribution of chain pre-stretch in polydispersed DNs with $\nu b^3 = 0.001$, $\mu_N = 100$, and various s_N. The degree of interpenetration is $\xi = 0.98$. Uniaxial stress-stretch responses of these networks. Scaling of (c) the elastic modulus and (d) the extensibility limit in polydispersed networks with different chain length distributions and different average chain pre-stretch, corresponding to different degrees of interpenetration $\xi = 0.98, 1.23, 1.47, 1.72,$ and 1.96.

3.5 Microsphere models

DN models allow the detailed investigation of the role of network topology on the network properties. However, they remain computationally expensive in view of numerical simulations at the structure scale. For this purpose, continuum constitutive theories remain necessary. In this Section, we outline several micromechanics based constitutive models of rubber elasticity. All these models describe individual chains as freely-jointed chains, but differ in the postulated stretch-partitioning assumption. Our objective is precisely to assess the accuracy of those stretch-partitioning assumptions, using DN simulations as reference.

We focus on so-called microsphere models, which consider a continuous distribution of chain orientations. The initial (reference) orientation of a chain is described by the unit vector $\boldsymbol{n}_0 = \boldsymbol{r}_0/\|\boldsymbol{r}_0\|$, with $\boldsymbol{r}_0$ the initial end-to-end vector of a chain. In the current configuration of the network subjected to the macroscopic deformation gradient $\boldsymbol{F}$, the end-to-end vector becomes $\boldsymbol{r}$. Polydispersity is described by the chain length distribution p_N. The considered microsphere models are based on the additional set of assumptions: (i) chains are randomly oriented in the initial configuration of the network; (ii) chains having the same number of Kuhn segments all have the same initial end-to-end distance: $r_0 = r_0(N)$; (iii) chains with the same initial orientation $\boldsymbol{n}_0$ and having the same number of Kuhn segments N all experience the same stretch: $\lambda_c = \lambda_c(\boldsymbol{F}, \boldsymbol{n}_0, N)$. According to this set of assumptions, the elastic free energy of a network with chain density ν can be expressed as:

$$W = \nu \int_N p_N(N) \iint_{\mathcal{S}_u} w(\lambda_c; N) d\mathcal{S}_u dN, \tag{3.29}$$

where we have used the notation $\iint_{\mathcal{S}_u} d\mathcal{S}_u = \frac{1}{4\pi}\int_0^{2\pi}\int_0^{\pi} \sin(\phi) d\phi d\theta$. Fig. 3.6 shows a schematic representation of the microsphere framework and the meaning of the spherical angles θ and ϕ. In Eq. (3.29), w is the free energy of a single chain given by the freely-jointed chain model (3.2). The macroscopic stress $\boldsymbol{P}^e$ derived from the free energy (3.29) is given by:

$$\boldsymbol{P}^e = \nu \int_N p_N(N) \iint_{\mathcal{S}_u} f(\lambda_c, N) r_0 \frac{\partial \lambda_c}{\partial \boldsymbol{F}} d\mathcal{S}_u dN, \tag{3.30}$$

where f is the chain force. Specific models differ in their assumptions used to calculate λ_c. In

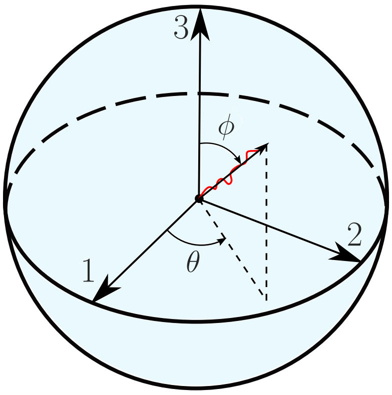

Fig. 3.6: Schematic representation of the microsphere model and the meaning of the spherical angles θ and ϕ.

the following, we consider the affine model (Treloar (1954); Wu and Van Der Giessen (1993); Itskov and Knyazeva (2016)), the hybrid equal-force model (Verron and Gros (2017)), and the non-affine fully-relaxed model (Tkachuk and Linder (2012); Diani and Le Tallec (2019); Govindjee et al. (2019); Mulderrig et al. (2021)).

3.5.1 Affine model

In the affine microsphere model, the chain stretch λ_c is identified with the (affine) line-stretch of the continuum for the initial chain direction:

$$\lambda_c = \lambda_{\text{aff}}, \quad \lambda_{\text{aff}} = \|\boldsymbol{F}\boldsymbol{n}_0\|. \tag{3.31}$$

The macroscopic stress (3.30) becomes:

$$\boldsymbol{P}^e = \nu \int_N p_N(N) \iint_{\mathcal{S}_u} \frac{f r_0}{\lambda_c} \boldsymbol{F}(\boldsymbol{n}_0 \otimes \boldsymbol{n}_0) d\mathcal{S}_u dN. \tag{3.32}$$

The elastic modulus can be readily obtained from the stress-stretch relation, assuming that all chains are in their Gaussian regime in the initial configuration. Eq. (3.4) for the chain force can be then used, and the following expression of the modulus is found:

$$G_{\text{aff}} = \nu kT \int_N p(N) \frac{r_0^2}{Nb^2} dN. \tag{3.33}$$

This expression is the continuum counterpart of the discrete Gaussian estimate (3.20) and reduces to the classical value νkT in the particular case where all chains adopt their random

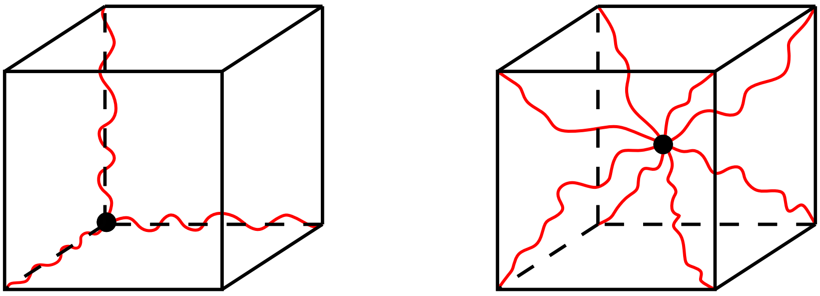
(a) (b)

Fig. 3.7: Unit cells of the three-chain (a) and eight-chain (b) reductions.

walk end-to-end distance $\sqrt{N}b$ in the initial configuration.

In the affine model, the chain stretch (3.31) is independent of the number of Kuhn segments. It follows that the limit extensibility is reached when a chain aligned in the maximum principal stretch direction reaches it contour length: $\lambda_{\max} = \left(\frac{Nb}{r_0}\right)_{\min}$. In the particular case where $r_0 = \sqrt{N}b$, then $\lambda_{\max} = \sqrt{N_{\min}}$ with $N_{\min}$ the number of Kuhn segments in the shortest chains.

Three-chain and eight-chain reductions. The three-chain model (Wang and Guth, 1952) can be seen as a reduction of the microsphere model where only the chains that are initially aligned with the principal stretch directions are considered. For a monodispersed network, the elastic energy is given by:

$$W = \frac{\nu}{3}\sum_{i=1}^{3} w(\lambda_i). \tag{3.34}$$

In the eight-chain model (Arruda and Boyce, 1993), only chains aligned with the diagonal of a cube aligned with the principal stretch directions in the initial configuration are considered:

$$W = \nu w(\Lambda_c), \tag{3.35}$$

where $\Lambda_c = \sqrt{\frac{\lambda_1^2+\lambda_2^2+\lambda_3^3}{3}}$. Fig. 3.7 illustrates the unit cells associated with the three-chain and eight-chain models.

3.5.2 Hybrid equal-force model

In the hybrid equal-force model proposed by Verron and Gros (2017), chains of different contour lengths that are oriented in the same direction in the initial configuration are assembled in series to form a hybrid chain with end-to-end distance R:

$$R = \int_N p_N(N) r(N) \; dN, \tag{3.36}$$

where $r(N)$ denotes the end-to-end distance of a chain with N Kuhn segments in the hybrid chain. Assuming that all chains in the hybrid chain are subjected to the same force f, Eq. (3.36) can be rewritten as:

$$R = \int_N p_N(N) N b \mathcal{L}\left(\frac{fb}{kT}\right) \; dN, \tag{3.37}$$

where we have used the force-extension relation of the FJC model (3.3). Inverting (3.37) then gives the force-extension relation of the hybrid chain:

$$f = \frac{kT}{b}\mathcal{L}^{-1}\left(\frac{R}{\bar{N}b}\right), \tag{3.38}$$

where $\bar{N}$ is the average number of Kuhn segments in the hybrid chain:

$$\bar{N} = \int_N p_N(N) N \; dN. \tag{3.39}$$

The stretch of the hybrid chain Λ_c is identified with the line-stretch of the continuum:

$$\Lambda_c = \lambda_{\text{aff}}, \tag{3.40}$$

where $\Lambda_c = \frac{R}{R_0}$ and the affine stretch was defined in Eq. (3.31). The initial end-to-end distance of the hybrid chain is defined consistently with Eq. (3.36) as $R_0 = \int_N p_N(N) r_0(N) dN$. The macroscopic stress is directly obtained from Eq. (3.32) applied to a monodispersed network of hybrid chains with initial end-to-end distance R_0:

$$\boldsymbol{P}^e = \nu \iint_{\mathcal{S}_u} \frac{f R_0}{\Lambda_c} \boldsymbol{F}(\boldsymbol{n}_0 \otimes \boldsymbol{n}_0) d\mathcal{S}_u. \tag{3.41}$$

Note that the initial end-to-end distances of individual chains cannot be prescribed a-priori, as it would violate the equal force assumption in the reference configuration. Instead, only the initial end-to-end distance R_0 of the hybrid chain can be prescribed, and the equal-force assumption gives the initial end-to-end distance of a chain with N Kuhn segments as: $r_0(N) = (N/\bar{N})R_0$.

The elastic modulus of the hybrid equal-force model (assuming that all chains are in their Gaussian regime in the initial configuration) is obtained as:

$$G_{\mathrm{EF}} = kT\nu \frac{R_0^2}{\bar{N}b^2}. \tag{3.42}$$

The modulus of the hybrid equal-force model reduces to the classical estimate νkT when $R_0 = \sqrt{\bar{N}}b$, which corresponds to $r_0(N) = \frac{N}{\sqrt{\bar{N}}}b$. The maximum extensibility of the hybrid equal-force model is reached when the hybrid chain aligned with the maximum principal stretch direction reaches its contour length $\lambda_{\max} = \bar{N}b/R_0$.

Remark 3 *Our presentation of the hybrid equal-force model differs from the original presentation by Verron and Gros (2017). These authors introduced a pre-assembly state, where individual chains adopt an initial end-to-end distance* $\tilde{r}_0$. *Subsequently, the chains are assembled in the hybrid chain while complying with the equal-force constraint. In this view, the function* $\tilde{r}_0(N)$ *can be arbitrarily set, and is used to define the initial pre-assembly length* $\tilde{R}_0 = \int_N p_N(N)\tilde{r}_0(N)dN$. *They then assumed that the length of the hybrid chains remained unchanged during assembly, i.e.,* $R_0 = \tilde{R}_0$. *In our approach, we do not introduce a pre-assembly state, and the chains are initially in equilibrium and subjected to the equal-force constraint. This is consistent with the DN model, where the initial distribution of end-to-end distances must satisfy the condition of mechanical equilibrium.*

3.5.3 Fully-relaxed non-affine model

In the fully-relaxed model, no a-priori assumption is made on the partitioning of stretches or forces among the chains. Instead, the chain stretches are determined in such a way that they minimise the total elastic energy of the network subjected to a kinematic constraint. For a polydispersed network, we take the kinematic constraint of the following form:

$$\frac{1}{3}\boldsymbol{F} = \int_N p_N(N) \iint_{\mathcal{S}_u} \boldsymbol{F}_m d\mathcal{S}_u dN, \tag{3.43}$$

where $\boldsymbol{F}_m$ is the microscopic deformation such that $\boldsymbol{r} = \boldsymbol{F}_m \boldsymbol{r}_0$. Introducing the deformed orientation vector $\boldsymbol{n}$, such that $\boldsymbol{r} = r_0 \boldsymbol{n}$, we have:

$$\boldsymbol{F}_m = \boldsymbol{n} \otimes \boldsymbol{n}_0. \tag{3.44}$$

The normalisation factor $1/3$ in Eq. (3.43) ensures that $\boldsymbol{F} = \boldsymbol{1}$ when $\boldsymbol{n} = \boldsymbol{n}_0$. The deformed orientations $\boldsymbol{n}$ are found by minimising the total elastic energy of the network under the constraint (3.43):

$$W = \inf_{\boldsymbol{n},\boldsymbol{\pi}} \left\{ \nu \int_N p_N(N) \iint_{\mathcal{S}_u} w d\mathcal{S}_u dN + \boldsymbol{\pi} : \left(\frac{1}{3}\boldsymbol{F} - \int_N p_N(N) \iint_{\mathcal{S}_u} \boldsymbol{n} \otimes \boldsymbol{n}_0 d\mathcal{S}_u dN \right) \right\}, \tag{3.45}$$

where $\boldsymbol{\pi}$ is the Lagrange multiplier enforcing the constraint (3.43). The stationary condition w.r.t. $\boldsymbol{n}$ gives, for each N:

$$\boldsymbol{f} = \frac{1}{\nu r_0} \boldsymbol{\pi} \boldsymbol{n}_0, \tag{3.46}$$

where $\boldsymbol{f} = f \frac{\boldsymbol{n}}{\|\boldsymbol{n}\|}$ and $f = \frac{dw}{dr}$. Remembering that r_0 in general depends on N, Eq. (3.46) shows that all chains with the same initial orientation are subjected to forces aligned in the same direction, but with different magnitudes depending on N. Taking the norm of the force, and using the FJC model (3.3), the end-to-end distance of a chain with initial orientation $\boldsymbol{n}_0$ and N Kuhn segments can be calculated:

$$r = Nb\mathcal{L}\left(\frac{\|\boldsymbol{\pi}\boldsymbol{n}_0\| b}{r_0 \nu k T} \right). \tag{3.47}$$

Taking the stationarity condition into account, the macroscopic stress $\boldsymbol{P}^e$ is derived from the free energy as:

$$\boldsymbol{P}^e = \frac{\boldsymbol{\pi}}{3}. \tag{3.48}$$

The fully-relaxed model is an implicit model, requiring an iterative procedure to calculate the macroscopic stress for a given macroscopic deformation gradient $\boldsymbol{F}$. At each iteration, the current value of the multiplier $\boldsymbol{\pi}$ is used to calculate the chain force $\boldsymbol{f}$ for each $(\boldsymbol{n}_0, N)$ according to Eq. (3.46). The corresponding end-to-end distances are obtained from Eq. (3.47) and the deformed vectors are calculated as $\boldsymbol{n} = \frac{r}{r_0} \frac{\boldsymbol{f}}{f}$. Iterations are carried out on the Lagrange multiplier until the constraint (3.43) is satisfied.

The minimisation (3.45) must also be carried out in the initial configuration of the network, so that the relation $r_0(N)$ cannot be set arbitrarily. First note that, from Eq. (3.46) the deformed orientations can be expressed as: $\boldsymbol{n} = \frac{r}{r_0}\frac{\boldsymbol{\pi}\boldsymbol{n}_0}{\|\boldsymbol{\pi}\boldsymbol{n}_0\|} = \frac{r}{r_0}\frac{\boldsymbol{\pi}\boldsymbol{n}_0}{\nu r_0 f}$. Using this expression into the kinematic constraint (3.43), and setting $\boldsymbol{F} = \mathbf{1}$, $r = r_0$ and $\boldsymbol{n} = \boldsymbol{n}_0$, we obtain the identity:

$$\mathbf{1} = \int_N \frac{p_N(N)}{\nu r_0 f_0} dN \boldsymbol{\pi}, \tag{3.49}$$

where f_0 is the force in the reference configuration and we also used the identity $\int_{\mathcal{S}_u} \boldsymbol{n}_0 \otimes \boldsymbol{n}_0 d\mathcal{S}_u = \frac{1}{3}\mathbf{1}$. Eq. (3.49) identifies the Lagrange multiplier in the reference configuration. Using its expression back into Eq. (3.46), we obtain the identity:

$$\frac{1}{r_0 f_0} = \int_N \frac{p_N(N)}{r_0 f_0} dN, \tag{3.50}$$

which implies that the product $r_0 f_0$ should be the same for all chains with various numbers of Kuhn segments. If all the chains are in their Gaussian regime in the initial configuration of the network, Eq. (3.50) becomes:

$$\frac{Nb^2}{r_0^2} = \int_N p_N(N) \frac{Nb^2}{r_0^2} dN. \tag{3.51}$$

The condition then becomes that r_0^2/N should be a constant, independent of N, i.e. $r_0(N) \propto \sqrt{N}$. Therefore, without loss of generality, we can write $r_0(N) = \lambda_{0,\mathrm{FR}}\sqrt{N}b$, where $\lambda_{0,\mathrm{FR}}$ is the (uniform) chain pre-stretch, which can be set arbitrarily. Consistent with our definition of the chain pre-stretch, the particular case $\lambda_{0,\mathrm{FR}} = 1$ gives $r_0(N) = \sqrt{N}b$. Note that conditions (3.50) or (3.51) only need to be satisfied for polydispersed networks. For monodispersed networks, r_0 is uniform and the conditions are satisfied automatically, independent of the relation between r_0 and N.

The Gaussian modulus of the fully-relaxed model is obtained following similar derivations. First, the deformed normal of the Gaussian chain is obtained from Eq. (3.46) and using Eq. (3.4) for the chain force:

$$\boldsymbol{n} = \frac{Nb^2 \boldsymbol{\pi}\boldsymbol{n}_0}{3kT\nu r_0^2}. \tag{3.52}$$

Inserting this relation into the kinematic constraint (3.43), and noting the relation (3.48), the macroscopic stress-stretch relation is obtained:

$$\boldsymbol{P}^e = \nu kT\lambda_{0,\mathrm{FR}}^2\boldsymbol{F}, \tag{3.53}$$

where we also used condition (3.51) on the initial end-to-end distances. The latter equation identifies the shear modulus as:

$$G_{\mathrm{FR}} = \nu kT\lambda_{0,\mathrm{FR}}^2. \tag{3.54}$$

Importantly, this expression for the modulus agrees with the exact expression for the modulus of a network of Gaussian chains, Eq. (3.20). In the particular case where $r_0 = \sqrt{N}b$ ($\lambda_{0,\mathrm{FR}} = 1$), Eq. (3.54) recovers the classical estimate νkT. To the best of our knowledge, an analytical expression of the maximum extensibility of the fully-relaxed model does not exist.

Remark 4 *The kinematic constraint (3.43) for polydispersed networks is different from the model previously proposed by Diani and Le Tallec (2019) and Mulderrig et al. (2021). These authors use the following averaging condition:*

$$\frac{1}{3}\boldsymbol{F} = \frac{\int_N p(N)r_0(N)\iint_{\mathcal{S}_u}\boldsymbol{F}_m d\mathcal{S}_u dN}{\int_N p(N)r_0(N)dN}. \tag{3.55}$$

Enforcing this constraint when minimising the elastic energy over the deformed orientations $\boldsymbol{n}$ *then gives the stationary condition:*

$$\boldsymbol{f} = \frac{1}{\nu\bar{r}_0}\boldsymbol{\pi}\boldsymbol{n}_0, \tag{3.56}$$

where $\bar{r}_0 = \int_N p(N)r_0(N)dN$. *It follows that all chains with the same initial orientation are subjected to the same force, independent of* N. *This is similar to the hybrid equal-force model. In contrast, the more intuitive constraint (3.43) appears more general as it does not lead to an equal-force condition. Another difference with the previous formulation is that, with the constraint (3.55), the relation* $r_0(N)$ *can be set arbitrarily, which might be seen as an advantage of the formulation. However, it can be verified that the Gaussian elastic modulus is now given by:*

$$G_{\mathrm{FR}} = \frac{\nu kT\bar{r}_0^2}{\int_N p_N(N)Nb^2dN}, \tag{3.57}$$

with $\bar{r}_0$ *defined above, and which in general differs from the exact result (3.20). The exact result is recovered only in the case of a monodispersed network.*

3.6 Comparison between Discrete Network and microsphere models

In this section, we systematically compare the predictions of the various microsphere models described in the previous section to DN model predictions taken as reference. Loading conditions are defined through the principal stretches: $\boldsymbol{F} = diag(\lambda_1, \lambda_2, \lambda_3)$. Considered loading conditions are i) uniaxial tension ($\lambda_2 = \lambda_3 = \frac{1}{\sqrt{\lambda_1}}$ and $\sigma_2 = \sigma_3 = 0$), and ii) biaxial tension ($\lambda_1 = \lambda_2 = \frac{1}{\lambda_3}$ and $\sigma_3 = 0$). The results for the pure shear case ($\lambda_1 = \frac{1}{\lambda_2}$, $\lambda_3 = 1$ and $\sigma_3 = 0$) are not shown here, as the results are very similar to those in uniaxial tension.

3.6.1 Monodispersed Networks

We first consider monodispersed networks with $\nu b^3 = 0.001$ and $N = 100$. In the affine and fully-relaxed microsphere models, the chain end-to-end distance is uniform and set as $r_0 = \sqrt{N}b$, so that $G_{\text{aff}} = G_{\text{FR}} = \nu kT$. Accordingly, DNs were generated to obtain an rms-average pre-stretch $\bar{\lambda}_0 = 1$. This ensures that the initial modulus of all models coincide. Note that the hybrid-equal force model reduces to the affine model in the case of monodispersed networks and is therefore not considered here.

Predictions of the microsphere and DN models are compared in Fig. 3.8 for the two loading cases. Predictions of the affine and fully-relaxed model are very similar, with the fully-relaxed model giving a slightly softer response. Both models underestimate the DN response for all loading conditions. Interestingly, the 3-chain model provides more accurate predictions than the affine microsphere model, despite the reduced number of orientations. In contrast, the 8-chain model is too soft. We also note that there is no substantial difference between the prediction of the 8-chain, affine fully-relaxed models in biaxial tension.

The relative performances of the various models shown in Fig. 3.8 can be related to their predictions of the chain stretch distribution. Fig. 3.9 shows distributions of the normalised chain end-to-end distances $\frac{r}{Nb}$ predicted by the various models at a macroscopic stretch $\lambda_1 = 5.5$. Overall, all the models fail to capture the DN distribution. In particular, in the analytical models the maximum chain stretch over all chain orientations is bounded by $r_0\lambda_1$, whereas the DN model contains a significant fraction of chains that are stretched beyond this value.

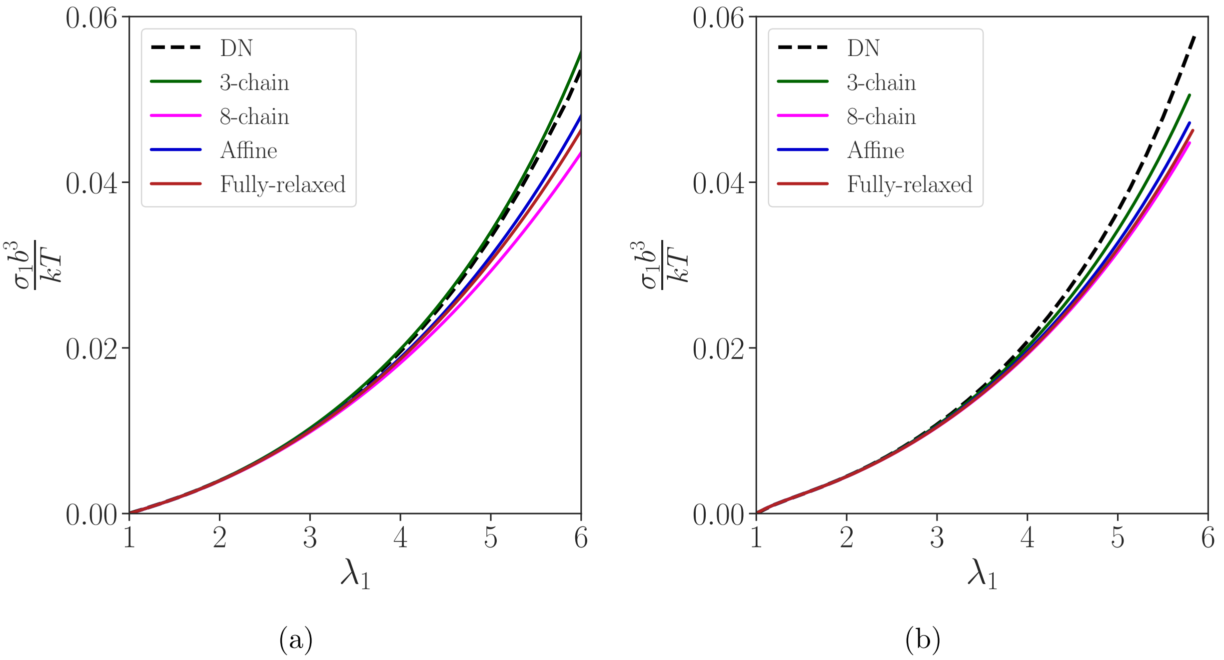

Fig. 3.8: Comparison between the stress-stretch curves of DN simulations and that of the affine microsphere model, fully-relaxed model, 3-chain model and 8-chain model in (a) uniaxial tension, (b) biaxial tension.

We attribute the stiffer response of the DN to the presence of these highly extended chains, bringing about higher forces. The apparent improved performance of the 3-chain model is then explained by the fact that this model gives a relatively higher weight to chains aligned with the first principal stretch direction. Interestingly, the response of the fully-relaxed model is softer than that of the affine, even though the fraction of highly stretched chains is higher than in the affine model. The presence of highly extended chains in the DN can be traced back to the initial distribution of r_0, as illustrated in Fig. 3.4(a), which leads to a broader distribution of stretches in the deformed state. In contrast, all analytical models assume a uniform value of r_0.

A fundamental assumption of the microsphere models is that there is a one-to-one map between the chain stretch and its initial orientation. To verify whether this one-to-one map is found in the DN, we directly compare the stretches of chains with the same initial orientation $\boldsymbol{n}_0$ in the DN to microsphere model estimates. Here we only consider chains that lie in planes parallel to the loading direction in a uniaxial tension test, with polar angle $\phi = 90° \pm 0.5°$ and arbitrary azimuthal angle θ. The stretches and normalised force of individual chains in the DN subjected to uniaxial tension at $\lambda_1 = 5.5$ are shown in Figs 3.10(a) and (b) as symbols. The predictions of the affine and fully relaxed models are also shown as continuous lines. It is clear

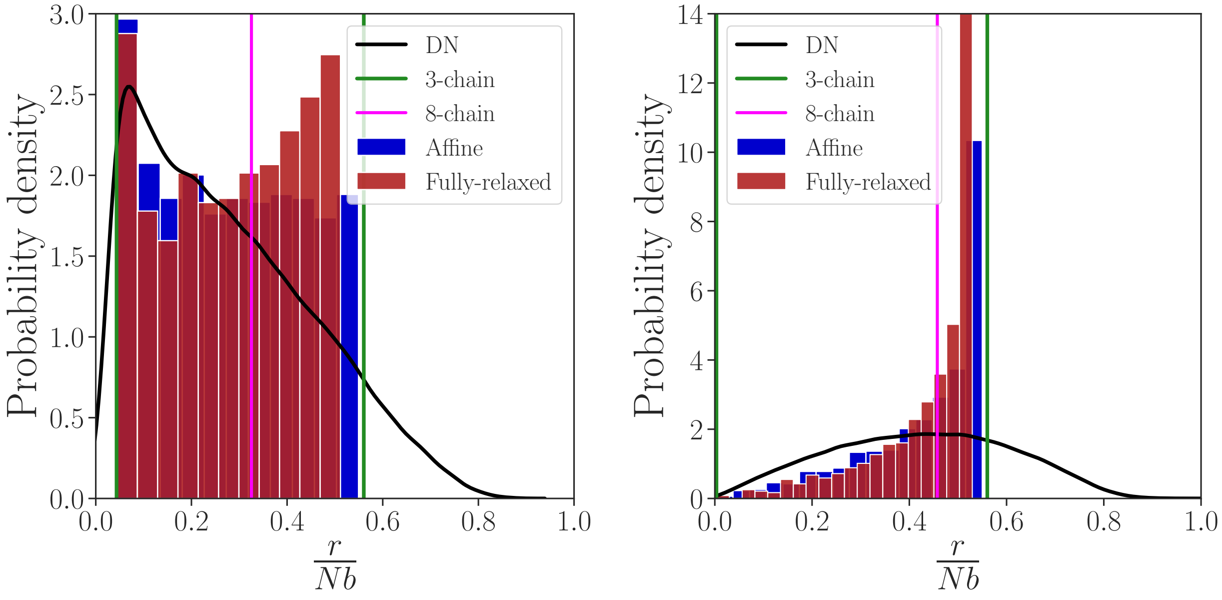

(a)

(b)

Fig. 3.9: Probability distribution of normalised chain end-to-end distances predicted by various models at $\lambda_1 = 5.5$ in (a) uniaxial tension, (b) biaxial tension.

that the orientation-stretch map hypothesised by microsphere models does not hold, as chains with the same initial orientations do not all see the same stretch in the DN (Fig. 3.10(a)). Deviations are particularly significant in the loading direction $\theta = 0°$, with chains experiencing stretches that are either lower or larger than the macroscopic stretch λ_1. However, in the directions transverse to the loading directions, the orientation-stretch map is more accurate, and DN predictions agree with microsphere model predictions. Overall, the affine model appears more accurate than the fully-relaxed model. A larger data scattering is observed in the chain force (Fig. 3.10(b)). This scattering is a consequence of the non-uniform pre-stretch present in the DN, such that chains with similar stretch but different r_0 experience a different force.

3.6.2 Polydispersed Networks

We next compare predictions of polydispersed microsphere models to DN predictions. We consider networks with $\nu b^3 = 0.001$ and log-normal chain length distribution with $\mu_N = 100$ and $s_N = 30$. In the affine and fully-relaxed microsphere models, the end-to-end distance was set as $r_0(N) = \bar{\lambda}_0\sqrt{N}b$, where $\bar{\lambda}_0$ is the rms average pre-stretch in the DN (here, $\bar{\lambda}_0 = 1.02$). This choice ensures that the elastic moduli of the DN and the microsphere models coincide. To recover the DN modulus with the hybrid equal force model, we set $R_0 = \bar{\lambda}_0\sqrt{\bar{N}}b$ in Eq. (3.42),

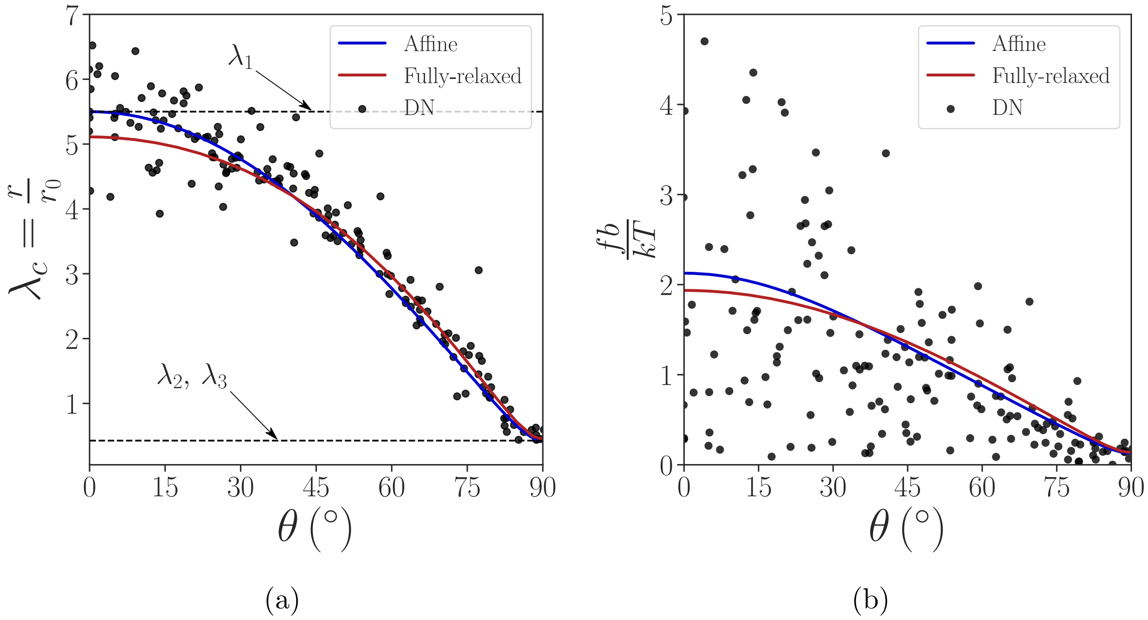

Fig. 3.10: (a) Relation between the chain stretch λ_c and chain orientation θ for chains in planes parallel to the loading direction in a uniaxial tension test at $\lambda_1 = 5.5$. (b) Corresponding relation between the normalised force $\frac{fb}{kT}$ and chain orientation θ.

which corresponds to $r_0 = \frac{Nb}{\sqrt{N}}\bar{\lambda}_0$ according to the equal-force assumption.

Fig. 3.11 compares the predictions of the polydispersed models to the DN response in (a) uniaxial and (b) biaxial tension. All models show the same modulus as the DN, as expected. All models underestimate the DN response at large deformation. The affine model being the stiffest, it is also the most accurate. The reasons behind the underestimation of the microsphere models are two-fold. First, like in the monodispersed case, the polydispersed DNs have a distribution of pre-stretches (Fig. 3.5(a)), so that highly stretched chains exist in the initial configuration and which bring about stronger stiffening at large deformation. The presence of highly pre-stretched chains is neglected by our choice of $r_0(N)$. Second, similar to the monodispersed case, the assumed one-to-one relationship between chain orientation and stretch underpinning microsphere models does not hold for polydispersed DNs. This is illustrated in Fig. 3.12, which shows (a) the chain stretches and (b) the normalised chain forces of chains with with polar angle $\phi = 90° \pm 0.5°$ and arbitrary azimuthal angle θ at $\lambda_1 = 4.2$ in a uniaxial tension test. In the polydispersed case, the chain force predicted by the affine model depends on the chain length, whereas in the fully-relaxed model, both the chain stretch and the chain force depend on the chain length. Model predictions falling between one standard deviation above and below the mean of the distribution over chain lengths are represented with shaded areas, with the continuous line representing the mean value. DN values (symbols) clearly show that

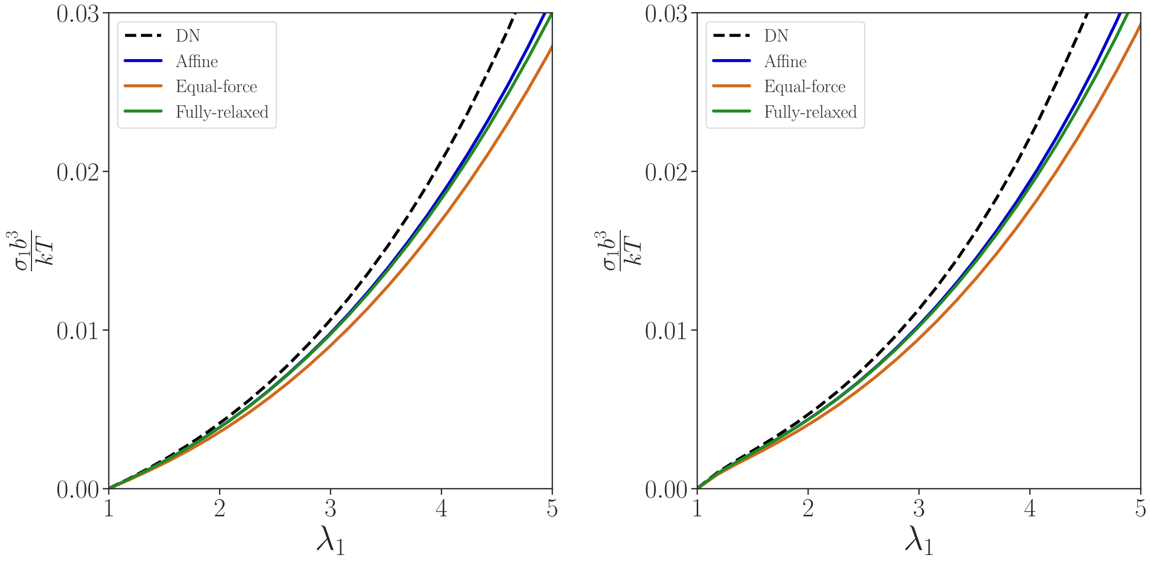

(a)

(b)

Fig. 3.11: Comparison between DN predictions and microsphere models for polydispersed networks in (a) uniaxial tension and (b) biaxial tension.

the assumption of one-to-one relation between chain orientation and chain stretch used in the microsphere models does not hold (Fig. 3.12(a)), and that the corresponding assumption for the chain force used in the hybrid equal-force model (not shown here for clarity) does not hold either. Overall, the affine and fully-relaxed models predict similar chain stretches. However, the affine model predicts higher chain forces, which explains the stiffer macroscopic response of the affine model.

The stress-stretch curves of the different microsphere models in Fig. 3.11 show small differences between them, especially the affine and fully-relaxed models. To investigate the conditions under which noticeable differences occur, we further compare the predictions of these models when the standard deviation of the chain length distribution varies. Fig. 3.13 shows the uniaxial responses of the three models for $s_N = 10$ (a), $s_N = 30$ (b) and $s_N = 50$ (c). All distributions had the same mean $\mu_N = 100$ and the same initial end-to-end distance $r_0(N) = \sqrt{N}b$. For the equal-force model, we set $R_0 = \sqrt{\bar{N}}b$ so that all models have the same initial modulus.

Overall, as the chain length distribution widens, the differences between the model predictions become more apparent. Moreover, we note that the affine and fully-relaxed responses stiffen with increasing chain length dispersion, whereas the equal-force ones remain unchanged. The discrepancies between affine and fully-relaxed predictions also become more distinguishable as s_N increases. The insensitivity of the hybrid equal-force model to variation in s_N is

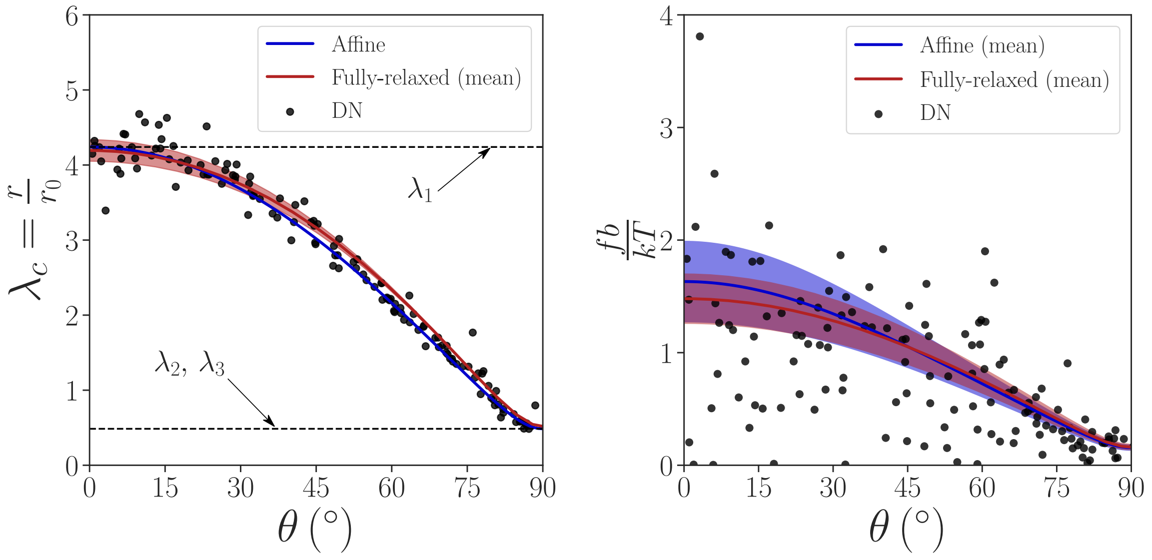

(a)

(b)

Fig. 3.12: (a) Relation between the chain stretch λ_c and chain orientation θ for chains in planes parallel to the loading direction in polydispersed networks ($\mu_N = 100$, $s_N = 30$) in a uniaxial tension test at $\lambda_1 = 4.2$. (b) Corresponding relation between the normalised force $\frac{fb}{kT}$ and chain orientation θ. Shaded regions represent model predictions that fall between one standard deviation above and below the mean of the distribution over chain lengths in the affine and fully-relaxed models.

a consequence of the choice $R_0 = \sqrt{\bar{N}}b$, and the fixed mean chain length $\mu_N = 100$. In this scenario, the relevant parameters for the equal-force model become independent of the standard deviation of the distribution. The growing differences between the affine and fully-relaxed models with increasing dispersion in the chain length distribution are directly linked to the increase in the amount of short chains. Non-affine models provide softer predictions, as they are not directly controlled by the response of the shortest chains.

3.6.3 Accounting for the initial distribution of chain end-to-end distance in microsphere models

Previous results suggest that the non-uniform pre-stretch distribution existing in DN models and overlooked by microsphere models is a key factor impacting the performance of analytical models. To further assess the impact of this simplifying assumption, we developed extended (monodispersed) microsphere models which account for a distribution of the chain end-to-end

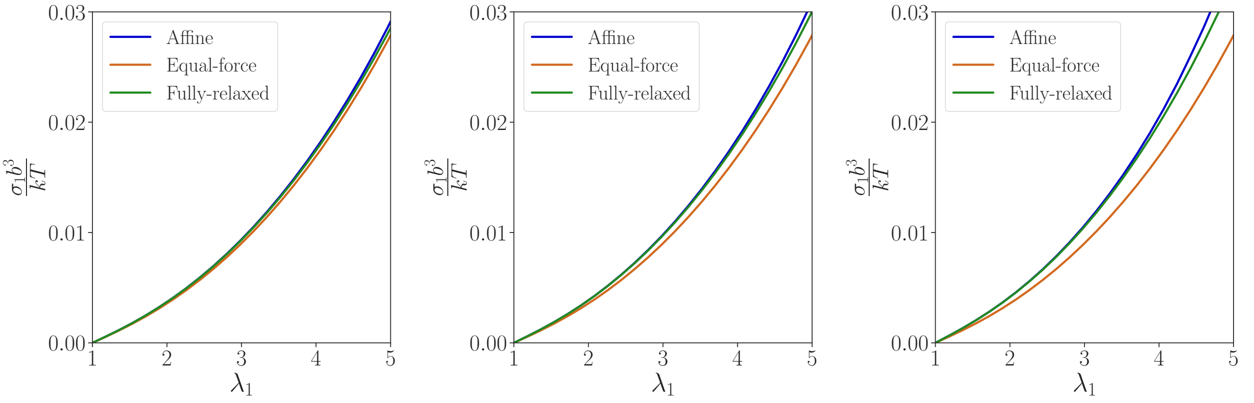

(a) (b) (c)

Fig. 3.13: Effect of the chain length distribution on the uniaxial tension predictions of microsphere models for (a) $s_N = 10$, (b) $s_N = 30$ and (c) $s_N = 50$.

distance. The free energy of the extended microsphere model is given by:

$$W = \nu \int_{r_0} p_{r_0}(r_0) \iint_{\mathcal{S}_u} w(\lambda_c; r_0) d\mathcal{S}_u dr_0, \tag{3.58}$$

where $p_{r_0}(r_0)$ is the probability density of the end-to-end distance. We have developed affine and fully-relaxed versions of the extended microsphere models. Derivation details are provided in Section 3.8.

Figs 3.14[3](a) and (b) compare the predictions of the affine and fully-relaxed microsphere models enriched with a pre-stretch distribution to DN reference predictions in uniaxial and biaxial tension, for $\nu b^3 = 0.001$ and $N = 100$. In the microsphere models, the pre-stretch distribution $p_{r_0}(r_0)$ was set identical to the numerical distribution extracted from the DN simulation. As expected, both analytical models have the same small strain response as the DN, as chains are in their Gaussian regime. At large deformations, the affine prediction is significantly stiffer than the DN one, which is attributed to the stiffer response of chains with large initial pre-stretch. On the other hand, the extended fully-relaxed model underestimates the DN response, as a result of the relaxation of the affine assumption. Interestingly, the predictions of the affine and fully-relaxed models are now markedly different at large strains, while their predictions were very similar in the case of uniform pre-stretch. This suggests that the effect of non-affine deformation is more pronounced in a network with non-uniform pre-stretch distribution, so that the fully-relaxed model provides much improved predictions compared to the affine

---

[3] This figure differs from the one published in the original paper. An error was identified in the published version and has been corrected in the thesis. A corrigendum will be submitted following thesis submission.

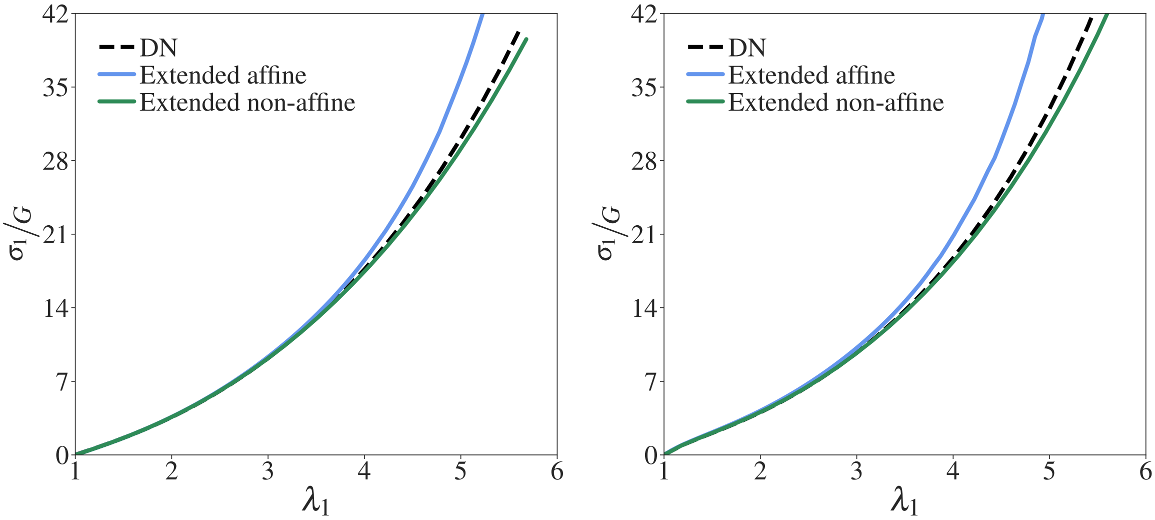

(a) (b)

Fig. 3.14: Predictions of extended affine and fully-relaxed microsphere models accounting for a pre-stretch distribution in (a) uniaxial (b) and biaxial tension.

model. Finally, we note that the proposed extensions of the affine and fully-relaxed models still rely on the assumption that chains with the same pre-stretch and orientation exhibit the same stretch. Although DN simulations have shown that this assumption is not strictly accurate (Fig. 3.10), the improved agreement observed in Fig. 3.14 suggests that it may nevertheless be acceptable when the pre-stretch distribution and non-affine deformation are appropriately accounted for. However, a key limitation of the fully-relaxed extension remains: the pre-stretch distribution must be known a priori, which in practice is difficult to estimate without DNs.

3.7 Conclusions

We have developed a DN-based computational framework to systematically investigate structure-property relationships in rubbery networks. The computational model relies on a novel random network generation algorithm that enables the independent control of the chain end-to-end distance and chain density by allowing the interpenetration of chains. Generalised scaling relations accounting for the chain pre-stretch were proposed for both monodispersed and polydispersed networks, which recover classical scaling relations of rubber elasticity theory when chains adopt their random walk end-to-end distance in the initial configuration. Our numerical results show that the chain pre-stretch is a key parameter controlling the mechanical response of rubbery networks, with a higher average pre-stretch leading to higher modulus and reduced maximum extensibility. For polydispersed networks, the short chains control the strain-stiffening behaviour.

We used the computational DN model to systematically assess the predictive capabilities of microsphere models under different stretch-partitioning assumptions. Surprisingly, the simpler affine microsphere model shows the best overall performance, with its three-chain reduction even giving the best agreement with DN results (in the monodispersed case). The affine assumption appears to compensate for the effect of the initial pre-stretch distribution, which introduces highly extended chains in the DN and which is overlooked in the microsphere models. To address this limitation of the microsphere models, we proposed extended affine and fully-relaxed models which account for a distribution of the chain end-to-end distance. While the affine extension could not yield accurate predictions, the fully-relaxed extension led to improved agreement, provided that the same pre-stretch distribution as that of the DN is used. However, obtaining the pre-stretch distribution without relying on DNs remains a practical challenge for the fully-relaxed model. Our DN simulation results also showed that the one-to-one map between the chain stretch and its initial orientation, which underpins the microsphere framework, is inaccurate. This point has recently been made by Britt and Ehret (2022) in the context of fibre networks. Future works should focus on addressing these limitations, possibly outside the microsphere framework.

The ability to generate interpenetrated networks is the main difference between the proposed network generation algorithm and existing network generation methods based on finite element meshes. An interesting open question is whether polymer networks with controlled degree of interpenetration can be produced experimentally. We hypothesise that this could be possible in networks produced by the end-linking reaction of linear or branched macromolecules with well-defined molecular weight. Assuming that chains in the network adopt the same (root-mean-square) end-to-end distance as the corresponding free chain at the same polymer concentration, the length r_0 then depends on the number of Kuhn segments N and volume fraction of polymer precursor ϕ_0 following the scaling theory of polymer solutions (Rubinstein and Colby, 2003). In contrast, the chain density scales as $\frac{\phi_0}{N}$. Thus, different degrees of interpenetration could (in principle) be achieved by tuning the chain length and polymer volume fraction.

In this study we represented network chains as freely-jointed chains. Other models of single chain behaviour could also be considered, such as the worm-like chain model, which is suitable for stiffer (semi-flexible) chains such as DNA. Chain scission could also be considered, for example by introducing a maximum stretch criterion (Sugimura et al., 2013; Wagner et al., 2022). Alternatively, an extensible freely-jointed chain model could be used, which also accounts for the change in internal energy associated with stretching the bonds, and where chain scission occurs when the bond energy reaches a critical value (Mao et al., 2017; Li and Bouklas, 2020). By introducing a chain scission criterion, the effect of network topology and chain pre-stretch on macroscopic strength and limit extensibility could be investigated.

Our DN model relies on the phantom network assumption, according to which chains only interact via shared crosslinks. However, chains are expected to interact in real networks, in particular at high polymer volume fraction or when chains are very long. Interactions between chains could be accounted for in an indirect manner using the tube model, according to which chain fluctuations are limited to a virtual tube representing topological constraints of other chains. The reduction in conformational entropy resulting from the tube constraint leads to an additional contribution to the chain free energy (Doi et al., 1988; Miehe et al., 2004). Several variations of the tube model have been proposed in the literature, which primarily differ in the way they evolve the tube diameter with the macroscopic deformation, see our recent work for a review of various tube formulations (Kumar and Brassart, 2023). In principle, any tube formulation where the tube diameter depends on the chain stretch could be implemented within the proposed framework. Another approach to describe chain interactions in a more direct manner would be to consider (possibly temporary) crosslinking points representing entanglements between interpenetrating chains.

Along similar lines, another possible extension of the model could be the modelling of rate-dependent processes associated with chain interactions. This could be achieved by considering a viscoelastic force-extension relation at the level of the network chains, possibly in combination with the tube representation, as proposed by Miehe and Göktepe (2005) in the miscrosphere context. Force-assisted, rate-dependent chain scission could also be considered, for example to simulate reversible bond breaking and reforming (Kothari et al., 2018; Wagner et al., 2021) or chemical degradation (Pan and Brassart, 2022). In all these rate-dependent processes, the chain pre-stretch (controlling the chain force) and its modulation through the degree of interpenetration is expected to play a role.

As previously mentioned, the DN model is computationally expensive and not suited for simulations at large scale. Beyond the homogenised analytical models discussed in this work, another route towards scalability would be to incorporate the proposed DN model within a quasi-continuum framework, as recently proposed by Ghareeb and Elbanna (2020). In this framework, the discrete network description is retained in regions of interest, such as near crack tips where chains are highly stretched, whereas a homogenised continuum description is used away from these high stretch regions. Such an approach would allow us to investigate the effect of network topology on fracture toughness, and will be considered in future works.

3.8 Appendix: Extended microsphere models with distribution of end-to-end distance

We develop extended microsphere models with free energy of the form (3.58), which accounts for a distribution of initial chain end-to-end distance. Under the affine assumption, the chain stretch is related to the macroscopic deformation gradient by Eq. (3.31), and the current chain end-to-end distances can be directly obtained. The macroscopic stress can be obtained in the usual way:

$$\boldsymbol{P}^e = \nu \int_{r_0} p_{r_0}(r_0) \iint_{\mathcal{S}_u} \frac{f r_0}{\lambda_c} \boldsymbol{F}(\boldsymbol{n}_0 \otimes \boldsymbol{n}_0) d\mathcal{S}_u dr_0. \tag{3.59}$$

The Gaussian modulus of this extended affine model is then given by:

$$G_{\text{EAff}} = \nu k T \int_{r_0} p_{r_0}(r_0) \frac{r_0^2}{N b^2} dr_0, \tag{3.60}$$

which coincides with the exact expression (3.20) for the modulus of a DN of Gaussian chains, as required.

We also propose a fully-relaxed version of the microsphere model with initial chain end-to-end distance distribution. We postulate the the chain stretches should minimise the elastic free energy (3.58) subjected to the following kinematic constraint:

$$\frac{1}{3}\boldsymbol{F} = \int_{r_0} p_{r_0}(r_0) r_0^2 \iint_{\mathcal{S}_u} \frac{\boldsymbol{n} \otimes \boldsymbol{n}_0}{\int_{r_0} p_{r_0}(r_0) r_0^2 dr_0} d\mathcal{S}_u dr_0. \tag{3.61}$$

As shown below, the weighting with r_0^2 was found necessary to ensure that the non-affine model with pre-stretch distribution recovers the affine modulus in the Gaussian regime, which is the exact result for a DN of Gaussian chains. The distribution of deformed chain orientations $\boldsymbol{n}$ is found by solving the minimum problem:

$$W = \inf_{\boldsymbol{n},\boldsymbol{\pi}} \left\{ \nu \int_{r_0} p_{r_0}(r_0) \iint_{\mathcal{S}_u} w d\mathcal{S}_u dr_0 + \boldsymbol{\pi} : \left[\frac{1}{3}\boldsymbol{F} - \int_{r_0} p_{r_0}(r_0) r_0^2 \iint_{\mathcal{S}_u} \frac{\boldsymbol{n} \otimes \boldsymbol{n}_0}{\int_{r_0} p_{r_0}(r_0) r_0^2 dr_0} dr_0 \right] \right\}, \tag{3.62}$$

where $\boldsymbol{\pi}$ is the Lagrange multiplier enforcing the kinematic constraint (3.61). The stationary condition w.r.t. $\boldsymbol{n}$ gives, for each r_0:

$$\boldsymbol{f} = \frac{r_0 \boldsymbol{\pi} \boldsymbol{n}_0}{\nu \int_{r_0} p_{r_0}(r_0) r_0^2 dr_0}, \tag{3.63}$$

which can be inserted into the constraint (3.61) to obtain an implicit equation for the Lagrange multiplier $\boldsymbol{\pi}$. Once $\boldsymbol{\pi}$ is known, Eq. (3.48) gives the macroscopic stress. Using the constraint (3.61) in the initial configuration where $\boldsymbol{F} = \mathbf{1}$ together with the stationary condition (3.63), the following condition on the pre-stretch distribution $p_{r_0}(r_0)$ is obtained:

$$\frac{f_0}{r_0} = \frac{\int_{r_0} p_{r_0}(r_0) r_0^2 dr_0}{\int_{r_0} p_{r_0}(r_0) \frac{r_0^3}{f_0} dr_0}, \tag{3.64}$$

where f_0 is the chain force in the initial configuration. This relation implies that the ratio f_0/r_0 should be constant, for all r_0. This condition is satisfied for any distribution $p_{r_0}(r_0)$ provided that all chains are in their Gaussian regime in the initial configuration, as in this case the chain force is simply linear in the end-to-end distance. Finally, we derive the expression of the elastic modulus in the Gaussian regime. Following the same steps as in Section 3.5.3, we obtain:

$$G_{\mathrm{EFR}} = \nu kT \int_{r_0} p_{r_0}(r_0) \frac{r_0^2}{Nb^2} dr_0, \tag{3.65}$$

which coincides with the exact expression (3.20) for a DN of Gaussian chains. We note that the specific form (3.61) was required to reach this important result. Using the more intuitive kinematic constraint $\frac{\boldsymbol{F}}{3} = \int_{r_0} p_{r_0}(r_0) \iint_{\mathcal{S}_u} \boldsymbol{n} \otimes \boldsymbol{n}_0 dr_0$ results in a different expression of the Gaussian modulus.

Data availability

A Matlab code implementing the Discrete Network generation algorithm is available on Github (Kryven, 2022). The code for DN simulations of random networks using LAMMPS is available on a separate Github repository (Araujo et al., 2024b).

Chapter 4

Micromechanical modelling of failure in rubbery networks: the role of local heterogeneities

This chapter presents the unpublished work entitled "Micromechanical modelling of failure in rubbery networks: the role of local heterogeneities". In this study, we analyse the microscopic mechanisms that govern failure in rubbery networks by incorporating deterministic chain scission into the DN model introduced in Chapter 3. Our results show that scission-induced force redistribution is key to understanding the macroscopic failure response. By comparing two classes of bimodal networks, we further demonstrate that failure is more sensitive to chain strength variability than to chain length variability. Finally, we use DN simulations to assess the predictive capability of conventional semi-analytical models, highlighting their limitations and proposing possible directions for refinement. Overall, this work highlights the highly heterogeneous and complex nature of failure in rubbery networks.

4.1 Introduction

Rubbery networks, such as elastomers and hydrogels, are found in many modern applications, from medical implants (Nonoyama and Gong, 2021) and soft electronics (Lee et al., 2018), to daily goods like tyres (Mars and Fatemi, 2002), diapers (Masuda, 1994), and contact lenses (Caló and Khutoryanskiy, 2015). In many of these applications, the structural integrity under mechanical loads is critical, making the strength of rubber-like materials a major concern. The underlying network architecture ultimately dictates the mechanical response of rubbery networks. Consequently, recent design strategies have exploited this connection to enhance the properties of these materials. For example, the crosslinking of well-defined four-armed macromonomers has been proposed to generate tetra-PEG gels with superior mechanical properties, which were attributed to their nearly ideal structure (Sakai et al., 2008; Matsunaga et al., 2009). Entanglements have been shown to increase resistance to crack growth under both monotonic and cyclic loading conditions (Kim et al., 2021; Nian et al., 2025). Recently, the insertion of mechanophores either along the backbone of polymer chains (Wang et al., 2021; Beech et al., 2023; Li and Gong, 2024) or as crosslinks (Wang et al., 2023a) has emerged as an effective reactivity-guided strategy to improve strength.

Modelling the mechanical failure in rubbery networks requires a bottom-up approach that accounts for both the network structure and the behaviour of individual chains. Discrete Network (DN) models have recently emerged as promising tools that meet these requirements, providing a more computationally efficient alternative to molecular dynamics while preserving essential microstructural features of the network (Sugimura et al., 2013; Alamé and Brassart, 2020; Wagner et al., 2022; Deng et al., 2023; Araujo et al., 2024a; Lei et al., 2025). In this framework, the molecular network is represented by a network of springs with force-extension behaviour obtained from statistical mechanics. Unlike continuum micromechanics models of rubber elasticity, the partition of forces and stretches among chains emerges naturally from mechanical equilibrium, rather than being imposed through ad hoc assumptions. As such, DNs offer a physically grounded and computationally tractable modelling tool to analyse the connections between microstructure and macroscopic response of rubber-like materials.

Structure-property relationships in rubbery networks have been extensively investigated through DN models (Alamé and Brassart, 2020; Wagner et al., 2022; Araujo et al., 2024a; Lei et al., 2025). In the context of fracture, DNs were recently used in crack propagation simulations to assess the validity of the Lake-Thomas model (Lei and Liu, 2022; Deng et al., 2023; Hartquist et al., 2025b,a), and to unveil the microscopic origins of crack paths typically observed in many soft materials (Ghareeb and Elbanna, 2020; Lei et al., 2021). Fracture simulations using DN models have provided insights into the role of network imperfections, such as dangling ends and loops, in shaping failure behaviour (Sugimura et al., 2013; Arora et al., 2022). These simulations were also used to elucidate how sacrificial bonds enhance toughness by introducing additional dissipation (Kothari et al., 2018). Chain scission kinetics have been included in DN frameworks to model failure in networks composed of chains of different strengths (Beech et al., 2023), as well as to capture rate-dependent damage and fracture (Kothari et al., 2018; Ghareeb and Elbanna, 2021; Arora et al., 2022).

Despite these recent contributions, DNs have not yet been fully explored for investigating the microscopic mechanisms governing failure in rubber-like materials. In this work, we incorporate chain scission into the DN framework introduced in our previous work (Araujo et al., 2024a) to explore how local heterogeneities, beyond structural defects, impact the failure response of rubbery networks. We show that fracture is a highly heterogeneous process, even in defect-free monodispersed networks. Moreover, by comparing two different types of bimodal networks, we show that a heterogeneous distribution of chain strengths can significantly alter the failure response of the network. These results provide a fresh perspective on the fracture of rubbery networks with hybrid chain populations, offering an alternative interpretation of recently reported findings (Beech et al., 2023; Hartquist et al., 2025b).

While DN models are useful for gaining mechanistic insights into the failure of rubber-like materials, their computational cost limits their application to structural-scale simulations. Consequently, continuum micromechanics approaches are still needed. Moreover, conventional models such as the three-chain (James and Guth, 1943) and eight-chain (Arruda and Boyce, 1993) models are frequently used to estimate the onset of failure in rubbery networks. We assess the predictive accuracy of these estimates using DNs as a reference. Using the peak in the stress-stretch response as a failure marker, our analysis shows that continuum models fail to predict failure, even for perfect networks. This occurs because these models neglect both the intrinsic heterogeneities of DNs and those that emerge during failure. To address this limitation, we further propose affine and fully-relaxed microsphere models with chain scission (Mulderrig et al., 2021; Araujo et al., 2024a), focusing on the monodispersed case. While the affine formulation yields better estimates for the peak, neither version of the model captures the abrupt stress drops observed in DN simulations.

4.2 Discrete Network model

4.2.1 Chain behaviour

The freely-jointed chain (FJC) model is used to describe the mechanical behaviour of individual chains in the network. In this model, the free energy of a chain with end-to-end distance r is given by:

$$w = Nk_BT\left[\frac{r}{Nb}\beta + \log\left(\frac{\beta}{\sinh\beta}\right)\right], \qquad \beta = \mathcal{L}^{-1}\left(\frac{r}{Nb}\right), \tag{4.1}$$

where b is the Kuhn length, N is the number of Kuhn segments, k_B is the Boltzmann constant, and T is the absolute temperature. The Langevin function is defined as $\mathcal{L}(x) = \coth(x) - 1/x$. The force f required to maintain the end-to-end distance r is derived from the free energy as $f = \frac{dw}{dr}$:

$$f = \frac{k_BT}{b}\mathcal{L}^{-1}\left(\frac{r}{Nb}\right). \tag{4.2}$$

For small elongations ($r \ll Nb$), $\mathcal{L}(x) \approx 3x$ and the force-extension relationship Eq. (4.2) becomes linear, recovering the Gaussian chain model:

$$f = \frac{3k_BT}{Nb^2}r. \tag{4.3}$$

Let r_0 denote the end-to-end distance of the chain in the reference configuration of the network. We then define the chain pre-stretch as the ratio of the initial end-to-end distance to the ideal random walk distance $\sqrt{N}b$: $\lambda_0 = \frac{r_0}{\sqrt{N}b}$.

At large chain elongations, the FJC model becomes less accurate since it neglects energetic effects associated with bond stretching and bond angle opening (Mao et al., 2017; Guo and Zaïri, 2021; Mulderrig et al., 2023; Zhu and Brassart, 2025). These effects can be incorporated with more sophisticated models, such as those with stretchable Kuhn segments (Smith et al., 1996; Mao et al., 2017; Mulderrig et al., 2023). However, the conventional FJC model is adopted here for its simplicity and computational efficiency, as it provides a closed-form expression for the force-extension relationship.

4.2.2 Network behaviour

We consider a network of chemically crosslinked long polymer chains, interacting with each other only through the crosslinks (phantom network). In the reference configuration, the network is stress-free, with force balance satisfied at each node. In the Discrete Network (DN) framework, polymer chains are represented as springs connected at nodes, corresponding to the crosslinks. A representative DN is shown in Fig. 4.1(a).

The macroscopic deformation gradient $\boldsymbol{F}$ is applied to the network by prescribing the displacement of n_b boundary nodes according to the affine relation:

$$\boldsymbol{x}_\alpha = \boldsymbol{F}\boldsymbol{X}_\alpha, \qquad \alpha = (1, n_b), \tag{4.4}$$

where $\boldsymbol{X}_\alpha$ and $\boldsymbol{x}_\alpha$ represent the position of the αth boundary node in the reference and current configurations, respectively. In the reference configuration, $\boldsymbol{F} = \mathbf{1}$. The position of the n_i interior nodes is found by minimising the energy of the network, which is equivalent to the force balance requirement at each node. At equilibrium, the macroscopic free energy density ψ^e of the network initially occupying a volume V_0 in the reference configuration is expressed as:

$$\psi^e = \frac{1}{V_0}\sum_{j=1}^{n} w_j(r_j, N_j), \tag{4.5}$$

where w_j, r_j and N_j are the free energy, current equilibrium end-to-end distance and number of Kuhn segments of the jth chain, respectively, and n represents the current number of chains in the network.

We focus on volume-preserving deformations, imposing the incompressibility constraint $J = \det(\boldsymbol{F}) = 1$. This constraint is enforced through a Lagrange multiplier P. Considering virtual deformations $\delta\boldsymbol{F}$ and the result $\delta J = J\boldsymbol{F}^{-T} : \delta\boldsymbol{F}$, the state law for the macroscopic stress tensor $\boldsymbol{P}$ is obtained from standard thermodynamics as:

$$\boldsymbol{P} = \boldsymbol{P}^e - JP\boldsymbol{F}^{-T}, \qquad \boldsymbol{P}^e \equiv \frac{\partial\psi^e}{\partial\boldsymbol{F}}, \tag{4.6}$$

where $\boldsymbol{P}^e$ is the network contribution to the macroscopic stress. Note that the Lagrange multiplier is identified from the boundary conditions. The Cauchy stress is computed from the classical relation $\boldsymbol{\sigma} = (1/J)\boldsymbol{P}\boldsymbol{F}^T$, giving

$$\boldsymbol{\sigma} = \boldsymbol{\sigma}^e - P\mathbf{1}, \qquad \boldsymbol{\sigma}^e = (1/J)\boldsymbol{P}^e\boldsymbol{F}^T. \tag{4.7}$$

The network contribution $\boldsymbol{P}^e$ is obtained as (Alamé and Brassart, 2020):

$$\boldsymbol{P}^e = \frac{1}{V_0}\sum_{\alpha=1}^{n_b} \boldsymbol{f}_{\boldsymbol{\alpha}} \otimes \boldsymbol{X}_\alpha, \tag{4.8}$$

where $\boldsymbol{f}_\alpha$ is the reaction force at the boundary node α. From Eq. (4.2), it follows that $\boldsymbol{f} = \mathbf{0}$ only when $\boldsymbol{r} = \mathbf{0}$, i.e., when the chain is fully coiled. This means that external forces must be applied to the boundary nodes in the reference configuration to balance the restoring forces of the chains with non-zero initial end-to-end distances. Therefore, $\boldsymbol{P}^e$ is not zero in the reference configuration. On the other hand, the Lagrange multiplier is identified from Eq. (4.7) as $P = \frac{1}{3}\mathrm{tr}(\boldsymbol{\sigma}^{\mathrm{e}})$ in the reference configuration, since the network is initially stress-free and isotropic.

Chain scission is included through a deterministic scission criterion to capture mechanical failure. A chain j is considered broken when its current end-to-end distance reaches a specified fraction η_j of its contour length $N_j b$, i.e., when $\frac{r_j}{N_j b} \geq \eta_j$. When scission occurs, the force balance on the corresponding nodes is disrupted, and the network must be re-equilibrated to restore mechanical equilibrium.

4.2.3 Numerical procedure

Discrete networks (DNs) are generated within cubic simulation volumes using our in-house network generation algorithm implemented in MATLAB. This algorithm allows for independent control over chain density and end-to-end distance distribution by allowing the chains to interpenetrate, see Araujo et al. (2024a) for details. As-generated DNs contained at least 50000 chains, which is sufficiently large to ensure that the networks are statistically representative and isotropic. For each set of input parameters, five independent network realisations were generated to capture variability in failure behaviour.

DNs are subjected to macroscopic deformation gradients $\boldsymbol{F} = \mathrm{diag}(\lambda_1, \lambda_2, \lambda_3)$, where λ_i $(i = 1, 2, 3)$ are the principal stretches along the faces of the cube, following Eq. (4.4). We limit

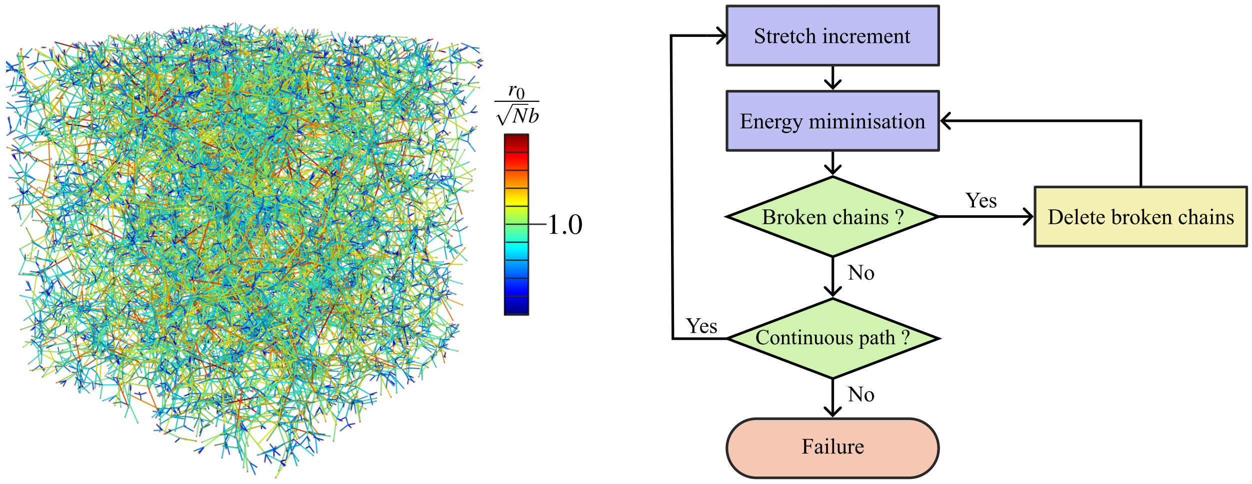

(a) (b)

Fig. 4.1: (a) Representative discrete network with $n = 20000$ chains in the equilibrated reference configuration, showing the initially-heterogeneous distribution of chain end-to-end distances. (b) Numerical procedure for the fracture of discrete networks.

ourselves to uniaxial tension along direction 1, which implies that $\lambda_2 = \lambda_3 = \lambda_1^{-0.5}$ from the incompressibility constraint. At each time-step, a stretch increment of $\Delta\lambda_1 = 0.04$ was applied to the equilibrated DNs from the previous time-step. This increment size was selected as a compromise between computational efficiency and accuracy, after verifying that it results in converged mechanical behaviour (see Section 4.7 for details). Following the stretch increment, the boundary nodes are kept fixed while the network is equilibrated using LAMMPS (Thompson et al., 2022). After each equilibration step, the network is scanned for broken chains. If no chains meet the breaking criterion, the simulation proceeds to the next time step. However, if some chains are found to have reached their cleavage thresholds, these chains are removed from the network, and the system is re-equilibrated. This scission detection and re-equilibration loop is repeated until no further chain breaking is detected (Ghareeb and Elbanna, 2021; Lei et al., 2021; Lavoie and Suo, 2024; Lei et al., 2025). Before proceeding to the next time step, the network is checked for global failure, which was defined as the loss of a continuous path connecting the faces of the simulation box being pulled apart (Araujo and Brassart, 2025a). At this point, the network loses connectivity, and the simulation stops. This numerical procedure is illustrated in Fig. 4.1(b).

4.2.4 Elastic modulus

The initial Young modulus E_0 of the networks can be obtained from the uniaxial deformation along direction 1 as:

$$E_0 = \lim_{\lambda_1 \to 1} \frac{d\sigma_1}{d\lambda_1}, \tag{4.9}$$

where σ_1 is the principal Cauchy stress in direction 1. For an incompressible, isotropic elastic material, the shear modulus is related to the Young modulus as $E_0 = 3G_0$. When all the chains of the network remain in their Gaussian regime, i.e., $r_0^{(j)} \lesssim 0.3N_j b$ for $j = 1, \ldots, n$, the shear modulus can be expressed as:

$$G_0 = \nu_0 k_B T \left\langle \frac{r_0^2}{Nb^2} \right\rangle = \nu_0 k_B T \langle \lambda_0^2 \rangle, \tag{4.10}$$

where ν_0 is the initial density of elastically effective chains (number of chains per unit volume in the reference configuration). The notation $\langle \cdot \rangle$ represents the ensemble average:

$$\langle \cdot \rangle = \frac{1}{n} \sum_{j=1}^{n} (\cdot)\,. \tag{4.11}$$

Eq. (4.10) is exact provided that the network is isotropic, and its validity was verified in our previous works (Alamé and Brassart, 2020; Araujo et al., 2024a). Note that Eq. (4.10) only recovers the classical expression $G_0 = \nu_0 k_B T$ in the specific case when all chains adopt the random walk distance $\sqrt{N_j} b$ in the reference configuration.

4.3 Monodisperse Networks

Monodisperse ideal networks with three different chain lengths $N = 100$, 150, and 200 were generated at the same normalised chain density $\nu_0 b^3 = 1 \times 10^{-3}$. To isolate the effect of chain length, all networks were constructed to have approximately the same average pre-stretch $\bar{\lambda}_0 := \sqrt{\langle \lambda_0^2 \rangle} \approx 1$, resulting in nearly identical initial elastic moduli (Eq. (4.10)). The Kuhn length was fixed at $b = 1\,\mathrm{nm}$ and the temperature at $T = 298\,\mathrm{K}$. A critical chain scission threshold of $\eta = 0.8$ was used for all chains.

Figs 4.2(a) and (b) show the nominal stress P_1 and fraction of broken chains f_b as a function of the uniaxial stretch λ_1 along direction 1, respectively. Each curve in these plots corresponds to a single DN realisation. The initial overlap of the stress-stretch curves confirms that the networks essentially have the same initial moduli, as expected from the matched $\bar{\lambda}_0$. All DNs exhibit a sharp stress drop before global failure, coinciding with a sudden increase in the number of broken chains. This suggests that the catastrophic loss of load-bearing capacity stems from a cascade of chain scissions.

Networks with longer chains sustain higher peak stresses and larger stretches before failure. This arises from the increased compliance at the chain level. According to Eq. (4.3), the shorter chains have higher stiffness and carry larger forces in their reference states at constant pre-stretch. As a result, chain scission occurs earlier in monodispersed networks of short chains. In contrast, scissions are delayed in DNs with longer chains due to the lower forces these chains sustain in the reference configuration, allowing the network to accommodate more macroscopic deformation and reach higher peak stresses. This trend is reflected in the evolution of the fraction of broken chains in Fig. 4.2(b). It can be seen that there is initially an incubation period, followed by a progressive increase in scissions before a sharp rise in f_b. Notably, the regions associated with incubation and gradual chain failure consistently span a wider stretch range for DNs with $N = 200$. Recently, Lei et al. (2025) reported similar damage accumulation trends in the context of failure of periodic DNs.

Interestingly, Fig. 4.2(b) shows that loss of connectivity occurs with a relatively low number of scissions (at most $f_b \approx 6.5\%$ for $N = 200$), well below mean-field estimates for loss of percolation ($f_b \approx 61\%$ for a diamond lattice (Stauffer and Aharony, 2018)). Although our failure detection method tracks the loss of a spanning path in the network, it differs fundamentally from classic percolation theory, where chains are removed at random. In our case, scission occurs in chains that carry large forces exceeding a critical threshold. The large discrepancies with mean-field predictions likely stem from this selective removal of highly-loaded, connectivity-critical chains.

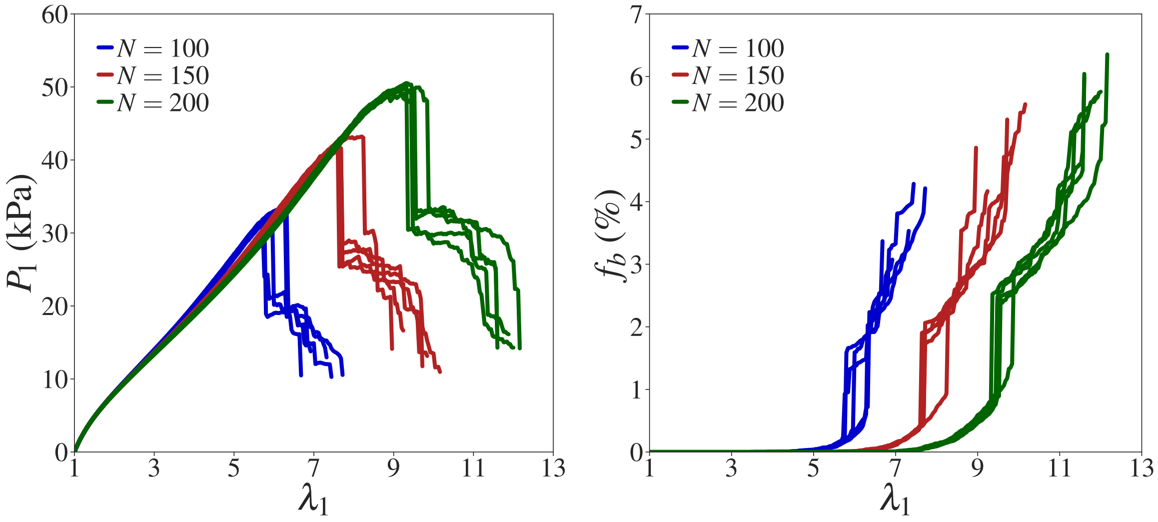

(a) (b)

Fig. 4.2: (a) Nominal stress P_1 versus uniaxial stretch λ_1 for DNs with the same initial chain density ν_0 and nearly identical average pre-stretch $\bar{\lambda}_0$, but different chain lengths N. (b) Evolution of the fraction of broken chains f_b during deformation. For each chain length, five independent network realisations were simulated to capture the variability in the failure behaviour. A uniform critical chain scission threshold of $\eta = 0.8$ is used for all chains.

To shed light on the sharp stress drop in Fig. 4.2(a), we examine the evolution of chain forces during the drop in a representative DN with $N = 100$. We focus on two populations of chains: (i) chains that eventually break during the drop, and (ii) chains in the top 10% of the force distribution (i.e., above the 90th percentile) at the onset of the drop. Note that the breaking chains are not necessarily a subset of the top-loaded ones. Figs 4.3(a) and (c) show the evolution of the average normalised chain force $\frac{f_{\text{avg}}b}{k_BT}$ for these two populations as a function of the number of equilibration steps. Shaded areas represent one standard deviation around the mean. The dashed line marks the critical scission threshold, which corresponds to a chain force of approximately 5.2 in normalised units according to Eq. (4.2), evaluated at $\frac{r}{Nb} = \eta = 0.8$.

Interestingly, Fig. 4.3(a) shows that the breaking chains are initially below the critical force on average, but their forces rise steadily as the drop progresses, ultimately reaching the scission threshold. This suggests that scissions among some of the most loaded chains trigger force redistribution, driving some of them to failure in a cascade. This process can be visualised in Fig. 4.3(b), which shows snapshots of the breaking chains coloured by their normalised force at three stages of the drop: the beginning, midpoint, and end (from top to bottom). These snapshots confirm that scission-induced force redistribution drives subcritical chains in this set to overstretch and break. In contrast, Fig. 4.3(c) reveals that the average force among the initially top-loaded chains decreases as the drop unfolds, indicating a net unloading effect. The corresponding snapshots in Fig. 4.3(d) illustrate this for the same three stages shown in Fig. 4.3(b), showing how force is redistributed within this population. Taken together, Figs 4.3(a)–(d) highlight the localised and complex nature of fracture in rubbery networks: while a subset of chains reach the scission threshold and break, others are unloaded as the network re-equilibrates. Overall, these results demonstrate that the sharp stress drops seen in Fig. 4.2(a) are governed by scission-induced force redistribution, rather than uniform overstretching.

The scission-induced force redistribution that occurs during the sharp stress drop also explains the presence of a post-peak regime in the DN model (Fig. 4.2(a)). In experiments, the sharp drop marks catastrophic specimen failure in the absence of a pre-crack, and no subsequent stabilisation is observed (Yang et al., 2019a; Fujiyabu et al., 2022; Nian et al., 2025). In contrast, the drop does not coincide with global failure in the DN model because the same force redistribution that drives the scission cascade also limits its extent. The net unloading occurring alongside the cascade (Figs 4.3(a)–(d)) prevents it from spreading through the network and disrupting connectivity. Therefore, this unloading shields the surviving chains, preserving network integrity once the cascade ends. As a result, additional stretching is needed to break connectivity-critical chains and induce global failure.

Semi-analytical models of rubber elasticity are frequently employed to estimate the failure of polymer networks. These models rely on idealised and simplified representations of the complex polymer network. Two commonly used examples are the three-chain (James and Guth, 1943) and the eight-chain (Arruda and Boyce, 1993) models. Fig. 4.4(a) compares one of the nominal stress-stretch curves of one DN repeat for $N = 100$, with the ones obtained from these models. To ensure matching initial elastic moduli, the initial end-to-end distance r_0 of the chains in the semi-analytical approach was set to $r_0 = \bar{\lambda}_0\sqrt{N}b$, where $\bar{\lambda}_0$ is the average pre-stretch in the corresponding DN. Among the two, the three-chain model shows markedly better agreement with the DN response across a broad stretch range, accurately capturing the initial stiffness and pre-failure elastic behaviour. In contrast, the eight-chain model systematically underestimates the stress, leading to a softer response even at moderate deformations. The observed agreement with the three-chain model is consistent with our earlier

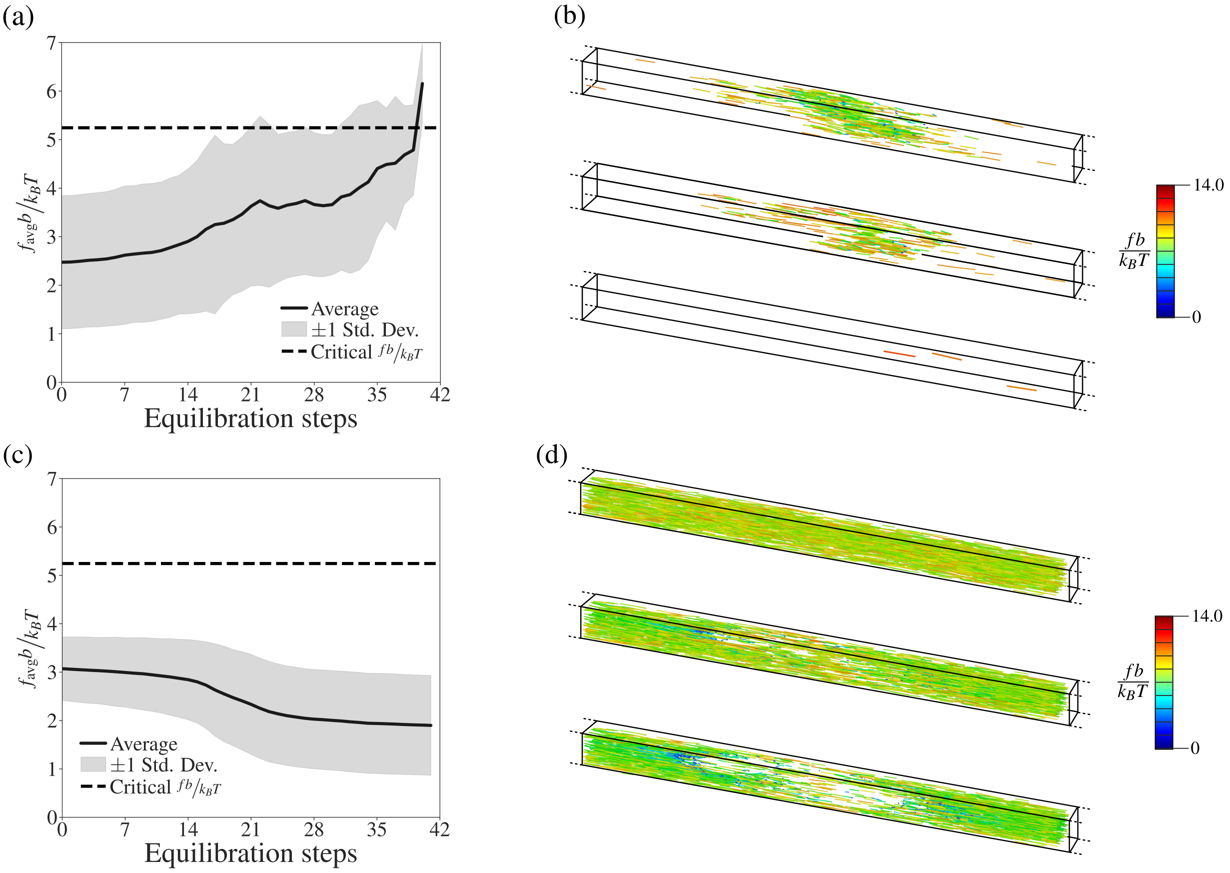

Fig. 4.3: Evolution of the average normalised chain force $\frac{f_{\text{avg}}b}{k_BT}$ and snapshots of the chains that break during the drop ((a) and (b)) and top-loaded chains at the onset of the drop ((c) and (d)). From top to bottom, the snapshots show the chains of the corresponding population at the beginning, midpoint, and end of the sharp stress drop. Chains are coloured by their chain force in normalised units. Dashed lines indicate the edges of the simulation box slice shown for visualisation; the full simulation box extends beyond this region.

findings, where it was shown to best approximate DN elasticity among conventional semi-analytical approaches (Araujo et al., 2024a).

The peak in the stress–stretch response is often used to characterise material failure. To estimate the peak stretch, we assume that failure occurs in the semi-analytical models when the most critical chain reaches the scission threshold, i.e., $\frac{r}{Nb} = \eta$. In the three-chain representation, this corresponds to the chain aligned with the loading direction reaching the threshold, yielding:

$$\lambda_{\text{peak}} = \frac{\sqrt{N}}{\bar{\lambda}_0}\eta. \tag{4.12}$$

In the eight-chain model, all chains experience the same stretch given by $\Lambda = \sqrt{\frac{\lambda_1^2+\lambda_2^2+\lambda_3^2}{3}}$, and the peak stretch is obtained by solving:

$$\lambda_{\text{peak}}^2 + \frac{2}{\lambda_{\text{peak}}} = 3\left(\frac{\sqrt{N}}{\bar{\lambda}_0}\eta\right)^2, \tag{4.13}$$

for λ_{peak}. In both models, the corresponding peak stress P_{peak} is obtained by evaluating the constitutive response at the predicted peak stretch.

Figs 4.4(b) and (c) respectively compare the predicted peak stretch and peak stress with those obtained from DN simulations for different chain lengths. Both semi-analytical models consistently overestimate λ_{peak} and P_{peak}. However, the three-chain model yields better predictions for the peak stretch, with relative errors around 30%, while the eight-chain model exhibits relative errors of approximately 130%. In contrast, both estimates for the peak stress deviate considerably from the ones obtained from DN simulations. This occurs because these models neglect the softening that DNs experience due to the progressive accumulation of broken chains before the sharp stress drop, as shown in Fig. 4.2(b).

The semi-analytical models used to predict failure implicitly assume an ideal network structure. This condition is satisfied in our simulations, as the DNs are monodisperse and defect-free by construction. However, Figs 4.2(b) and (c) show that even under these idealised conditions, the models fail to accurately predict the onset of failure. This discrepancy arises not only from heterogeneities developed during failure, but also from an intrinsic heterogeneity present in the DNs: the distribution of initial end-to-end distances r_0, dictated by mechanical equilibrium (see Fig. 4.1(a)). These findings demonstrate that inaccurate estimates based on conventional

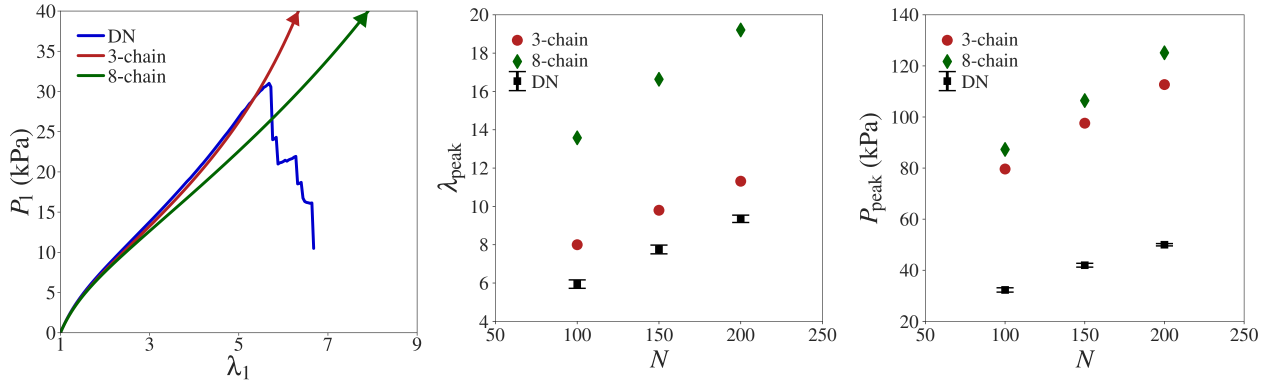

(a) (b) (c)

Fig. 4.4: (a) The nominal stress versus stretch curve from a single DN realisation for $N = 100$ is compared to the predictions from the three-chain and eight-chain models. Triangular markers on the continuum model curves indicate that failure in these models is reached beyond the y-axis limit. (b) Comparison of peak stretches λ_{peak} from DN simulations and semi-analytical models. (c) Comparison of peak nominal stresses P_{peak}. DN values represent averages over five realisations, with error bars indicating one standard deviation around the average.

semi-analytical models are not necessarily attributed to structural defects.

In the three-chain and eight-chain models considered previously, as well as in many other continuum models, it is commonly assumed that the chains deform affinely with the continuum. The inaccuracy of these models is often attributed to this assumption. DN simulations in the context of elasticity have shown that this affine approximation becomes progressively less accurate at large deformations (Alamé and Brassart, 2020; Britt and Ehret, 2022; Araujo et al., 2024a). To examine whether the introduction of chain scission further amplifies deviations from affinity, we quantify non-affinity using the parameter Γ, defined as (Alamé and Brassart, 2020):

$$\Gamma = \frac{\langle \lambda_c - \lambda_{\mathrm{aff}} \rangle}{\lambda_1}, \tag{4.14}$$

where λ_c is the actual chain stretch and λ_{aff} is the corresponding stretch assuming affine deformation.

Fig. 4.5 shows the evolution of Γ as a function of the uniaxial macroscopic stretch λ_1 for representative DNs of each chain length considered in Fig. 4.2. For comparison, we also include results from the corresponding purely elastic simulations, in which chain scission is disabled. Initially, the non-affinity parameter is small across all cases, indicating that most chains deform affinely at the beginning. As deformation progresses, non-affine effects become significant, and consequently Γ increases gradually and it closely follows the elastic evolution. However, as

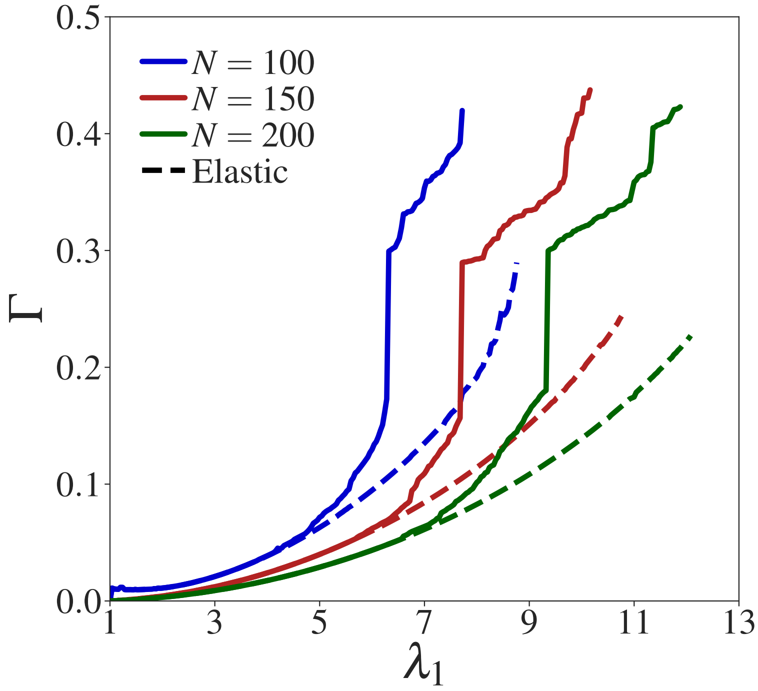

Fig. 4.5: Evolution of affinity deviation parameter Γ with the applied uniaxial stretch λ_1 for representative DNs of each chain length considered in Fig. 4.2. Dashed lines represent simulations without chain scission.

the sharp stress drop is approached, Γ grows more rapidly than its elastic counterpart. This acceleration coincides with the smooth growth in the fraction of broken chains f_b observed in Fig. 4.2(b). At the drop, Γ surges due to the scission avalanche and the resulting force redistribution among the remaining chains. Overall, these results indicate that chain scission amplifies the non-affine deformation of the chains, which is a mechanism that conventional semi-analytical models typically overlook.

Beyond the affine assumption, the three-chain and eight-chain models assume the same initial end-to-end distance for all chains. In contrast, DNs possess a heterogeneous initial end-to-end distribution, which likely contributes to the poor predictions for the peak obtained from these models. Motivated by this, we now propose a semi-analytical model inspired by the damage formulation of Mulderrig et al. (2021) and built upon the extended microsphere model introduced in our previous work (Araujo et al., 2024a), which explicitly accounts for a distribution of initial chain end-to-end distances. Accordingly, the free energy of the network ψ is given by:

$$\psi = \nu_0 \int_{r_0} p_{r_0}(r_0) \iint_{\mathcal{S}_u} \mathcal{H}(t) w(\lambda_c; r_0) d\mathcal{S}_u dr_0, \tag{4.15}$$

where ν_0 is the initial chain density, w is the free energy of a chain (Eq. (4.1)), $\lambda_c = \frac{r}{r_0}$ is the chain stretch, and $p_{r_0}(r_0)$ represents the distribution of initial end-to-end distances. The notation $\iint_{\mathcal{S}_u}(\cdot)d\mathcal{S}_u$ represents the integration over the unit sphere $\mathcal{S}_u$:

$$\iint_{\mathcal{S}_u}(\cdot)d\mathcal{S}_u = \frac{1}{4\pi}\iint(\cdot)\,\sin(\phi)\,d\phi d\theta, \tag{4.16}$$

where θ and ϕ are the azimuthal and polar angles, respectively. Chain scission is irreversibly introduced in the model through the history variable (Miehe et al., 2010):

$$\mathcal{H}(t) = H\left(\eta - \max_{\tau\leq t}\frac{r(\tau)}{Nb}\right), \tag{4.17}$$

where $H(x)$ denotes the Heaviside function. This variable tracks the maximum normalised elongation $\frac{r}{Nb}$ experienced by a chain up to time t. If this elongation ever exceeds the scission threshold η, $\mathcal{H}(t)$ is set to 0, indicating that the chain has broken and can no longer carry load. Otherwise, $\mathcal{H}(t) = 1$, and the chain remains intact. The model is developed in both affine and fully-relaxed formulations. Further details of the derivation and numerical implementation of the fully-relaxed case are presented in Section 4.8.

Fig. 4.6(a) compares the predicted nominal stress P_1 as a function of the uniaxial stretch λ_1 of the continuum models and that of a representative DN with $N = 100$ previously considered in Fig. 4.2. For comparison, we also include the response predicted by the three-chain model using the same average pre-stretch $\bar{\lambda}_0$ as that of the DN. Since the distribution $p_{r_0}(r_0)$ was directly extracted from the DN, the continuum and DN curves initially coincide. At larger deformations, the continuum predictions deviate from the DN curve due to scissions and intrinsic limitations of the microsphere framework (see Britt and Ehret (2022) and Araujo et al. (2024a)). In particular, the proposed models do not capture the sharp stress drop observed in the DN, instead predicting a progressive loss of load-bearing capacity. Taking the peak in the stress-stretch response as a failure marker, the extended affine model provides better predictions for DN failure than its fully-relaxed counterpart and the conventional three-chain and eight-chain models considered in Fig. 4.4.

To understand the relative performances of the affine and fully-relaxed models, we analyse the evolution of damage in each model. To this end, we introduce the macroscopic damage D, which serves as a continuum analogue to the fraction of broken chains f_b in the DN model. D

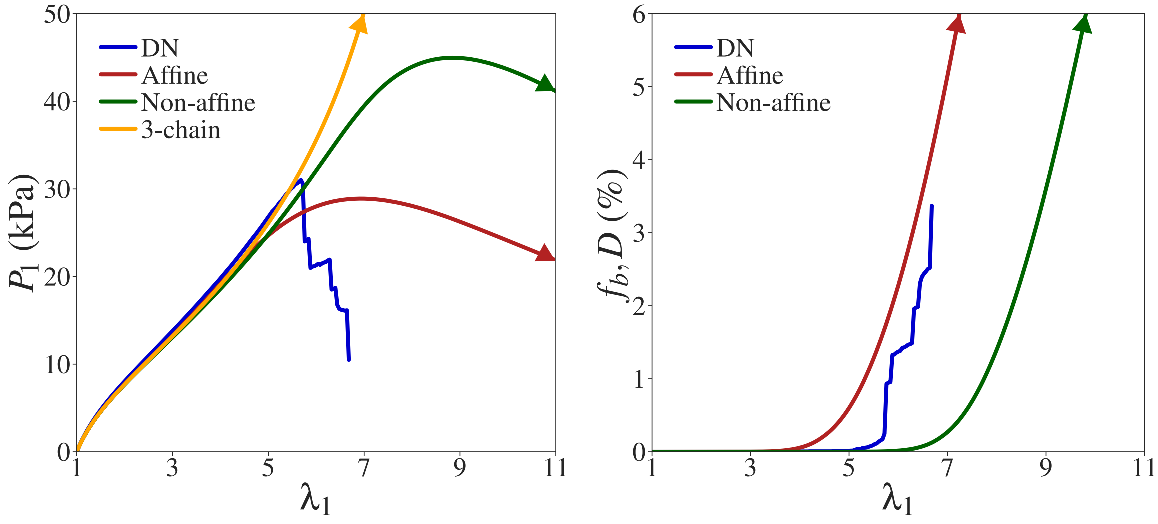

(a)

(b)

Fig. 4.6: (a) The nominal stress P_1 versus stretch λ_1 curve from a single DN realisation for $N = 100$ is compared to the predictions from the extended affine and extended non-affine microsphere models with chain scission. Three-chain prediction is also included for reference, where the triangular marker on the corresponding curve indicates that failure (i.e., the peak) is reached beyond the y-axis limit. (b) Comparison between the fraction of broken chains f_b and the macroscopic damage D predicted by the extended models. In both figures, triangular markers on affine and fully-relaxed curves indicate that the corresponding curves extend beyond the axis limits, but are truncated for visual clarity.

is computed as (Guo and Zaïri, 2021; Mulderrig et al., 2021; Arunachala et al., 2023):

$$D = \int_{r_0} p_{r_0}(r_0) \iint_{\mathcal{S}_u} 1 - \mathcal{H}(t) d\mathcal{S}_u dr_0, \tag{4.18}$$

for both affine and fully-relaxed models. Fig. 4.6(b) shows the evolution of the macroscopic damage D with the uniaxial stretch λ_1. For reference, the evolution of the fraction of broken chains f_b from the DN simulation is also included. As in the DN results, the onset of damage accumulation is preceded by an incubation period in the continuum models. However, D exhibits a smooth growth once damage initiates in both formulations. In the affine case, chains with initially large end-to-end distances reach their scission threshold earlier, leading to premature damage initiation. In contrast, relaxing the affine assumption delays the cleavage of these chains, postponing the onset of damage accumulation in the fully-relaxed model. Consequently, the extended affine model experiences earlier softening, leading to better predictions for the peak observed in the DN simulation. However, this enhanced performance stems from premature damage initiation rather than a more accurate representation of the underlying failure process of the DN.

4.4 Bimodal networks

To explore the effects of other heterogeneities beyond the distribution of initial end-to-end distances, we considered the failure in uniaxial tension of a network with an underlying bimodal distribution of chain parameters. Two representative cases are considered: (i) chains of two distinct chain lengths (short N_S and long N_L), but uniform strength, and (ii) chains with the same length, but different scission thresholds (low η_w and high η_s). As a basis to construct both types of bimodal networks, we take the reference configuration of one of the monodispersed DNs used in Section 4.3 with $N = 100$. This ensures that the initial network topology is fixed across all bimodal simulations. The Kuhn length was fixed at $b = 1$ nm, the normalised density at $\nu_0 b^3 = 1 \times 10^{-3}$, and the temperature at $T = 298$ K.

Networks with a bimodal chain length distribution were generated by randomly assigning each chain in the base network a chain length of $N_S = 100$ or $N_L = 200$, according to a prescribed fraction φ_L of long chains. All chains were endowed with the same scission threshold $\eta = 0.8$. For the bimodal strength case, each chain was randomly assigned a scission threshold of either $\eta_w = 0.4$ or $\eta_s = 0.8$, based on a prescribed fraction of strong chains φ_s. In this case, all chains had the same chain length $N = 100$, matching that of the monodisperse base network. To account for statistical variability, five bimodal network realisations were constructed for each value of φ_L and φ_s.

4.4.1 Bimodal chain length distribution

Fig. 4.7 shows (a) the nominal stress P_1 and (b) the fraction of broken chains f_b as a function of the applied stretch λ_1 in direction 1 for selected values of φ_L. Each curve corresponds to one DN realisation. Note that the limiting cases $\varphi_L = 0$ and $\varphi_L = 1$ correspond to monodispersed networks composed entirely of short and long chains, respectively. As these networks share the same underlying network architecture based on the monodisperse reference network ($\varphi_L = 0$), only one curve is shown for each.

We note from Fig. 4.7(a) that the growing population of long chains causes the softening of the initial deformation response, while increasing the toughness (area under the P_1 versus λ_1 curve) of the networks by delaying global failure. Similar to the monodisperse case (Fig. 4.2),

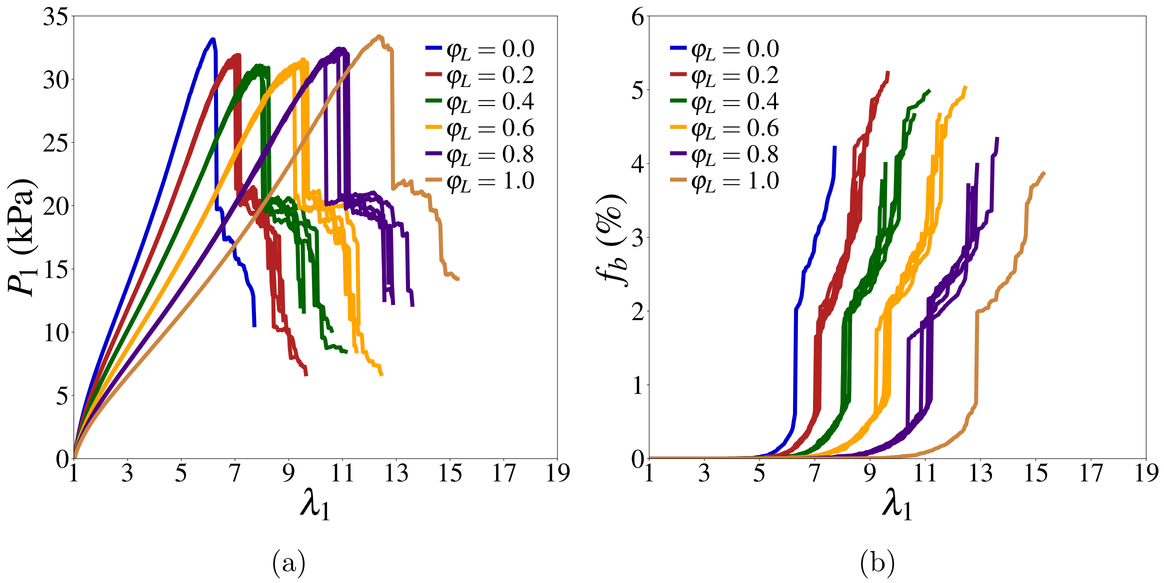

Fig. 4.7: (a) Nominal stress P_1 versus uniaxial stretch λ_1 in direction 1 of DNs with different fractions of long chains φ_L. (b) Corresponding evolution of the fraction of broken chains f_b. Each curve represents the result of one DN repeat at a given φ_L, except for the end points $\varphi_L = 0$ and $\varphi_L = 1$, where only one curve is shown.

the sharp stress drop and the surge in the fraction of broken chains are also observed across different fractions of long chains. Interestingly, Fig. 4.7(b) shows that the fraction of broken chains required for loss of connectivity is mildly affected by the chain length distribution. Moreover, the end points $\varphi_L = 0$ and $\varphi_L = 1$ require virtually the same critical value of f_b. These observations suggest that the critical fraction of broken chains required to disrupt network connectivity is largely insensitive to the chain length distribution.

The contribution of short and long chains to the total fraction of broken chains f_b (Fig. 4.7(b)) is non-uniform and varies both with the stage of deformation and the fraction of long chains φ_L. To illustrate this, Fig. 4.8 presents a breakdown of individual contributions to f_b from each chain type across different values of φ_L. Three key deformation stages are considered: (a) the peak, (b) the end of the sharp stress drop, and (c) loss of connectivity. At the peak (Fig. 4.8(a)), scissions occur predominantly among the short chains except for $\varphi_L = 0.9$ and the end point $\varphi_L = 1$. However, the short chains contribute progressively less to the total amount of scission at the end of the drop (Fig. 4.8(b)), and loss of connectivity (Fig. 4.8(c)) as the population of long chains grows. In particular, long chains account for a larger fraction of broken chains when network connectivity is disrupted for $\varphi_L \geq 0.7$. Fig. 4.8(c) also confirms that the limiting cases $\varphi_L = 0$ and $\varphi_L = 1$ fail with essentially the same critical value of f_b.

To gain more insight into the sharp stress drop observed in Fig. 4.7(a), we examine how

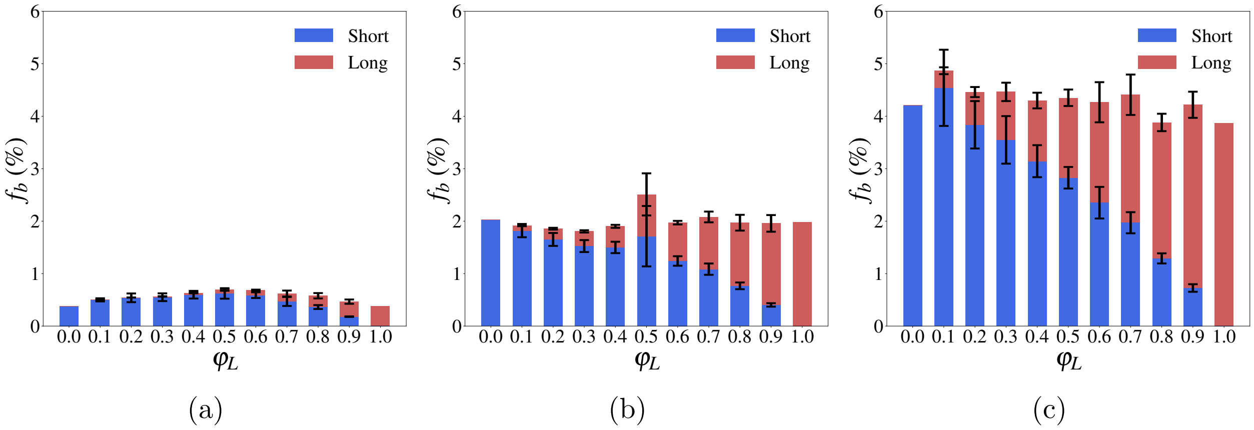

(a) (b) (c)

Fig. 4.8: Breakdown of the total fraction of broken chains f_b into individual contributions from each chain type for different fractions of long chains φ_L at (a) the peak, (b) the end of the sharp stress drop, and (c) loss of connectivity. Bars represent the average over five network repeats at a given value of φ_L, except for the end points $\varphi_L = 0$ and $\varphi_L = 1$. Error bars indicate one standard deviation around the mean.

forces redistribute among chains during this event. Analogously to the monodisperse case, we track the evolution with the number of equilibration steps of the normalised average chain force $\frac{f_{\text{avg}}b}{k_BT}$ across two population of chains: (i) those that eventually break during the drop, and (ii) the top 10% most loaded chains at the drop onset. Figs 4.9(a)-(c) show this evolution for the breaking chains for representative DNs with $\varphi_L = 0.4, 0.6$ and 0.8, respectively. Initially, short and long chains carry forces below the scission threshold on average. However, as the drop unfolds and additional chains break, the redistribution of forces progressively drives more chains toward the critical breaking threshold. Figs 4.9(d)-(f) show the average chain force evolution for the corresponding top 10% most loaded chains. Both short and long chains within this highly loaded population experience comparable force levels and undergo similar unloading processes as the drop unfolds. This indicates that both chain types actively participate in the redistribution process underlying the sharp stress drop.

In the monodisperse case, the sharp stress drop was identified as the result of a scission cascade within a spatially localised cluster of near-critical chains, where the rupture of one or more chains locally amplifies the forces on neighbouring chains and triggers further breakages. Figs 4.9(a)-(c) demonstrate that a similar mechanism operates in DNs with a bimodal chain length distribution.

Fig. 4.7(a) shows that increasing the fraction of long chains softens the initial deformation response of DNs with a bimodal chain length distribution. To quantitatively analyse this

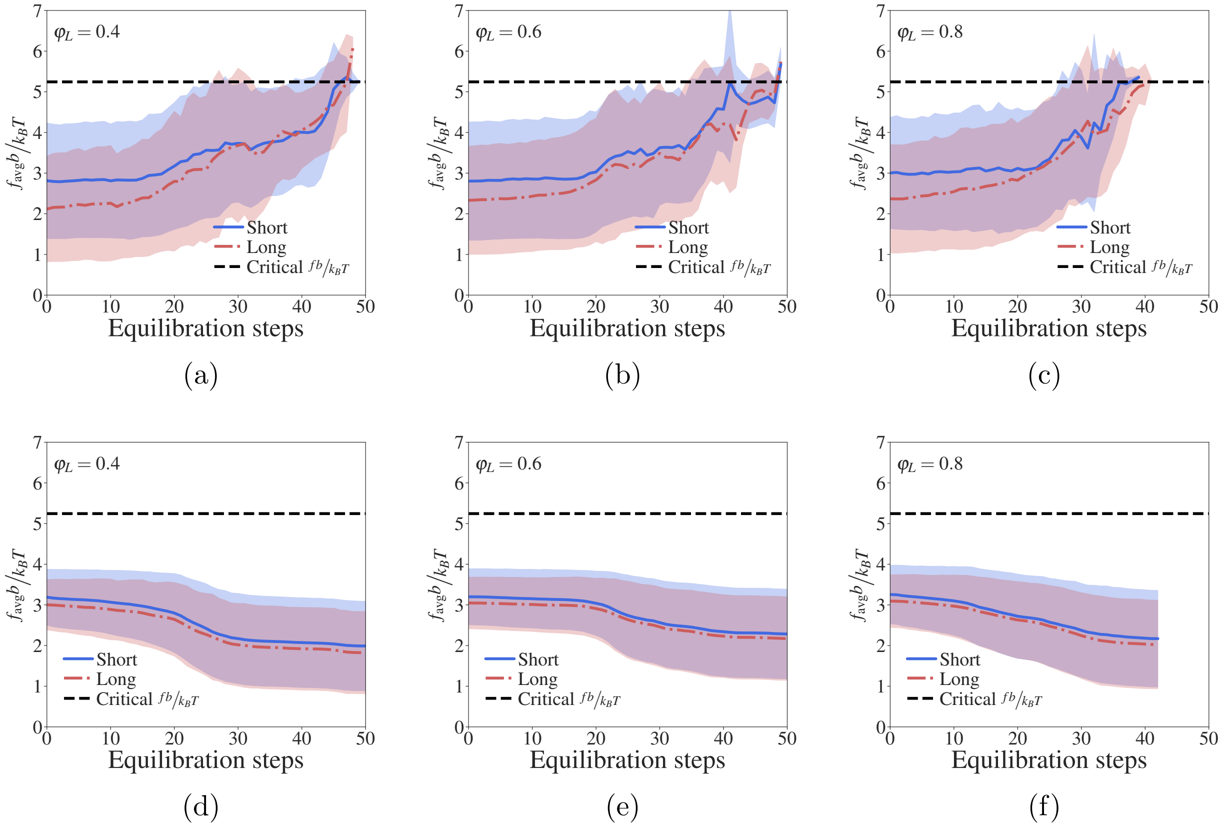

(a) (b) (c)

(d) (e) (f)

Fig. 4.9: Evolution of the normalised average force $\frac{f_{\mathrm{avg}}b}{k_BT}$ per chain type during the steep stress drop for bimodal DNs with varying fractions of long chains $\varphi_L = 0.4$ ((a), (d)), 0.6 ((b), (e)), and 0.8 ((c), (f)). Panels (a)-(c) present this evolution for the chains that eventually break, while (d)-(f) show the force redistribution among the top 10% most loaded chains at the onset of the drop. Short and long chains are plotted separately, with shaded regions representing one standard deviation around the average force. The horizontal dashed line marks the scission threshold.

softening, we present in Fig. 4.10 the dependence of the initial shear modulus G_0 on the fraction of long chains φ_L. As expected, the shear modulus decreases with increasing fractions of long, more compliant chains. For reference, we also include in Fig. 4.10 the classical Voigt (Voigt, 1889) and Reuss (Reuß, 1929) bounds, which provide upper and lower estimates for the effective shear modulus of composite systems under uniform strain and stress, respectively. Let G_S and G_L denote the shear modulus of networks composed entirely of short ($\varphi_L = 0$) and long ($\varphi_L = 1$) chains, respectively. The Voigt bound is:

$$G_{\mathrm{Voigt}} = \varphi_L G_L + (1 - \varphi_L) G_S, \tag{4.19}$$

and the Reuss bound is:

$$G_{\mathrm{Reuss}} = \left(\frac{\varphi_L}{G_L} + \frac{1 - \varphi_L}{G_S} \right)^{-1}. \tag{4.20}$$

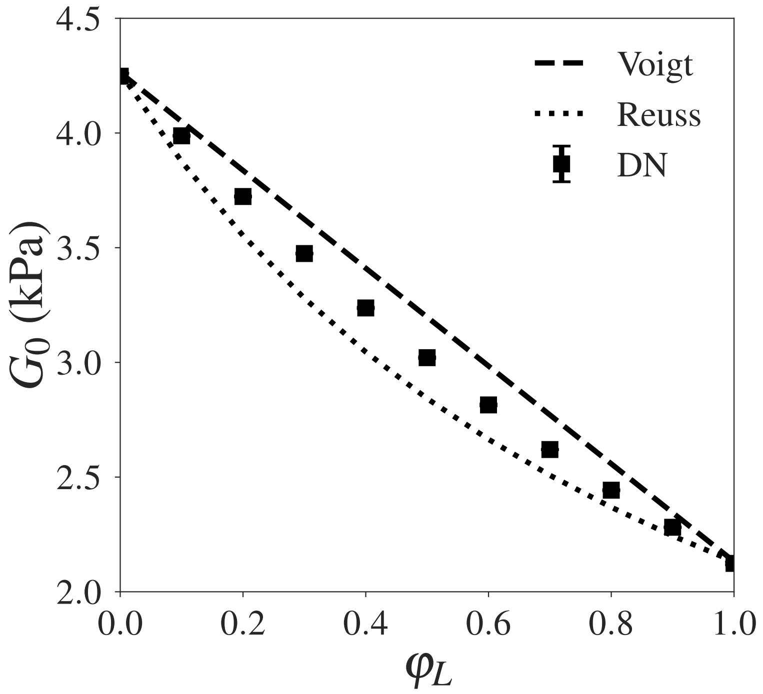

Fig. 4.10: Initial shear modulus G_0 of DNs with a bimodal chain length distribution as a function of the fraction of long chains φ_L. DN data points represent the average over five network repeats at a given fraction, except for the end points $\varphi_L = 0$ and $\varphi_L = 1$. Error bars are included but are barely visible. The Voigt and Reuss bounds are also shown as dashed and dotted lines, respectively.

The shear modulus of the bimodal DNs lies within these theoretical bounds, indicating that these networks exhibit an intermediate behaviour, not fully described by idealised mixtures of monodispersed short-chain and long-chain systems governed by uniform strain or stress conditions.

As in the monodisperse case, we take the peak in the stress-stretch curves as a failure marker in DNs with bimodal chain length distributions. The dependence of the peak stretch λ_{peak} on the fraction of long chains φ_L is shown in Fig. 4.11(a). As expected, increasing the fraction of long chains enables the networks to sustain larger deformations before reaching the peak. However, this gain in extensibility is accompanied by a reduction in the initial shear modulus, as shown in Fig. 4.10. A simple estimate for the peak stretch can be obtained from Eq. (4.12) in combination with a linear rule of mixtures:

$$\lambda_{\text{peak}} \approx (1 - \varphi_L)\lambda^S_{\text{peak}} + \varphi_L \lambda^L_{\text{peak}}, \tag{4.21}$$

where λ^S_{peak} and λ^L_{peak} are the peak stretches of DNs composed entirely of short ($\varphi_L = 0$)

and long chains ($\varphi_L = 1$), respectively. These values are computed from Eq. (4.12) using the corresponding chain lengths and average pre-stretches. We have verified that the average initial end-to-end distance $\bar{r}_0 = \sqrt{\langle r_0^2 \rangle}$ remains nearly constant across different fractions of long chains. Consequently, Eq. (4.21) may be rewritten as:

$$\lambda_{\text{peak}} \approx \frac{N_{\text{avg}} b}{\bar{r}_0} \eta, \tag{4.22}$$

where $N_{\text{avg}} = \varphi_L N_L + (1 - \varphi_L) N_S$ represents the average chain length. The approximation (4.22) highlights that extensibility increases with the average chain length. An alternative estimate is provided by considering a hybrid assembly of short and long chains under an equal-force constraint (Verron and Gros, 2017). The contour length and initial end-to-end distance of the hybrid chain are given by $N_{\text{avg}} b$ and $\varphi_L \sqrt{N_L} b + (1 - \varphi_L) \sqrt{N_S} b$, respectively. In this case, the peak stretch occurs when the hybrid chain satisfies the breaking criterion:

$$\lambda_{\text{peak}} = \frac{N_{\text{avg}} \eta}{\varphi_L \sqrt{N_L} + (1 - \varphi_L) \sqrt{N_S}}. \tag{4.23}$$

Estimates (4.21) and (4.23) are compared to DN results in Fig. 4.11(a). Similar to the monodisperse case, the rule of mixture prediction systematically overestimates the peak stretches observed in DN simulations, whereas the equal-force one provides better quantitative agreement. However, this apparent agreement should be interpreted cautiously: the equal-force model assumes that short and long chains adopt their corresponding ideal random-walk distances in the reference configuration, a condition not satisfied by the present bimodal DNs.

Fig. 4.11(b) shows the dependence of the peak stress P_{peak} on the fraction of long chains φ_L. Interestingly, P_{peak} is only mildly affected by the chain length distribution and displays a non-monotonic dependence on φ_L. In particular, the limiting cases $\varphi_L = 0$ and $\varphi_L = 1$ exhibit nearly identical peak stresses (approximately 33 kPa), in contrast to the monotonic increase in P_{peak} observed in the previous monodispersed case (Fig. 4.4(c)). This apparent contradiction can be rationalised for the limiting cases using the three-chain model. When the chain aligned with the loading direction reaches its scission threshold, the corresponding nominal stress can be approximated by:

$$P_{\text{peak}} \approx \frac{\nu_0}{3} r_0 f_c, \tag{4.24}$$

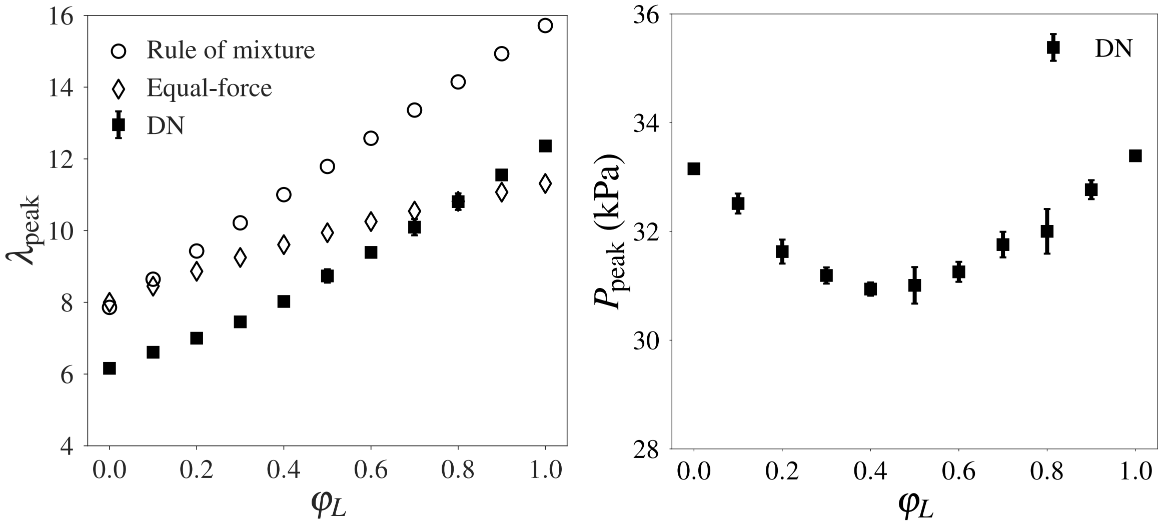

(a) (b)

Fig. 4.11: (a) Peak stretch λ_{peak}, and (b) peak nominal stress P_{peak} as a function of the fraction of long chains φ_L. DN data points represent the average over five network repeats at a given fraction, except for the end points $\varphi_L = 0$ and $\varphi_L = 1$. Error bars correspond to one standard deviation around the average.

where f_c represents the chain force at the scission threshold, and r_0 is the initial end-to-end distance of the representative chain. Since the chain density and breaking thresholds are fixed, the peak stress is modulated by r_0. For the monodisperse systems discussed in Section 4.3, $r_0 \sim \sqrt{N}$, so longer chains yield higher peak stresses. However, for the limiting cases $\varphi_L = 0$ and $\varphi_L = 1$, the average initial end-to-end distance is essentially the same, resulting in similar peak stress values despite the different chain compliances.

Note that applying Eq. (4.24) within a weighted structure similar to that of Eq. (4.21) yields a constant value of P_{peak} across all values of φ_L, since both short and long chains have the same scission threshold. Alternatively, combining the equal-force model with the approximation (4.24) leads to a monotonically increasing prediction of P_{peak} with φ_L. Therefore, these estimates are omitted from Fig. 4.11(b), as neither of them captures the trends observed in DN results.

4.4.2 Bimodal chain strength distribution

Fig. 4.12 presents (a) the nominal stress P_1 and (b) the fraction of broken chains f_b as functions of the stretch along direction 1 for selected fractions of strong chains φ_s. Each curve represents the simulation results of one DN realisation. Note that only one curve is shown for the limiting cases $\varphi_s = 0$ and $\varphi_s = 1$, since they correspond to DNs composed entirely of weak chains and strong chains, respectively.

In contrast to DNs with bimodal chain length distributions, increasing the fraction of strong chains enhances the network toughness (area under the P_1 versus λ_1 curve) without compromising the initial deformation response. This is expected, as the scission threshold does not impact the chain stiffness, leaving the initial shear modulus unchanged (Eq. (4.10)). Fig. 4.12(b) reveals another notable distinction: the critical value of f_b at which network connectivity is lost varies considerably with φ_s.

Remarkably, the sharp stress drop and the sudden rise in the fraction of broken chains are suppressed for intermediate values of φ_s. We have verified that these abrupt transitions are less prominent or absent for fractions φ_s in the range of $0.4 - 0.6$. This suggests that the scission cascade triggered by force redistribution is attenuated by the growing population of strong chains. Interestingly, this shielding effect becomes less effective at preventing abrupt loss of load-bearing capacity as φ_s increases beyond 0.6, and sharp stress drops reappear. However, these drops are preceded by a softening regime, during which scissions accumulate progressively over a broader stretch range. As the limiting case $\varphi_s = 1$ is approached, this softening becomes less pronounced, and the macroscopic failure response resembles that of a strong-chain system.

Based on these findings, the failure behaviour of DNs with a bimodal strength distribution can be classified into three regimes: (I) low ($\varphi_s \leq 0.3$), (II) intermediate ($0.4 \leq \varphi_s \leq 0.6$), and (III) high ($\varphi_s \geq 0.7$) fractions of strong chains. Regime I is characterised by steep stress reductions with minimal pre-drop softening. Regime II marks a transition response in which the sizes of the populations of strong and weak chains are comparable, and the abrupt loss of load-bearing capacity is suppressed. Regime III features the re-emergence of sharp stress drops, which are now preceded by a softening phase whose extent decreases as the limiting case $\varphi_s = 1$ is approached. As shown later, the three regimes can be explained by how forces are redistributed between weak and strong chains.

Paralleling the analysis for the bimodal chain length case, we now investigate how weak and strong chains contribute to the total fraction of broken chains f_b across different fractions of strong chains φ_s. Fig. 4.13 shows the breakdown of f_b at three key deformation stages: (a) the peak, (b) the end of the sharp stress drop, and (c) global failure (loss of connectivity). For DNs

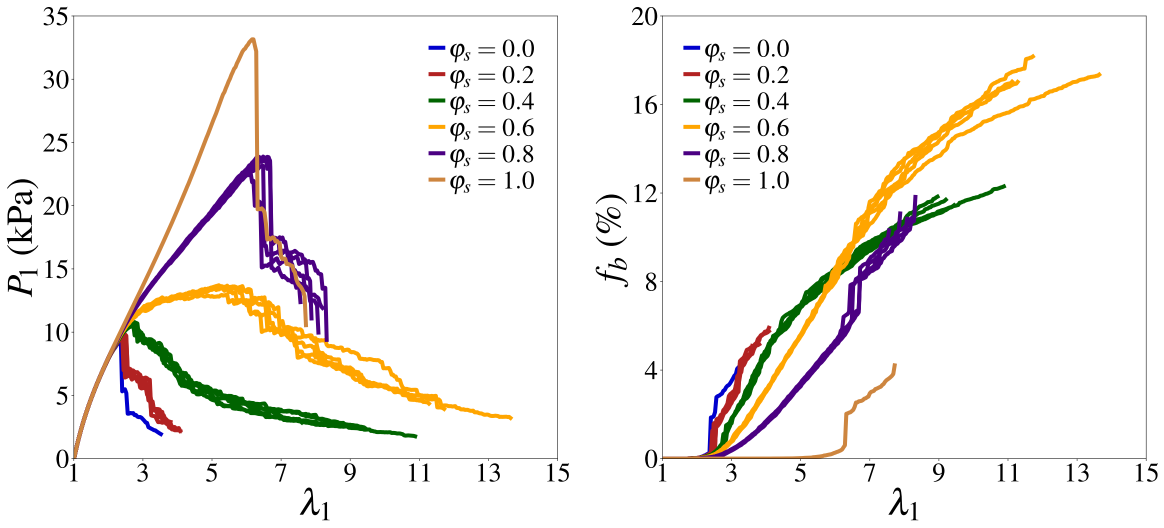

(a) (b)

Fig. 4.12: (a) Nominal stress P_1 versus uniaxial stretch λ_1 in direction 1 of DNs with different fractions of strong chains φ_s. (b) Corresponding evolution of the fraction of broken chains f_b. Each curve represents the result of one DN repeat at a given φ_s, except for the end points $\varphi_s = 0$ and $\varphi_s = 1$, where only one curve is shown.

falling within regime II ($0.4 \leq \varphi_s \leq 0.6$), where no pronounced stress drop is observed, the corresponding point in Fig. 4.13(b) represents data extracted at the end of the largest stress reduction. This allows for a consistent comparison with regimes I and III, where sharp drops are more clearly defined.

Fig. 4.13 reveals that chain cleavage is consistently dominated by weak chains throughout all deformation stages. At the peak (Fig. 4.13(a)), strong chains remain virtually intact, and their contribution becomes noticeable only at the end of the largest stress drop (Fig. 4.13(b)) and at loss of connectivity (Fig. 4.13(c)), particularly in networks where the strong chains outnumber weak ones ($\varphi_s \geq 0.6$). Moreover, Fig. 4.13(c) confirms that the fraction of broken chains needed to disrupt network connectivity varies considerably with the fraction of strong chains. Notably, the critical value of f_b exhibits a non-monotonic trend, reaching a maximum at $\varphi_s = 0.6$, within regime II. This provides further evidence that regime II marks a transition zone. Unlike the bimodal chain length case (Fig. 4.8), the total fraction of broken chains at a given deformation stage is not uniform across different fractions of strong chains. This observation highlights the key role that chain strength heterogeneity plays in shaping the failure response of these networks.

To elucidate the microscopic origins underlying the three regimes, we examine the evolution of the average normalised chain force $\frac{f_{\text{avg}}b}{k_BT}$ for chains that are critical to failure. Specifically,

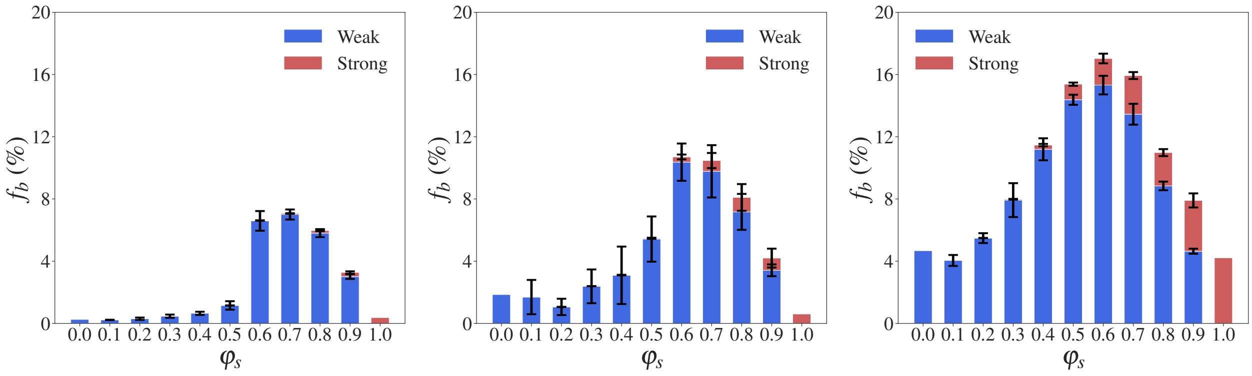

(a) (b) (c)

Fig. 4.13: Breakdown of the total fraction of broken chains f_b into individual contributions from each chain type for different fractions of strong chains φ_s at (a) the peak, (b) the end of the largest stress drop, and (c) loss of connectivity. Bars represent the average over five network repeats at a given value of φ_s, except for the end points $\varphi_s = 0$ and $\varphi_s = 1$. Error bars indicate one standard deviation around the mean.

we track two key groups during the most severe stress drop: (i) the chains that eventually break, and (ii) the top 10% most highly loaded chains at the onset of the drop. Figs 4.14(a)-(c) show this evolution for the breaking chains of representative DNs with $\varphi_s = 0.2$ (regime I), 0.6 (regime II) and 0.8 (regime III), respectively. For $\varphi_s = 0.2$, only weak chains break during the stress drop. As in the bimodal chain length case, both weak and strong chains progressively approach their respective breaking thresholds due to force redistribution triggered by prior scissions. This suggests that the cascade mechanism is still active, although its macroscopic manifestation varies across regimes. Figs 4.14(d)-(f) present the corresponding evolution for the top 10% most loaded chains. Weak chains are absent from these highly loaded groups for $\varphi_s = 0.6$ and $\varphi_s = 0.8$ due to their lower scission threshold and the greater overall deformation at which the stress drop occurs. However, the average force carried by strong chains is noticeably larger and experiences a more severe unloading process in $\varphi_s = 0.8$ compared to $\varphi_s = 0.6$. This indicates a more active involvement of strong chains in the sharp stress drop at high values of φ_s.

Based on these findings, we propose the following rationale underlying the emergence of the three failure regimes. A steep stress drop requires two key conditions to occur: (i) the activation of a scission cascade, and (ii) the presence of a sufficiently large and spatially localised population of near-critical chains that can propagate that cascade. The second condition is central to understanding the origin of these regimes.

In regime I (low φ_s), failure is governed by the weak chains, which are both the majority and are closer to their breaking thresholds. This facilitates the formation of localised clusters of critical chains that can sustain a cascade. The network behaves effectively as a monodispersed weak-chain system.

In regime II (intermediate φ_s), weak chains remain preferential scission sites, but their population size is comparable to that of strong chains. As a result, weak chains approaching failure are increasingly surrounded by strong chains far from scission. This disperses the force redistribution and inhibits the formation of clusters of critical chains capable of propagating the cascade. Consequently, scissions are more diffuse, reflected in the absence of sharp stress drops and the smooth evolution of the fraction of broken chains f_b.

In regime III (high φ_s), weak chains are still the first to break, but they are now the minority and insufficient to propagate the cascade. The resulting accumulation of diffuse scissions leads to a softening phase. However, as deformation increases, the strong chains accumulate higher forces and eventually reach their breaking thresholds. Once a sufficiently large cluster of near-critical chains becomes vulnerable, a cascade can emerge, producing the delayed but sharp stress drop observed in this regime.

We now analyse how the resistance of the networks varies with the fraction of strong chains φ_s. As before, the peak stretch λ_{peak} and peak nominal stress P_{peak} are used as metrics to quantify this resistance. Fig. 4.15(a) shows the dependence of λ_{peak} on φ_s. The peak stretch follows a sigmoid evolution that aligns with the failure regimes outlined previously. In regime I, λ_{peak} remains nearly constant despite the addition of strong chains. In regime II, λ_{peak} increases sharply, indicating a transition in the failure response. In regime III, the peak stretch flattens, suggesting a saturation effect as the network becomes dominated by strong chains. Interestingly, at $\varphi_s = 0.8$ and $\varphi_s = 0.9$, the peak stretch slightly exceeds that of the fully strong-chain system ($\varphi_s = 1$). This deviation is likely due to the delay in the onset of catastrophic failure caused by the diffuse scission of weak chains, which temporarily inhibits cascade formation. Minor random oscillations may also contribute to this result. The evolution of the peak nominal stress P_{peak} is shown in Fig. 4.15(b). Similar to the peak stretch, the peak nominal stress remains nearly unchanged for small to intermediate fractions of strong chains ($\varphi_s < 0.6$). However, P_{peak} experiences a less abrupt increase as the strong chains become the majority, growing almost

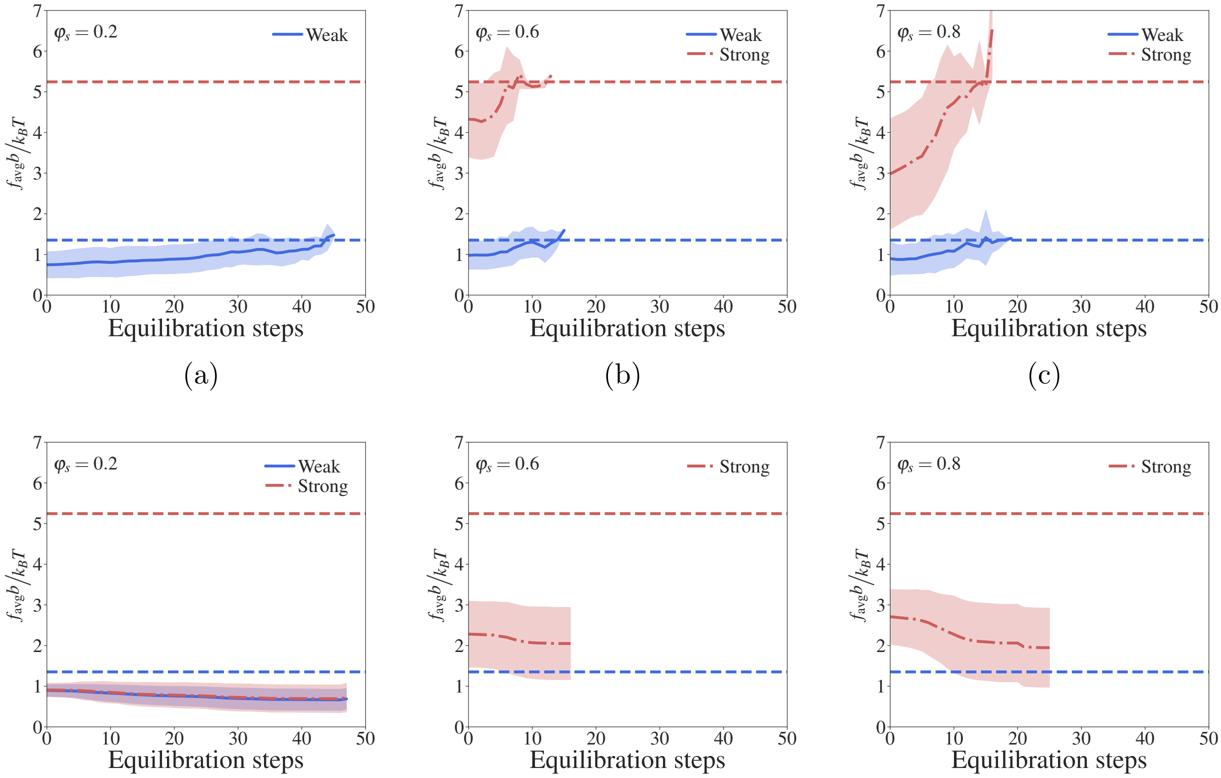

(a) (b) (c)

(d) (e) (f)

Fig. 4.14: Evolution of the normalised average force $\frac{f_{\text{avg}}b}{k_B T}$ per chain type during the largest stress drop for bimodal DNs with varying fractions of strong chains $\varphi_s = 0.2$ ((a), (d)), 0.6 ((b), (e)), and 0.8 ((c), (f)). Panels (a)-(c) present this evolution for the chains that eventually break, while (d)-(f) show the force redistribution among the top 10% most loaded chains at the onset of the drop. Weak and strong chains are plotted separately, with shaded regions representing one standard deviation around the average force. The horizontal dashed line marks the scission threshold for weak and strong chains.

linearly with φ_s.

To estimate the peak stretch, we adapt the three-chain estimate (4.12) by assuming a scission threshold equal to the average chain strength $\eta_{\text{avg}} = (1 - \varphi_s)\,\eta_w + \varphi_s \eta_s$, yielding:

$$\lambda_{\text{peak}} \approx \frac{\sqrt{N}}{\bar{\lambda}_0} \eta_{\text{avg}}, \tag{4.25}$$

which can then be used to evaluate the corresponding peak nominal stress P_{peak} from the constitutive response of the three-chain model. The resulting predictions for λ_{peak} and P_{peak} are included in Figs 4.15(a) and (b), respectively. For the peak stretch, estimate (4.25) misses the sigmoid evolution observed in DN simulations. As for the peak nominal stress, the predicted P_{peak} increases more rapidly than observed in the simulations for low to intermediate fractions of strong chains. As in the previous cases, the semi-analytical predictions consistently overestimate

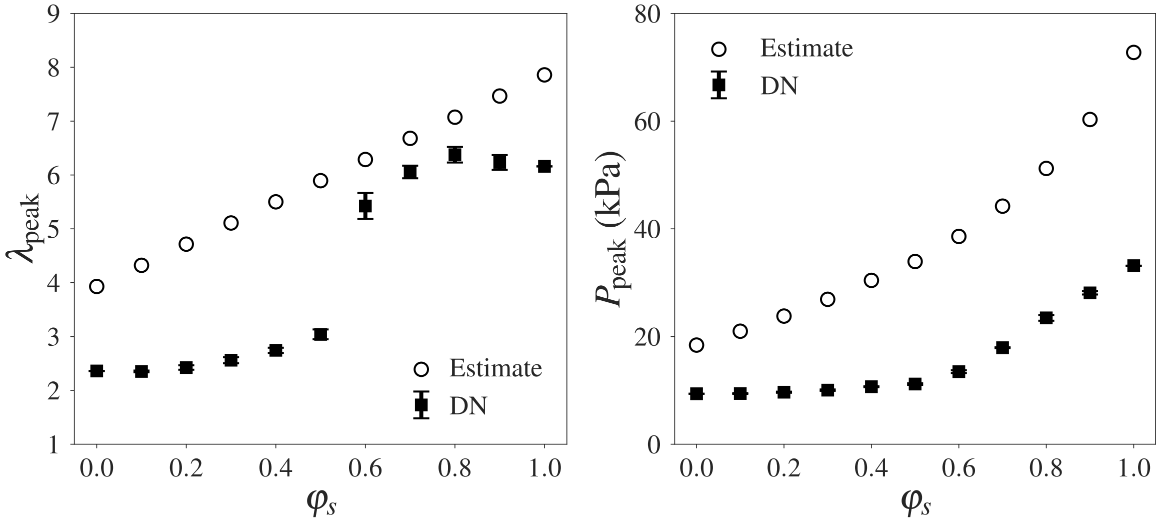

(a) (b)

Fig. 4.15: (a) Peak stretch λ_{peak}, and (b) peak nominal stress P_{peak} as a function of the fraction of strong chains φ_s. DN data points represent the average over five network repeats at a given fraction, except for the end points $\varphi_s = 0$ and $\varphi_s = 1$. Error bars correspond to one standard deviation around the average. Semi-analytical estimates are also included in both figures.

λ_{peak} and P_{peak}.

The contrasting failure behaviours observed for the two bimodal cases investigated arise from fundamentally different governing mechanisms. For DNs with a bimodal chain length distribution, short and long chains play similar mechanical roles, and both effectively participate in the force redistribution process underlying the sharp stress drop. In contrast, the asymmetric scission thresholds in the bimodal chain strength case allow the strong chains to act as shields that modulate the formation and propagation of the scission cascades. This leads to the failure regime transitions that are directly controlled by the chain strength distribution. Therefore, while both bimodal conditions introduce local heterogeneities in the network, only chain strength heterogeneity fundamentally alters the failure response of the network.

4.5 Discussion

4.5.1 Monodisperse networks

The failure response of the monodispersed networks consistently exhibited a sharp stress drop across all chain lengths (Fig. 4.2(a)), which coincided with a surge in the fraction of broken chains (Fig. 4.2(b)). Sharp stress drops have been experimentally reported in hydrogels

(Fujiyabu et al., 2022; Kim et al., 2021) and elastomers (Ducrot et al., 2014; Nian et al., 2025). Similar drops were also recently observed in periodic random DNs (Lei et al., 2025) adopting the same deterministic chain scission approach as our model. By monitoring the evolution of the chain force within populations of critical chains of a representative monodispersed network, we linked this catastrophic event to an avalanche of scissions occurring within a spatially localised cluster of highly-loaded chains. In these clusters, the scission of one or more chains drives the overstretching of surrounding chains through force redistribution, which in turn propagates the scission cascade. Interestingly, Fig. 4.3 showed that this cascade is confined to a small set of chains, and that the overall effect of force redistribution is the net unloading of the most loaded chains of the network.

Notably, Fig. 4.2(b) revealed that the peak in the stress-stretch curves is attained after breaking less than 1% of chains. Additionally, the critical fraction of broken chains required for loss of connectivity differed considerably from mean-field estimates for loss of percolation. This contrast suggests that loss of connectivity depends not only on the network topology, but also on the nature of chain removal. In classical percolation, chains are removed at random, whereas in our model, chain scission targets those carrying the largest forces. The small fraction of broken chains required to disrupt network connectivity also indicates that highly loaded chains are critical to maintain connectivity. We observed a similar trend in a stochastic setting where scissions were biased by the force carried by individual chains (Araujo and Brassart, 2025a). Understanding how topological and mechanical heterogeneities jointly influence failure remains an important avenue for future investigation.

4.5.2 Bimodal networks

The stress-stretch curves of DNs with bimodal chain length distributions (Fig. 4.7(a)) show a stiffness-toughness conflict: the increase in toughness is accompanied by stiffness reduction. This conflict is well-known for single-network rubbery materials (Zhou et al., 2020; Kim et al., 2021; Zhong et al., 2024). In these materials, conventional synthesis methods lead to a coupling: increasing the chain length to improve toughness requires lowering the chain density, which in turn reduces the modulus (Zhou et al., 2020; Kim et al., 2021; Wang et al., 2023b). In our DNs with bimodal chain length distribution, while the chain density remains constant across different fractions of long chains, the initial modulus still decreases with increasing average chain length due to the nearly constant average initial end-to-end distance (Eq. (4.10)). As a result, the stiffness-toughness conflict persists in these bimodal DNs.

In contrast, Kondo et al. (2013) did not observe this conflict in tetra-PEG gels with bimodal chain length distribution. Their results showed that these gels become more resistant as the average chain length increases, without compromising stiffness. They attributed this behaviour to two key features: (i) the initial end-to-end distances are independent of chain length, and (ii) short and long chains break simultaneously. In our corresponding bimodal DNs, the first condition is satisfied, but as shown in Figs 4.8(a) and (b), the second is not. However, according to Eq. (4.10), a constant modulus would require all chains to adopt their ideal random-walk distance in the reference configuration, which in turn would violate condition (i). Designing DNs with bimodal chain length distribution that circumvent the stiffness–toughness conflict is a necessary step toward understanding the mechanisms behind the behaviour observed in experimental systems. Whether such networks can be constructed within our current modelling framework remains an open question.

Contrary to the bimodal chain length case, DNs with a bimodal chain strength distribution exhibit increased toughness without a reduction in modulus. In practice, this was achieved in tetra-PEG gels by incorporating mechanophores of different reactivities (i.e., rupture strengths) into the chains of the network, a modification that does not alter chain stiffness (Wang et al., 2021; Beech et al., 2023). As a result, these gels show enhanced fracture resistance with increasing fractions of strong chains, while maintaining constant stiffness (Beech et al., 2023; Hartquist et al., 2025b). Remarkably, gels with a small fraction of weak chains outperformed their purely strong-chain counterparts in intrinsic fracture energy. A similar, though less pronounced, trend was observed in the peak stretch of our bimodal DNs (Fig. 4.15(a)). On the other hand, the sigmoid-like evolution of the peak stretch with increasing fractions of strong chains qualitatively resembles that reported experimentally for these tetra-PEG gels (Beech et al., 2023).

Beech et al. (2023) and Hartquist et al. (2025b) also proposed DN models to understand the behaviour of rubbery networks with bimodal chain strength distributions. In the first work, different chain strengths were included through different reaction rates in the kinetic treatment for scission used in the framework. In the second, scission was treated deterministically, as in our model, with strong and weak chains assigned different critical bond forces via a modified FJC model. In both works, the breakdown of broken chains by chain type reported closely resembles our DN simulation results (Fig. 4.13). Although the chain scission treatment adopted by these studies is aligned with the well-established energetic description of fracture, our findings indicate that heterogeneity in chain strength alone can govern the failure response of these bimodal networks. Our DN model does show a slight increase in peak stretch at high strong-chain fractions compared to the fully strong-chain system, but this increase is modest relative to the overshoot in intrinsic fracture energy observed experimentally for the previous tetra-PEG gels with mechanophores. Hartquist et al. (2025b) successfully captured this behaviour by using idealised 2D lattice structures with a pre-crack. However, such networks neglect the disorder and structural heterogeneities intrinsic to rubber-like materials. Therefore, it remains unclear whether their findings can be generalised to real rubbery networks.

4.5.3 Continuum models

Taking the peak as a failure marker, conventional semi-analytical models systematically overestimated failure resistance when compared to DN simulations. Notably, these models predicted higher peak stretches and peak nominal stresses even in monodispersed, defect-free networks. Beyond the complex failure mechanisms captured by the DN model, two key factors contribute to these discrepancies: (i) the heterogeneous distribution of initial end-to-end distances, and (ii) the loss of affinity at large deformations (Fig. 4.5). To address both limitations in the monodispersed case, we proposed affine and fully-relaxed microsphere models with chain scission, incorporating the distribution of initial end-to-end distances. Surprisingly, the extended affine model provided better estimates for the onset of failure due to the premature damage initiation caused by affinity. While the fully-relaxed model induces non-affine deformation of the chains, it also delays damage initiation, allowing the network to accommodate more macroscopic deformation before reaching the peak.

The stress-stretch curves predicted by the extended microsphere models in Fig. 4.6(a) exhibit a gradual softening after the peak. In fact, the continuation of these curves beyond the axis of the figure shows that the stress does not vanish, even at very large macroscopic stretches. This persistent residual stress reveals a fundamental limitation of microsphere damage models with orientation-dependent chain deformation for failure and fracture problems. Since chains only break in tension, chains oriented transversely to the loading direction remain intact and continue to store elastic energy. As a result, a complete loss of load-bearing capacity cannot be captured (Mulderrig et al., 2021; Arunachala et al., 2024). Addressing this limitation may require the development of new continuum micromechanics models beyond the microsphere framework.

4.6 Conclusions

To summarise, we developed a Discrete Network (DN) model with chain scission to investigate the microscopic mechanisms underlying failure in rubbery networks. This computational framework was applied to study the failure behaviour of monodisperse networks, as well as networks with bimodal distributions of chain length and chain strength. The simulation results also served to evaluate the predictive capabilities of conventional semi-analytical models for failure onset. The key findings of this study are the following:

- Catastrophic loss of load-bearing capacity is a result of a highly heterogeneous force redistribution process triggered by chain scission: while some chains overstretch and break, others unload as the network re-equilibrates.

- A small fraction of broken chains is sufficient to disrupt the connectivity of monodispersed networks. Introducing a bimodal chain length distribution has a limited impact on this behaviour, unlike a bimodal chain strength distribution, which significantly alters the critical fraction of broken chains.

- While chain length heterogeneity has a secondary effect on the failure response of the corresponding bimodal DNs, heterogeneous scission thresholds significantly impact the failure behaviour of DNs with a bimodal chain strength distribution, leading to distinct failure regimes depending on the fraction of strong chains.

- In general, conventional semi-analytical models overestimate the onset of failure. The proposed extended microsphere model can yield improved predictions, but fails to reproduce the sharp stress drops observed in DN simulations due to intrinsic limitations of the microsphere framework.

In this work, we considered the FJC model to describe the force-extension relationship at the chain level for simplicity. However, chain scission is an energy-dominated process, making the purely entropic formulation of the classic FJC model physically inconsistent. This inconsistency can be resolved by considering single chain models with bond stretching (Smith et al., 1996; Mao et al., 2017; Guo and Zaïri, 2021; Mulderrig et al., 2023; Zhu and Brassart, 2025) and bond angle opening (Guo and Zaïri, 2021; Lavoie et al., 2020; Zhu and Brassart, 2025), which introduce energetic contributions to the chain free energy. Additionally, chain scissions were described in our DN model through a deterministic chain scission criterion, which limits the current framework to rate-independent failure. However, rubber-like materials can exhibit rate-dependent failure even in the absence of noticeable viscoelastic effects (Hassan et al., 2022; Wang et al., 2024; Wang and Fan, 2023). Capturing rate-dependent effects will require replacing the current deterministic scission approach with a stochastic one using the kinetic treatment of chain scission (Arora et al., 2022; Beech et al., 2023; Araujo and Brassart, 2025a). Addressing these points will be the focus of future work.

4.7 Appendix A: Effect of stretch increment size

To assess the effect of the stretch increment size $\Delta\lambda_1$, we conducted uniaxial tension simulations with different values of $\Delta\lambda_1$ using one of the monodisperse DNs considered in Section 4.3 with $N = 100$. The scission threshold was set to $\eta = 0.95$, and the temperature $T = 298$ K. Figs 4.16(a) and (b) show the nominal stress P_1 and the fraction of broken chains f_b as functions of the applied uniaxial stretch λ_1, respectively. As the increment size decreases below a certain threshold, the sharp stress drop emerges consistently and always near the same location. With further reduction, the curves nearly collapse one on top of the other, with only minor variations at the terminal point corresponding to global failure. Similar trends are also observed in the evolution of the fraction of broken chains. We have verified that these observations are not affected when other scission thresholds are used.

Interestingly, the larger the increment size $\Delta\lambda_1$, the higher the stretch and fraction of broken chains at global failure. In particular, the largest increment considered yields a bell-shaped nominal stress–strain curve and a smooth damage accumulation process, indicating a more gradual failure response. This behaviour reflects the path-dependency of failure: when

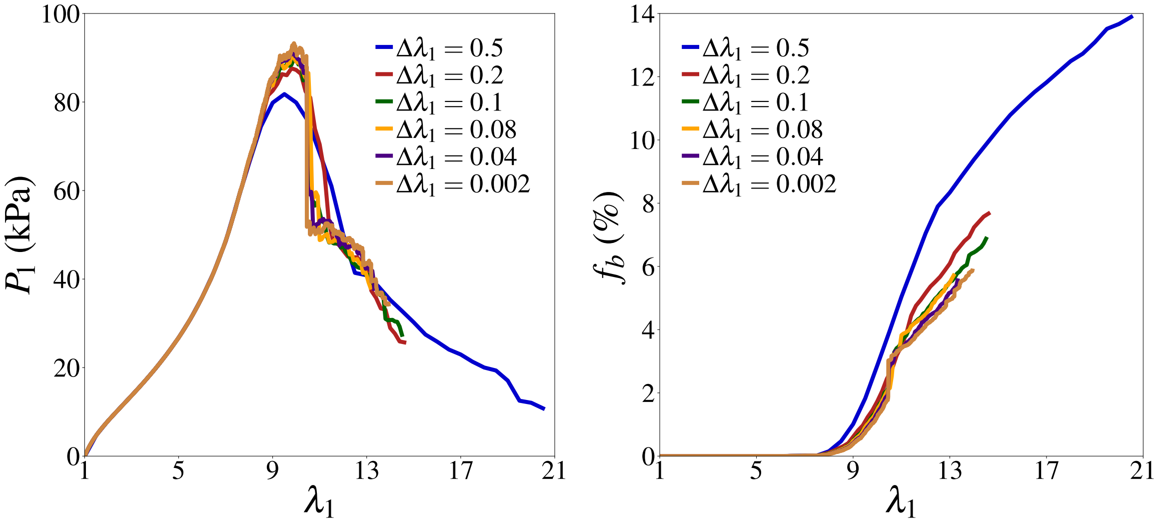

(a) (b)

Fig. 4.16: Nominal stress P_1 (a) and fraction of broken chains f_b as functions of the applied uniaxial stretch λ_1 for different stretch increment sizes $\Delta\lambda_1$ for a representative monodisperse network with $N = 100$ and $\eta = 0.95$.

increments are too large, many highly loaded chains can be removed in a single step, preventing the formation of the spatially localised cluster of critically loaded chains within which the cascade responsible for the sharp drop develops (Fig. 4.3). As a result, the network bypasses this catastrophic event and can be stretched further, reaching a higher apparent stretchability and a larger fraction of broken chains before losing connectivity. In contrast, smaller increment sizes allow clusters to form consistently, leading to sharp stress drops occurring at nearly the same stretches and close agreement of the terminal points.

4.8 Appendix B: Extended microsphere models with distribution of end-to-end distance and chain scission

4.8.1 Derivations

We derive the full constitutive response of the extended microsphere models accounting for chain scission, using the free energy form given in Eq. (4.15). Under the assumption of affine deformation, the initial chain orientation $\boldsymbol{n}_0$ is mapped by the deformation gradient $\boldsymbol{F}$ to the current orientation $\boldsymbol{n} = \boldsymbol{F}\boldsymbol{n}_0$, and the chain stretch can be expressed as $\lambda_c = \|\boldsymbol{F}\boldsymbol{n}_0\|$. Following standard thermodynamics, the network contribution $\boldsymbol{P}^e$ to the macroscopic stress $\boldsymbol{P}$ (Eq. (4.6)) is obtained as:

$$\boldsymbol{P}^e = \nu_0 \int_{r_0} p_{r_0}(r_0) \iint_{\mathcal{S}_u} \mathcal{H}(t) \frac{f r_0}{\lambda_c} \boldsymbol{F}(\boldsymbol{n}_0 \otimes \boldsymbol{n}_0) d\mathcal{S}_u dr_0. \tag{4.26}$$

We also propose a fully-relaxed version of the model to include non-affine effects. Similar to Mulderrig et al. (2021), we postulate that chain stretches should minimise the free energy of the network under the following kinematic constraint:

$$\int_{r_0} p_{r_0}(r_0) \frac{r_0^2}{\bar{r}_0^2} \iint_{\mathcal{S}_u} \mathcal{H}(t) \boldsymbol{F}\boldsymbol{n}_0 \otimes \boldsymbol{n}_0 d\mathcal{S}_u dr_0 = \int_{r_0} p_{r_0}(r_0) \frac{r_0^2}{\bar{r}_0^2} \iint_{\mathcal{S}_u} \mathcal{H}(t) \boldsymbol{n} \otimes \boldsymbol{n}_0 d\mathcal{S}_u dr_0, \tag{4.27}$$

where $\boldsymbol{n}$ represents the deformed orientation vector, and $\bar{r}_0^2 = \int_{r_0} p_{r_0}(r_0) r_0^2 dr_0$. The distribution of deformed orientations is obtained by solving the minimum problem:

$$\begin{aligned} \psi = \inf_{\boldsymbol{n},\boldsymbol{\pi}} \Bigg\{ \nu_0 \int_{r_0} p_{r_0}(r_0) \iint_{\mathcal{S}_u} \mathcal{H}(t) w \, d\mathcal{S}_u \, dr_0 + \boldsymbol{\pi} : \Bigg[\int_{r_0} p_{r_0}(r_0) \frac{r_0^2}{\bar{r}_0^2} \iint_{\mathcal{S}_u} \mathcal{H}(t) \boldsymbol{F}\boldsymbol{n}_0 \otimes \boldsymbol{n}_0 \, d\mathcal{S}_u dr_0 \\ - \int_{r_0} p_{r_0}(r_0) \frac{r_0^2}{\bar{r}_0^2} \iint_{\mathcal{S}_u} \mathcal{H}(t) \boldsymbol{n} \otimes \boldsymbol{n}_0 \, d\mathcal{S}_u dr_0 \Bigg] \Bigg\}, \end{aligned} \tag{4.28}$$

where $\boldsymbol{\pi}$ is the Lagrange multiplier enforcing the constraint (4.27). The stationary condition with respect to $\boldsymbol{n}$ gives, for each r_0:

$$\boldsymbol{f} = \frac{r_0}{\nu_0 \bar{r}_0^2} \boldsymbol{\pi} \boldsymbol{n}_0, \tag{4.29}$$

which can be inserted back into Eq. (4.27) to yield an implicit equation to the multiplier $\boldsymbol{\pi}$. Taking the stationary condition into account, the network contribution $\boldsymbol{P}^e$ to the macroscopic stress $\boldsymbol{P}$ is obtained as:

$$\boldsymbol{P}^e = \int_{r_0} p_{r_0}(r_0) \frac{r_0^2}{\bar{r}_0^2} \iint_{\mathcal{S}_u} \mathcal{H}(t) \boldsymbol{\pi} \boldsymbol{n}_0 \otimes \boldsymbol{n}_0 d\mathcal{S}_u dr_0. \tag{4.30}$$

4.8.2 Implementation of the fully-relaxed model

The fully-relaxed model is implemented using a staggered approach that mimics the quasi-static procedure employed in the DN simulations (see Fig. 4.1(b)). At initialisation, the end-to-end distance distribution $p_{r_0}(r_0)$ is directly extracted from a representative DN. This distribution is then discretised into n_{r_0} points. For each value of r_0 in the discretisation, we associate a list $\mathcal{I}(r_0)$ that encodes the history-dependent indicator function $\mathcal{H}(t)$ evaluated over orientations on the unit sphere. All chains are assumed to be intact at initialisation.

At each macroscopic stretch increment, the implicit equation for the multiplier $\boldsymbol{\pi}$ is solved using the list $\mathcal{I}(r_0)$ from the previous increment. Once $\boldsymbol{\pi}$ is determined, the distribution of deformed orientations is evaluated via Eq. (4.29), and $\mathcal{I}(r_0)$ is updated accordingly to reflect newly broken chains. If chain scission occurred during this update, the implicit equation for $\boldsymbol{\pi}$ is resolved with the updated $\mathcal{I}(r_0)$, and the cycle repeats: a new $\boldsymbol{\pi}$ is computed, leading to a new distribution of deformed orientation and a new list $\mathcal{I}(r_0)$. This iterative procedure continues until no additional cleavage is detected.

Chapter 5

Force-biased chemical degradation in rubbery networks: insights from discrete network simulations

This chapter presents work that has been published as "Araujo, L. M. and Brassart, L. (2025a). Force-biased chemical degradation in rubbery networks: Insights from discrete network simulations. *Extreme Mechanics Letters*, 77:102344". In this investigation, we analyse the force-biased degradation of rubbery networks using a DN-based framework. Building on the DN model introduced in Chapter 3, we incorporate a stochastic chain scission algorithm to capture the effect of force-dependent kinetics on the degradation response of rubber-like materials. Our results show that force-biased degradation not only accelerates degradation but can also induce anisotropic damage when degradation occurs under external loads. Finally, we propose a simple micromechanical continuum model. While this model captures the general trends associated with force-accelerated degradation, it fails to reproduce many important mechanisms observed in DN simulations, highlighting the importance of explicitly accounting for network topology and heterogeneous force distributions.

5.1 Introduction

Rubbery networks are susceptible to chemical degradation when exposed to environmental factors, such as moisture, oxygen, heat, or light (Lyu and Untereker, 2009; Bensalem et al., 2023). Chemical degradation often involves the breaking of load-bearing polymer chains, leading to a reduction in mechanical properties such as elasticity, strength and toughness. Conversely, chemical degradation in rubbery networks can be accelerated by mechanical forces. Under an applied force, the potential energy landscape of reactive bonds along the polymer chain shifts, facilitating chain scission by bond rupture (Ribas-Arino and Marx, 2012). Previous experimental works suggest that force-biased chain scission determines the strength of polymers degrading under load (Zhurkov and Korsukov, 1974; Bershtein et al., 1977), and could be responsible for environmental cracking of elastomers (Yang et al., 2019b; Qari and Cai, 2024). Force-assisted chemical reactions are also exploited by incorporating mechanophores into rubbery networks to achieve various mechano-responsive effects, such as toughening, self-growth, or directed degradation (Lloyd et al., 2023; Aydonat et al., 2024; Wang and Gong, 2025). In these scenarios, the evolving structure of the network plays a key role, as it governs the partitioning of forces among the chains.

In recent years, Discrete Network (DN) computational models have emerged as promising tools to investigate structure-property relationships in rubbery networks (Kothari et al., 2018; Alamé and Brassart, 2019; Lei and Liu, 2022; Wagner et al., 2022; Araujo et al., 2024a). In this approach, the rubbery network is represented as a network of nonlinear springs with force-extension relationship derived from statistical mechanics considerations. The distribution of forces among the chains is determined from the condition of force balance at the crosslinks. Compared to semi-analytical micromechanical models of rubber elasticity, such as the eight-chain or full-network models (Arruda and Boyce, 1993; Wu and Van Der Giessen, 1993), their main advantage is that they explicitly account for the network topology and do not require ad-hoc assumptions regarding the partitioning of the chain stretches. They are also much more cost-effective than (coarse-grained) molecular dynamics simulations. DN models have been used to investigate the role of network defects and heterogeneities on the properties of rubbery networks (Gusev, 2019; Alamé and Brassart, 2019, 2020; Wagner et al., 2022; Araujo et al., 2024a), as well as their damage and fracture mechanisms (Lei and Liu, 2022; Arora et al., 2022; Beech et al., 2023; Deng et al., 2023; Li et al., 2024). However, DN models of elastomers and hydrogels have rarely been exploited in the context of mechanically-activated chemical reaction.

In this work, we combine a DN model with a stochastic chain scission algorithm to investigate force-biased chemical degradation in rubbery networks. For the sake of generality, we consider swollen networks (e.g. hydrogels), where degradation is accompanied by swelling and mass loss, which are also accounted for in our modelling framework. Examples of applications include biodegradable hydrogels for biomedical applications such as bioabsorbable implants, drug delivery and tissue engineering (Bryant and Vernerey, 2018; Turner et al., 2022; Hosseinzadeh and Ahmadi, 2023), where precise control of the degradation and mechanical properties is critically needed. Recent experimental evidence suggests that the swelling of cross-linked networks can generate chain forces that are sufficient to assist bond cleavage reactions (Lee et al., 2014; Kim et al., 2020; Metze et al., 2023).

We use our DN model to elucidate the role of force-biased degradation kinetics on the evolution of mechanical and swelling properties. We show that force-biased reaction kinetics accelerates degradation (as expected), and further that it amplifies the reduction in elastic modulus for a given number of chain scission events, due to preferential scission of highly-stretched chains. We also show that force-biased reaction kinetics induces anisotropic damage when degradation occurs under constraint. These trends cannot be captured by a simple continuum model based on the commonly used eight-chain assumption, where all chains carry the same force. Overall, our work demonstrates the potential of DN models to simulate coupled chemo-mechanical phenomena in rubbery networks and highlights the role of heterogeneous force distribution in the evolving network on the mechanical and degradation behaviour.

5.2 Discrete network model

5.2.1 Thermodynamics

We consider a network of long polymer chains held together by chemical (non-degradable) crosslinks. In the reference configuration, taken as the initial, undegraded configuration, the network is stress-free and the water concentration is C_0. The use of a pre-swollen state as a reference state is convenient to describe hydrogels prepared in solution. In the DN modelling framework, polymer chains are represented as entropic springs connected at nodes representing the crosslinks. A representative DN structure is shown in Fig. 5.1. At any degradation stage, the free energy associated with stretching the polymer chains in the network is given by:

$$\psi^e = \frac{1}{V_0} \sum_{j=1}^{n} w^{(j)}, \tag{5.1}$$

where V_0 is the volume of the network in the reference configuration, $w^{(k)}$ is the free energy of the j^{th} chain and n is the current number of chains in the network. The chain behaviour is described by the freely-jointed chain model:

$$w = N k_B T \left[\frac{r\beta}{Nb} + \log\left(\frac{\beta}{\sinh \beta} \right) \right], \quad \beta = \mathcal{L}^{-1}\left(\frac{r}{Nb} \right), \tag{5.2}$$

where b is the Kuhn length, N is the number of Kuhn segments, k_B is the Boltzmann constant, T is the absolute temperature, and r is the chain end-to-end distance. The Langevin function $\mathcal{L}(x)$ is defined as $\mathcal{L}(x) = \coth(x) - 1/x$. The force needed to maintain a given end-to-end distance r is derived from the free energy as $f = \frac{dw}{dr}$:

$$f = \frac{k_B T}{b} \mathcal{L}^{-1}\left(\frac{r}{Nb} \right). \tag{5.3}$$

The end-to-end distance of a chain in the reference configuration is denoted as r_0. For small chain extension $r \ll Nb$, the force-extension relation (5.3) reduces to the Gaussian chain model:

$$f = 3 k_B T \frac{r}{Nb^2}. \tag{5.4}$$

The Gaussian chain approximation holds for $r \lesssim 0.3Nb$. In this work, we limit ourselves to monodisperse networks where the number of Kuhn segments is the same in each (undegraded) chain.

We also endow the network with a mixing free energy to describe swelling by absorption of water. Let C be the nominal concentration of water (number of water molecules per unit volume in the reference state) and ϕ be the current volume fraction of polymer. The free energy contribution due to mixing the water molecules with the long polymer chains is given by the Flory-Huggins model (Flory, 1942; Huggins, 1942):

$$\psi^c = \mu_0 C + \frac{k_B T}{\Omega} J \left[(1-\phi) \log(1-\phi) + \chi \phi (1-\phi) \right], \tag{5.5}$$

where μ_0 is a reference chemical potential for water, Ω is the volume per water molecule, χ is the affinity parameter, and $J \equiv \det(\boldsymbol{F})$ is the swelling ratio with respect to the reference configuration. Note that water molecules are not represented explicitly in the DN framework. The total free energy of the swollen network is given by $\psi = \psi^e + \psi^c$.

Coupling between rubber elasticity and absorption of water is achieved by assuming molecular incompressibility. The swelling ratio J (ratio of current volume to the volume in the reference configuration) is then directly related to the current amount of polymer and water by (Pan and Brassart, 2022):

$$J = 1 - m\phi_0 + \Omega(C - C_0), \tag{5.6}$$

where ϕ_0 represents the polymer volume fraction in the reference configuration. $m \equiv \frac{V_{p0}-V_p}{V_{p0}}$ is the polymer mass loss fraction, with V_{p0} and V_p the reference and current volumes of polymer (the density of polymer is assumed constant). Thus, Eq. (5.6) accounts for the change in volume due to releasing polymer chains during degradation, in addition to the change in volume due to absorption of water. In the initial, reference state, $C = C_0$, $m = 0$ and $J = 1$, as required. Also note the following relation between the polymer volume fraction and the water concentration: $(1 - \phi) = \frac{\Omega C}{J}$. In the reference state, $J = 1$ and $(1 - \phi_0) = \Omega C_0$.

The network is subjected to a prescribed deformation gradient $\boldsymbol{F}$, with $J = \det(\boldsymbol{F})$. The reference configuration is defined such that $\boldsymbol{F} = \mathbf{1}$ and $C = C_0$. In the current configuration, the network is subjected to a macroscopic stress $\boldsymbol{P}$ and is in contact with a reservoir of water with chemical potential μ. We assume that the network is always at equilibrium with respect to the applied stress and chemical potential:

$$\boldsymbol{P} : \delta\boldsymbol{F} + \mu\delta C + \Pi(\delta J - \Omega\delta C) - \delta\psi = 0, \tag{5.7}$$

where Π represents a Lagrange multiplier enforcing the kinematic constraint (5.6). In writing Eq. (5.7), we consider virtual deformation and concentration changes $(\delta\boldsymbol{F}, \delta C)$ with no chain degradation or mass loss. Eq. (5.7) means that we do not account for viscoelasticity, and that we assume chemical equilibrium. This assumption holds considering that water diffusion is much faster than chemical degradation. Noting the result $\delta J = J\boldsymbol{F}^{-T} : \delta\boldsymbol{F}$, the state laws for the stress and chemical potential are obtained:

$$\boldsymbol{P} = \frac{\partial \psi^e}{\partial \boldsymbol{F}} - J\Pi \boldsymbol{F}^{-T}, \tag{5.8}$$

$$\mu = \frac{\partial \psi^c}{\partial C} + \Omega\Pi. \tag{5.9}$$

The Cauchy stress is obtained from the classical relation $\boldsymbol{\sigma} = (1/J)\boldsymbol{P}\boldsymbol{F}^T$.

The macroscopic deformation $\boldsymbol{F}$ is applied by prescribing the displacement of the n_b boundary nodes of the network according to the affine relation:

$$\boldsymbol{x}_\alpha = \boldsymbol{F}\boldsymbol{X}_\alpha, \quad \alpha = (1, n_b), \tag{5.10}$$

where $\boldsymbol{X}_\alpha$ and $\boldsymbol{x}_\alpha$ respectively represent the coordinates of the α^{th} boundary node in the reference and current configurations. Consistent with Eq. (5.7), the network is assumed to be at equilibrium at all times, i.e. force balance is satisfied at each node. The network stress contribution can then be obtained as (Alamé and Brassart, 2020):

$$\boldsymbol{P}^e \equiv \frac{\partial \psi^e}{\partial \boldsymbol{F}} = \frac{1}{V_0}\sum_{\alpha=1}^{n_b} \boldsymbol{f}_\alpha^r \otimes \boldsymbol{X}_\alpha, \tag{5.11}$$

where $\boldsymbol{f}_\alpha^r$ is the reaction force on boundary node α. The corresponding Cauchy stress is given by $\boldsymbol{\sigma}^e = (1/J)\boldsymbol{P}^e\boldsymbol{F}^T$. Note that the network stress $\boldsymbol{P}^e$ does not vanish in the reference configuration. According to the force extension relation (5.3), a non-zero initial chain end-to-end distance r_0 requires a non-zero chain force, leading to a non-zero macroscopic stress $\boldsymbol{P}^e$ according to Eq. (5.11). A representative initial distribution of r_0 in the equilibrated reference configuration is shown in Fig. 5.1. Using the Flory-Huggins model (5.5), the state law for the chemical potential (5.9) can be re-expressed as:

$$\mu = \mu_0 + k_B T\left[\log(1-\phi) + \phi + \chi\phi^2\right] + \Pi\Omega. \tag{5.12}$$

The Lagrange multiplier Π is determined from the boundary conditions.

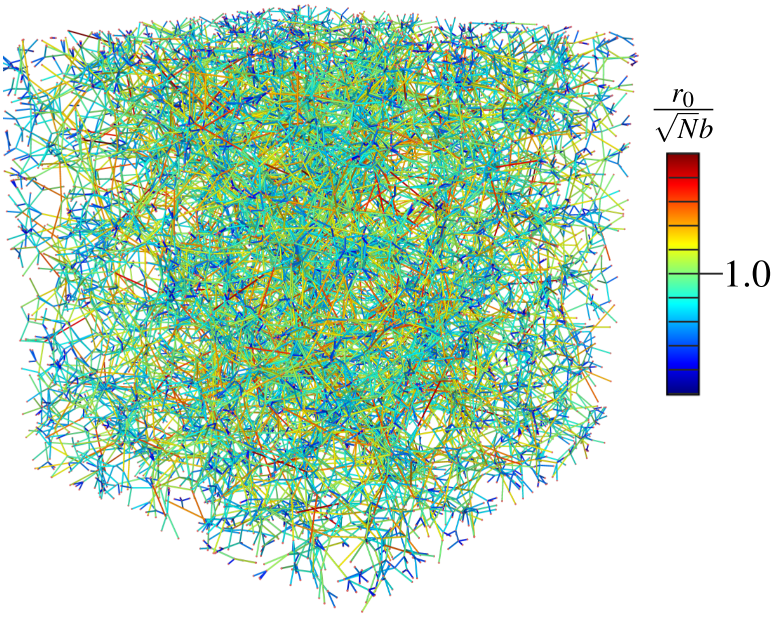

Fig. 5.1: Representative discrete network with $n = 20000$ chains in the equilibrated reference configuration, showing the initially-heterogeneous distribution of chain end-to-end distances.

5.2.2 Degradation: Kinetic Monte Carlo algorithm

The kinetics of chain scission by chemical reaction of susceptible backbone bonds is described using an Eyring-type model (Kauzmann and Eyring, 1940; Bell, 1978):

$$k = \gamma \exp\left(-\frac{U_b - fa}{k_B T}\right) = k_0 \exp\left(\frac{fa}{k_B T}\right), \tag{5.13}$$

where γ is the attempt frequency, U_b is the activation energy for bond scission by chemical reaction in the absence of an applied force, and a is an activation length. $k_0 \equiv \gamma \exp\left(-U_b/k_B T\right)$ represents the scission rate in the absence of an applied force. In this work, we assume that each chain contains at most one reactive bond, so that Eq. (5.13) directly provides the chain scission rate under a given applied force. For chains that do not contain any reactive bond, the rate constant k_0 is simply set to zero. Given a population of n identical chains subjected to a constant force, the number of surviving chains is described by a first-order kinetic model: $\dot{n} = -kn$, and the survival probability of a chain after time t is given by: $p_s(t) = \exp(-kt)$.

In writing Eq. (5.13), we have implicitly identified the chain force f with the bond force, which is a strong approximation. In a real polymer chain, the bond force becomes significant only when the chain is highly extended under large force, whereas it is negligible when the chain stretch is small. In this work, we used the (purely entropic) freely-jointed chain model to describe the force-extension response of a single chain for simplicity. Since this model does not provide an estimate of the bond force, the chain force was used in Eq. (5.13). Within the DN framework, the distinction between bond force and chain force could be captured by adopting a single-chain model that accounts for energetic effects to the chain behaviour, such as the extendable freely-jointed chain model (which accounts for stretchable bonds) (Mao et al., 2017) or the deformable freely-rotating chain model (which accounts for both bond stretching and bond angle opening) (Zhu and Brassart, 2025). This extension of the DN framework will be considered in a future work.

In the DN, the distribution of forces among the chains is non-homogeneous, giving a distribution of chain scission rates $k^{(j)}$. Any chain scission event corresponds to a change of state of the network as a whole. The rate of escape of the network from its current state is given by:

$$k_{tot} = \sum_{j=1}^{n} k^{(j)}. \tag{5.14}$$

The rate k_{tot} represents the total escape rate in a population of identical networks. The survival probability of the network in its current state is given by: $P_s(t) = \exp(-k_{tot}t)$, i.e. $P_s(t)$ is the probability that no chain scission occurs in the network within at time interval t. Equivalently, $(1 - P_s(t))$ is the probability that (at least) one chain scission occurs within the same time t. By definition of the cumulative distribution function, the probability distribution of the time of first chain scission event $P(t)$ is obtained by integrating the function $(1 - P_s(t))$ (Voter, 2007):

$$P(t) = k_{tot} \exp(-k_{tot}t). \tag{5.15}$$

In the Kinetic Monte Carlo (KMC) algorithm, the degradation process is simulated by cutting one chain every time interval Δt, where Δt is drawn from the probability distribution of the time of first chain scission (5.15). In practice, this is readily achieved by drawing a uniformly distributed random number $\xi_1 \in]0, 1]$, and using the following formula (Voter, 2007):

$$\Delta t = -\frac{1}{k_{tot}} \log(\xi_1), \tag{5.16}$$

which is obtained by inverting the cumulative distribution function $(1 - P_s)$, also using the fact that ξ_1 and $1-\xi_1$ follow the same distribution. The chain j to be broken is randomly selected, such that it satisfies the following criterion:

$$\sum_1^{j-1} k^{(j)} < \xi_2 k_{tot} < \sum_1^{j} k^{(j)}, \tag{5.17}$$

where $\xi_2 \in [0,1]$ is a second uniformly distributed random number. In the case where the chain force has no effect on the chain scission rate ($k^{(j)} = k_0$), all the chains are equally likely to be broken according to the selection criterion (5.17). However, when reaction is accelerated by the chain force, the criterion (5.17) favours the scission of chains experiencing large forces.

5.2.3 Mass loss

We assume that mass loss occurs due to the formation of elastically-ineffective chains, or chain clusters, and which are detached from the main network due to chain scission. Chain clusters are identified with the connected components of the network, treated as a graph. Two connected components of the network (graph) are such that there is no chain (edge) connecting their respective nodes. Chain clusters are removed from the network if the following two conditions are met: 1) all the chains in the cluster are elastically ineffective (i.e. they bear zero force), and 2) the number of chains in the cluster is less than a threshold value n_d. The second condition physically corresponds to the requirement that chain clusters should be small in comparison to the mesh size to be able to diffuse out of the network. Note that we assume that diffusion of the clusters is much faster than degradation, and therefore we do not account for diffusion kinetics.

After removal of a chain cluster, the number of remaining chains n in the network is re-calculated. We also count the number n_1 of complete chains with N Kuhn segments, and the number n_2 of dangling chains with $\frac{N}{2}$ Kuhn segments, so that $n = n_1 + n_2$. The mass loss m is then calculated as:

$$m = 1 - \frac{\left(n_1 + \frac{n_2}{2}\right)}{\left(n_{1,0} + \frac{n_{2,0}}{2}\right)}, \tag{5.18}$$

where $n_0 = n_{1,0} + n_{2,0}$ is the initial number of chains. Eq. (5.18) accounts for the fact that dangling chains contribute half the mass of a complete chain.

5.2.4 Numerical procedure

Discrete networks were generated in cubic simulation volumes using our in-house algorithm implemented in Matlab, which allows control of chain density and end-to-end distance distribution independently by allowing chains to interpenetrate, see Araujo et al. (2024a) for details. All the crosslinks have a coordination of four, and we do not consider second-order loops. Discrete networks had at least 20000 chains in their initial undegraded state, which is sufficiently large to ensure that the networks are statistically representative and isotropic.

Networks were subjected to macroscopic deformation gradients $\boldsymbol{F} = \{\lambda_1, \lambda_2, \lambda_3\}$, where λ_i ($i = 1, 2, 3$) are the principal stretches along the cube faces, following Eq. (5.10). At every time step, networks were equilibrated using LAMMPS (Thompson et al., 2022) and the chain forces were calculated. Network structures were then updated to account for chain scission and mass loss, following the procedure outlined in Sections 5.2.2 and 5.2.3. We assume that the network fails at the percolation threshold, also called reverse gelation point, identified here as the time where there is no continuous chain path connecting any pair of opposing faces in the simulation volume. At this point, the simulation stops. The stochastic degradation model was implemented in `Python` using the `networkx` library for graph-related operations. In practice, to reduce the computational cost, mass loss calculation, loss of percolation detection and network re-equilibration were carried out every 60 chain scission events. We have verified that this simplification has negligible impact on the numerical results. The numerical steps are illustrated in Fig. 5.2. The different degradation scenarios considered in this work are illustrated in Fig. 5.3, and details of the boundary conditions are provided in Appendix 5.6. As an illustration, the DN model is used to simulate degradation-induced swelling in tetra-PEG hydrogels in Appendix 5.7, where numerical predictions are also compared to the experimental data of Li et al. (2011).

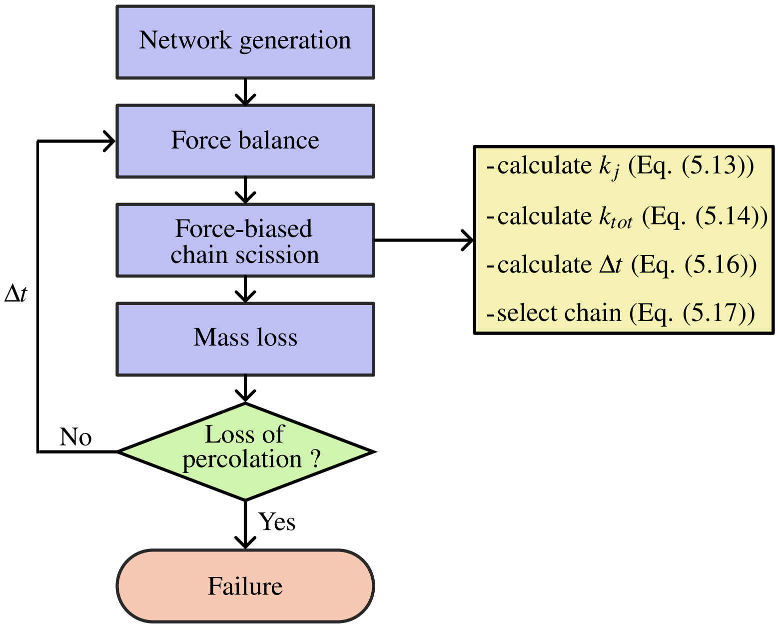

Fig. 5.2: Numerical procedure for coupled mechanics and degradation of discrete networks using a Kinetic Monte Carlo algorithm.

5.2.5 Degraded elastic modulus

We characterise the effect of chemical degradation on the mechanical properties by calculating the elastic modulus of the network in the undegraded and degraded states. For uniaxial deformation along direction 1 at constant water content, $\lambda_2 = \lambda_3 = 1/\sqrt{\lambda_1}$, and the Young modulus can be calculated as:

$$E_0 = \lim_{\lambda_1 \to 1} \frac{d\sigma_1}{d\lambda_1}, \tag{5.19}$$

where σ_1 is the principal Cauchy stress in direction 1. For an incompressible, isotropic elastic material, the shear modulus is related to the Young modulus by $E_0 = 3G_0$. In the particular case where all the network chains are in their Gaussian regime in the reference configuration, i.e. $r_0 \lesssim 0.3Nb$, the shear modulus can alternatively be calculated as (Alamé and Brassart, 2020):

$$G_0 = \nu_0 k_B T \left\langle \frac{r_0^2}{Nb^2} \right\rangle, \tag{5.20}$$

where ν_0 is the number density of elastically-effective chains in the undegraded network (number of chains per unit volume in the reference configuration). The notation $\langle \cdot \rangle$ denotes the average over all the chains in the network. Eq. (5.20) is exact provided that the network is isotropic. The validity of formula (5.20) has been verified in our previous work (Araujo et al., 2024a). Eq. (5.20) recovers the classical expression $G = \nu_0 k_B T$ only in the specific case where the root-mean-square average of the chain end-to-end distance is equal to the random walk distance $\sqrt{N}b$.

We define the elastic moduli of the degraded network w.r.t. to a fictitious "damaged reference configuration", which is obtained by bringing the degraded network to a state with $\boldsymbol{F} = \mathbf{1}$. The incompressibility condition (5.6) for $J = 1$ and the current mass loss fraction m together dictate the value of C in the degraded configuration. The degraded Young modulus in direction i can be obtained by subjecting the degraded network to a uniaxial tension test in direction i:

$$E_i = \lim_{\tilde{\lambda}_i \to 1} \frac{d\sigma_i}{d\tilde{\lambda}_i}, \tag{5.21}$$

where $\tilde{\lambda}_i$ is the principal stretch in direction i measured w.r.t. the damaged reference configuration. As shown later, force-induced degradation can result in anisotropic elastic properties in the damaged state, so that the three degraded Young moduli may differ. In the particular case where the network remains isotropic in the degraded state, $E_1 = E_2 = E_3 \equiv 3G$. Further assuming Gaussian chain behaviour, the degraded shear modulus G can be obtained as:

$$G = \nu k_B T \left\langle \frac{\tilde{r}_0^2}{Nb^2} \right\rangle, \tag{5.22}$$

where ν is the current density of elastically-effective chains (number of chains per unit volume in the reference configuration), and $\tilde{r}_0$ is the end-to-end distance of a chain in the damaged reference configuration. In general, $\tilde{r}_0 \neq r_0$ for a given chain, because the topology of the degraded network differs from that of the undegraded network, impacting the partitioning of stretches among the chains and hence the modulus.

5.3 Continuum model

We also consider a simple analytical model and compare its performance against predictions of the DN model to gain better understanding of the impact of simplifying assumptions. For simplicity, we neglect mass loss and focus on the effect of degradation on the elastic and swelling behaviour. Like in the DN model, the mixing energy is described using the Flory-Huggins model, Eq. (5.5). For the elastic energy of the network, we adopt the eight-chain representation

(Arruda and Boyce, 1993), which is based on a simplified unit cell of the network consisting of eight identical freely-jointed chains meeting at its centre. The eight chains all experience the same stretch, so that the network free energy is simply given by:

$$\psi^e = \nu N k_B T \left[\frac{r\beta}{Nb} + \log\left(\frac{\beta}{\sinh \beta} \right) \right], \quad \beta = \mathcal{L}^{-1}\left(\frac{r}{Nb} \right). \tag{5.23}$$

For a degrading network, the density of elastically-effective chains ν is not constant but decreases with the extent of degradation. Consistent with the kinetic model of degradation introduced in Section 5.2.2, the chain density is taken to evolve following a first-order kinetic equation (Lavoie et al., 2016):

$$\dot{\nu} = -\nu k_0 \exp\left(\frac{fa}{k_B T} \right), \tag{5.24}$$

where the chain force is related to the current chain end-to-end distance by the force-extension relation (5.3). The initial condition is $\nu = \nu_0$ at $t = 0$, corresponding to the undegraded reference state. We also define the ratio $\eta \equiv \frac{\nu}{\nu_0}$.

The chain end-to-end distance in the degraded network is calculated as:

$$r = \Lambda \tilde{r}_0, \tag{5.25}$$

where Λ is the chain stretch, which in the eight-chain representation is given by:

$$\Lambda = \sqrt{\frac{I_1}{3}}, \quad I_1 = \lambda_1^2 + \lambda_2^2 + \lambda_3^2. \tag{5.26}$$

In Eq. (5.25), $\tilde{r}_0$ is the chain end-to-end distance in the degraded reference configuration. The localisation rule (5.25) thus accounts for the effect of damage on the localisation of chain stretch. In the reference, undegraded state, $\tilde{r}_0 = r_0$. As the network degrades, $\tilde{r}_0$ evolves. Note that the continuum damage model is isotropic, since the effect of damage is described via scalar parameters only: the current density of elastically-effective chains ν and the chain end-to-end distance in the degraded state $\tilde{r}_0$.

The evolution of $\tilde{r}_0$ is defined based on the following considerations. First, using the localisation rule (5.25) into the elastic energy (5.23), it can be shown that the elastic shear modulus of the eight-chain model w.r.t. the reference and degraded reference states are respectively given by:

$$G_0 = \nu_0 k_B T \frac{r_0^2}{Nb^2}, \tag{5.27}$$

and:

$$G = \nu k_B T \frac{\tilde{r}_0^2}{Nb^2}, \tag{5.28}$$

which parallel Eqs (5.20) and (5.22) for an (isotropic) DN. In particular, Eqs (5.20) and (5.27) show that the shear modulus of the eight-chain model coincides with the undegraded DN modulus provided that r_0 is set to the root-mean-square average of the initial chain end-to-end distance $\sqrt{\langle r_0^2 \rangle}$ in the DN. The importance of matching the initial chain end-to-end distance in DN and continuum models for meaningful comparison was highlighted in our previous works (Alamé and Brassart, 2020; Araujo et al., 2024a). Taking the ratio of Eqs (5.28) and (5.27), we obtain:

$$\frac{G}{G_0} = \eta \frac{\tilde{r}_0^2}{r_0^2}. \tag{5.29}$$

For a network of Gaussian chains with fixed volume but decreasing number of chains, the evolution of the modulus as a function of η can be reasonably well described by the Effective Medium Approximation (EMA) (Nishi et al., 2012, 2017; Alamé and Brassart, 2020):

$$\frac{G}{G_0} \approx 2\eta - 1. \tag{5.30}$$

Using the EMA into Eq. (5.29), the evolution equation for the reference degraded distance is obtained:

$$\frac{\tilde{r}_0}{r_0} = \sqrt{\frac{2\eta - 1}{\eta}}. \tag{5.31}$$

Under the EMA, the evolution equation (5.31) ensures that the ratio G/G_0 predicted by the eight-chain model and the DN coincide by construction.

Application of the continuum model as an approximation of a given DN simulation involves the following steps. Consistent with the DN model, the reference state, taken as the initial undegraded state, corresponds to $\boldsymbol{F} = \mathbf{1}$ (by definition), $C = C_0$ and $\boldsymbol{P} = \mathbf{0}$. For a given initial chain density ν_0 (the same as in the corresponding DN model), the chain end-to-end distance r_0 is set to the root-mean-square average of the chain end-to-end distance in the DN, which ensures that the initial modulus G_0 coincides with the DN modulus. Also, $\tilde{r}_0 = r_0$ in the initial, undegraded state. For a given deformation gradient, the chain stretch is calculated according to Eq. (5.26), and the chain force is calculated using the freely-jointed chain model. Next, the chain density is evolved according to Eq. (5.24) and η is updated. The degraded end-to-end distance $\tilde{r}_0$ is updated using Eq. (5.31). At each degradation stage, the stress, chemical potential and Lagrange multiplier are calculated from the state laws (5.8)-(5.9) and boundary conditions. The simulation is terminated when $\eta = 0.5$, corresponding to $G = 0$ according to the EMA (5.30).

5.4 Results

We use the DN model to investigate the effect of force-assisted chemical degradation on the mechanical and swelling behaviour of rubbery networks. We also compare DN results semi-analytical estimates using the continuum model. The following scenarios were considered: a) free degradation, b) degradation under a constant pre-stretch, and c) degradation under a dead load, as represented in Fig. 5.3. Material parameters were set as follows: $N = 29$ and $b = 1.1$ nm, and $\phi_0 = 10\%$, giving the initial water concentration as $C_0 = \frac{1-\phi_0}{\Omega}$ with $\Omega = 0.03$ nm^3. The initial chain density ν_0 was obtained from the initial volume fraction as $\nu_0 = \phi_0/v_{ch}$, where $v_{ch} = N v_m$ is the volume of a polymer chain and and v_m the volume of a Kuhn monomer, set as $v_m/\Omega = 2.2$. Random discrete networks were generated so that the square average initial end-to-end distance is $\langle r_0^2 \rangle \approx N b^2$, so that $G_0 = \nu_0 k_B T$ according to Eq. (5.20). Finally, we set $\chi = 0.45$, $T = 310$ K and $k_0 = 16.5 \times 10^{-4}$ h^{-1}.

5.4.1 Free degradation

We first consider free degradation, as illustrated in Fig. 5.3(a). At time $t = 0^+$, the undegraded network is immersed in a water bath with chemical potential $\mu = \mu_0$ and instantaneously swells to its equilibrium value $J = J_0$. At $t > 0$, the network degrades and swells further, until it reaches the point of reverse gelation. Details of boundary conditions are given in Appendix 5.6.1. For illustration, snapshots of a discrete network at different stages of degradation are shown in Fig. 5.4, where the degradation state is quantified by the normalised number of chain scissions ζ (the ratio of the number of chain scission events to the initial number of chains).

Fig. 5.5(a) shows the evolution of the normalised number of chain scissions ζ for different

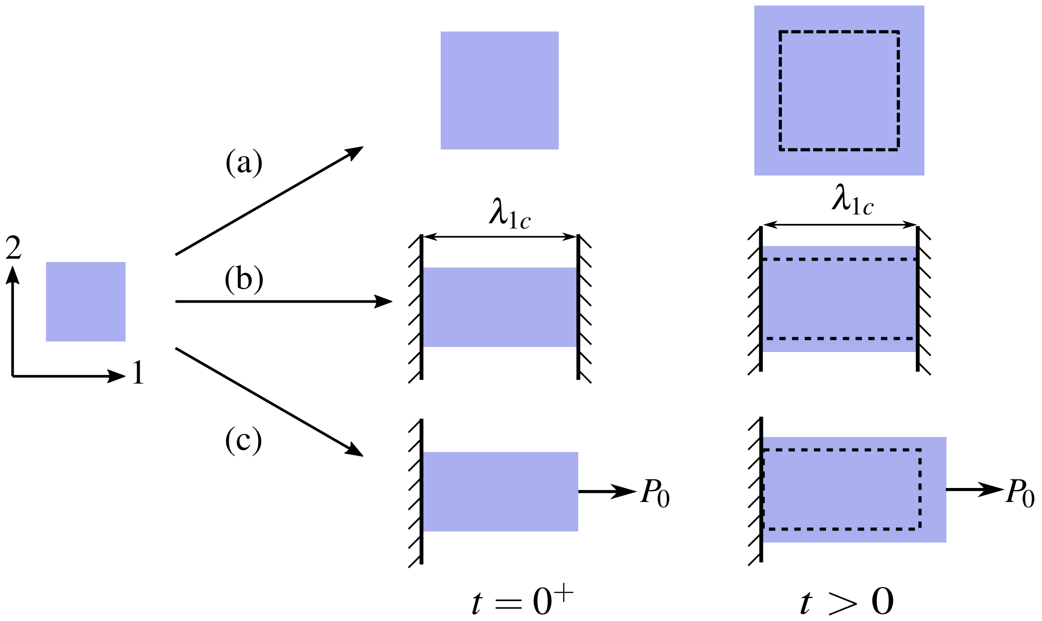

Fig. 5.3: Degradation scenarios considered in this work: (a) free degradation, (b) degradation under a constant pre-stretch λ_{1c}, and (c) degradation under a dead load P_0. Diffusion of water and detached chain clusters is assumed much faster than degradation.

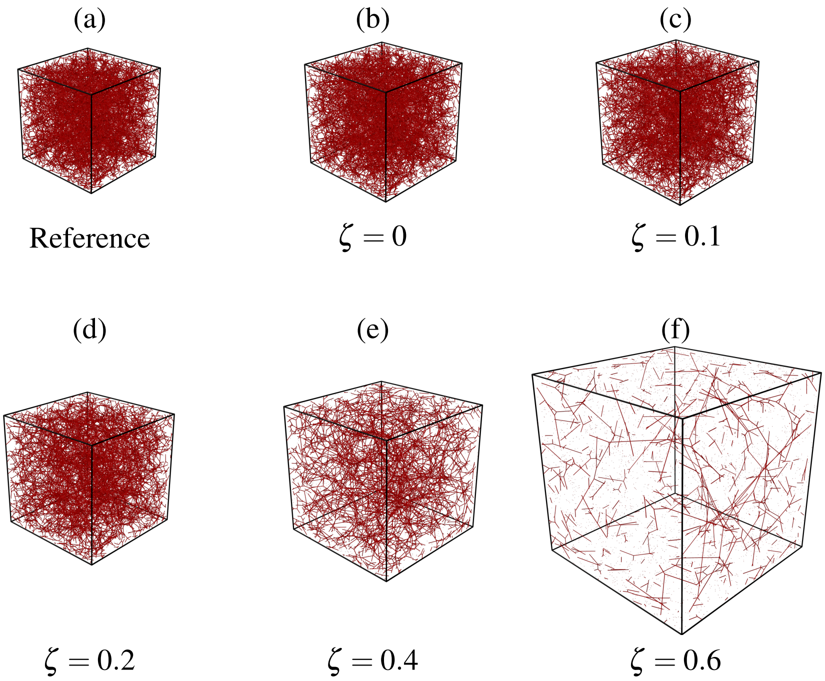

Fig. 5.4: Visualisation of degradation-induced swelling in the absence of applied stress for a network with $a = 0$ and $n_d = 0$. Only the non-broken chains are shown. (a) Reference configuration of the undegraded network. (b) Equilibrium free-swollen state at the onset of degradation ($\zeta = 0$). (c)-(f) Equilibrium free-swollen states at different degradation stages: (c) $\zeta = 0.1$, (d) $\zeta = 0.2$, (e) $\zeta = 0.4$ and (f) $\zeta = 0.6$. The final snapshot represents the state immediately before loss of percolation.

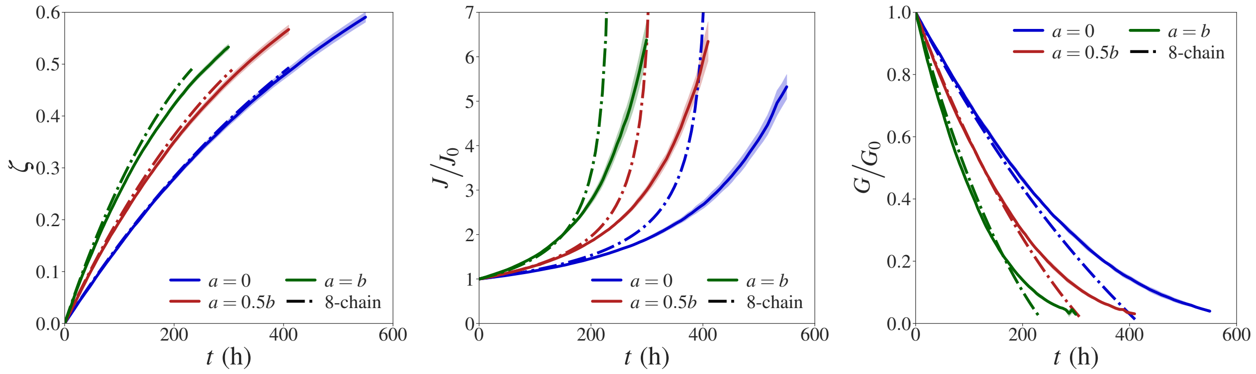

(a) (b) (c)

Fig. 5.5: (a) Normalised number of chain scissions, (b) normalised swelling ratio, and (c) normalised degraded shear modulus as a function of time. Continuous lines represent average DN predictions over 5 repeats, with shaded areas indicating one standard deviation above and below the average. Dashed lines represent predictions of the eight-chain model.

values of the activation length a and $n_d = 0$ (no mass loss). As expected from the kinetic model (5.13), increasing a results in accelerated degradation, noting that chains are always under tension even when the network is subjected to zero stress. The critical value ζ_c at the percolation threshold is in good agreement with classical mean-field estimates: $\zeta_c \approx 0.6$ for diamond lattices (Stauffer and Aharony, 2018), and $\zeta_c \approx 0.66$ for Bethe lattices (Rubinstein and Colby, 2003). Accelerated degradation kinetics in turn gives faster swelling (Fig. 5.5(b)) due the reduction in network elasticity, illustrated in Fig. 5.5(c), according to the Flory-Rehner condition (5.32). Fig. 5.5 also shows the predictions of the continuum model, where we assumed that $\eta = 1 - \zeta$. The performance of the continuum model is mainly limited by its ability to capture the elastic modulus, in particular near the percolation threshold. According to the EMA, the modulus tends to zero for $\zeta = 0.5$, which is significantly lower than the DN value (Fig. 5.5(c)). As a result, the continuum model overestimates the swelling ratio when ζ approaches the percolation threshold (Fig. 5.5(b)). The rate of chain scissions is however well predicted by the continuum model (Fig. 5.5(a)). It is in fact exact in the case $a = 0$ since the KMC algorithm is the discrete counterpart of the continuum kinetic model.

Interestingly, force-biased reaction ($a > 0$) leads to a larger reduction in the elastic modulus compared to the random chain scission case ($a = 0$) at the same degradation state ζ. This effect is shown in Fig. 5.6(a), where the evolution of degraded modulus is represented as a function of ζ. This directly contradicts the EMA (5.30), which assumes that the modulus reduction is one-to-one related to ζ. This additional kinetic effect on the modulus predicted

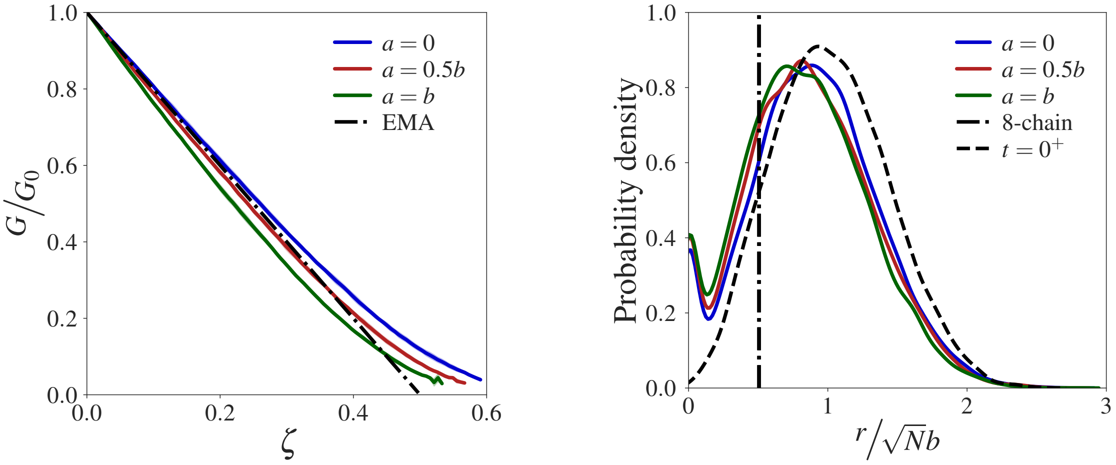

(a) (b)

Fig. 5.6: (a) Normalised shear modulus as a function of the normalised number of chain scissions for different values of a. (b) Probability density of normalised chain end-to-end distance $\frac{r}{\sqrt{N}b}$ in undegraded ($\zeta = 0$) and degraded networks ($\zeta = 0.3$) for different values of activation length a. The chain end-to-end distance predicted using the eight-chain model is shown as a vertical dashed line.

by the DN model can be rationalised as follows. In random networks, the distribution of chain end-to-end distances and chain forces is heterogeneous. According to Eqs (5.20) and (5.22), the highly-stretched chains have a larger contribution to the elastic modulus. When $a > 0$, these highly-stretched chains are also more likely to be cut, therefore leading to a larger drop in modulus. This effect is illustrated in Fig. 5.6(b), which shows the probability distribution of chain end-to-end distance in undegraded ($\zeta = 0$) and degraded networks ($\zeta = 0.3$), for different values of a. As a increases, the distribution of chain end-to-end distances shifts to the left. Thus, force-biased degradation impacts the degradation pathway at the network level, which in turn leads to a reduced elastic modulus for the same number of chain scissions. This effect cannot be predicted by the continuum model, which assumes that all chains experience the same stretch and hence the same force. The effect of kinetics on network degradation is also apparent from the dependence of ζ_c on the activation length a. Close examination of Fig. 5.5 shows that ζ_c decreases as a increases. This suggests that chains experiencing larger forces, and which are degraded preferentially when $a > 0$, are also more critical to the network connectivity. This phenomenon is closely related to the percolation of networks in which links are added or removed with a bias, which is a topic of current research (Spencer and Wormald, 2007; Achlioptas et al., 2009).

We next examine the role of mass loss on degradation-induced swelling, as predicted by the

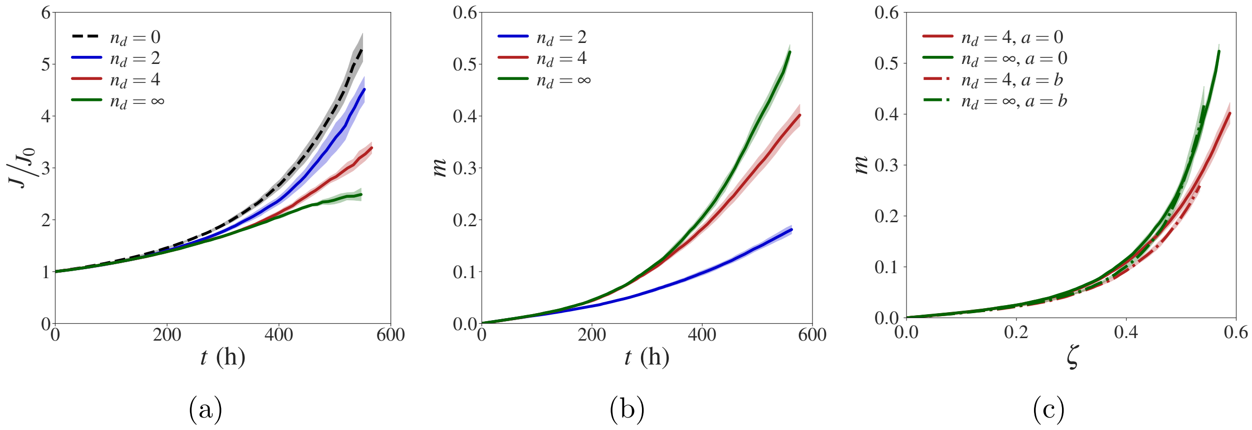

(a) (b) (c)

Fig. 5.7: DN predictions of (a) the normalised swelling ratio and (b) mass loss fraction as a function of time for different critical cluster sizes. The case $n_d = 0$ corresponds to no mass loss, whereas the case $n_d = \infty$ corresponds to the case where clusters of any size can diffuse. (c) DN predictions of the mass loss fraction for $a = 0$ and $a = b$ and two different critical cluster sizes. Lines represent the average DN predictions over 5 repeats, with shaded areas indicating one standard deviation above and below the average.

DN model. Fig. 5.7 shows the evolution of (a) normalised swelling ration J/J_0 and (b) mass loss fraction as a function of time for $a = 0$ and different critical cluster sizes n_d (similar trends are seen for $a > 0$). As expected, increasing n_d results in faster mass loss with no impact on the modulus (results not shown), since only elastically-ineffective clusters are removed. According to the Flory-Rehner condition (5.32), mass loss reduces the amount of swelling. Fig. 5.7(c) shows the mass loss fraction as a function of the normalised number of chain scissions ζ for two different critical cluster sizes and two values of the activation length. Results show that mass loss is largely independent of a for a given number of chain scissions ζ and given cluster size n_d. Note, however, that loss of percolation is reached at a lower value of ζ in the case where $a > 0$, as previously observed in the case where $n_d = 0$.

5.4.2 Constrained degradation

Force-assisted degradation is expected to play a role in scenarios where degradation occurs under applied external forces. To illustrate this, we first consider degradation under a prescribed stretch, as illustrated in Fig. 5.3(b). At $t = 0^+$, the hydrogel is subjected to a uniaxial stretch λ_{1c} and let to swell freely in the two transverse directions to reach the equilibrium swelling ratio J_0. For $t > 0$, the hydrogel degrades while maintaining the applied stretch λ_{1c}. Details of the boundary conditions are given in Section 5.6.2.

Fig. 5.8 shows the time evolution of (a) the normalised number of chain scissions ζ, (b)

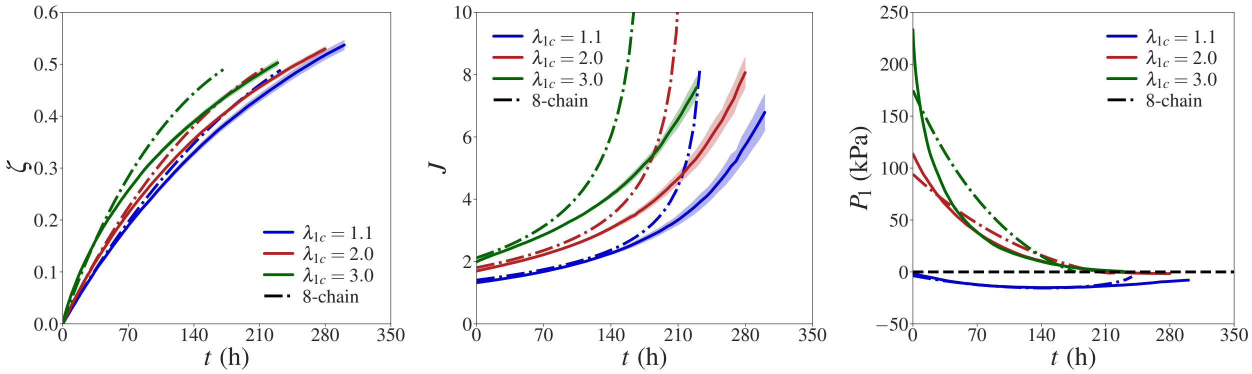

(a) (b) (c)

Fig. 5.8: (a) Normalised number of chain scissions, (b) swelling ratio, and (c) nominal stress P_1 as a function of time. Continuous lines represent the average DN predictions over 5 repeats, with shaded areas indicating one standard deviation above and below the average. Dashed lines represent predictions of the eight-chain model.

the swelling ratio J and (c) the nominal stress P_1 for three different values of the applied pre-stretch λ_{1c}, $a = b$ and no mass loss ($n_d = 0$). DN simulation results show an acceleration of the number of chain scissions with increasing pre-stretch, which directly follows from force-biased reaction kinetics (5.13). Like in the free-degradation case, DN results suggest that the percolation threshold ζ_c decreases with increasing pre-stretch. Accelerated degradation in turn leads to faster swelling and faster stress relaxation as λ_{1c} increases. In the case where $\lambda_{1c} = 1.1$, the evolution of P_1 is non-monotonic, which results from the competition between reduction in elasticity and swelling. The pre-stretch value $\lambda_{1c} = 1.1$ was selected so that is corresponds to the free swelling stretch, i.e. $P_1 = 0$ at $t = 0^+$. As the network starts to degrade under constant stretch λ_{1c}, a compressive state of stress develops since further swelling of the gel is hindered by the applied stretch. However, as degradation progresses, the elasticity of the gel reduces and the stress tends to zero. For $\lambda_{1c} = 2$ and $\lambda_{1c} = 3$, the applied pre-stretch is larger than the free-swelling stretch. Consequently, both degradation-induced swelling and elasticity reduction tend to decrease the stress, and P_1 monotonically relaxes to zero. Fig. 5.8 also shows the predictions of the continuum model. Overall, the continuum model is in good agreement with the DN model at early degradation stages, while deviations become more significant at advanced degradation stages. We conducted the same numerical experiments in the presence of mass loss. Similar to the free degradation case, mass loss does not impact the stress, but hinders swelling (results not shown for brevity). We also found that the activation length no significant impact on mass loss.

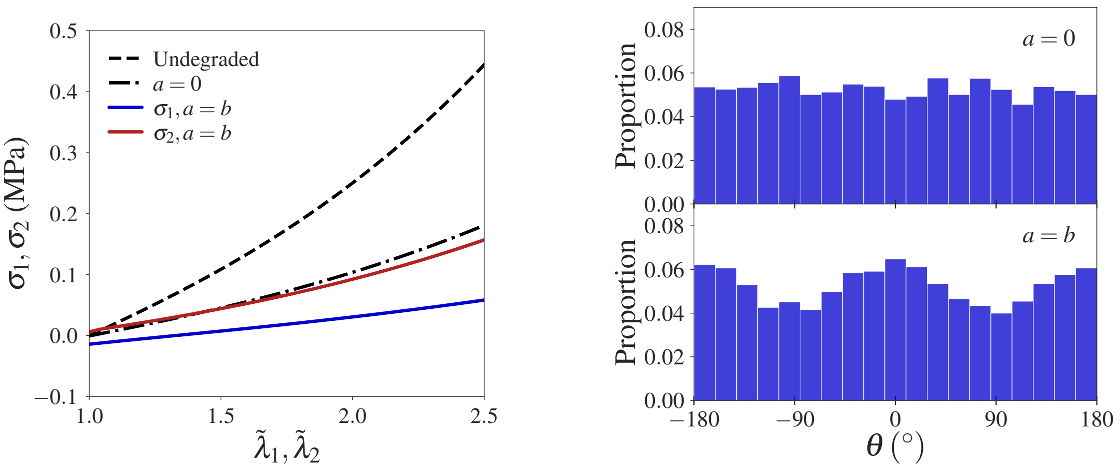

(a) (b)

Fig. 5.9: (a) Stress-stretch curves of a network previously degraded for 80 hours under a constant stretch $\lambda_{1c} = 3$. for $a = b$ and $a = 0$. Stretches $\tilde{\lambda}_i$ are measured relative to the degraded reference configuration. The responses of the undegraded network and that of a network with $a = 0$ and degraded up to the same value of ζ are also shown for comparison. (b) In a spherical coordinate system, the orientation of a chain in the reference configuration can be described by the polar and azimuthal angles (φ, θ). The distribution of θ for the broken chains for $\zeta = 0.3$ and $a = b$ shows that chains aligned with the loading direction ($\theta = 0° \pm 180°$) are preferentially broken, whereas the distribution is uniform for $a = 0$.

Force-biased degradation introduces anisotropy in the elastic properties. Fig. 5.9(a) shows the uniaxial stress-stretch response of networks previously subjected to constrained degradation with $\lambda_{1c} = 3$ for 80 hours, corresponding to $\zeta = 0.3$. Uniaxial tension tests in direction 1 and 2 were performed w.r.t. to the degraded reference configuration. As expected, we observe anisotropy in the elastic response of degraded networks under force-accelerated kinetics in networks with $a = b$, with a softer response in direction 1 compared to direction 2. The figure also shows the response of the undegraded network, as well as that of a network with $a = 0$ and the same extent of degradation, $\zeta = 0.3$, which remains isotropic. The origin of anisotropic behaviour in the case $a = b$ is due to the preferential cutting of chains initially aligned in direction 1, whereas random cutting occurs in the case $a = 0$, see Fig. 5.9(b). In experiments, anisotropic behaviour of the degraded network could be used to probe whether force-assisted degradation occurs or not.

Finally, we consider degradation of a network under under a dead load, as illustrated in Fig. 5.3(c). At $t = 0^+$, the hydrogel is subjected to a constant nominal stress P_0 in direction 1 and let to swell under zero stress in the other two directions. For $t > 0$, the hydrogel degrades under the constant dead load, see Section 5.6.3 for details of boundary conditions. Fig. 5.10

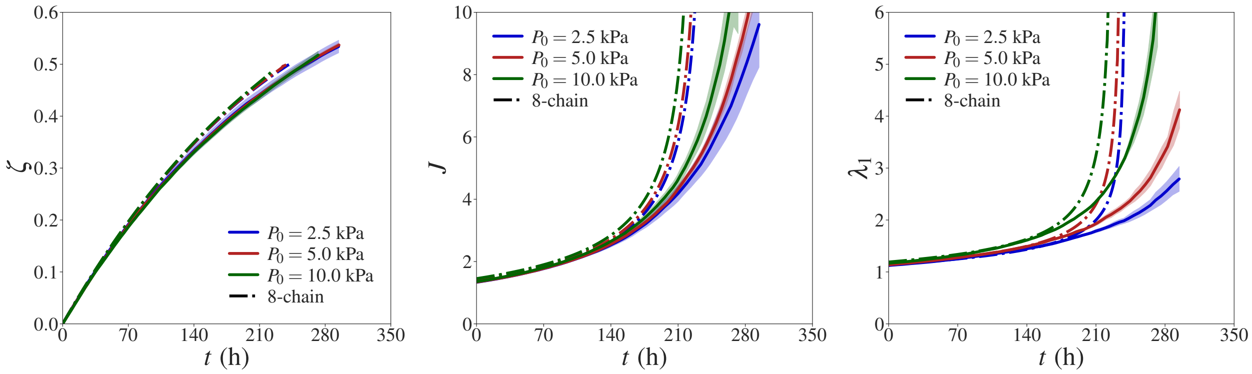

(a) (b) (c)

Fig. 5.10: (a) Normalised number of chain scissions, (b) swelling ratio, and (c) stretch as a function of time. Continuous lines represent the average DN predictions over 5 repeats, with shaded areas indicating one standard deviation above and below the average. Dashed lines represent predictions of the eight-chain model.

shows (a) the normalised number of chain scissions, (b) the swelling ratio J and (c) the stretch λ_1 as a function of time in the case where $a = b$ and different values of the dead load P_0. Mass loss is neglected for simplicity ($n_d = 0$). Note that we used relatively small dead loads, because larger dead load values led to convergence issues in the numerical model. As a result, results in Fig. 5.10(a) show only a slight acceleration in the number of scission events as P_0 increases. However, the results indicate a decrease in the percolation threshold ζ_c with increasing loads, consistent with the previous degradation scenarios analysed. Despite the moderate acceleration in the number of scission events, the swelling ratio J and the stretch λ_1 evolve more rapidly with increasing dead load. Highly-stretched chains contributing the most to the network stiffness are more likely to break when $a > 0$, which in turn impacts the values of λ_1 and J. Predictions of the continuum model are also shown in Fig. 5.10. Like in the previous degradation cases, the continuum model has a good initial agreement with DN results, which is progressively lost as the percolation threshold is approached.

5.5 Conclusions

Force-biased degradation in rubbery networks was simulated in discrete networks using a Kinetic Monte Carlo (KMC) algorithm. By explicitly describing the evolving network structure, discrete networks naturally account for heterogeneous force distribution among the chains, which is turn impacts the local kinetics of chain scission. The discrete network model was also used to simulate mass loss following detachment of chain clusters from the main network. While this work focused on monodisperse network for simplicity, the computational model could be readily extended to polydisperse networks (Araujo et al., 2024a) or double networks (Li et al., 2024). The KMC algorithm could also be generalised to account for multiple reactive bonds along each chain, or for bonds with different reaction rate constants (Beech et al., 2023).

We have used the computational model to investigate the effect of force bias on free and constrained degradation. Key findings of this study are the following:

1. Force-biased reaction kinetics ($a > 0$) leads to a faster reduction in elastic modulus compared to the random case ($a = 0$), which in turn leads to faster swelling.
2. Furthermore, for a given degradation stage (i.e. a given number of chain scissions), the reduction in modulus is more significant in the case of force-biased degradation, because chains bearing larger loads are cut preferentially. Loss of percolation also requires a smaller number of chain scission events with force-biased degradation.
3. Force-biased reaction kinetics induces damage anisotropy when degradation occurs under external loads. We propose that anisotropy in the elastic properties after degradation under loads could be used to experimentally verify whether reaction kinetics is biased by forces or not.

We also developed a simple micromechanics-based continuum model, building on the widely used 8-chain representation (Arruda and Boyce, 1993) combined with a rate-dependent chain scission model following Lavoie et al. (2016). The effect of damage by chain scission on the modulus was captured using an Effective Medium Approximation (Nishi et al., 2012), which holds at early degradation stages (Alamé and Brassart, 2019), but fails to capture reverse gelation. This limitation of the EMA was identified in our previous work (Pan and Brassart, 2022). Advanced models are needed to describe the reduction in modulus with degradation up to the point of reverse gelation, and ideally such models should be micromechanics-based. Better predictions have been obtained based on tree-like theory (Li et al., 2011; Pan and Brassart, 2022), however the micromechanics-basis of these approaches is unclear and therefore they remain largely phenomenological. Another intrinsic limitation of a continuum model based on the eight-chain representation is that it does not account for the heterogeneous chain force distribution. To address this issue, a model that explicitly accounts for the distribution of chain stretches and its evolution during degradation should be adopted, and non-affine localisation rules for the chain stretch should be considered, see e.g. (Vernerey et al., 2018; Diani and Le Tallec, 2019; Mulderrig et al., 2021; Araujo et al., 2024a). The model should also be able to describe anisotropic damage.

5.6 Appendix A: Details of boundary conditions

5.6.1 Free degradation

Degradation-induced swelling of a network under no external loads is illustrated in Fig. 5.3(a). The deformation gradient is of the form $\boldsymbol{F} = \lambda_s \mathbf{1}$, where λ_s is the swelling stretch, and $J = \lambda_s^3$. At time $t = 0^+$, the undegraded network is immersed in a water bath with $\mu = \mu_0$ and instantaneously swells to its equilibrium value, $J = J_0$. As the network degrades ($t > 0$), its elastic modulus decreases and the equilibrium swelling ratio increases. Affine boundary conditions corresponding to the current swelling stretch are applied according to Eq. (5.10). For isotropic, free swelling, $\boldsymbol{\sigma} = \mathbf{0}$ and the network stress is of the form $\boldsymbol{\sigma}^e = \sigma^e \mathbf{1}$. The state law (5.8) identifies the Lagrange multiplier as $\Pi = \sigma^e = \frac{1}{\lambda_s^2} \frac{\partial \psi^e}{\partial \lambda_s}$, which can be calculated for a given value of λ_s from the reaction forces on the DN according to Eq. (5.11). The state law (5.12) provides:

$$0 = k_B T \left[\log(1 - \phi) + \phi + \chi \phi^2 \right] + \Omega \sigma^e, \tag{5.32}$$

where we recall that $(1 - \phi) = \Omega C / J$ and $J = \lambda_s^3$ is related to water concentration (and mass loss fraction) by the incompressibility condition (5.6). At each time step, Eq. (5.32) is solved iteratively for λ_s using the `scipy.optimize` library in Python, adjusting the affine boundary conditions (5.10). Eq. (5.32) is equivalent to the Flory-Rehner model (Flory and Rehner, 1943), according to which equilibrium swelling follows from the balance of elastic and mixing energies. Simulations are interrupted when the percolation criterion is met, corresponding to a critical number of chain scissions ζ_c.

5.6.2 Degradation under a constant stretch

Degradation of a network subjected to a constant stretch is illustrated in Fig. 5.3(b). At $t = 0^+$, the network is subjected to a uniaxial stretch λ_{1c} and let to swell freely in the two transverse directions: $\sigma_2 = \sigma_3 = 0$ to reach the equilibrium swelling ratio J_0. For $t > 0$, the network degrades while maintaining the applied stretch λ_{1c}. The Lagrange multiplier during degradation is obtained from Eq. (5.8): $\sigma_2^e = \Pi$, and the stretches in the transverse directions $\lambda_2 = \lambda_3$ are obtained from the state law (5.12):

$$0 = k_B T \left[\log(1-\phi) + \phi + \chi\phi^2\right] + \Omega\sigma_2^e. \tag{5.33}$$

Similar to the free swelling case, Eq. (5.33) is solved iteratively for the transverse stretches. The true stress in the direction of the applied stretch is given by $\sigma_1 = \sigma_1^e - \Pi = \sigma_1^e - \sigma_2^e$, and the corresponding nominal stress is calculated as:

$$P_1 = \lambda_2^2 \left(\sigma_1^e - \sigma_2^e\right). \tag{5.34}$$

5.6.3 Swelling under a dead load

Degradation-induced swelling of a hydrogel under a dead load is illustrated in Fig. 5.3(c). At $t = 0^+$, the network is subjected to a constant nominal stress P_0 in direction 1 and let to swell under zero stress in other two directions: $\sigma_2 = \sigma_3 = 0$. For $t > 0$, the network degrades under the constant dead load. The equilibrium state of the gel is found by solving the following system of equations:

$$P_0 = \frac{J}{\lambda_1}\left(\sigma_1^e - \Pi\right), \tag{5.35}$$

$$0 = \sigma_2^e - \Pi, \tag{5.36}$$

$$0 = k_B T \left[\ln(1-\phi) + \phi + \chi\phi^2\right] + \Omega\Pi, \tag{5.37}$$

for the three unknowns λ_1, λ_2 and Π.

5.7 Appendix B: Application to tetra-PEG hydrogels

To illustrate the DN modelling framework capability using realistic parameters, we compare its predictions to experimental data for tetra-PEG hydrogels with tunable degradability developed by Li et al. (2011). These gels were formed by the crosslinking in solution of four-arm PEG macromolecules with well-defined arm length, leading to near-ideal network structures (Sakai et al., 2008). Degradability of the hydrogel was achieved by functionalising a given fraction of the tetra-arm precursors with degradable ester bonds. The ester bonds can react with water molecules, causing hydrolytic chain scission. In the experiments, as-prepared hydrogels with different fractions r_{deg} of degradable chains were immersed in a water bath, and let to swell freely as hydrolytic degradation proceeds, and the swelling ratio as a function of time was recorded.

Material parameters used in the DN model were directly obtained from experimental testing conditions whenever possible. The molecular weight of the four-arm precursors was $M_w = 10$ kDa in the experiments, giving $n_m = \frac{M_w}{2M_1} = 113$ PEG monomers per chain (a chain consists of two arms of the four-arm macromolecule precursor), with $M_1 = 44$ g/mol the molar mass of one PEG molecule. The contour length of each chain was estimated as $L_c = n_m l_p$, where $l_p = 0.28$ nm is the projected monomer length in the trans-trans-gauche configuration (Oesterhelt et al., 1999). The Kuhn length of PEG was set to $b = 1.1$ nm (Dittmore et al., 2011), giving the number of Kuhn segments as $N = L_c/b = 29$. The volume per water molecule was set to $\Omega = 3 \times 10^{-29}$ m^3, the temperature was set to $T = 310$ K and the Flory-Huggins interaction parameter was set to $\chi = 0.45$ (Li et al., 2011). To simplify parameter identification, we neglected the effect of force-assisted degradation and set $a = 0$. In fact, it is unclear from the literature whether hydrolytic degradation of ester bonds is activated by force or not (Akbulatov et al., 2013; Wang et al., 2022; Lei et al., 2023). Answering this question is outside the scope of this paper. In the DN simulations, the only fitting parameters were the reaction rate constant k_0 and the critical cluster size for mass loss, n_d.

Perfect random networks were generated with chain density given by:

$$\nu^* = \frac{2\phi_0 \rho N_a}{M_w}, \tag{5.38}$$

where $\rho = 1.12$ g/cm^3 is the density of PEG, $\phi_0 = 0.053$ is the volume fraction of polymer (Li et al., 2011), and N_a is the Avogadro number. The average end-to-end distance between crosslinks in the random network was set to the corresponding distance in a diamond lattice at the same density ν^*, $\langle r_0 \rangle \approx \frac{\sqrt{3}}{4^{1/3}}(\nu^*)^{-1/3}$ (Matsunaga et al., 2009) using our network generation algorithm allowing independent control of chain density and average chain end-to-end distance (Araujo et al., 2024a). Next, connectivity defects were introduced by randomly cutting a fraction $(1-p_0)$ of the chains, with $p_0 = 0.86$ (Li et al., 2011), creating dangling ends. Finally, a fraction r_{deg} of the chains was flagged as degradable. In the equilibrated reference configuration, the average end-to-end distance of the chains was $\langle r_0 \rangle \approx 0.96\sqrt{N}b$.

Degradation-induced swelling was simulated by instantaneously swelling the undegraded network to its equilibrium value under chemical potential $\mu = \mu_0$ at time $t = 0^+$, and then letting the network degrade and swell further for $t > 0$, see Fig. 5.3(a). Fig 5.11(a) shows the normalised swelling ratio $\frac{J}{J_0}$ predicted by the model for tetra-PEG gels with varying fractions of degradable chains r_{deg}, where J_0 is the equilibrium swelling ratio at $t = 0^+$. The reaction constants, fitted for each curve, are listed in Table 5.1, and we set $n_d = 4$ in all simulations. The model generally produces satisfactory predictions at all values of r_{deg}, and the fitted k_0 are all relatively close, consistent with a single reaction mechanism. Simulations were interrupted upon reaching the percolation transition, which occurred before the experimental final degradation time. However, simulations stopped close to the point where the experimental curve sharply increases, which is an indication of reverse gelation in the experiments. Figs. 5.11(b) and (c) respectively show the predicted evolution of the mass loss m and normalised shear modulus $\frac{G}{G_0}$ (experimental data were not reported for these quantities). Overall, model predictions appear reasonable, indicating that gels with a lower fraction of degradable chains display slower mass loss and modulus reduction.

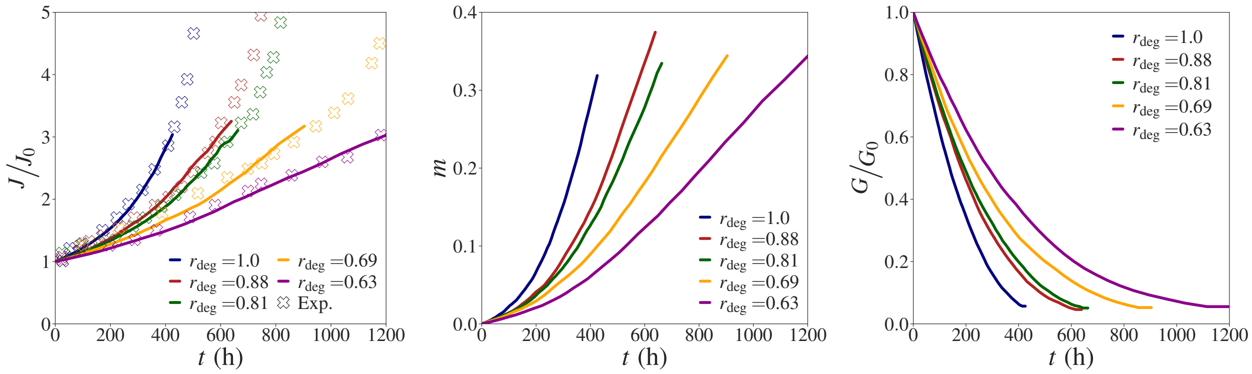

(a) (b) (c)

Fig. 5.11: Degradation behaviour of tetra-PEG hydrogels with different fractions of degradable chains r_{deg}: (a) normalised swelling ratio, (b) mass loss fraction, and (c) normalised degraded shear modulus. Continuous lines represent the average response of five DN simulations, and symbols are experimental data taken from (Li et al., 2011).

Table 5.1: Fitted values of the reaction constant k_0 for different fractions of degradable chains r_{deg}. The average reaction constant over all r_{deg} is $k_0 = 15.1 \times 10^{-4}$ h^{-1}.

Fraction of degradable chains r_{deg}	Reaction constant k_0 (h^{-1})
1.0	16.5×10^{-4}
0.88	14.5×10^{-4}
0.81	15.0×10^{-4}
0.69	15.5×10^{-4}
0.63	14.0×10^{-4}

Chapter 6

Conclusions

6.1 Overview

The central objective of this thesis was the development of a comprehensive micromechanical modelling framework capable of addressing multiple physical scenarios relevant to rubber-like materials. DNs formed the foundation of this framework. By explicitly accounting for the network topology, our DN model enabled a systematic investigation of the relationships between macroscopic response and microstructural features. Moreover, DNs allowed us to access chain-level information during deformation, providing detailed insights into how individual chains respond to macroscopic loading. This information was fundamental for systematically assessing existing continuum semi-analytical models and for extending them to reflect the insights gained from DN simulations.

In Chapter 3, we focused on the elasticity of rubbery networks. Using a newly developed network generation algorithm that allows independent control of chain density and end-to-end distance, we analysed the elastic behaviour of network architectures previously inaccessible to many of the existing network generation techniques. Our results highlight the central role that the initial end-to-end distance distribution plays in the macroscopic response of the network. We further proposed generalised structure-property relationships for the shear modulus and the limit of extensibility of the networks. In a second effort, we used DNs as a tool to benchmark conventional semi-analytical approaches based on the microsphere framework. Discrepancies between discrete and continuum approaches were attributed to two main factors: loss of affinity at large deformation, and the heterogeneous distribution of initial end-to-end distances.

Interestingly, extending the fully-relaxed model to account for the distribution of initial end-to-end distances led to improved agreement with DN results compared to the affine extension. However, a practical limitation of the extended fully-relaxed model is that it requires prior knowledge of this distribution, which is not readily available without DN simulations. A further limitation shared by both extensions is the assumed one-to-one map between chain stretch and initial orientation, which does not hold in DN models.

In Chapter 4, we analysed the mechanical failure of rubbery networks. To that end, chain scission was included in the DN model through a deterministic breaking criterion. With the extended DN platform, we conducted a series of uniaxial tension simulations to elucidate the microscopic mechanisms governing failure. By analysing the evolution of the network topology in key deformation stages, we established a direct link between the catastrophic loss of load-bearing capacity and cascades of scission triggered by force redistribution within spatially localised clusters of highly loaded chains. Our analysis further showed that chain scissions amplify the non-affine effects already observed at larger elongations in the elastic case. We also examined the failure of networks with bimodal distributions of either chain length or chain strength. While the overall failure response of DNs with bimodal chain length distribution resembled that of their monodispersed counterparts, three distinct failure regimes were observed in the bimodal chain strength case. These regimes emerged from the preferential scission of weak chains and the shielding effect provided by strong ones, which delayed the onset of catastrophic failure or prevented it in some cases. A second objective of this study was to evaluate whether semi-analytical models could capture the failure behaviour observed in DN simulations. Notably, these models consistently failed to capture the onset of failure, even in defect-free networks. Improved agreement was obtained by considering the affine and fully-relaxed models enriched with the distribution of initial end-to-end distances. However, fully-damaged states could not be predicted by these extended models.

In Chapter 5, we examined the chemical degradation of rubber-like materials. To that end, we combined our DN framework with a stochastic scission algorithm incorporating force-dependent kinetics. We used hydrogels as a model system, where degradation is accompanied by swelling and mass loss, both of which were included in our model. Our results showed that force-biased chain scission accelerates degradation while amplifying modulus erosion for the same number of scission events. Additionally, fewer scissions were needed to cause loss of percolation under force-biased conditions. Remarkably, degradation-induced anisotropy was observed in networks degrading under loads when scissions were force-biased. Finally, we formulated a simple micromechanics-based model by combining the eight-chain model with a rate-dependent chain scission damage law and a mean-field approach to capture the effect of degradation on the elastic modulus. While the continuum model successfully captured the acceleration of degradation caused by force-dependent kinetics, it could not predict degradation-induced anisotropy because damage was described through a scalar quantity. Moreover, the mean-field approach we used treated the degraded modulus as a function of the scission count alone. In contrast, DN results showed larger modulus reductions for the same number of scission events as force-biased effects increased.

6.2 Scope and limitations

Despite the new insights gained into the mechanics of rubbery networks from a bottom-up perspective, our micromechanical modelling framework also has limitations. In particular, few quantitative comparisons were made between the predictions yielded by our new DN model and experimental data. In fact, this is a general challenge faced by DN approaches (Sugimura et al., 2013; Kothari et al., 2018; Ghareeb and Elbanna, 2020; Alamé and Brassart, 2020; Lei et al., 2021; Britt and Ehret, 2022). A key obstacle to direct validation is the limited knowledge of the actual microstructure of rubber-like materials and the uncertainty over whether synthesis parameters can be reliably used to construct network topologies. For instance, the distribution of initial end-to-end distances, chain density, and distribution of chain lengths are rarely known a priori, yet they are essential inputs in our framework. Although some approximations may be invoked to infer this information from preparation parameters (Rubinstein and Colby, 2003; Mark and Erman, 2007; Wang et al., 2023b), it remains unclear how representative the resulting structures are of real materials. As a result, direct comparison between DN predictions and experimental data is not straightforward. When such attempts are made, they often rely on fitting parameters that lack a clear link to microstructure (Wagner et al., 2022; Araujo and Brassart, 2025a; Lei et al., 2025), or on ad hoc rescalings (Beech et al., 2023; Hartquist et al., 2025b).

Nevertheless, despite the current challenges in direct experimental validation, our DN-based modelling tool offers improvements over previous approaches that may facilitate future experimental comparisons, especially in systems where the microstructure is well controlled. A notable example is tetra-PEG gels, which are often employed as model systems to test theoretical assumptions because of their near-ideal structure with few defects. These gels are synthesised by AB-type crosslink-coupling of star-like macromonomers with well-defined molecular weight, enabling independent tuning of chain density and chain length (Sakai et al., 2008; Akagi et al., 2013; Kondo et al., 2014). Since the initial end-to-end distance of a free chain in solution can be related to its chain length (Rubinstein and Colby, 2003; Sakai, 2020), the new network generation algorithm introduced in this thesis offers a promising tool to investigate microscopic mechanisms underlying the macroscopic response of tetra-PEG gels. Such insights could inform the development of new theoretical assumptions to rationalise experimental trends and serve as a benchmark for existing ones. Moreover, the structure–property relationships obtained from our DN model could provide estimates of the expected properties of gels synthesised with a given set of preparation parameters. Finally, the network generation algorithm could also be adapted to represent rubber-like materials produced by conventional synthesis routes, where chain density and chain length are coupled, such as free-radical polymerisation of hydrogels (Yang et al., 2019a; Kim et al., 2021; Wang et al., 2023b) and random crosslink vulcanisation of elastomers (Treloar, 1973; Mark and Erman, 2007).

6.3 Future research directions

This thesis provided new insights into various aspects of the mechanistic modelling of soft materials. However, several key challenges remain before the framework developed here can be fully representative of real rubbery networks. One major simplification throughout this work was the assumption that the networks are composed of phantom chains, which can interpenetrate freely. In reality, this interpenetration creates entanglements, which have important consequences for the macroscopic response of the network (Doi et al., 1988; Rubinstein and Colby, 2003). Overall, entanglements act as topological constraints restricting the number of accessible conformations to a fluctuating chain. One way to indirectly account for entanglement effects without substantially changing the current DN model is to modify the single chain behaviour through tube models (Doi et al., 1988; Miehe et al., 2004; Darabi and Itskov, 2021; Kumar and Brassart, 2023). The general idea of these models is that the fluctuations of a free chain are confined to a fictitious tube that evolves with chain deformation, leading to an additional contribution to the chain free energy. A more direct alternative is to place slip links at chain intersections, which allow us to explicitly account for entanglements (Assadi et al., 2025). These links fix the spatial position where the chains interpenetrate, while allowing segments to slide through, thus controlling tension transmission and disentanglement. This approach opens a promising path to investigate how entanglements influence viscoelasticity and toughening.

The single chain behaviours we adopted, combined with the phantom chain hypothesis, required initial forces on the boundary nodes to prevent the network from collapsing to a point. These initial forces prevented us from running our mechanical failure simulations until a complete loss of load-bearing capacity (i.e., zero stress) could be achieved. They also hindered our ability to use the DN model for crack propagation problems, as we were unable to create traction-free crack surfaces. Given the network generation technique used in this work, the most promising strategy to solve the collapse problem is to include volumetric contributions to the free energy of the network that penalise local volume changes around the nodes. Lamont et al. (2025) recently proposed an interesting approach in that direction. Inspired by models for cell growth (Barton et al., 2017), these authors used Voronoi tessellation to define cells associated with each node in the network. Accordingly, the volumetric energy contribution is linked to the relative changes in the size of the cells as the network is deformed. An important feature introduced by this idea is that the volumetric interactions between the nodes are not pairwise, unlike the excluded volume potentials used in molecular dynamics. However, this approach would need to be adapted to our purposes, since it has only been tested on relatively small 2D periodic networks.

Many rubber-like materials experience a stress softening process known as the Mullins effect (Mullins, 1948; Diani et al., 2009), in which there is a deterioration of the elastic properties when the material is loaded for the first time. This phenomenon typically manifests as hysteresis in the stress-stretch response under cyclic loading conditions. In multi-network elastomers and hydrogels, the Mullins effect is associated with the breaking of chains in secondary brittle networks (Ducrot et al., 2014; Mai et al., 2019; Zhou et al., 2020). Such hysteresis arising from chain scission could readily be analysed using our DN model in cyclic loading. In contrast, the Mullins effect in carbon-filled rubbers is believed to stem from the debonding of polymer chains from filler particles (Diani et al., 2009; Diaz et al., 2014), leading to an increase in the effective length of the chains. Capturing this damage mechanism within the DN model would require explicitly introducing the filler particles into the network and modelling their interactions with the polymer chains. Incorporating these features would also enable a quantitative assessment of strain amplification effects induced by the fillers (Mullins and Tobin, 1965; Govindjee, 1997; Bergström and Boyce, 1999).

Throughout this thesis, we have consistently shown that microsphere models fail to capture several mechanisms revealed by DN simulations. The simplifying assumptions underlying these models were among the reasons attributed to that. In particular, we showed an intrinsic flaw in the microsphere concept: the assumption of a one-to-one map between chain stretch and its initial orientation does not hold in general. This finding encourages the development of new continuum micromechanics approaches out of the microsphere framework. Britt and Ehret (2022) proposed an interesting approach in which the network free energy is formulated as a power series in the moments of the chain stretch distribution. However, this approach still requires ad hoc assumptions and depends on calibration against a ground-truth model, such as a DN simulation, which may limit its use in practice.

To conclude, while damage-induced anisotropy emerges naturally in microsphere damage models, it proves to be problematic for failure and fracture applications. These models predict a persistent residual elastic energy in some deformation modes, which prevents them from capturing the catastrophic loss of load-bearing capacity observed in DNs and experiments. A general solution grounded in micromechanics that resolves this issue remains an open question. Interestingly, the direction-dependent damage observed in microsphere models is one of the key elements missing from the continuum model for chemical degradation introduced in Chapter 5. However, adopting a microsphere damage model for degradation introduces new challenges. Specifically, the relationship between the degraded modulus and the extent of degradation becomes more complex. Addressing the limitations identified across both mechanical damage and chemical degradation will likely require the development of a new generation of continuum micromechanics models.

Appendix A

Overview of the GitHub code

This appendix presents an overview of the open-source code available on GitHub, published alongside the paper "Araujo, L. M., Kryven, I., and Brassart, L. (2024a). Micromechanical modelling of rubbery networks: The role of chain pre-stretch. *International Journal of Non-Linear Mechanics*, 166:104834". A detailed description of the code is available in the "README.md" file available on GitHub. The code contains two main building blocks: (i) the network generation block, and (ii) the simulation block. In the network generation step, the user defines a set of parameters required to construct the discrete network. These include, for example, the number of nodes, chain density, average end-to-end distance, and the polydispersity distribution. Once generated, the network geometry is saved to a text file, which serves as input for the simulation module.

Before starting the simulation, the user has to specify some simulation parameters. The main ones are the loading type (e.g., uniaxial, biaxial), the chain model (e.g., Gaussian, non-Gaussian), the target stretch, and the size of the stretch increment. The simulation begins with an initial equilibration step, ensuring force balance at every interior node in the reference configuration. The network is then incrementally deformed according to the prescribed loading type and stretch increment size. After each increment, the network is re-equilibrated. If convergence is not achieved during this step, the simulation terminates. Otherwise, the macroscopic stress is computed, and the current macroscopic stretch is compared to the target stretch. The simulation continues until the target stretch is reached or convergence fails. Fig. A.1 shows a summary of the workflow implemented in the code to simulate the elastic response of Discrete Networks.

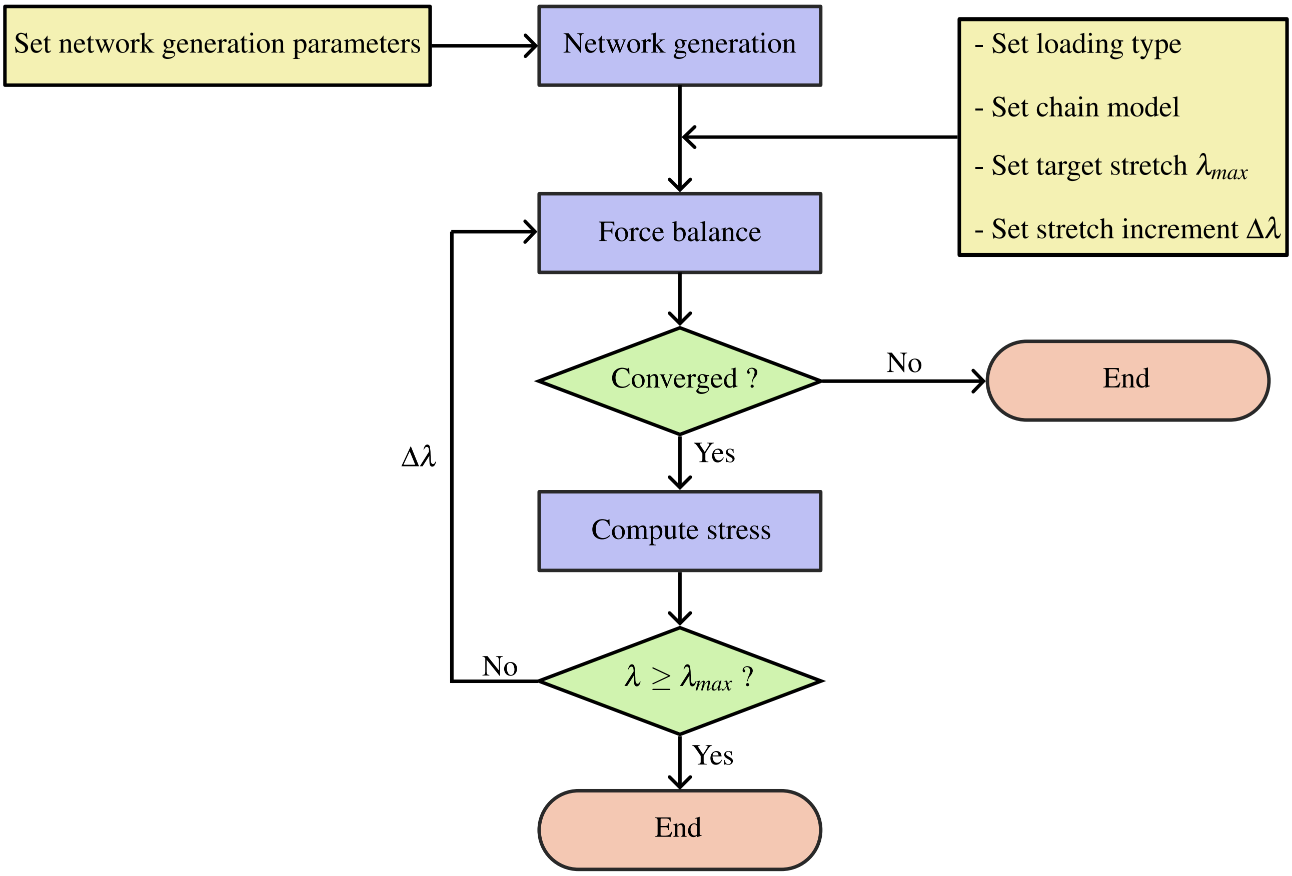

Fig. A.1: Flowchart summarising the main steps in the elastic simulations of Discrete Networks implemented in the open source code available on GitHub.

Bibliography

Achlioptas, D., D'souza, R. M., and Spencer, J. (2009). Explosive percolation in random networks. *Science*, 323(5920):1453–1455.

Akagi, Y., Katashima, T., Sakurai, H., Chung, U. I., and Sakai, T. (2013). Ultimate elongation of polymer gels with controlled network structure. *RSC Advances*, 3(32):13251–13258.

Akbulatov, S., Tian, Y., Kapustin, E., and Boulatov, R. (2013). Model studies of the kinetics of ester hydrolysis under stretching force. *Angewandte Chemie*, 125(27).

Alamé, G. and Brassart, L. (2019). Relative contributions of chain density and topology to the elasticity of two-dimensional polymer networks. *Soft Matter*, 15:5703–5713.

Alamé, G. and Brassart, L. (2020). Effect of topological defects on the elasticity of near-ideal polymer networks. *Journal of Applied Mechanics*, 87:1–10.

Amores, V. J., Nguyen, K., and Montáns, F. J. (2021). On the network orientational affinity assumption in polymers and the micro–macro connection through the chain stretch. *Journal of the Mechanics and Physics of Solids*, 148:104279.

Anand, L. and Govindjee, S. (2020). *Continuum mechanics of solids*. Oxford University Press.

Andia, P., Costanzo, F., and Gray, G. (2005). A lagrangian-based continuum homogenization approach applicable to molecular dynamics simulations. *International Journal of Solids and Structures*, 42(24-25):6409–6432.

Anssari-Benam, A. (2023). Large isotropic elastic deformations: on a comprehensive model to correlate the theory and experiments for incompressible rubber-like materials. *Journal of Elasticity*, 153(2):219–244.

Anssari-Benam, A. and Bucchi, A. (2021). A generalised neo-hookean strain energy function for application to the finite deformation of elastomers. *International Journal of Non-Linear Mechanics*, 128:103626.

Anssari-Benam, A., Bucchi, A., and Saccomandi, G. (2021). On the central role of the invariant i2 in nonlinear elasticity. *International Journal of Engineering Science*, 163:103486.

Anssari-Benam, A. and Hossain, M. (2024). A unified pseudo-elastic model of continuous and discontinuous softening in the finite deformation of isotropic soft solids. *International Journal of Solids and Structures*, 290:112670.

Araujo, L. M. and Brassart, L. (2025a). Force-biased chemical degradation in rubbery networks: Insights from discrete network simulations. *Extreme Mechanics Letters*, 77:102344.

Araujo, L. M. and Brassart, L. (2025b). Micromechanical modelling of failure in rubbery networks: the role of local heterogeneities. Manuscript in preparation.

Araujo, L. M., Kryven, I., and Brassart, L. (2024a). Micromechanical modelling of rubbery networks: The role of chain pre-stretch. *International Journal of Non-Linear Mechanics*, 166:104834.

Araujo, L. M., Kryven, I., and Brassart, L. (2024b). Micromechanical simulations of rubbery networks using LAMMPS. `https://github.com/LucasMangasAraujo/Discrete_Nets`.

Argento, G., Simonet, M., Oomens, C., and Baaijens, F. (2012). Multi-scale mechanical characterization of scaffolds for heart valve tissue engineering. *Journal of Biomechanics*, 45(16):2893–2898.

Arora, A., Lin, T.-S., and Olsen, B. D. (2022). Coarse-grained simulations for fracture of polymer networks: Stress versus topological inhomogeneities. *Macromolecules*, 55(1):4–14.

Arruda, E. M. and Boyce, M. C. (1993). A three-dimensional constitutive model for the large stretch behavior of rubber elastic materials. *Journal of the Mechanics and Physics of Solids*, 41(2):389–412.

Arunachala, P. K., Abrari Vajari, S., Neuner, M., Sim, J. S., Zhao, R., and Linder, C. (2024). A multiscale anisotropic polymer network model coupled with phase field fracture. *International Journal for Numerical Methods in Engineering*, 125(13):e7488.

Arunachala, P. K., Vajari, S. A., Neuner, M., and Linder, C. (2023). A multiscale phase field fracture approach based on the non-affine microsphere model for rubber-like materials. *Computer Methods in Applied Mechanics and Engineering*, 410:115982.

Assadi, S., Lamont, S. C., Hansoge, N., Liu, Z., Crespo-Cuevas, V., Salmon, F., and Vernerey, F. J. (2025). Nonaffine motion and network reorganization in entangled polymer networks. *Soft Matter*, 21(11):2096–2113.

Aydonat, S., Hergesell, A. H., Seitzinger, C. L., Lennarz, R., Chang, G., Sievers, C., Meisner, J., Vollmer, I., and Göstl, R. (2024). Leveraging mechanochemistry for sustainable polymer degradation. *Polymer Journal*, 56(4):249–268.

Bai, R., Yang, J., Morelle, X. P., Yang, C., and Suo, Z. (2018). Fatigue fracture of self-recovery hydrogels. *ACS Macro Letters*, 7(3):312–317.

Barney, C. W., Ye, Z., Sacligil, I., McLeod, K. R., Zhang, H., Tew, G. N., Riggleman, R. A., and Crosby, A. J. (2022). Fracture of model end-linked networks. *Proceedings of the National Academy of Sciences*, 119(7):e2112389119.

Barton, D. L., Henkes, S., Weijer, C. J., and Sknepnek, R. (2017). Active vertex model for cell-resolution description of epithelial tissue mechanics. *PLoS Computational Biology*, 13(6):e1005569.

Beatty, M. F. (2003). An average-stretch full-network model for rubber elasticity. *Journal of Elasticity*, 70:65–86.

Beech, H. K., Wang, S., Sen, D., Rota, D., Kouznetsova, T. B., Arora, A., Rubinstein, M., Craig, S. L., and Olsen, B. D. (2023). Reactivity-guided depercolation processes determine fracture behavior in end-linked polymer networks. *ACS Macro Letters*, 12(12):1685–1691.

Bell, G. I. (1978). Models for the specific adhesion of cells to cells: a theoretical framework for adhesion mediated by reversible bonds between cell surface molecules. *Science*, 200(4342):618–627.

Bensalem, K., Eesaee, M., Hassanipour, M., Elkoun, S., David, E., Agbossou, K., and Nguyen-Tri, P. (2023). Lifetime estimation models and degradation mechanisms of elastomeric materials: a critical review. *Polymer Degradation and Stability*, 220:110644.

Bergström, J. and Boyce, M. (2001). Deformation of elastomeric networks: relation between molecular level deformation and classical statistical mechanics models of rubber elasticity. *Macromolecules*, 34(3):614–626.

Bergström, J. S. and Boyce, M. C. (1999). Mechanical behavior of particle filled elastomers. *Rubber Chemistry and Technology*, 72(4):633–656.

Bershtein, V., Egorova, L., and Solov'ev, V. (1977). Disintegration of polymers by a hydrolytic mechanism. *Polymer Mechanics*, 13(5):715–721.

Bian, C., Cheng, Y., Zhu, W., Tong, R., Hu, M., and Gang, T. (2020). A novel optical fiber mach–zehnder interferometer based on the calcium alginate hydrogel film for humidity sensing. *IEEE Sensors Journal*, 20(11):5759–5765.

Bitzek, E., Koskinen, P., Gähler, F., Moseler, M., and Gumbsch, P. (2006). Structural relaxation made simple. *Physical Review Letters*, 97(17):170201.

Blanco, P. J., Sánchez, P. J., de Souza Neto, E. A., and Feijóo, R. A. (2016). Variational foundations and generalized unified theory of RVE-based multiscale models. *Archives of Computational Methods in Engineering*, 23:191–253.

Boyce, M. C. and Arruda, E. M. (2000). Constitutive models for rubber elasticity: A review. *Rubber Chemistry and Technology*, 73(3):504–523.

Breger, J. C., Yoon, C., Xiao, R., Kwag, H. R., Wang, M. O., Fisher, J. P., Nguyen, T. D., and Gracias, D. H. (2015). Self-folding thermo-magnetically responsive soft microgrippers. *ACS Applied Materials and Interfaces*, 7(5):3398–3405.

Bresolin, F. and Vassoler, J. (2022). A variational full-network framework with anisotropic damage and viscoelasticity induced by deformation. *Journal of the Mechanics and Physics of Solids*, 160:104777.

Britt, B. R. and Ehret, A. E. (2022). Constitutive modelling of fibre networks with stretch distributions. part i: Theory and illustration. *Journal of the Mechanics and Physics of Solids*, 167:104960.

Bryant, S. J. and Vernerey, F. J. (2018). Programmable hydrogels for cell encapsulation and neo-tissue growth to enable personalized tissue engineering. *Advanced Healthcare Materials*, 7(1):1700605.

Buche, M. R. and Silberstein, M. N. (2021). Chain breaking in the statistical mechanical constitutive theory of polymer networks. *Journal of the Mechanics and Physics of Solids*, 156:104593.

Buche, M. R., Silberstein, M. N., and Grutzik, S. J. (2022). Freely jointed chain models with extensible links. *Physical Review E*, 106(2):024502.

Cai, W., Lu, S., Wei, J., and Cui, S. (2019). Single-chain polymer models incorporating the effects of side groups: An approach to general polymer models. *Macromolecules*, 52(19):7324–7330.

Caló, E. and Khutoryanskiy, V. V. (2015). Biomedical applications of hydrogels: A review of patents and commercial products. *European Polymer Journal*, 65:252–267.

Censi, R., Di Martino, P., Vermonden, T., and Hennink, W. E. (2012). Hydrogels for protein delivery in tissue engineering. *Journal of Controlled Release*, 161(2):680–692.

Chester, S. A. and Anand, L. (2010). A coupled theory of fluid permeation and large deformations for elastomeric materials. *Journal of the Mechanics and Physics of Solids*, 58(11):1879–1906.

Cook, R. L. (1986). Stochastic sampling in computer graphics. *ACM Transactions on Graphics*, 5(1):51–72.

Coyle, S., Majidi, C., LeDuc, P., and Hsia, K. J. (2018). Bio-inspired soft robotics: Material selection, actuation, and design. *Extreme Mechanics Letters*, 22:51–59.

Creton, C. and Ciccotti, M. (2016). Fracture and adhesion of soft materials: A review. *Reports on Progress in Physics*, 79(4):046601.

Dal, H., Açıkgöz, K., and Badienia, Y. (2021). On the performance of isotropic hyperelastic constitutive models for rubber-like materials: A state of the art review. *Applied Mechanics Reviews*, 73(2):020802.

Darabi, E. and Itskov, M. (2021). A generalized tube model of rubber elasticity. *Soft Matter*, 17(6):1675–1684.

Dargazany, R. and Itskov, M. (2009). A network evolution model for the anisotropic mullins effect in carbon black filled rubbers. *International Journal of Solids and Structures*, 46(16):2967–2977.

Deng, B., Wang, S., Hartquist, C., and Zhao, X. (2023). Nonlocal intrinsic fracture energy of polymerlike networks. *Physical Review Letters*, 131(22):228102.

Diani, J., Fayolle, B., and Gilormini, P. (2009). A review on the mullins effect. *European Polymer Journal*, 45(3):601–612.

Diani, J. and Le Tallec, P. (2019). A fully equilibrated microsphere model with damage for rubberlike materials. *Journal of the Mechanics and Physics of Solids*, 124:702–713.

Diaz, R., Diani, J., and Gilormini, P. (2014). Physical interpretation of the Mullins softening in a carbon-black filled sbr. *Polymer*, 55(19):4942–4947.

Diederich, V. E., Villiger, T., Storti, G., and Lattuada, M. (2017). Modeling of the degradation of poly (ethylene glycol)-co-(lactic acid)-dimethacrylate hydrogels. *Macromolecules*, 50(14):5527–5538.

Dittmore, A., McIntosh, D. B., Halliday, S., and Saleh, O. A. (2011). Single-molecule elasticity measurements of the onset of excluded volume in poly (ethylene glycol). *Physical Review Letters*, 107(14):148301.

Doi, M., Edwards, S. F., and Edwards, S. F. (1988). *The theory of polymer dynamics*, volume 73. Oxford University Press.

Ducrot, E., Chen, Y., Bulters, M., Sijbesma, R. P., and Creton, C. (2014). Toughening elastomers with sacrificial bonds and watching them break. *Science*, 344(6180):186–189.

Flory, P. J. (1942). Thermodynamics of high polymer solutions. *The Journal of Chemical Physics*, 10(1):51–61.

Flory, P. J. (1976). Statistical thermodynamics of random networks. *Proceedings of the Royal Society of London. A. Mathematical and Physical Sciences*, 351(1666):351–380.

Flory, P. J. (1979). Molecular theory of rubber elasticity. *Polymer*, 20(11):1317–1320.

Flory, P. J. and Rehner, J. (1943). Statistical mechanics of cross-linked polymer networks II. swelling. *The Journal of Chemical Physics*, 11(11):521–526.

Fujiyabu, T., Sakumichi, N., Katashima, T., Liu, C., Mayumi, K., Chung, U. I., and Sakai, T. (2022). Tri-branched gels: Rubbery materials with the lowest branching factor approach the ideal elastic limit. *Science Advances*, 8(14):1–10.

Gent, A. N. (1996). A new constitutive relation for rubber. *Rubber Chemistry and Technology*, 69(1):59–61.

Ghareeb, A. and Elbanna, A. (2020). An adaptive quasicontinuum approach for modeling fracture in networked materials : Application to modeling of polymer networks. *Journal of the Mechanics and Physics of Solids*, 137:103819.

Ghareeb, A. and Elbanna, A. (2021). Modeling fracture in rate-dependent polymer networks: A quasicontinuum approach. *Journal of Applied Mechanics*, 88(11):111007.

Gong, J. P., Katsuyama, Y., Kurokawa, T., and Osada, Y. (2003). Double-network hydrogels with extremely high mechanical strength. *Advanced Materials*, 15(14):1155–1158.

Gong, Z., Zhang, G., Zeng, X., Li, J., Li, G., Huang, W., Sun, R., and Wong, C. (2016). High-strength, tough, fatigue resistant, and self-healing hydrogel based on dual physically cross-linked network. *ACS Applied Materials & Interfaces*, 8(36):24030–24037.

Govindjee, S. (1997). An evaluation of strain amplification concepts via Monte Carlo simulations of an ideal composite. *Rubber Chemistry and Technology*, 70(1):25–37.

Govindjee, S. and Simo, J. (1991). A micro-mechanically based continuum damage model for carbon black-filled rubbers incorporating mullins' effect. *Journal of the Mechanics and Physics of Solids*, 39(1):87–112.

Govindjee, S., Zoller, M. J., and Hackl, K. (2019). A fully-relaxed variationally-consistent framework for inelastic micro-sphere models: Finite viscoelasticity. *Journal of the Mechanics and Physics of Solids*, 127:1–19.

Guo, Q. and Zaïri, F. (2021). A micromechanics-based model for deformation-induced damage and failure in elastomeric media. *International Journal of Plasticity*, 140:102976.

Gurtin, M. E., Fried, E., and Anand, L. (2010). *The mechanics and thermodynamics of continua*. Cambridge University Press.

Gusev, A. A. (2019). Numerical estimates of the topological effects in the elasticity of gaussian polymer networks and their exact theoretical description. *Macromolecules*, 52(9):3244–3251.

Hartquist, C., Wang, S., Cui, Q., Matusik, W., Deng, B., and Zhao, X. (2025a). Scaling law for intrinsic fracture energy of diverse stretchable networks. *Physical Review X*, 15(1):011002.

Hartquist, C. M., Wang, S., Deng, B., Beech, H. K., Craig, S. L., Olsen, B. D., Rubinstein, M., and Zhao, X. (2025b). Fracture of polymer-like networks with hybrid bond strengths. *Journal of the Mechanics and Physics of Solids*, 195:105931.

Hashemi, S. J., Sadooghi, A., Rahmani, K., and Nokhbehroosta, S. (2020). Experimental determining the mechanical and stiffness properties of natural rubber frt triangle elastic joint composite reinforcement by glass fibers and micro/nano particles. *Polymer Testing*, 85:106461.

Hassan, S., Kim, J., and Suo, Z. (2022). Polyacrylamide hydrogels. IV. Near-perfect elasticity and rate-dependent toughness. *Journal of the Mechanics and Physics of Solids*, 158:104675.

Hill, R. (1967). The essential structure of constitutive laws for metal composites and polycrystals. *Journal of the Mechanics and Physics of Solids*, 15(2):79–95.

Holzapfel, G. A. (2002). *Nonlinear solid mechanics: a continuum approach for engineering science*. Kluwer Academic Publishers Dordrecht.

Hong, W., Zhao, X., Zhou, J., and Suo, Z. (2008). A theory of coupled diffusion and large deformation in polymeric gels. *Journal of the Mechanics and Physics of Solids*, 56(5):1779–1793.

Horgan, C. O. (2021). A note on a class of generalized neo-hookean models for isotropic incompressible hyperelastic materials. *International Journal of Non-Linear Mechanics*, 129:103665.

Horkay, F. and Lin, D. C. (2009). Mapping the local osmotic modulus of polymer gels. *Langmuir*, 25(15):8735–8741.

Hosseinzadeh, B. and Ahmadi, M. (2023). Degradable hydrogels: Design mechanisms and versatile applications. *Materials Today Sustainability*, 23:100468.

Huebsch, N., Kearney, C. J., Zhao, X., Kim, J., Cezar, C. A., Suo, Z., and Mooney, D. J. (2014). Ultrasound-triggered disruption and self-healing of reversibly cross-linked hydrogels for drug delivery and enhanced chemotherapy. *Proceedings of the National Academy of Sciences of the United States of America*, 111(27):9762–9767.

Hugel, T., Rief, M., Seitz, M., Gaub, H. E., and Netz, R. R. (2005). Highly stretched single polymers: Atomic-force-microscope experiments versus ab-initio theory. *Physical Review Letters*, 94(4):048301.

Huggins, M. L. (1942). Some properties of solutions of long-chain compounds. *The Journal of Physical Chemistry*, 46(1):151–158.

Ihsan, A. B., Sun, T. L., Kuroda, S., Haque, M. A., Kurokawa, T., Nakajima, T., and Gong, J. P. (2013). A phase diagram of neutral polyampholyte–from solution to tough hydrogel. *Journal of Materials Chemistry B*, 1(36):4555–4562.

Islam, M. and Picu, R. (2018). Effect of network architecture on the mechanical behavior of random fiber networks. *Journal of Applied Mechanics*, 85(8):081011.

Itskov, M. and Knyazeva, A. (2016). A rubber elasticity and softening model based on chain length statistics. *International Journal of Solids and Structures*, 80:512–519.

James, H. M. (1947). Statistical properties of networks of flexible chains. *The Journal of Chemical Physics*, 15(9):651–668.

James, H. M. and Guth, E. (1943). Theory of the elastic properties of rubber. *The Journal of Chemical Physics*, 11(10):455–481.

Ju, J., Sanoja, G. E., Cipelletti, L., Ciccotti, M., Zhu, B., Narita, T., Yuen Hui, C., and Creton, C. (2024). Role of molecular damage in crack initiation mechanisms of tough elastomers. *Proceedings of the National Academy of Sciences*, 121(45):e2410515121.

Kauzmann, W. and Eyring, H. (1940). The viscous flow of large molecules. *Journal of the American Chemical Society*, 62(11):3113–3125.

Kearsley, E. (1989). Strain invariants expressed as average stretches. *Journal of Rheology*, 33(5):757 – 760.

Khiêm, V. N. and Itskov, M. (2016). Analytical network-averaging of the tube model:: Rubber elasticity. *Journal of the Mechanics and Physics of Solids*, 95:254–269.

Khiêm, V. N., Mai, T.-T., Urayama, K., Gong, J. P., and Itskov, M. (2019). A multiaxial theory of double network hydrogels. *Macromolecules*, 52(15):5937–5947.

Kim, D. W., Medvedev, G. A., Caruthers, J. M., Jo, J. Y., Won, Y.-Y., and Kim, J. (2020). Enhancement of mechano-sensitivity for spiropyran-linked poly (dimethylsiloxane) via solvent swelling. *Macromolecules*, 53(18):7954–7961.

Kim, J., Yin, T., and Suo, Z. (2022). Polyacrylamide hydrogels. V. some strands in a polymer network bear loads, but all strands contribute to swelling. *Journal of the Mechanics and Physics of Solids*, 168:105017.

Kim, J., Zhang, G., Shi, M., and Suo, Z. (2021). Fracture, fatigue, and friction of polymers in which entanglements greatly outnumber cross-links. *Science*, 374(6564):212–216.

Kondo, S., Chung, U.-i., and Sakai, T. (2014). Effect of prepolymer architecture on the network structure formed by ab-type crosslink-coupling. *Polymer Journal*, 46(1):14–20.

Kondo, S., Sakurai, H., Chung, U.-i., and Sakai, T. (2013). Mechanical properties of polymer gels with bimodal distribution in strand length. *Macromolecules*, 46(17):7027–7033.

Kothari, K., Hu, Y., Gupta, S., and Elbanna, A. (2018). Mechanical Response of Two-Dimensional Polymer Networks: Role of Topology, Rate Dependence, and Damage Accumulation. *Journal of Applied Mechanics, Transactions ASME*, 85(3):031008.

Kouznetsova, V. (2002). *Computational homogenization for the multi-scale analysis of multi-phase materials*. Phd thesis, Eindhoven University of Technology.

Kryven, I. (2022). Generation of random networks with controlled edge length distribution and degrees. `https://github.com/ikryven/geometric_graph`.

Kryven, I. and Versendaal, R. (2022). Sequential construction of spatial networks with arbitrary degree sequence and edge length distribution. *Preprint: arXiv:2207.08527*.

Kuhl, E. and Goriely, A. (2024). I too i2: A new class of hyperelastic isotropic incompressible models based solely on the second invariant. *Journal of the Mechanics and Physics of Solids*, 188:105670.

Kuhn, W. and Grün, F. (1946). Statistical behavior of the single chain molecule and its relation to the statistical behavior of assemblies consisting of many chain molecules. *Journal of Polymer Science*, 1(3):183–199.

Kumar, G. and Brassart, L. (2023). On tube models of rubber elasticity: fitting performance in relation to sensitivity to the invariant I2. *Mechanics of Soft Materials*, 5(1):6.

Lake, G. J. and Thomas, A. G. (1967). The strength of highly elastic materials. *Proceedings of the Royal Society of London. Series A. Mathematical and Physical Sciences*, 300(1460):108–119.

Lamont, S. C., Bouklas, N., and Vernerey, F. J. (2025). Cohesive instability in elastomers: insights from a crosslinked van der waals fluid model. *International Journal of Fracture*, 249(1):20.

Lamont, S. C., Mulderrig, J., Bouklas, N., and Vernerey, F. J. (2021). Rate-Dependent Damage Mechanics of Polymer Networks with Reversible Bonds. *Macromolecules*, 54(23):10801–10813.

Lavoie, S. R., Long, R., and Tang, T. (2016). A rate-dependent damage model for elastomers at large strain. *Extreme Mechanics Letters*, 8:114–124.

Lavoie, S. R., Long, R., and Tang, T. (2020). Modeling the mechanics of polymer chains with deformable and active bonds. *The Journal of Physical Chemistry B*, 124(1):253–265.

Lavoie, S. R. and Suo, Z. (2024). Flaw sensitivity of stochastic elastic materials. *Mathematics and Mechanics of Solids*, 29(6):1228–1238.

Lee, C. K., Diesendruck, C. E., Lu, E., Pickett, A. N., May, P. A., Moore, J. S., and Braun, P. V. (2014). Solvent swelling activation of a mechanophore in a polymer network. *Macromolecules*, 47(8):2690–2694.

Lee, H.-R., Kim, C.-C., and Sun, J.-Y. (2018). Stretchable ionics–a promising candidate for upcoming wearable devices. *Advanced Materials*, 30(42):1704403.

Lei, H., Ma, Q., Wang, Z., Zhang, D., Huang, X., Qin, M., Ma, H., Wang, W., and Cao, Y. (2023). Ester bond: chemically labile yet mechanically stable. *ACS nano*, 17(17):16870–16878.

Lei, J., Gao, Y., Xu, S., He, L., and Liu, Z. (2025). The effect of the effective polymer network on the extremely large deformation and fracture behaviors of polyacrylamide hydrogels. *Journal of the Mechanics and Physics of Solids*, 200:106124.

Lei, J., Li, Z., Xu, S., and Liu, Z. (2021). A mesoscopic network mechanics method to reproduce the large deformation and fracture process of cross-linked elastomers. *Journal of the Mechanics and Physics of Solids*, 156:104599.

Lei, J. and Liu, Z. (2022). A network mechanics method to study the mechanism of the large-deformation fracture of elastomers. *Journal of Applied Physics*, 132(13):135101.

Li, B. and Bouklas, N. (2020). A variational phase-field model for brittle fracture in polydisperse elastomer networks. *International Journal of Solids and Structures*, 182-183:193–204.

Li, H., Lei, J., Wang, D., and Liu, Z. (2024). The fracture and toughening mechanism of double-network hydrogel using the network mechanics method. *Engineering Fracture Mechanics*, 309:110413.

Li, X. and Gong, J. P. (2024). Design principles for strong and tough hydrogels. *Nature Reviews Materials*, 9(6):380–398.

Li, X., Tsutsui, Y., Matsunaga, T., Shibayama, M., Chung, U.-i., and Sakai, T. (2011). Precise control and prediction of hydrogel degradation behavior. *Macromolecules*, 44(9):3567–3571.

Li, Z. and Liu, Z. (2020). The elongation-criterion for fracture toughness of hydrogels based on percolation model. *Journal of Applied Physics*, 127(21):215101.

Lin, S. and Zhao, X. (2020). Fracture of polymer networks with diverse topological defects. *Physical Review E*, 102(5):052503.

Lin, T.-S., Wang, R., Johnson, J. A., and Olsen, B. D. (2019). Revisiting the elasticity theory for real gaussian phantom networks. *Macromolecules*, 52(4):1685–1694.

Lloyd, E. M., Vakil, J. R., Yao, Y., Sottos, N. R., and Craig, S. L. (2023). Covalent mechanochemistry and contemporary polymer network chemistry: A marriage in the making. *Journal of the American Chemical Society*, 145(2):751–768.

Lu, W., Wang, C., Zhou, Z., Xu, S., and Liu, Z. (2025). Quantify the failure zone and elastic release zone: A new insight into intrinsic fracture of polymer networks. *Extreme Mechanics Letters*, (78):102362.

Lyu, S. and Untereker, D. (2009). Degradability of polymers for implantable biomedical devices. *International Journal of Molecular Sciences*, 10(9):4033–4065.

Mai, T. T., Matsuda, T., Nakajima, T., Gong, J. P., and Urayama, K. (2019). Damage cross-effect and anisotropy in tough double network hydrogels revealed by biaxial stretching. *Soft Matter*, 15(18):3719–3722.

Manikkavel, A., Kumar, V., and Lee, D.-J. (2020). Simple fracture model for an electrode and interfacial crack in a dielectric elastomer under tensile loading. *Theoretical and Applied Fracture Mechanics*, 108:102626.

Mao, Y. and Anand, L. (2018). A theory for fracture of polymeric gels. *Journal of the Mechanics and Physics of Solids*, 115:30–53.

Mao, Y., Talamini, B., and Anand, L. (2017). Rupture of polymers by chain scission. *Extreme Mechanics Letters*, 13:17–24.

Mark, J. E. and Erman, B. (2007). *Rubberlike elasticity: a molecular primer*. Cambridge University Press.

Mars, W. and Fatemi, A. (2002). A literature survey on fatigue analysis approaches for rubber. *International Journal of Fatigue*, 24(9):949–961.

Masuda, F. (1994). Trends in the development of superabsorbent polymers for diapers. ACS Publications.

Matsunaga, T., Sakai, T., Akagi, Y., Chung, U. I., and Shibayama, M. (2009). Structure characterization of Tetra-PEG gel by small-angle neutron scattering. *Macromolecules*, 42(4):1344–1351.

Merino, S., Martín, C., Kostarelos, K., Prato, M., and Vázquez, E. (2015). Nanocomposite hydrogels: 3d polymer–nanoparticle synergies for on-demand drug delivery. *ACS nano*, 9(5):4686–4697.

Metze, F. K., Sant, S., Meng, Z., Klok, H.-A., and Kaur, K. (2023). Swelling-activated, soft mechanochemistry in polymer materials. *Langmuir*, 39(10):3546–3557.

Miehe, C. and Göktepe, S. (2005). A micro–macro approach to rubber-like materials. Part II: the micro-sphere model of finite rubber viscoelasticity. *Journal of the Mechanics and Physics of Solids*, 53(10):2231–2258.

Miehe, C., Göktepe, S., and Lulei, F. (2004). A micro-macro approach to rubber-like materials – Part I: the non-affine micro-sphere model of rubber elasticity. *Journal of the Mechanics and Physics of Solids*, 52(11):2617–2660.

Miehe, C., Hofacker, M., and Welschinger, F. (2010). A phase field model for rate-independent crack propagation: Robust algorithmic implementation based on operator splits. *Computer Methods in Applied Mechanics and Engineering*, 199(45-48):2765–2778.

Mooney, M. (1940). A theory of large elastic deformation. *Journal of Applied Physics*, 11(9):582–592.

Mousavi, S. M., Mulderrig, J., Talamini, B., and Bouklas, N. (2025). A chain stretch-based gradient-enhanced model for damage and fracture in elastomers. *Computer Methods in Applied Mechanics and Engineering*, 444:118103.

Mulderrig, J., Li, B., and Bouklas, N. (2021). Mechanics of Materials Affine and non-affine microsphere models for chain scission in polydisperse elastomer networks. *Mechanics of Materials*, 160:103857.

Mulderrig, J., Talamini, B., and Bouklas, N. (2023). A statistical mechanics framework for polymer chain scission, based on the concepts of distorted bond potential and asymptotic matching. *Journal of the Mechanics and Physics of Solids*, 174:105244.

Mullins, L. (1948). Effect of stretching on the properties of rubber. *Rubber chemistry and technology*, 21(2):281–300.

Mullins, L. (1969). Softening of rubber by deformation. *Rubber Chemistry and Technology*, 42(1):339–362.

Mullins, L. and Tobin, N. (1965). Stress softening in rubber vulcanizates. Part I. Use of a strain amplification factor to describe the elastic behavior of filler-reinforced vulcanized rubber. *Journal of Applied Polymer Science*, 9(9):2993–3009.

Nian, G., Chen, Z., Bao, X., Tan, M. W. M., Kutsovsky, Y., and Suo, Z. (2025). Natural rubber with high resistance to crack growth. *Nature Sustainability*, 8:1–10.

Nishi, K., Chijiishi, M., Katsumoto, Y., Nakao, T., Fujii, K., Chung, U.-i., Noguchi, H., Sakai, T., and Shibayama, M. (2012). Rubber elasticity for incomplete polymer networks. *The Journal of Chemical Physics*, 137(22).

Nishi, K., Fujii, K., Chung, U.-i., Shibayama, M., and Sakai, T. (2017). Experimental observation of two features unexpected from the classical theories of rubber elasticity. *Physical Review Letters*, 119(26):267801.

Noll, W., Coleman, B. D., and Noll, W. (1974). The thermodynamics of elastic materials with heat conduction and viscosity. *The Foundations of Mechanics and Thermodynamics: Selected Papers*, pages 145–156.

Nonoyama, T. and Gong, J. P. (2021). Tough double network hydrogel and its biomedical applications. *Annual Review of Chemical and Biomolecular Engineering*, (1):393–410.

Oesterhelt, F., Rief, M., and Gaub, H. (1999). Single molecule force spectroscopy by afm indicates helical structure of poly (ethylene-glycol) in water. *New Journal of Physics*, 1(1):6.

Ogden, R. W. (1972). Large deformation isotropic elasticity–on the correlation of theory and experiment for incompressible rubberlike solids. *Proceedings of the Royal Society of London. A. Mathematical and Physical Sciences*, 326(1567):565–584.

Ogden, R. W., Saccomandi, G., and Sgura, I. (2004). Fitting hyperelastic models to experimental data. *Computational Mechanics*, 34:484–502.

Ogouari, L., Guo, Q., Zaïri, F., Mai, T. T., Gong, J. P., and Urayama, K. (2024a). A multiscale model for the multiaxial anisotropic damage of double-network gels. *Mechanics of Materials*, 196:105058.

Ogouari, L., Guo, Q., Zaïri, F., Mai, T. T., and Urayama, K. (2024b). An anisotropic damage visco-hyperelastic model for multiaxial stress-strain response and energy dissipation in filled rubber. *International Journal of Plasticity*, 182:104111.

Pal, K., Pal, S. K., Das, C. K., and Kim, J. K. (2011). Elastomeric nanocomposites for tyre applications. In *Recent Advances in Elastomeric Nanocomposites*, pages 201–231. Springer.

Pan, Z. and Brassart, L. (2022). Constitutive modelling of hydrolytic degradation in hydrogels. *Journal of the Mechanics and Physics of Solids*, 167:105016.

Patel, H., Salehi, S., Ahmed, R., and Teodoriu, C. (2019). Review of elastomer seal assemblies in oil gas wells: Performance evaluation, failure mechanisms, and gaps in industry standards. *Journal of Petroleum Science and Engineering*, 179:1046–1062.

Peleg, O., Peters, J. M., Salcedo, M. K., and Mahadevan, L. (2018). Collective mechanical adaptation of honeybee swarms. *Nature Physics*, 14(12):1193–1198.

Qari, N. and Cai, S. (2024). Stress-assisted erosion of poly (glycerol-co-sebacate) acrylate elastomer. *Macromolecular Chemistry and Physics*, 225(4):2300268.

Reuß, A. (1929). Berechnung der fließgrenze von mischkristallen auf grund der plastizitätsbedingung für einkristalle. *ZAMM-Journal of Applied Mathematics and Mechanics/Zeitschrift für Angewandte Mathematik und Mechanik*, 9(1):49–58.

Ribas-Arino, J. and Marx, D. (2012). Covalent mechanochemistry: theoretical concepts and computational tools with applications to molecular nanomechanics. *Chemical Reviews*, 112(10):5412–5487.

Rivlin, R. S. (1948). Large elastic deformations of isotropic materials IV. further developments of the general theory. *Philosophical Transactions of the Royal Society of London. Series A, Mathematical and Physical Sciences*, 241(835):379–397.

Rivlin, R. S. and Saunders, D. (1951). Large elastic deformations of isotropic materials VII. experiments on the deformation of rubber. *Philosophical Transactions of the Royal Society of London. Series A, Mathematical and Physical Sciences*, 243(865):251–288.

Rubinstein, M. and Colby, R. H. (2003). *Polymer physics.* Oxford University Press.

Sakai, T. (2020). *Physics of polymer gels.* John Wiley & Sons.

Sakai, T., Matsunaga, T., Yamamoto, Y., Ito, C., Yoshida, R., Suzuki, S., Sasaki, N., Shibayama, M., and Chung, U. I. (2008). Design and fabrication of a high-strength hydrogel with ideally homogeneous network structure from tetrahedron-like macromonomers. *Macromolecules*, 41(14):5379–5384.

Shariff, M. (2014). Direction dependent orthotropic model for Mullins materials. *International Journal of Solids and Structures*, 51(25-26):4357–4372.

Smith, S. B., Cui, Y., and Bustamante, C. (1996). Overstretching B-DNA: the elastic response of individual double-stranded and single-stranded dna molecules. *Science*, 271(5250):795–799.

Sorichetti, V., Ninarello, A., Ruiz-Franco, J. M., Hugouvieux, V., Kob, W., Zaccarelli, E., and Rovigatti, L. (2021). Effect of Chain Polydispersity on the Elasticity of Disordered Polymer Networks. *Macromolecules*, 54(8):3769–3779.

Spencer, J. and Wormald, N. (2007). Birth control for giants. *Combinatorica*, 27:587–628.

Stauffer, D. and Aharony, A. (2018). *Introduction to percolation theory.* Taylor & Francis.

Sugimura, A., Asai, M., Matsunaga, T., Akagi, Y., Sakai, T., Noguchi, H., and Shibayama, M. (2013). Mechanical properties of a polymer network of Tetra-PEG gel. 45(3):300–306.

Sun, J. Y., Zhao, X., Illeperuma, W. R., Chaudhuri, O., Oh, K. H., Mooney, D. J., Vlassak, J. J., and Suo, Z. (2012). Highly stretchable and tough hydrogels. *Nature*, 489:133–136.

Tabuteau, H., Mora, S., Porte, G., Abkarian, M., and Ligoure, C. (2009). Microscopic mechanisms of the brittleness of viscoelastic fluids. *Physical Review Letters*, 102(15):155501.

Talamini, B., Mao, Y., and Anand, L. (2018). Progressive damage and rupture in polymers. *Journal of the Mechanics and Physics of Solids*, 111:434–457.

Thompson, A. P., Aktulga, H. M., Berger, R., Bolintineanu, D. S., Brown, W. M., Crozier, P. S., in 't Veld, P. J., Kohlmeyer, A., Moore, S. G., Nguyen, T. D., Shan, R., Stevens, M. J., Tranchida, J., Trott, C., and Plimpton, S. J. (2022). LAMMPS - a flexible simulation tool for particle-based materials modeling at the atomic, meso, and continuum scales. *Computer Physics Communications*, 271:108171.

Tkachuk, M. and Linder, C. (2012). The maximal advance path constraint for the homogenization of materials with random network microstructure. *Philosophical Magazine*, 92(22):2779–2808.

Treloar, L. (1954). The photoelastic properties of short-chain molecular networks. *Transactions of the Faraday Society*, 50:881–896.

Treloar, L. G. (1973). *The physics of rubber elasticity.* Oxford University Press.

Turner, B., Ramesh, S., Menegatti, S., and Daniele, M. (2022). Resorbable elastomers for implantable medical devices: highlights and applications. *Polymer International*, 71(5):552–561.

Valanis, K. and Landel, R. F. (1967). The strain-energy function of a hyperelastic material in terms of the extension ratios. *Journal of Applied Physics*, 38(7):2997–3002.

Vernerey, F. J., Brighenti, R., Long, R., and Shen, T. (2018). Statistical Damage Mechanics of Polymer Networks. *Macromolecules*, 51(17):6609–6622.

Verron, E. and Gros, A. (2017). An equal force theory for network models of soft materials with arbitrary molecular weight distribution. *Journal of the Mechanics and Physics of Solids*, 106:176–190.

Voigt, W. (1889). Ueber die beziehung zwischen den beiden elasticitätsconstanten isotroper körper. *Annalen der Physik*, 274(12):573–587.

Voter, A. F. (2007). Introduction to the kinetic Monte Carlo method. In *Radiation effects in solids*, pages 1–23. Springer.

Wagner, R. J., Dai, J., Su, X., and Vernerey, F. J. (2022). A mesoscale model for the micromechanical study of gels. *Journal of the Mechanics and Physics of Solids*, 167:104982.

Wagner, R. J., Hobbs, E., and Vernerey, F. J. (2021). A network model of transient polymers: Exploring the micromechanics of nonlinear viscoelasticity. *Soft Matter*, 17(38):8742–8757.

Wagner, R. J., Lamont, S. C., White, Z. T., and Vernerey, F. J. (2024). Catch bond kinetics are instrumental to cohesion of fire ant rafts under load. *Proceedings of the National Academy of Sciences*, 121(17):e2314772121.

Wagner, R. J. and Silberstein, M. N. (2025). A foundational framework for the mesoscale modeling of dynamic elastomers and gels. *Journal of the Mechanics and Physics of Solids*, 194:105914.

Wagner, R. J. and Vernerey, F. J. (2023). Coupled bond dynamics alters relaxation in polymers with multiple intrinsic dissociation rates. *Soft Matter*, 19(15):2716–2725.

Wang, J., Gao, X., Boarino, A., Célerse, F., Corminboeuf, C., and Klok, H.-A. (2022). Mechanical acceleration of ester bond hydrolysis in polymers. *Macromolecules*, 55(22):10145–10152.

Wang, M. C. and Guth, E. (1952). Statistical theory of networks of non-gaussian flexible chains. *The Journal of Chemical Physics*, 20(7):1144–1157.

Wang, Q., Gossweiler, G. R., Craig, S. L., and Zhao, X. (2015). Mechanics of mechanochemically responsive elastomers. *Journal of the Mechanics and Physics of Solids*, 82:320–344.

Wang, R., Li, J., Chen, W., Xu, T., Yun, S., Xu, Z., Xu, Z., Sato, T., Chi, B., and Xu, H. (2017). A biomimetic mussel-inspired -poly-l-lysine hydrogel with robust tissue-anchor and anti-infection capacity. *Advanced Functional Materials*, 27(8):1604894.

Wang, S., Beech, H. K., Bowser, B. H., Kouznetsova, T. B., Olsen, B. D., Rubinstein, M., and Craig, S. L. (2021). Mechanism dictates mechanics: a molecular substituent effect in the macroscopic fracture of a covalent polymer network. *Journal of the American Chemical Society*, 143(10):3714–3718.

Wang, S., Hu, Y., Kouznetsova, T. B., Sapir, L., Chen, D., Herzog-Arbeitman, A., Johnson, J. A., Rubinstein, M., and Craig, S. L. (2023a). Facile mechanochemical cycloreversion of polymer cross-linkers enhances tear resistance. *Science*, 380(6651):1248–1252.

Wang, S., Panyukov, S., Rubinstein, M., and Craig, S. L. (2019). Quantitative adjustment to the molecular energy parameter in the lake–thomas theory of polymer fracture energy. *Macromolecules*, 52(7):2772–2777.

Wang, S.-Q. and Fan, Z. (2023). Investigating the dependence of elastomeric fracture on temperature and rate. *Rubber Chemistry and Technology*, 96(4):530–550.

Wang, S.-Q., Fan, Z., Siavoshani, A., Wang, M.-c., and Wang, J. (2024). Fresh considerations regarding time-dependent elastomeric fracture. *Extreme Mechanics Letters*, 74:102277.

Wang, Y., Nian, G., Kim, J., and Suo, Z. (2023b). Polyacrylamide hydrogels. vi. synthesis-property relation. *Journal of the Mechanics and Physics of Solids*, 170:105099.

Wang, Z. J. and Gong, J. P. (2025). Mechanochemistry for on-demand polymer network materials. *Macromolecules*, 58(1):4–17.

Weiner, J. H. (2012). *Statistical mechanics of elasticity.* Courier Corporation.

Wineman, A. (2005). Some results for generalized neo-hookean elastic materials. *International Journal of Non-Linear Mechanics*, 40(2):271–279.

Wu, P. and Van Der Giessen, E. (1993). On improved network models for rubber elasticity and their applications to orientation hardening in glassy polymers. *Journal of the Mechanics and Physics of Solids*, 41(3):427–456.

Xue, X., Hu, Y., Deng, Y., and Su, J. (2021). Recent advances in design of functional biocompatible hydrogels for bone tissue engineering. *Advanced Functional Materials*, 31(19):2009432.

Yang, C., Yin, T., and Suo, Z. (2019a). Polyacrylamide hydrogels. I. Network imperfection. *Journal of the Mechanics and Physics of Solids*, 131:43–55.

Yang, X., Yang, J., Chen, L., and Suo, Z. (2019b). Hydrolytic crack in a rubbery network. *Extreme Mechanics Letters*, 31:100531.

Yeoh, O. (1997). Hyperelastic material models for finite element analysis of rubber. *Journal of Natural Rubber Research*, 12(1997):142–153.

Zhan, L., Wang, S., Qu, S., Steinmann, P., and Xiao, R. (2023). A new micro–macro transition for hyperelastic materials. *Journal of the Mechanics and Physics of Solids*, 171(November 2022):105156.

Zhang, H. J., Sun, T. L., Zhang, A. K., Ikura, Y., Nakajima, T., Nonoyama, T., Kurokawa, T., Ito, O., Ishitobi, H., and Gong, J. P. (2016). Tough physical double-network hydrogels based on amphiphilic triblock copolymers. *Advanced Materials*, 28(24):4884–4890.

Zhao, X., Chen, X., Yuk, H., Lin, S., Liu, X., and Parada, G. (2021). Soft materials by design: unconventional polymer networks give extreme properties. *Chemical Reviews*, 121(8):4309–4372.

Zhong, D., Wang, Z., Xu, J., Liu, J., Xiao, R., Qu, S., and Yang, W. (2024). A strategy for tough and fatigue-resistant hydrogels via loose cross-linking and dense dehydration-induced entanglements. *Nature Communications*, 15(1):1–12.

Zhou, Y., Zhang, W., Hu, J., Tang, J., Jin, C., Suo, Z., and Lu, T. (2020). The stiffness-threshold conflict in polymer networks and a resolution. *Journal of Applied Mechanics*, 87(3):031002.

Zhu, J. and Brassart, L. (2025). Stretching response of a polymer chain with deformable bonds. *Physical Review Letters*, 134:218101.

Zhurkov, S. and Korsukov, V. (1974). Atomic mechanism of fracture of solid polymers. *Journal of Polymer Science: Polymer Physics Edition*, 12(2):385–398.

Zimmerman, J. A., Jones, R. E., and Templeton, J. A. (2010). A material frame approach for evaluating continuum variables in atomistic simulations. *Journal of Computational Physics*, 229(6):2364–2389.

Zündel, M., Mazza, E., and Ehret, A. E. (2017). A 2.5 d approach to the mechanics of electrospun fibre mats. *Soft Matter*, 13(37):6407–6421.